MASS TRANSFER ACROSS THE TURBULENT GAS-LIQUID INTERFACE

XU ZHIFENG

(B. Eng., M. Eng., Huazhong University of Sci. & Tech., China)

A THESIS SUBMITTED

FOR THE DEGREE OF DOCTOR OF PHILOSOPHY

DEPARTMENT OF MECHANICAL ENGINEERING

NATIONAL UNIVERSITY OF SINGAPORE

2007

ACKNOWLEDGEMENT

I would like to express my deepest gratitude to my supervisors Profs. B C Khoo and C B Ching for their invaluable guidance, encouragement and patience throughout this study. Prof. Khoo has taught me a great deal not only on the research work, but also in other fields. It would be of great help for my future endeavors. I also would like to extend my gratitude to Prof. N E Wijeysundera, Dr. K Carpenter and Dr. T Pavel. Their comments and suggestions improved my work and this thesis.

In addition, I thank the staffs and students working in the Fluid Mechanics Lab for their warm-hearted help and excellent service during the course of this work. Thanks to Mr. Yap C S, Mr. Looi S W, Mr. Tan K W, Ms. Iris Chew, Ms. Lee C F, and many more, their rich experiences help me overcome many difficulties during this study.

My gratitude also extends to my wife and my families for their support and encouragement all the way. Their support and encouragement provide the motivation for me to finish this work. This experience has shown me much blessed to be a part of such a wonderful family.

Finally, I want to thank the National University of Singapore and Institute of Chemical & Engineering Science for providing me the research scholarship and an opportunity to pursue the Ph.D degree in the Department of Mechanical Engineering.

TABLE OF CONTENTS

SUMMARY

Mass transfer across the turbulent gas-liquid interface is important in many fields. However, the present understanding of the scalar transport as mediated by the complex near surface turbulence is still far from complete. Investigation by Hanratty and co-workers have suggested using a single critical parameter β (the gradient of the vertical fluctuating velocity at the interface) to determine the scalar transfer across the gas-liquid interface. It is found that in the immediate region next to the interface on the liquid side, there exists a linear distribution region for the vertical rms velocity, where Hanratty's β is defined. Since the concentration boundary layer thickness at the interface is much less than the thickness of the momentum boundary layer, performing direct velocity measurements very close to the gas-liquid interface to quantify such a parameter can be challenging. Law & Khoo (2002) have successfully measured this parameter under two distinct flow conditions and presented an empirical relation to correlate the mass transfer velocity across the gas-liquid interface with the selected turbulence parameter β. However, the validity and accuracy of the model are not tested more extensively.

In this work, an improved measurement method was developed to quantify β in the immediate vicinity region near the gas-liquid interface. A series of experiments with more varied flow conditions were carried out. In particular, the critical parameter β was measured for several representative flow arrangements encountered in the environment: turbulence generated from above (in the gaseous phase) as in

wind-induced flow, turbulence generated simultaneously from above and below in the same direction, and separately generated in the opposite direction. In the midst of such measurements, the mass transfer experiments were carried out with the aim of providing a relationship between the mass transfer velocity and the selected hydrodynamic parameter β. In this work, oxygen was selected as the tracer gas instead of carbon dioxide used in Law & Khoo (2002), and gas evasion and absorption rate were measured to provide a more general relationship. Based on these experimental works, a more general correlation was presented, which concurs reasonably with other reported works covering more complex and typical flow conditions.

The second major aspect of this work is on the falling film configuration. Falling film is widely found in chemical engineering and other fields, where mass/heat featured prominently across the thin film interface. Being so, a series of experiments in an inclined thin falling film apparatus were carried out to determine the β distribution and the associated mass transfer velocity. It has been found that β is equivalent to the surface divergence as first implemented by Tamburrino (1994). Following Tamburrino, the film surface motion was captured by a high speed camera and the surface divergence was deduced to yield β to correlate with the associated mass transfer velocity. There is broad agreement with the above mentioned general correlation. Separately, numerical simulation was also carried out in the present work for a vertical falling film arrangement. The falling film wave dynamics were discussed and compared with previous experiments. The simulated falling film gives rise to β which can be made to relate monotonically to the mass transfer velocity in a

form very similar to the scalar transport empirical relationship as Law & Khoo (2002). Overall, the agreement for the thin film flow arrangement with the general correlation based on β obtained previously in Law & Khoo and further refined to accommodate recent experiments indicates well that there may exist an universal correlation for the scalar transport across the turbulent gas-liquid interface essentially independent of the means of turbulence generation.

LIST OF FIGURES

NOMENCLATURE

A area of the interface [m^2]

C concentration of the gas species in liquid [mol/m^3]

Ci initial concentration of gas species in liquid [mol/m^3]

$C_{i/f}$ dissolved gas concentration at the interface [mol/m^3]

C_f final concentration of gas species in liquid after time t_f [mol/m^3]

C_s gas species concentration at the water surface [mol/m^3]

C_b gas species concentration in bulk region of the liquid side [mol/m^3]

D diffusion coefficient [m^2/s]

F transport of gaseous species across an interface per unit area [$mol \cdot m^{-2} \cdot s^{-1}$]

F_{vol} volume force [N]

f disturbance frequency [hz]

g acceleration of gravity [m/s^2]

h_p wave peak height [m]

h_{am} wave amplitude [m]

K_L liquid side mass transfer velocity [m/s]

K_F physical properties group ($K_F = \rho^3 \nu^4 g / \sigma^3$)

L macro length scale [m]

N_{hp} dimensionless wave peak height ($N_{hp} = h_p (g / \nu^2)^{1/3}$)

N_{uw} dimensionless phase velocity ($N_{uw} = u_w / (\nu g)^{1/3}$)

N_λ dimensionless wave separation ($N_\lambda = \lambda (g / \nu^2)^{1/3}$)

P pressure [pa]

Q Volumetric flow rate [m^3/s]

Re Reynolds number

R distance from the center of the rotation to the center of the water channel [m]

Sc Schmidt number

Δt time step [s]

T temperature of the water [^oC]

U_{mean} mean flow velocity in the direction of x [m/s]

u* interfacial friction velocity [m/s]

u_w wave speed [m/s]

V_β velocity scale where $v_{r\text{-}rms}$ departs from the linear behavior [m/s]

V_w the volume of water in the system [m^3]

v velocity component in the direction of y [m/s]

v_i interface vertical velocity [m/s]

v_r vertical velocity with respect to the interface [m/s]

W width of the test section in falling film setup [m]

w velocity component in the direction of z (m/s)

x coordinate in direction parallel to the interface along the mean flow direction [m]

y coordinate in the direction normal to the water surface [m]

z coordinate in the direction parallel to the interface, perpendicular to x [m]

Greek symbols

α volume of fraction

β vertical velocity gradient at the interface [1/s]

δ thickness of the mass boundary layer [m]

ε rate of turbulence dissipation [m^2/s^3]

θ inclined angle of the test section to the horizontal [degree]

λ wave length [m]

μ liquid dynamic viscosity [kg/(m·s)]

υ liquid kinematic viscosity [m^2/s]

ρ density [kg/m^3]

σ surface tension [N/m]

τ surface renewal time [s]

ω rotation speed of the rotor driving the paddles [rad/s]

Δ thickness of falling film [m]

Λ_β distance from the interface where the variation of $v_{r\text{-}rms}$ remains linear [m]

Subscript

rms root–mean-square

Chapter 1 Introduction

1.1 Definitions and Motivations

Mass transfer across the gas-liquid interface has enormous importance in various natural and industrial processes, such as ocean-atmosphere interactions, carbonation of soft drinks in the beverage industries as well as sanitation methods used in water quality management and waste water treatment processes. Because of its wide application, a general model capable of predicting the mass transfer velocity across the gas-liquid interface would be most invaluable.

The mass transfer across the gas-liquid interface is a form of interfacial mass transfer. It can be complex since the gas and the liquid may be in turbulent motion, and the interface between them is often highly irregular, and possibly accompanied by waves with wave breaking and leading to the entrainment and formation of bubbles. Fundamentally, the scalar transfer between a less soluble gas and liquid occurs through the thin mass boundary layer near the interface on the liquid side, which is embedded within the hydrodynamic/momentum boundary layer. For sparingly soluble gases like oxygen and carbon dioxide, the diffusivity in the gas side is much larger than that in the liquid side, and hence the resistance is determined predominantly by the liquid side hydrodynamics.

In this thesis, all the cases studied were under the conditions of unbroken gas-liquid interface. The more complex situation of a liquid surface that is broken due to waves or through strong upwelling events is not considered.

Mass transfer of less soluble gas through the gas-liquid interface is affected by many factors, such as the difference of concentration between the phases, temperature,

flow conditions and especially the conditions right at the interface. It has been reported that surfactants or insoluble compounds adsorbed onto the interface will inhibit gas transfer through the gas-liquid surface (Molder et al. (2002), Vasconcelos et al. (2003), and McKenna & McGillis (2004)). Many theories (e.g. eddy diffusivity model and eddy structure model) have been proposed to describe the mechanism governing the gas-liquid mass transfer, and many works have been conducted in the attempt to determine the primary parameters governing the gas-liquid mass transfer (see Theofanous (1984) for a review). However, there has been no consensus on a general and yet sufficiently robust model which is capable of predicting the transfer velocity over different flow conditions. Most of the models proposed are based on such parameters that are directly dependent on the experimental conditions like the particular means of turbulence generation and/or experimental setup geometries. Such models will not be applicable under other turbulence conditions. A robust model should be based primarily on the hydrodynamic parameters obtained from the turbulence structure in the very vicinity of the interface. In the past few years, some progresses have been made towards the development of a robust model, like the work found in Law and Khoo (2002). They demonstrated the role of a key parameter (β) --- the interfacial vertical fluctuation velocity gradient---for the mass transfer process. Their experiments were only carried out for the above gaseous species absorbed into the below liquid phase under two distinct flow conditions: one with turbulence generated from beneath the interface, and the other via wind shear from above the interface. Although the validity and accuracy of the model were not tested more extensively, their work was probably the first few where two separate means of turbulence were generated and a consistent scalar transport model based on β was obtained. One main objective of this work is to test the model against a wider range of

flow conditions, such as the generation of turbulence in the liquid via co-current and counter-current flows, and thin-film flow arrangement.

1.2 Basic Mechanisms

The transfer of gases across the gas-liquid interface is determined by the interaction of turbulent and molecular transport processes. Both transport processes can be characterized by diffusion coefficients. The flux density **F** (mass flux per unit area) is proportional to the diffusion coefficient D and the concentration gradient:

$$F = D\nabla c \qquad \text{(Fick's law).} \qquad (1\text{-}1)$$

The dimensionless ratio $Sc = \nu / D$ known as the Schmidt number is used to express the diffusion coefficients of a scalar tracer relative to that of momentum in the transporting medium. It plays a role in convective mass transfer analogous to the role played by the Prandtl number in convective heat transfer. Away from the interface, the turbulent transfer is typically orders of magnitude higher than the molecular transfer, while toward the interface, molecular transport eventually takes control. This leads to the formation of viscous and mass boundary layers on both sides of the gas-liquid interface. In the gas phase, these two (viscous and mass) layers are about the same order of thickness, because the values of diffusion for various gaseous species and momentum are about the same (for example values of Sc in air at normal temperature: CO_2 1.00; O_2 0.83; CO 0.77; NO 0.87). The situation is completely different in the liquid phase. For example the Schmidt number for oxygen is 400 at 300K in water (Mills (2001)). It indicates that the molecular diffusion of oxygen is 400 times slower than the diffusion of momentum. Thus the mass boundary layer is significantly thinner than the viscous boundary layer in the water side by at least two orders of magnitude. The significantly lower diffusivities also shift a much larger fraction of the

resistance for transport into the mass boundary layer, so almost all of the concentration change occurs there. This is the reason more attention should be paid to the immediate vicinity of the interface in the liquid and it can be assumed that the concentration away from the interface is well mixed.

The overall properties of the mass transfer across the boundary layer near the interface show characteristic mean properties that can be described by a transfer velocity K_L, the mass boundary layer thickness **δ** and a time constant **τ**. The transfer velocity K_L, also known as transfer coefficient, is defined as the net flux density divided by the concentration difference between the interface and the bulk region:

$$K_L = \frac{F}{C_s - C_b}. \tag{1-2}$$

The boundary layer thickness **δ** is entirely within the viscous sublayer, and can be approximated as:

$$\delta = \frac{D}{K_L}. \tag{1-3}$$

And the time constant **τ** for the transport across the boundary layer is given by:

$$\tau = \frac{\delta}{K_L} = \frac{D}{K_L^2}. \tag{1-4}$$

These scaling parameters are not independent. They are coupled via the diffusion coefficient D. Therefore, only one of the parameters needs to be measured in order to determine the scaling parameters of the scalar transport across the interface.

1.3 Conceptual Models Description

Various models have been proposed to correlate the liquid side mass transfer velocity K_L to suitable liquid side hydrodynamic parameters. Theofanous (1984), in a

review of various conceptual models, classified these different models into two major categories: eddy diffusivity model and eddy structure model.

1.3.1 Eddy Diffusivity Model

Possibly, the earliest and perhaps simplest model for interfacial mass transfer is the film theory presented in 1904 by Nernst (see also Cussler (1984)). It assumes that a stagnant film exists very near the interface. The mass flux across the film is solely by molecular diffusion. Because molecular diffusion is a much slower process than turbulent diffusion, the resistance to mass transfer is localized mainly in the film. Due to the steady uniform laminar flow in the film region, the gradient of concentration is linear, and a relation between the mass transfer velocity K_L, the diffusion coefficient D, and the thickness of the diffusion film δ is found as:

$$K_L = \frac{D}{\delta}. \tag{1-5}$$

In this model, the thickness of the diffusion film δ is selected to characterize the hydrodynamics near the interface. For example, Davies & Rideal (1963) studied a clean air-water interface case, and showed through a more detailed analysis that $K_L = D/2\delta$ where δ is taken to be the molecular diffusion layer thickness and is considered stagnant for mathematical purposes. Through turbulent boundary layer scaling, they found that

$$\delta = \left(\frac{D\sigma_e}{0.4\rho u_0^3} \right)^{1/2}, \tag{1-6}$$

where u_0 is a velocity scale for the near-surface bulk turbulence and σ_e is an equivalent surface tension that includes gravitational effects.

The primary difficulty of this model lies in the fact that δ is not constant, but it is

a function of time, space, and diffusivity in a turbulent flow field. Since this model is too difficult to apply in real applications, further theories were proposed to estimate δ. This leads to the development of eddy structure model.

1.3.2 Eddy Structure Model

Eddy structure model is also known as surface renewal model. The model is expressed in the form as:

$$K_L = \sqrt{\frac{D}{\tau}}. \tag{1-7}$$

The free surface is assumed to be populated with an array of surface parcels that are periodically replaced by bulk fluid elements by the turbulent flow. The averaged surface renewal time (τ) is thought to govern the mass transfer across the liquid interface. In such models, turbulent eddies larger than the thickness of the mass boundary layer play the dominant role. Statistically they replace the whole or parts of the surface layer by volume elements from the bulk. The classical surface renewal model was firstly presented by Higbie (1935), and was improved upon by Dankwerts (1951). The ramifications of these models for δ are described by Gulliver (1990). They assumed that the film thickness is reduced to zero by turbulent eddies coming from the bulk of the fluid at prescribed frequencies. There are other attempts to estimate the surface renewal time, such as using various velocity and length scales to estimate the renewal time. For example, in the large eddy model (such as in Fortescue & Pearson (1967)), the macro-scale L and the intensity V are used as the length and velocity scales, respectively, to approximate the renewal time: $\tau \approx L/V$. On the other hand, in the small eddy model (such as in Lamont & Scott (1970)), eddy sizes with

the order of turbulence dissipation (ε) are used: $\tau \approx (\nu/\varepsilon)^{1/2}$. The difficulties with the surface renewal models are that they are conceptual and are not directly related to near interface turbulence. Therefore, the measurements of surface renewal eddies are difficult to correlate with the mass transfer velocity, as the investigators have to define what constitutes a surface renewal eddy by themselves.

1.3.3 Surface Divergence Model

In a review of studies in various mass transfer models, Hanratty (1991) highlighted the development of a model that relates the mass transfer velocity directly to the hydrodynamics near interface without resorting to the above mentioned conceptual models. Hanratty and co-workers developed the boundary layer equation for concentration in a turbulent flow field near slip-free interface. Using a coordinate system embedded on the gas-liquid interface, the mass balance equation relating the concentration field in the water side to the velocity field near the interface is given as:

$$\frac{\partial C}{\partial t} + u\frac{\partial C}{\partial x} + v\frac{\partial C}{\partial y} + w\frac{\partial C}{\partial z} = D\left(\frac{\partial^2 C}{\partial x^2} + \frac{\partial^2 C}{\partial y^2} + \frac{\partial^2 C}{\partial z^2}\right), \tag{1-8}$$

where x- and z- are on the plane parallel to the interface, and y- is in the direction normal to the interface. C is the instantaneous concentration of the gaseous specie dissolved in the water. D is the diffusivity of the gaseous species in water. u, v and w are the fluctuating velocity components in the x, y and z directions, respectively. Since the characteristic thickness of the concentration boundary layer at the interface is very thin, derivatives in the normal direction (y-) are much larger than those in the other two directions. Hence Equation (1-8) can be simplified as:

$$\frac{\partial C}{\partial t} + v\frac{\partial C}{\partial y} = D\frac{\partial^2 C}{\partial z^2}. \tag{1-9}$$

McCready et al. (1986) conducted a series expansion and order of magnitude analysis near the interface and deduced the following relation for the vertical fluctuating velocity:

$$v = \beta y . \tag{1-10}$$

That is, at the vicinity of the interface, v varies linearly with y with a gradient of β. From Equations (1-9) and (1-10), the importance of β is apparent to mass transfer across the gas-liquid interface. The vertical fluctuating velocity gradient is a function of time and distance along the interface.

In recent years, the name 'surface divergence model' has been given to the model for a quantitative description of the gas-liquid interfacial mass transfer given nominally by the parameter ($\nabla_h \cdot V$),

$$\nabla_h \cdot V = \frac{\partial u}{\partial x} + \frac{\partial w}{\partial z} \quad \left(= -\frac{\partial v}{\partial y} = -\beta\right), \tag{1-11}$$

where ∇_h is the horizontal two dimensional divergence operator and V is the velocity fluctuation vector. For the cases where the interface is relatively smooth, these two parameters ($\nabla_h \cdot V$ and β) are equivalent, as shown by Tamburrino (1994), and also noted in Tamburrino & Gulliver (2002) and McKenna & McGills (2004). However, when the interface is highly undulating in the presence of large amplitude waves, Banerjee et al. (2004) modified the mentioned equivalence by taking into account the surface curvature. In their expression, an additional term relating to the curvature of the fluctuating interface as opposed to a flat interface, i.e.

$$\nabla_h \cdot V = \frac{\partial u'}{\partial x} + \frac{\partial v'}{\partial y} - 2w'\nabla \cdot n . \tag{1-12}$$

1.3.4 Advantages of Surface Divergence Model

It has been found that in the immediate region next to the free surface there exists a linear distribution region of the vertical velocity according to Equation (1-10). That is to say, β can be estimated through the linear vertical velocity distribution in that region. The importance of β is apparent from the concentration boundary equation. The development of β as the critical parameter governing the mass transfer across the gas-liquid interface has significant advantages over the prior conceptual models. Firstly, β is located directly in the region critical to the mass transfer process. It is taken from the immediate vicinity of the interface, where the largest resistance to mass transfer exists. Secondly, β is not related directly to any turbulence generation mechanism. This is important to ensure the model based on β is robust and applicable to a wide range of turbulent interface conditions and independent of the means of turbulence generation.

Though the role of β as the crucial parameter to determine the interfacial mass transfer velocity has gradually been acknowledged by researchers, there is still a lack of studies on the measurement of such parameters in the vicinity region of the interface and the quantitative correlation to the mass transfer velocity. This gives us the motivation for the present study. The objective is to measure and quantify β near the interface, and investigate its relationship to the scalar transport velocity across the gas-liquid interface. This study will also help to build up database on near-surface turbulence in the liquid side. It would be beneficial for a better understanding of the mass transfer mechanism across the gas-liquid turbulent interface. Finally, the scalar transfer model proposed in the present study would be helpful to quantitatively predict the scalar transport in practical applications.

1.4 Structure and Scope

The aim of this study was to develop reliable methods for the near surface flow field measurement and to present a mass transfer model based on the surface divergence model or β. For the near surface flow field measurement, the velocity distribution in the immediate vicinity of the interface is the foremost problem for developing a mass transfer model. As such, one focus is on developing reliable measuring methods for the velocity distribution in the near surface region.

For simulating the real-life complex turbulent flow conditions, we chose three kinds of flow conditions: 1) the turbulence generated in the liquid from above the water surface as induced via wind shear; 2) the turbulence generated simultaneously from above and below the water surface in the same direction (i.e. co-current); and 3) the turbulence generated simultaneously from above and below the water surface in the opposite direction (i.e. counter-current). The real-life turbulence generation methods can be regarded as a combination of these three kinds of turbulence generation methods. In the midst of such measurements, the mass transfer experiments were carried out. For the mass transfer experiments, oxygen (O_2) was chosen as the tracer gas since it is regarded as not so soluble in water and has wide applications in industries. Gas absorption and evasion experiments were carried out to provide a more comprehensive understanding. The detailed information about the experimental setup and measurement technique are described in Chapter 2. The near surface flow conditions and the key parameter β are provided in Chapter 3. Based on these measurements and combination with prior works, a mass transfer

model/correlation is presented in Chapter 3. For an ever wider range of flow conditions, experimental works were carried out for the thin film flow configuration. The experimental setups and correlated techniques are described in Chapter 4. Experimental results and the role of β for this kind of setup are discussed in Chapter 5. A numerical simulation work was carried out for a vertical falling film with forcing disturbance frequency in Chapter 6. The characteristic of β, concentration profile and local mass transfer velocity were obtained and analyzed in the light of the mass transfer model presented in Chapter 3. Finally, some concluding remarks on the general applicability of the mass transfer correlation obtained and recommendations for future work are presented in Chapter 7.

Chapter 2 Experiments in Circular Wind Wave Tunnel

2.1 Introduction

As we have discussed before, the key parameter governing the interfacial mass transfer is the gradient of the vertical fluctuating velocity taken with respect to the moving interface. As such, a required measurement technique must be able to track the moving interface and simultaneously measure the flow field at locations just beneath it.

The almost continuous fluctuation of the interface makes such simultaneous measurements extremely difficult and effectively ruled out the use of Eulerian-based instruments like hot-wire anemometer and LDV employed in the conventional way. This is because these traditional measurement methods are based on measurement at specific location(s) and do not have the ability to track the fluctuating interface. In the early works, Jahne et al. (1987) and Duke et al. (1995) proposed the use of surface wave slope as proxy to the vertical velocity just beneath the interface. The assumption is made as the normal velocities caused by the interface fluctuation are directly related to the wave slopes. It is expected that the key parameter β, defined as the gradient of the vertical fluctuating velocity taken with respect to the interface at the interface, should be strongly affected by the variations of wave slope. Based on this assumption, some experimental techniques for the measurement of surface wave slope were developed, such as the works of Jahne & Reimer (1990) and Zhang & Cox (1994). Some researchers (such as Duke et al. (1995) and Saylor & Handler (1997)) reported that the measured wave slope correlated well with the measured interfacial mass transfer rate. It is noted that such studies were required to be carried out on fairly strong wind induced turbulent interface or in situations where there are significant

amplitude of surface fluctuation for the convenience of wave slope measurement. Such requirements may limit the application of these methods. The use of wave slope can not be applied in the situations where the interface is relatively quiescent, which can be found for the cases where the turbulence is generated beneath the interface. Typical examples can be found in the grid stirred tank cases (such as George et al. (1994), and Mckenna & McGillis (2004)) where the turbulent is generated by a deep submerged jet (Law et al. (1999)), and for cases where the interface is damped (due to presence of surfactant).

It is clear that direct measurement and quantification of β near the gas-liquid interface can be challenging. PIV-based techniques which provide the advantage of non-interference with the flow and, at the same time allow spatial measurements at various depths beneath the interface and the interface tracking may be the key for the quantification of β. The principle of PIV-based techniques is to visualize the interface and the fluid movement beneath it on a single image. The movement of the interface and the flow field beneath it can then be analyzed by examining sequence of images taken at a known time interval Δt. Interface tracking routine is then applied to the images to detect the position and the movement of the interface. Thus entirely velocity profile can be obtained, which represents a significant advantage over the traditional single point measurement methods. The PIV technique used to obtain the velocity profile beneath the interface is well established. The main difficulty lies in the interface visualization and tracking method. Several researchers have attempted such measurements and the following paragraphs review some of the techniques.

In the early PIV-based experiments, such as Jahne & Wierzimok (1990), the interface is usually visualized as a fairly thick horizontal wavy line probably because of the effect of the meniscus formed at the contacting positions of water and channel.

The use of 'line thinning' technique as suggested by the authors to locate the interface can be rather inaccurate. This is because the thickness of the wavy line observed can and will easily overwhelm the depth of the concentration boundary layer thickness next to the interface. Hassan et al. (1996) used a different approach and identified the interface through illumination of floating particles. However, as the interface fluctuation causes the floating particles to move, continuous visualization of the interface profile is difficult, and the interface is often seen as 'broken'. The interpolation method used to determine the interface profile from patches of floating particles is not very viable, as occasionally, pretty large section of the interface is not visualized. The use of many floating particles helps to overcome the problem of 'broken' interface. However, this method brings into contention whether the flow field near to the interface is affected by the very presence of the many said particles.

Another class of method is based on the optic property of laser light. Lorencez et al. (1997) used thin laser beams to activate the dye tracer presented in the flow field and formed a certain pattern by the underside of the water surface. Baumann & Muhlfriedel (2001) used total (internal) reflection of a laser beam at the interface to determine the vertical position of the interface. These techniques, though capable of obtaining the interface profile, do not allow or facilitate the simultaneous measurement of the flow field beneath the water surface. Lin & Perlin (1998) also utilized the total (internal) reflection principle and arranged the camera at a special angle to observe the interface. In this method, besides the difficulty of simultaneous observing the flow field beneath the interface, there is a special requirement for laying out the test section.

To avoid the effect of the meniscus, which is commonly formed at the contacting position of the liquid and the container, Munsterer & Jahne (1998) suggested

observing the interface and the beneath flow field from a position slightly below the water surface. While this arrangement will cause the flow field be mirrored above the water surface by reflection at the water surface, the authors suggested using an image processing technique which finds the local maximum symmetry as the water surface position. Since the water surface is usually undulating and the mirror image will be distorted when waves are present, this method is less reliable in the presence of large wave amplitude. Peirson (1997) adopted a similar method to observe the flow field from beneath the interface, while he used another camera to observe the interface from a position above the interface. The additional view from above produced an unobstructed and good visualization of the interface. Configuration software is needed to make the two cameras to be aligned in space. The referenced scale for the subsurface imagery was set to puncture the initial still water surface. Images were captured by each of cameras and overlaid on a display monitor. Software was then used to scale and reposition the images so that both the horizontal and vertical alignment was achieved. Based on this method, Law & Khoo (2002) attempted to use two pairs of viewing mirrors to reflect these two different views onto a single plane. But using only one camera brings two issues: one is focusing difficulty, and the other is the possible difference in magnification. Focusing difficulty means the above and below images cannot be focused well simultaneously because of the changes of optical medium. The difference in magnification is also caused by the changes of optical medium, and this may lead to difficulties in correlating the two different viewing angles. The obvious advantage of this kind of method is the absence of any meniscus effect and the interface can be detected accurately. It is noted that this method entails a carefully managed and accurate image capture system and critical arrangement and calibration to avoid the effect of image distortion caused by tilted

arrangement of cameras.

In the present work, following Law & Khoo (2002), with the availability of two independent camera systems, further improvements can be made for a more accurate quantification of the interface position and improvement of the spatial resolution of the flow field close to the interface.

2.2 Experimental Setups

2.2.1 Circular Wind Wave and Jet Stream Channel Tank

The experiment was carried out in a circular wind-wave channel tank with two water jet streams at separate locations directed in the tangential streamwise direction along the channel bottom. Figure 2.1 shows the schematic diagram of the circular water tank. It consists of an annular water tank with water in the circular channel. The channel is of 10cm depth and 10cm width. The outer diameter of the tank is 75cm, while the inner diameter of the tank is 40cm. The entire setup is made of transparent Perspex material, so as to facilitate flow visualization and measurement. Air flow is generated by means of a rotor with four Perspex paddles (20cm width) arranged at right angles above the annular channel. The distance between the paddles and the water surface can be adjusted, and the rotating speed and rotating direction of the paddles is controlled by a rotor. The two water jet streams through four 3-mm diameter nozzles (placed diametrically opposite) beneath the interface can generate a clockwise direction flow along the bottom of the circular tank via the inlets and outlets connected to a water pump. The speed of the water jet generated by the water pump can be varied using a ball valve and the volumetric flow rate was measured with a flow meter. So by using these two independent means of turbulence generation from

above and beneath the gas-liquid interface, a variety of flow conditions imposed on the liquid surface and its vicinity can be obtained. In this work, several representative kinds of flow conditions were chosen: turbulence generated by solely wind shear from above, turbulence simultaneously generated by wind shear from above and water jet from below in the same direction (co-current) and in the opposite direction (counter-current). These representations of turbulence generation methods are deemed more general and perhaps all encompassing. They can be considered as a reasonable simplification of the most real life complex flow conditions.

For the present experiments, pure water was filled to a depth of 7.5 cm in the channel, and the paddles were located at 7.5cm above the water surface. The flow rate through the water pump was adjusted with the combination of a ball valve and a flow meter. With a given flow rate from beneath, the turbulence intensity near the interface is still a function of the variable imposed wind speed from above. Table 2.1 summarizes the groups of different flow conditions studied.

For purpose of reference, the notional air flow speed above the water surface is assumed to be the same as paddle speed, which is taken directly above the center of the 10cm width water channel. This method of referencing follows that of Law & Khoo (2002)

$$V_{wind} \approx R\omega . \tag{2-1}$$

Here ω is the rotation speed of the rotor driving the paddles, and R is the distance from the center of the rotation shaft to the center of the water channel. The rotation speed of the rotor is measured using a tachometer. The paddle speed above the center of the water channel is taken as the parameter denoting the intensity of turbulence generated at the water surface of the wind wave channel. Since the major or practically all of the resistance to the mass transfer in this experiment (low solubility

gas is used) resides in the liquid side, accurate measurement of wind velocity profile in the vicinity of the interface is deemed unnecessary, and will not aid further in the quantification of the critical parameter influencing the interfacial mass transfer.

Table 2.1: Summary of the PIV experimental conditions

Flow conditions	Flow rate (ml/s)	Direction	Nominal wind speed (m/s)
Case 1	0		3, 3.5, 4, 4.5, 5, 5.5, 6, 6.5, 7
Case 2	6.3	Opposite	3, 3.5, 4, 4.5, 5, 5.5, 6, 6.5, 7
Case 3	6.3	Same	3, 3.5, 4, 4.5, 5, 5.5, 6, 6.5, 7
Case 4	3.2	Opposite	3.5, 4.5, 6, 6.5
Case 5	3.2	Same	3.5, 4.5, 6, 6.5
Case 6	10.5	Opposite	3.5, 4.5, 6, 6.5
Case 7	10.5	Same	3, 3.5, 4.5, 6, 6.5

The range of nominal wind speeds carried out in this study is 3.00m/s to 7.00m/s. The range is sufficient for development of a model relating near surface turbulence parameters to the interfacial mass transfer velocity. The upper limit wind speed is chosen such that the turbulence intensity generated is well below the margin where wave breaking occurs.

For mass transfer experiments, the circular wind wave channel can be sealed by a

gas tight lid. The tracer gas is input through the opening at the side of the tank, and the residual gas (mainly air, lighter than the tracer gas) is naturally exhausted out of the system through the outlet opening located at the top. In this study, oxygen was selected as the tracer gas for its common usage in industrial and low solubility. As the supplied gas is stored at a temperature cooler than the bulk tank water in the test section, it needs to be preheated to the same temperature before being introduced into the setup. This is done by passing the gas through a heat exchanger, immersed in a large water bath. In the test section, the tracer gas is introduced just above the interface and with special care taken so as not to induce any interface disturbance. Before each experiment, the tracer gas is introduced for at least 20 minutes (for evasion experiments) or 10 minutes (for absorption experiments) to ensure uniform initial conditions. The most important aim is to prevent any buildup of non-condensable gases (notably air) residing close to the interface.

This setup is quite compact and tends to produce a fairly homogeneous interface conditions that are not fetch-dependent like in other traditional linear wind wave facilities. It also has smaller enclosed air volume compared with the latter. Because of these merits, this setup is deemed suitable for the study of interfacial mass transfer. Numerous interfacial turbulence characteristic and mass transfer studies had been conducted using this type of setup (Jahne et al. (1979), Jahne et al. (1984), and Law & Khoo (2002)).

2.2.2 Image Recording System

In PIV measurements, as in other optical experiments, image recording is the basis and its quality is all important and needs to be optimized. In this experiment,

two high quality digital cameras (Pixelfly, HiRes model) mounted with a macro lens were adopted. Some key specifications and typical values of the camera are shown in the following table. It has the potential to record two subsequent images within a very short time interval. The time interval between two subsequent images can be adjusted and controlled by using an external TTL signal.

Table 2.2: some key specification and typical values for the camera

Number of pixels	Pixel size	Spectral range	Interframe time
1360(H) ×1024(V)	4.65μm×4.65μm	280---1000nm	15μs ± 5μs

This system has several advantages over other experimental setups based on standard video format such as used by Law & Khoo (2002). It has a higher spatial (around 20μm/pixel) and temporal resolution (2ms). And the most important thing is it bypasses the digitization process, which is necessary for video format processing. Raffel et al. (1998) pointed out that due to the analog nature of the standard video signal, a small frame-to-frame jitter during the digitization process can cause pixels to be slightly misaligned which in turn increases the measurement uncertainty in the displacement data. This problem typically worsens when a standard (analog) video recorder is used.

2.2.3 Light Source

Lasers are widely used in PIV because of their ability to emit monochromatic light with high energy density, which can easily be bundled into thin light sheet for illuminating and recording of the tracer particles without chromatic aberrations.

Generally, it is preferred to use pulse laser for PIV measurements. This is because the duration of the illumination light pulse should be short enough that the motion of the particles is frozen during the pulse exposure in order to avoid blurring of the images (no streaks). The streaks bring difficulty to the displacement estimation. Modern pulse lasers (such as Nd: YAG laser) can provide nanosecond (ns) scale of duration time. In this study, Nd: YAG laser (QUANTA system, model: P.I.L.S) is used as the light source. The delay time between two successive illumination pulses can be adjusted through the front panel, and the laser can provides an external synchronized signal to control other equipments (TTL signal for camera control).

2.3 Experimental Techniques

2.3.1 Technique for Measuring Near Surface Turbulence

Figure 2.2 gives the schematic diagram for arrangement of the two titled cameras. Camera 1 and camera 2 were adjusted separately and titled at a small angle 7.5° to the horizontal. These small titled angles, obtained after numerous trials, ensure unobstructed and clear visualization of the flow field for all of the imposed flow conditions, while keeping the magnification difference between the top and bottom (known as distortion) not exceeding 5%. To visualize the water surface as a continuous edge, fluorescent dye was introduced to illuminate the visualization plane, which is similar to the work of Law et al. (1999, 2002). In this work, 30μm PSP (Polyamide seeding particles) particles were adopted after taking account of the similar density (1.03g/cm^3) as water and its ability to provide sufficient light reflection after introducing fluorescent dye.

It is noted that the two cameras and the laser must be synchronized to capture the

required images. This requirement was performed with the aid of a DA card (DT3000, Data Translation Ltd). The laser system can provide a synchronized signal when it emits the laser sheet. This signal is input into the Counter/Timer channel of the DA card to act as an external gate. When the gate is active, a pulse signal is generated to trigger the two cameras. The time-interval between successive images is 2ms-5ms depends on the flow conditions. Generally, the time interval increases with the flow velocity. The time-interval between successive image-pairs was set to be constant 100ms.

The typical images captured from camera 1 and camera 2 are also shown in Figure 2.2. With the introduction of fluorescent dye, the liquid side glows with certain luminance intensity, different from those of the particles. The interface is located at the edge of the contrast between the fluid and the air. The advantage of using fluorescent dye to visualize the interface is that, regardless of the interface fluctuation, the interface will always be visualized as a continuous edge with luminance contrast. The dye also produces contrasting luminance intensity from the particle seeding to allow the employment of PIV technique.

Before the start of an experiment, a careful scale calibration step is needed to correlate the images captured by camera 1 and camera 2. A referenced scale is set to 'puncture' the water surface at the plane of observation (coincide with the laser sheet plane). Images are captured by each camera and compared pixel by pixel. After obtaining the interface location from camera 1, a program is written to 'transform' the interface location to the bottom view (camera 2) using the bottom view local scaling. The program is used to scale and correlate the images so that both horizontal and vertical alignment is achieved. Some parts of the referenced scale images captured by the two cameras and the 'transforming process' from camera 1 to camera 2 are also

shown in Figure 2.2.

On a typical image of the gas-liquid interface captured from camera 1, the gas phase is distinguished as the dark region while the water body is of higher luminance intensity, due to the effect of the fluorescent dye. The conventional edge detection technique is based on finding the 'maximum gradient' point. Since the particles are brighter than the water body, edge detection worked directly on the gray image of the gas-liquid interface (captured from camera 1) will simultaneously reveal the edge of particles and the interface (see Figure 2.3). To filter out the particle points, an optimal threshold value of intensity is chosen to do binary operation. All of the pixels with intensity higher than the threshold will be turned into 1, and the other dark points will be turned into 0. Taking account of the possible uneven distribution of light intensity along the interface, the interface region is divided into a subset of discretized surface regions and the binary operation is performed in each small part. The threshold level is determined by an auto iterative technique developed by Ridler and Calvard (1978). The histogram of each corresponding small part is initially segmented into two parts using a starting threshold value, such as half the maximum intensity dynamic range. The sample mean gray values associated with the foreground pixels and the sample mean gray values associated with the background pixels are computed. A new threshold value is now computed as the average of these two sample means. This process is repeated, based upon the new threshold, until the threshold value does not change any more. A Matlab (The MathWorks, Natick, MA) program is written to perform all of these operations based on the described technique. After the binary operation, edge detection can be used to find out the interface location. Figure 2.4 shows the interface detected by this method. It is shown to be accurate via comparison with the original image. Figure 2.3 and Figure 2.4 show just the region near the

interface.

Compared to the prior work of Law et al. (1999, 2002), the present use of two independent camera systems help to overcome the previous mentioned two difficulties encountered by trying to capture the two distinct views onto a single image plane. In addition, these two independent cameras provide a much higher resolution (about $20\ \mu m/pixel$). These improvements ensure a clearer visualization of the interface and the associated flow field in the liquid side. The interface position can be determined more accurately. Because the image resolution is the major source of the measurement uncertainty, the present higher resolution has improved the experimental accuracy (increased from 40μm/pixel to 20μm/pixel in this work).

Analysis for the flow field beneath the water surface is performed using a commercial PIV software (Dantec, FlowManager). An adaptive correlation technique was adopted to calculate the velocity profile of the flow field because it can provide an increased dynamic range and accuracy. The fundamental principle of adaptive correlation is an iterative procedure: from an initial guessed offset value, an offset is introduced from the first window (the interrogation area in the image frame from laser pulse one) to the second window. The obtained vector is validated and is used as a new estimate for the window offset. Then a new run is made, but this time with a smaller window (interrogation area). The initial interrogation area is 128×64 pixels, and the final interrogation area is 32×16 pixels. The main benefit derived from using the shift window is capturing the particle images that moved out the interrogation area during the interval time (the time between the two light pulses). Loss of these particle images is known as the ‘in-plane dropout’, which reduce signal strength and, as a result, the number of successful vectors that can be obtained. Capturing more particle images for each vector permits the interrogation area to be refined while still

obtaining an adequate number of successful vectors without increasing the seeding density in the flow.

Following Law et al. (1999, 2002), the velocity with respect to the interface can be deduced by taking the difference between the flow field velocity (v) and the interface velocity located directly above the interrogation area of the velocity vector (v_i):

$$v_r(y) = v(y) - v_i . \tag{2-2}$$

To obtain the variation of vertical rms velocity with depth, many image pairs have to be analyzed and the vertical rms velocity is calculated by ensemble averaging of velocity located at similar depth from the interface. Every 100 images pairs were captured for each run, and the operation was repeated at least 5 times for each flow conditions. Precision uncertainty is reduced to about 2% by the ensemble average operation.

2.3.2 Technique for Measuring Interfacial Mass Transfer Velocity

In this study, the mass transfer velocity is determined by measuring both the dissolved oxygen evasion rate and absorption rate. Gas exchange velocities are determined by a disturbed equilibrium method. Tank water concentrations of the dissolved oxygen to be measured are perturbed from equilibrium before an experiment and the gas transfer velocity is computed by measuring the rate of return to equilibrium. The time rate of dissolved oxygen concentration change in the tank water is given by:

$$\frac{dC}{dt} = K_L A(C_s - C)/V_w , \tag{2-3}$$

where V_w is the volume of water in the test system, A is the nominal area of the

interface without waves, C is the bulk concentration of dissolved oxygen in water, C_s is the saturated concentration of oxygen at the interface, and K_L is the bulk liquid-side mass transfer velocity. The solution to Equation (2-3) is as follows:

$$K_L = (\frac{V_w}{At_f}) \ln \frac{(C_s - C_i)}{(C_s - C_f)}, \tag{2-4}$$

where C_i is the initial concentration of oxygen in bulk water, and C_f is the final concentration after time t_f.

The mass transfer velocity measurements were carried out separately from the turbulence measurements, and it is noted that precaution were taken to clean the interface well before each experiment. The tracer gas is preheated to the same temperature before being introduced into the test section. The temperature of the water in the test section is monitored with a thermometer to ensure that the variation is below ± 0.5 ºC.

For the gas evasion experiments, CO_2 was used to continually flush the tank headspace to yield a known zero oxygen surface concentration, i.e. $C_s(t) \approx 0\ mg/l$. For the gas absorption experiments, pure O_2 was introduced such that the total gaseous volume above the interface was considered to be saturated. Under such condition, C_s is maintained at the water surface at the corresponding water temperature. This value can be obtained from the manual supplied by the sensor manufacture (and in agreement with published measurements).

By measuring C_i and C_f, the liquid side mass transfer velocity K_L can be determined. In this study, bulk water side dissolved oxygen concentration was measured using a commercial fiber optic oxygen sensor (Model 210, Instech laboratories) with an accuracy of 1%. Figure 2.5 is the operation interface of the software used by the sensor. Water samples were taken from bulk region where the

dissolved oxygen concentration is assumed to be well mixed and independent of the location where samples were obtained**.** Table 2.3 lists the property of water in the experiments.

Table 2.3 Property of water in this experiment conditions

T(^{o}C)	**ρ**($\times 10^{3}$kg/m^{3})	**υ**($\times 10^{-6}$m^{2}/s)	**Sc**
21	0.99799	0.9798	558
22	0.99777	0.9569	532
23	0.99754	0.9348	506

The density and viscosity value are obtained from Lange's Handbook of Chemistry. The Schmidt number value for oxygen dissolved in water is obtained from Mills (2001).

The sensor uses two standards of known oxygen concentration and a linear algorithm for calibration. In this study, the two known oxygen concentration standards are zero concentration standard and atmospheric saturated concentration standard. The zero oxygen standards are obtained by adding sodium sulfite to DI (Deionization) water. This method is recommended by the operation manual of the optic oxygen probe. To prepare the atmospheric saturated standards, starting with DI water from a bottle held at ambient temperature for an extended period of time, and transferring it from cup to cup with ample turbulence at least 20 times. This procedure followed the instruction of DQM standard operating procedure (Katzenlson (2004)).

According to the theory of operation, the sensor will be most sensitive to low levels of oxygen and deviations from the linear relation occur primarily at higher oxygen concentration levels. The working range for oxygen evasion experiment was within the calibration range, whereas the absorption experiment was conducted in the

extrapolated range of calibration. A shorter time interval was therefore adopted to obtained the final water samples in the gas absorption experiments, which helps to ensure that the working range in the absorption experiments is not far away from the linear calibration range, although it may be mentioned that the gas absorption experiment is still less accurate than the gas evasion experiment. The oxygen evasion experimental results are deemed to be more credible than the absorption. In addition, the dissolved oxygen concentration at the surface remains to be zero, irrespective of the temperature in evasion experiment. While the surface concentration is assumed to be the same as saturation concentration in absorption experiment, it is known that the saturated concentration is strongly affected by the water temperature. Nevertheless these two means were used as a self-consistent check and to demonstrate that essentially the correlation relationship obtained is independent of the direction of scalar transport.

Concentration of C_i and C_f were obtained as the average values of at least five samples with a variation less than 2%. Taking into account the measurement uncertainty introduced by the instrument calibration, the overall measurement uncertainty for the gas evasion experiment is estimated to be around 5%. On the other hand, the measurement uncertainty for the gas absorption experiment is estimated to be about 10% or higher and attributed to the limitation posed by the oxygen probe.

Chapter 3 Experimental Results and Mass Transfer Model

In this chapter, the experimental results from the circular wind wave tunnel were analyzed. The key parameter β was deduced from the near surface vertical velocity profile, and its role was discussed in different flow conditions. Finally, the correlation between this selected parameter and the mass transfer velocity K_L was derived through a mass transfer model.

3.1 Near Surface Vertical Velocity Distribution

Figure 3.1 shows the typical variation of the vertical fluctuating velocity with respect to the interface (for Case 3 with nominal wind speed = 5 m/s). It can be seen that the vertical fluctuating velocity measured with respect to the interface increases with the depth. This quantity tends toward zero as the interface is approached. Such behavior follows the definition of V_r, as at the interface, there is zero velocity taken with respect to the interface itself.

It can be seen clearly from Figure 3.1 that a linear region appears to exist near the interface. This phenomenon is in agreement with the analysis of McCready et al. (1986) and confirmed in the experiments of Law & Khoo (2002). A linear fit through the origin can be performed on the data points located at the immediate vicinity of the interface. In this work, these linear least square fits were obtained employing as many data points as possible to provide a R^2 coefficient (coefficient of determination) still greater than 0.85. This value is considered to be reasonable after taking into account the measurement uncertainty of the experiments for all the studied flow conditions.

The most important parameter β_{rms} is defined as the gradient of the $V_{r\text{-}rms}$ profile near the interface, whose role has been discussed before and can be used to correlate with the mass transfer velocity across the turbulent gas-liquid interface. Together with the gradient of the linear variation, two other parameters can be obtained to characterize the near surface turbulence conditions as carried out in Law & Khoo (2002): Λ_β and $v_{\beta-rms}$. Λ_β is defined as the region where the variation of $V_{r\text{-}rms}$ remains linear; $v_{\beta-rms}$ is taken to be a velocity scale denoting the magnitude of $V_{r\text{-}rms}$ at the distance of Λ_β beneath the interface. After obtaining the value of β_{rms}, a second non-linear fit can be carried outside the linear region. The extrapolated interception of the linear fit with the non-linear curve fit is obtained and chosen to determine the value of Λ_β and $v_{\beta-rms}$ (see Figure 3.1). Figure 3.2 to Figure 3.45 present the variation of the vertical fluctuating velocity with respect to the interface for all the studied flow conditions. The x- coordinate has been made non-dimensional by the water depth in the channel.

Figure 3.46 shows the variation of β_{rms} with the nominal wind speed for all of the flow conditions studied. The results of Law & Khoo (2002) for only wind induced flow conditions are also included. It can be seen that this selected parameter generally increased with the wind speed. It clearly indicates that the near surface turbulence intensity expressed in terms of β_{rms} in the linear region is dependent on the imposed wind speed from above and the water flow velocity from beneath. On the comparison of the different β_{rms} value under the same water flow rate, it can be seen that turbulence generated in co-current flow (i.e. the wind above and water below the interface are imposed in the same direction) is deemed to have the largest turbulence

intensity in the vicinity of the interface region, while turbulence generated in counter-current has the smallest turbulence intensity in that region. Under the lower water flow rate conditions (3.2ml/s and 6.3ml/s), Figure 3.46 indicates that the near surface turbulence is primarily determined by the wind speed induced from above. It is suggested that the effect of the turbulence induced by the jet streams beneath the water surface barely reaches the near surface region or the associated influence on the vertical fluctuating velocity is very limited. It is also conceivable for the turbulence generated via the opposite direction, because at an elevation somewhere in the liquid the mean stream-wise velocity must tend towards a null quantity, the turbulence intensity associated with the vertical fluctuation of the interface has intuitively assumed a lower magnitude compared to the case of same direction where there is deemed some degrees of augmentation at a given wind speed. This general trend is applicable for the whole range of wind speed tested for the lower water flow rate conditions. With the increasing of the water flow rate from beneath via the jet streams, the near surface turbulence is obvious affected by the turbulence induced by the jet streams under the low wind speed conditions. A complete study of the relative importance of wind speed vis-a-vis the jet streams beneath the water surface whether in the same or opposite direction on β_{rms} is outside the scope of the present work, since the present intent is focused on correlating the measured β_{rms} generated from the vastly different means to the scalar transport rate. Lastly, it may be mentioned that regarding the comparison of the present results to Law & Khoo (2002) for the only wind induced turbulence cases, the deviations occur primarily in the low wind speed

range, which are usually associated with lower flow velocities (especially in the normal direction) and larger measurement errors or uncertainties; the differences are limited to be less than 20%.

3.2 Mass Transfer Velocity

Figure 3.47 presents the mass transfer velocity for the studied flow conditions. From this figure, it can be seen that the mass transfer velocity generally increases with the wind speed. This again demonstrates the general trend between turbulence intensity and mass transfer velocity. The mass transfer velocity in Figure 3.47(a) shows a fairly linear behavior passing through the origin for the case where only wind speed is imposed. A closer scrutiny reveals that for the case of same direction (Fig. 3.47(b)), K_L assumes a value perceptibly higher than the linear profile as obtained in Fig .3.47(a). On the other hand, K_L for the case of opposite direction (Fig. 3.47(c)) takes on quantities clearly below the linear region depicted in Fig. 3.47(a). This observation is not too surprising as deduced from Figure 3.46 if one presupposed that the mass transfer is directly proportional to β_{rms}. A careful examination of Figure 3.47(a), 3.47(b) and 3.47(c) suggests that on comparing to the gas evasion results, the mass transfer velocity obtained via the gas absorption experiment seems to assume a larger quantity and the difference tends to increase as the wind speed increases. Nevertheless, the difference in the measured K_L was limited to about 10%. As discussed before, the uncertainty arising from the dissolved oxygen concentration

measurement via gas absorption approach was higher due to the extrapolation technique employed during calibration. Overall, both sets of results depicted the same trend as the wind speed increases. More importantly, the still reasonable agreement of the K_L values, albeit with the gas absorption indicating a tendency of higher magnitude though limited by about 10% on comparison to the gas evasion approach, portends well that the present finding and the subsequent deduction of a correlation function relating the scalar transport to some hydrodynamic parameter(s) would be applicable for both absorption and evasion.

For direct comparison with the previous results of Law & Khoo (2002) and Jahne & Munnich (1979) carried out in a similar circular wind-wave channel, the mass transfer velocity is depicted together with Sc as $K_L Sc^{0.5}$ for the ordinate axis and plotted versus the wind speed on the abscissa axis. The use of $K_L Sc^{0.5}$ assumes a relationship of K_L to diffusion coefficient of the gas in water that has been employed by many others, and also to account for the different tracer gas utilized in the different experiments. It is noted that in Law & Khoo (2002), CO_2 was used at the water temperature of around 27^{o}C (Sc≈420). In Jahne & Munnich's work, CO_2 was used at the water temperature of around 20^{o}C (Sc≈600), while in this work, O_2 was used and employed at the water temperature of around 22^{o}C (Sc≈532). Figure 3.48 shows reasonably good concurrence in value and trend with Law & Khoo (2002) and Jahne & Munnich (1979).

3.3 Mass Transfer Model

Correlations of the mass transfer velocity and near surface turbulence parameters

have been investigated by previous researchers, such as McCready et al. (1986), Khoo & Sonin (1992) and Tamburino & Gulliver (2002). The relation can be expressed as:

$$K_L^+ \equiv \frac{K_L}{v_{\beta-rms}} = f\left((\frac{\beta_{rms} \nu}{v_{\beta-rms}^2})^{0.5} \right) Sc^{-0.5}. \quad (3\text{-}1)$$

Here $K_L^+ \equiv K_L / v_{\beta-rms}$ is the non-dimensional mass transfer velocity, $\beta_{rms}^+ \equiv \frac{\beta_{rms} \nu}{v_{\beta-rms}^2}$ is the non-dimensional form of β_{rms}, and $f(\ )$ indicates a functional relationship. The exponent for Sc is governed by the surface conditions. McKenna & McGillis (2004) investigated the role of surfactant in gas-water mass transfer and presented an expression for the Schmidt number exponent as $n = \frac{2}{3} - \frac{1}{6} e^{-\zeta/2}$ where ζ is defined as stress ratio. In this work, mass transfer experiment is done under the condition of a clean surface. As such, the stress ratio is zero and so the exponent of Sc is set to 0.5.

It is noted that the non-dimensional parameter β_{rms}^+ encompasses all the three parameters (β_{rms}, Λ_β and $v_{\beta-rms}$) which define the hydrodynamic characteristics in the vicinity of the interface region. Even though Λ_β does not appear explicitly in the definition of this non-dimensional parameter, its influence is implicitly represented via the definition of β_{rms}. For sparingly soluble gases (such as CO_2 and O_2), the concentration boundary layer next to the interface is very thin. Hence, the hydrodynamic characteristics in the immediate vicinity of the interface region are deemed to be crucial for the mass transfer process, and the other important issue is that such parameters exist irrespective of the turbulence generation mechanism. The above mentioned features found in the mass transfer correlation model based on β in Law & Khoo (2002) looks promising and possesses the potential to be further

developed into a robust model and applicable to different flows.

Figure 3.49 shows the plot of $K_L^+ Sc^{0.5}$ versus $(\beta_{rms}^+)^{0.5}$ for all the studied flow conditions based on both gas evasion and absorption measurements in our experiments. The result of Law & Khoo (2002) is also included. In the work of Law & Khoo, turbulence is imposed through two distinct methods namely a wind-induced shear turbulence from above and separately a confined-jet turbulence induced from beneath in a half-filled cylinder with water. A wide range of various water-glycerol mixtures as the liquid and carbon dioxide gas were tested at different temperatures. A combination of their works where β_{rms} were explicitly measured together with the present data is employed to build a more universal correlation. It can be observed that a linear behavior (slope=0.20 with R^2=0.981) can still be realized for all of the presented flow conditions. From Figure 3.49, a general relation can be proposed to correlate the mass transfer velocity with the near surface turbulence parameters:

$$K_L^+ Sc^{0.5} = 0.2\,(\beta_{rms}^+)^{0.5}. \tag{3-2}$$

Figure 3.50 shows a re-plot of all the results expressed in terms of $\dfrac{K_L^+ Sc^{0.5}}{(\beta_{rms}^+)^{0.5}}$ versus $(\beta_{rms}^+)^{0.5}$. For the gas absorption only experiments in our measurements, the data presents a mean value of 0.21, whereas for only the gas evasion experiments, a mean value is obtained as 0.19. For all of the presented data points including the data from Law & Khoo (2002), the overall mean quantity is 0.20. The difference noted for the different mean quantities is less than 10% and broadly suggests the correlation obtained is valid for both gas absorption and evasion, albeit the larger experimental uncertainty associated with the gas absorption measurements.

A very recent work on direct numerical simulation (DNS) of a vertical rotating open-channel flow with heat transfer at the free surface can be found in Li et al. (2006). Li et al. employed the correlation relation of Law & Khoo (2002) and re-expressed as

$$Nu\,\mathrm{Pr}^{0.5} = 0.22(\mathrm{Re}_\tau \left| \frac{\partial v'_{rms}}{\partial y} \right|_{y=1})^{0.5}. \tag{3-3}$$

Their DNS results concur very well with Equation (3-3) in terms of trend as the rotational speed increases as depicted in their Figure 7. The magnitude also agrees reasonably well except that the computed results indicated a slight under-prediction. In fact if the coefficient in Equation (3-3) is reduced to say 0.20 as proposed in Equation (3-2), the concurrence would have been even better. The most important observation is that in Li et al., the turbulence near the free surface is generated via the rotation and yet the scalar transport in terms of heat transfer across the turbulent air-water interface behaves remarkably as determined by Equation (3-2). This further supports the possible universality of Equation (3-2).

3.4 Discussion and Comparison with Other Similar Models

In the recent years, the name 'surface divergence model' has been given to the model for a quantitative description of the gas-liquid interface given nominally by the parameter ($\nabla_h \cdot V$), where ∇_h is the horizontal two dimensional divergence operator and V is the velocity fluctuation vector. It is cleared that ($\nabla_h \cdot V$) is equivalent to β as firstly shown by Tamburrino (1994), and also noted in Tamburrino & Gulliver (2002)

and McKenna & McGills (2004). To consider the possible large deformation of the interface, Banerjee et al. (2004) modified the mentioned equivalence by an additional terms relating to the curvature of the fluctuating interface as opposed to a flat interface (see Equation (3-7) below). Nevertheless, in most experiments, if the fluctuating amplitude of the interface is kept deliberately limited and in an absence of wave breaking, the relationship between the gradient of vertical velocity taken with respect to the interface and defined as β here is still closely linked by to the negative two-dimensional divergence of the free surface.

A detailed experimental work has been carried out by Tamburrino & Gulliver (2002) in a fully developed straight section channel flow, where turbulence is generated from beneath the interface (in the absence of any wind-imposed shear from above). Tamburrino & Gulliver emphasized and employed the maximum value of β frequency spectrum instead of the mean value of β in the near surface region. Together with the mass transfer measurements from Gulliver & Halverson (1989) and Lau (1975), they proposed a correlation of the form:

$$K^{+}\sqrt{Sc} = 0.24\sqrt{S^{+}_{\beta\max}}\ . \tag{3-4}$$

However, from an estimate of the various relevant tabulated quantities found from their Tables 1 and 3 like $\overline{\beta^{+2}}$, $\overline{\beta^{2}}$ and $S^{+}_{\beta\max}$, we can obtain a re-worked relationship as:

$$K_L^{+}Sc^{0.5} \Big/ (\beta^{+}_{rms})^{0.5} \approx 0.151\,. \tag{3-5}$$

This relationship and the experimental measurements of Tamburrino & Gulliver (2002) are also plotted in Figure 3.51 for comparison, which indicates a fair concurrence with

the present results. This suggests the critical importance of $S^+_{\beta\max}$ in the correlation for the mass transfer across the gas-water interface as argued and put forth by Tamburrino & Gulliver (2002) can be viewed alternatively in terms of β^+_{rms}. It may be mentioned that the deviation mainly lies in the lower β value region, which corresponds to low turbulence intensity region. Taking account of the measurement uncertainty and the limited experimental conditions carried out in Tamburrino & Gulliver (2002), the difference in the coefficients of Equations (3-2) and (3-5) is deemed to be acceptable.

In McKenna & McGillis's work (2004), they used an innovative DPIV technique to measure the surface divergence under an oscillating grid-stirred turbulent condition. Their work is focused on the role of surfactant on the scalar transport across the gas-liquid interface and presents a relationship in the form as:

$$K^+ = \frac{k}{aL} = \frac{1}{2}\mathrm{Re}_a^{-1/2} Sc^{-n}, \qquad n = \frac{2}{3} - \frac{1}{6}e^{-\varphi/2}, \tag{3-6}$$

where $a = (\nabla_h \cdot V)$ is defined as surface divergence, $\mathrm{Re}_a = aL^2/\nu$ and the Schmidt number exponent n is governed by the surface conditions. Under a clean surface condition, n=0.5. A macro-length scale L is used to get a dimensionless quantity. For direct comparison with the results from Law & Khoo (2002) and the present work, the dimensional parameter β (or α) is used on the abscissa axis and plotted in Figure 3.51. The general trend of the present results fits well with the measurements of McKenna & McGills, while an obvious difference exists in term of the magnitude. Their results show a significant scattered pattern. In Mckenna's thesis (2000), it was pointed out that there were several contributory factors to the experimental uncertainty for their

work. One such factor arose from the uncertainty in the DPIV measurement giving rise to around 10-30%. The other part is the limitation of the measurement determined by the spatial resolution. Brumley and Jirka (1988) have derived some theoretical results and suggested that the smallest scales contribute the most to the surface divergence, while the finite spatial resolution of around 6mm in McKenna & McGillis's work omits the contributions of such smaller scales, which can result in the underestimation of the flow dynamics parameters. This would be an essentially consistent shift over all the measurements, rather than a random measurement uncertainty. This part of uncertainty is hard to estimate, but the magnitude is reckoned to be not negligible. We can only surmise qualitatively that the difference observed between Equations (3-2) and (3-6) is largely attributed to the vastly difference measurement techniques for β (or α).

Banerjee et al. (2004) in their DNS study of the surface divergence models for scalar exchange between turbulent streams suggested a relationship which can be re-expressed as:

$$\frac{KSc^{0.5}}{u} \approx \frac{C}{\mathrm{Re}_t^{0.5}}\left[\left(\frac{\partial u'}{\partial x}+\frac{\partial v'}{\partial y}-2w'\nabla\cdot n\right)^2\right]^{1/4}. \qquad (3\text{-}7)$$

Here the term in the bracket embedded within the square bracket on the RHS is the surface divergence taking into consideration the curvature of the deforming surface, and C is a coefficient. Their DNS calculations showed that the said surface divergence term with the dilation contribution is numerically the same as another form obtained based on the Hunt-Graham (1978) blocking theory (their Fig. 8), such that C ≈ 0.20

for Equation (3-7) appears to concur rather well with the experimental data of Komori et al. (1989) for an un-sheared interface of an open channel flow (see their Table 2 for comparison of the measured mass transfer rate from Komori et al. and their prediction). For the DNS of the sheared turbulent air and water streams, from the rather limited data set, Banerjee et al. (2004) obtained a higher coefficient of C≈ 0.35 (for the lower Sc of 1.0-1.2) and C≈ 0.45 (for the higher Sc up to about 200). It is unfortunate that the quantitative values of equivalent β_{rms}^{+} (or dimensional β) are not provided explicitly and cannot be easily deduced to be reflected directly in either Figures 3.50 or 3.51 for more detailed comparison and evaluation. Nevertheless, despite the differences in the coefficient in Equations (3-7) and (3-2) which can be attributed to how the surface divergence is defined and related to β, the trend is unmistakenly similar and valid for a varied range of flow conditions irrespective of how the surface turbulence is generated.

Finally, as already and somewhat discussed at length in Law & Khoo (2002), McCready et al. (1986) performed a computer simulation of liquid flow beneath a flat mobile interface next to the gaseous medium. As pointed out by the authors that there is not enough experimental information to determine β(z,t) completely, they just assumed that the spatial variation of the velocity field was represented by a single harmonic of the form as:

$$\beta(z,t) = \sqrt{2}\beta(t)\cos(2\pi z/\lambda_z) \quad \text{and} \quad v = \beta(z,t)y\,, \tag{3-8}$$

with β(t) being a random function of time and z- is the transverse coordinate. The transverse wavelength λ_z was taken to be 100 (made dimensionless with interfacial

friction velocity and kinematic viscosity) for most of the calculations so as to be consistent with the measured behavior near a solid boundary. Though these and several other several assumptions were employed in their derivation, McCready et al. obtained a relation linking the scalar transport across the interface to β as:

$$K_L^+ Sc^{0.5} = 0.71(\beta_{rms}^+)^{0.5}. \quad (3\text{-}9)$$

This relation is plotted in Figure 3.51 for comparison. It is appropriate to note the characteristic velocity employed in the non-dimensionalisation appeared on the both sides of Equation (3-9) (and/or Equation (3-2) and others) can be cancelled out thus leaving the function completely unaffected. McCready et al. (1986) had used a different characteristic velocity scale for their non-dimensionalisation. It is clear that Equation (3-9) concurs with Equation (3-2) except for the magnitude of the coefficient, which can be easily attributed to the assumptions made in McCready et al..

Chapter 4 Experiments in Liquid Wavy Film

4.1 Introduction

Thin liquid films falling under the influence of gravity along vertical or inclined solid surface are encountered in a wide range of industrial process equipments, including wetted-wall absorbers, falling-film chemical reactors, condensers, and vertical tube evaporators. Reliable design of these processes depends on the ability to accurately predict the transport rates of heat and mass to the flowing film. However, the interfacial and wall-to-liquid heat and mass transport processes for wavy falling films are significantly affected by the unsteady hydrodynamic characteristics of the wavy films such as the film thickness, velocity distribution, wall shear stress variation and others, which are not yet fully understood over a wide range of Reynolds numbers.

In this Chapter 4 and the next two chapters, the interest on the scalar transport across the turbulent air-water interface culminating with the correlation given in Equation (3-2) is being extended to thin film flow arrangement. In other words, the intent is to ascertain whether Equation (3-2) is still applicable to thin film flow where hydrodynamic influence the scalar transport across the thin film interface. Both experiments and numerical simulations will be carried out.

4.1.1 Wave Pattern and Thin-Film Flow Regimes

The hydrodynamics of falling film have been studied by numerous researchers.

However, in several of these studies, the theoretical and experimental results are not in good agreement. The cause of the discrepancy is possibly attributed to the inadequate modeling of waves and associated inadequate resolutions in the experiments. According to the hydrodynamic studies carried out by Grossman (1984), the film flows can be broadly categorized into three regimes depending on the film Reynolds number (defined as $\mathrm{Re}_s = 4\,\mathrm{Re} = 4\Gamma/\mu = 4\overline{w}\,\overline{\delta}/\nu$):

(1) the smooth laminar flow, for $\mathrm{Re}_s \le 20$;

(2) flow with surface waves, of partially laminar and partially turbulent nature, in $20 < \mathrm{Re}_s < 4000$;

(3) fully turbulent flow, for $\mathrm{Re}_s \ge 4000$.

In the wavy flow regime (2), transition to turbulence and the surface disturbances become more significant with increasing Reynolds number. This transition regime can then be subdivided into capillary wavy-laminar, inertial-wavy-laminar, and inertial wavy-turbulent flow regimes, corresponding approximately to the Reynolds number ranges, $20<\mathrm{Re}_s<200$, $200<\mathrm{Re}_s<1000$, and $1000<\mathrm{Re}_s<4000$, respectively. The inertial waves are known as 'roll' waves; this is because of their appearance of rolling down over a film substrate.

Increasing the Reynolds number causes the roll waves to develop a steep front. The increase in curvature increases surface tension force, which, in turn, leads to the growth of smaller push waves just in front of the larger waves. An excellent illustration of these differing flow regimes was experimentally observed by Morioka et al. (1993). They observed that the push waves collapse as they flow downstream.

However, the roll and push wave combination appears to persist after the collapse. Increasing the Reynolds number causes the wave interval to increase, and the wave fronts lose their ring-like symmetry. The flow has become chaotic in the last transient regime, and the waves are starting to interfere with adjacent waves. Continuing to increase the flow strength leads to a blending of the roll and push waves, and the surface becomes covered with small, jagged, turbulent waves.

In the low Reynolds number range of $20<Re_s<200$, surface tension force plays a key role in the evolution of the wave. These forces appear to be important when their magnitude is comparable to that of the gravity and viscous forces. The capillary waves appear as ripple on the film surface, being of their high frequency and small amplitude.

Roll waves are governed by the interaction of inertia (attributable to the higher Reynolds number) and gravity. In such forms of waves, surface tension effects becoming negligible in comparison. These waves have longer wavelengths and much lower frequencies than capillary waves. The waves occur at Reynolds numbers ranging from 200 to 4000, and tend to overtake the smaller, capillary waves, resulting in a complicated surface structure that appears to be random in nature. Experimental studies have shown that, under constant operating conditions, roll waves travel with an almost constant celerity (wave velocity normalized with respect to average fluid velocity) and can be identified quite easily over a wide range of Reynolds numbers (Karapantsios and Karabelas (1990)). Figure 4.1 presents the schematic diagram of these two wave shapes.

4.1.2 Previous Experimental Methods

Numerous researchers have used various measurement methods to investigate the wave patterns and characteristics of liquid films (The motivation lies in relating the wave patterns and characteristics of film flow to the scalar transport across the interface). These characteristics are important in estimating the effects that waves have on heat or mass transfer. Making reliable experimental measurements of the local flow structure in the film is exceedingly difficult due to the extremely small film heights (≈1mm), very short passage time of each wave (≈60ms) and the random location of the wave height. Many film thickness measurements have been conducted in the past to better understand the film characteristics such as the variation of mean or time-averaged film thickness with Reynolds number, axial variation of mean film thickness, temporal variation in local film thickness and statistical nature of interfacial waves.

Previous experimental methods can be divided into two broad categories: (1) intrusive method, such as time-recording of film thickness at one or more location(s) using various probes; (2) Non-intrusive methods, such as shadowgraph method and light absorption and reflection method.

Karapantsios et al. (1989) evaluated the statistical characteristics of a falling film within a vertical pipe by means of the ‘parallel-wire conductance probe’ technique. The technique is based on the inverse proportionality between the electrical resistance and the liquid layer thickness covering the wires. Lyu and Mudawar (1991) developed an alternative technique based on the principle of hot-wire anemometry. Nosoko et al.

(1996) used a needle contact technique to measure the wavy peak thickness. Intermittent contacts of the film with the needle were detected using a laser beam. The obvious disadvantage of this class of methods is that no matter how small the size of the probes, it will affect the flow field in the falling film to varying extent. At the same time, limited by the responding speed and/or the finite size of the probes, the obtained film thickness is based on time or spatial averaging.

The methods of category (2) have mainly been used to measure the wavelength, thickness, frequency and phase velocity. Alekseenko et al. (1985) utilized the shadowgraph method to record the instantaneous thickness of the film. Based on the continuous record, the mean thickness and the phase velocity can be determined. Furthermore, Alekseenko et al. used stroboscopic visualization of spherical aluminum particles to track the film motion. Miller (1992), and Vikas & Horacio (1996) used similar method to get a magnified film shadow and recorded in analog or digital form. They used video recording to observe the development stages of the flow field and the film thickness variation with time. Nosoko et al. (1996) used the shadowgraph method to record two dimensional falling films on a vertical flat plate with controlled disturbance. When light from the stroboscope illuminates the wave, the concave and convex surface of the wave causes the light rays to diverge and converge, producing a train of dark and light strips on the back screen. The frequency of the two-dimensional waves was determined with the stroboscope by adjusting its frequency to the minimum so that the shadows of waves were fixed on the screen. The wavelength and phase velocity can also be determined. Methods of above category (2) will not affect

the flow field in the falling film and provide a good means to observe the flow pattern and phase velocity. However, these can not be employed to obtain the instantaneous velocity profile within the falling film.

Ho and Hummel (1970) used the photochromic dye activation technique to measure the velocity profiles in vertical, annular falling films of aqueous alcohol solutions and alcohol-glycerol mixtures. This technique involves the reversible activation of a photochromic dye dissolved in the working fluid, and has been applied recently by Kawaji (1998) to various two-phase flow studies. Moran et al. (2002) extended this method to measure the instantaneous film thickness and velocity distribution. Lel et al. (2005) used the light reflection from the wavy surface and the fluorescence intensity technique to measure the film thickness and phase velocity. These mentioned methods make a good attempt to reveal the velocity profiles, but it seems difficult to provide sufficiently fine resolution in the vicinity of the interface.

On the theoretical side, much progress has been made on the analysis of wave evolution in laminar film flow, and considerable efforts have been made on better physical understanding of falling liquid films. Numerical simulations of wavy laminar falling films have also been conducted to simultaneously predict the temporal and spatial variations in film thickness, wall shear stress and/or velocity fields. However, to our knowledge, velocity field predictions for wavy films have not been compared in great detail with instantaneous flow field data, since such experimental data are still rather scarce.

In this work, we focused mainly on the surface structure of the falling film. Based

on the measured surface velocity profiles, the key parameter of β which is compatible to that determined in Chapter 2 and 3 will be determined. Mass transfer experiments are next carried out to provide a possible relation to β for comparison to Equation (3-2).

4.2 Experimental Apparatus for Falling Film

Figure 4.2 shows the schematic diagram of the experimental apparatus for the falling film arrangement. The test section consists of a smooth plate and equipped with two side walls. All of the experimental components are made of transparent Perspex material. The dimensions of the test section plate are 25cm long and 80mm wide. To avoid any unwanted or extraneous light reflection from the plate surface, the exterior is covered with dull, self-adhesive black foil paper. The plate is inserted into a slot and fastened with screws. The other end of the test section plate is extended towards the water collection vessel. The slot (upper) surface is designed to ensure the flow transit smoothly to the test section plate surface. One end of the slot is attached to the upper water box (10cm (L) × 8cm (W) × 10cm (H)) and is smoothly rounded to ensure evenly distributed flow across the entire width of the test section plate. Figure 4.3 shows a more detailed schematic for the slot part. To reduce the water velocity fluctuation and to streamline the flow in the upper water box, some sponges and honeycomb collimators (0.32cm cell diameter) are placed in the box.

The upper water box is installed on a separate bottom plate with dimension of

30cm long and 10cm wide. Two M3 screws are placed at the frontal side of the plate. They are aligned perpendicular to the test section plate and are used to adjust the system to make that the test section plate is horizontal across the entire width. A screw shaft located at the rear side of the plate is designed to adjust the incline angle of the test section plate.

The water flow rate is monitored and can be controlled by means of a flow meter with a valve in the measurement range of 0—4 lit/min. The water is collected at the end of the test section in a deep collection vessel (6cm (W) × 13cm (L) × 7cm (H)) and recirculated via a water pump to the upper water box and flows down the inclined test section plate.

For the mass transfer experiments, the whole apparatus is enclosed in a transparent case (73cm (L) × 18cm (W) × 20cm (H)). To minimize the unnecessary exposed area outside the thin film flow test section, the collection vessel and the upstream water box are designed with small cross section area. A fit cover is also added in the upstream water box to further reduce the unnecessary exposed area. The tracer gas is input from a location at height 50mm from the horizontal case bottom at the upstream position, and is exhausted from a location at height 180mm from the case bottom towards the downstream end. Since the input gas used in this work (carbon dioxide) is heavier than the air, the non-condensable gases (notably air) will be naturally exhausted out through the outlet opening located at a higher elevation. The input gas is supplied from a cylinder to the enclosed chamber, and its flow rate is controlled so that it does not induce any additional shear on the thin film flow in the

test section. In this work, the input gas flow rate was kept to be below about 80ml/s. Similar to the mass transfer experiments in Xu et al. (2006), the input gas is preheated to the same temperature as the working liquid (water) before being introduced into the system.

The present set up is fairly similar to that employed in Moran et al. (2002). The present set up is, however, deemed more suitable for the study of falling film hydrodynamics with scalar transport across the interface. The relative high wave speed and thin film thickness constitute the main challenges for a viable falling film experiment. Compared with other types of falling film setups, this present set up provides more ways to control the wave speed and film thickness through fine adjustment of the inclined falling film angle and the flow rate can be varied independently, all of which allows a wide range of flow conditions.

Table 4.1: Flow conditions in falling film experiment

Flow conditions	Inclined angle θ (degree)	Flow rate (lit/min)
Case I	5	0.8
Case II	5	1.2
Case III	5	1.6
Case IV	15	0.8
Case V	15	1.2
Case VI	15	1.6

In this preliminary work, the experiments were conducted at two different

inclined plane angles of 5^o and 15^o with three flow rates at 0.8 lit/min, 1.2 lit/min and 1.6 lit/min applicable for each inclined angle. Table 4.1 summarizes the experimental flow conditions. All of the experiments were carried out at the temperature of 25^oC.

4.3 Experimental Techniques

4.3.1 Surface Field Measurement

As we have discussed earlier, previous experimental works on thin falling film flows mainly focused on the mean parameters such as film thickness, phase velocity, frequency and wave length. Though some attempts have been made to get the instantaneous velocity field within the thin film, the limited spatial resolution does not permit a clear revelation of the flow structure, especially in the vicinity of the interface. The small and yet continuously fluctuating thickness of the thin falling films presents considerable difficulties to the measurements of the local flow structure. PIV based technique, however, provides a possible means to reveal the entire flow field at the same time, which is especially so following the development of the micro-PIV technique. To reveal the flow structure, two observation views can be adopted. One is to site the camera from the side elevation to observe the falling film flowing down the inclined plate (termed the normal view), and the other one is put the camera directly above and looking down on the thin film surface to observe the layer parallel with the surface (also called the parallel view).

For the former view, the thin film thickness poses the biggest challenge. If this

approach is adopted, the detailed information on the instantaneous interface position and the entire velocity profile would invariably require very fine spatial resolution. The mean film thickness is usually of the order of 1mm or less. It is thus expected the spatial resolution should be much less than 0.1mm with even finer resolution near the interface if one is interested to measure the vertical fluctuating velocity gradient at the interface to evaluate β. The highly irregular wavy surface and the fine spatial resolution make such kind of measurement very difficult.

For the latter view, the challenge comes from how to determine accurately the depth of the observation layer relative to the fluctuating interface. With a fixed focus length, the variation of the optical media (caused by the interface fluctuation) will change the observation layer position. A lens with good magnification and reasonable depth of view is absolutely necessary. In our experiments, the key parameter β is related to the surface divergence as also shown by Tamburrino & Gulliver (2002) and McKenna & McGillis (2004), and the surface divergence can be derived from the surface velocity profile (see below).

As such, the parallel view approach is adopted in this work. A high speed video camera (Photron ultima APX) with frame speed at 2000 frames per second was used to capture the surface motion images. A 55mm macro lens was attached to the high speed camera to obtain a view field size (image) of approximately 3.3cm by 3.3cm on the focal plane. The high speed camera was fixed on a moving carriage (Manfrotto Art. 454) with a range of 0—120mm. Two stages were combined to enable a larger range so that the camera can track the whole length of the thin film flow test section. With

the help of the carriage, the camera is able to move along the streamwise direction such that the variation of surface divergence with the axis position can be systematically obtained. For each x position in the streamwise direction, the surface motion was captured separately for five times. For each run, at least 100 images were obtained at equally space time intervals. These 500 images or more were used to compute the ensemble average parameters for each position. A high intensity lamp (ARRILUX 400) was used to provide sufficient light source for image capturing. Figure 4.4 shows the arrangement of each part for the whole system.

Three further measures are adopted to eliminate unwanted light coming from the region beneath the wavy surface. Firstly, commercially available dark blue dye was introduced to reduce the light coming from the region beneath the film surface. In this work, 1.5ml dye was mixed with 2000ml pure water. Its effect on the viscosity and other physical properties are deemed negligible. Figure 4.5 shows the different effects before and after introducing dye into a still water drop. Some particles were left on the plate initially, and then a still water drop (with and without dye) was introduced by a small syringe. The images before and after the introduction of dye were captured and compared in Figure 4.5. From this figure, it can be clearly seen that before introducing the dye, the particles (beneath the surface) can be seen clearly. As the dye was introduced, the light reflected by the particles was overshadowed or ‘blocked’ by the dye. The second measure relates to the procedure for releasing the particles into the thin film. Polypropylene (PP) particles were added into through a fine sieve with 50μm grid spacing. This kind of particles was also employed by Weitbrecht et al.

(2002) after consideration of the density requirement with the property of less conglomerating tendency. Although these particles are considered neutrally buoyant, they still float on the surface when firstly introduced directly into the thin film flow. During the experiments, the particles were poured on the free surface at the upstream location by shaking the sieve gently. This procedure of particle introduction is similar to the action by Tamburrino and Gulliver (2002) in their investigation of the surface motion. Finally, the third measure relates to the intensity threshold value based on observation of the collected images which was used to filter out the possible extraneous light reflected by the particles located beneath the surface.

From the surface field images, an adaptive correlation algorithm is used to obtain the surface velocity distribution (with integration window area 16(x-) × 32(z-) pixels and 25% overlap). The surface velocity gradient is calculated via second-order central differences method in the domain view area, such as:

$$\frac{\partial u}{\partial x} = \frac{u_{i+1} - u_{i-1}}{x_{i+1} - x_{i-1}},$$

$$\frac{\partial w}{\partial z} = \frac{w_{j+1} - w_{j-1}}{z_{j+1} - z_{j-1}}, \tag{4-1}$$

where the i- and j- are in the direction of x- (streamwise) and z- (lateral) correspondingly. Next, the surface divergence defined as

$$\nabla_h \cdot V = \frac{\partial u}{\partial x} + \frac{\partial w}{\partial z} \tag{4-2}$$

is evaluated. Here u and w are the surface velocities in the streamwise (x-) and transverse (z-) directions. With the continuity equation, it is found that β is related to the surface divergence as

$$\beta = \frac{\partial v}{\partial y}\Big|_{y=i/f} = -\left(\frac{\partial u}{\partial x} + \frac{\partial w}{\partial z}\right) \equiv -\nabla_h \cdot V \,. \tag{4-3}$$

This relationship is also revealed in Tamburrino & Gulliver (2002), McKenna & McGillis (2004) and Banerjee et al. (2004).

4.3.2 Mass Transfer Velocity Measurement

As discussed earlier, the mass transfer velocity of sparingly soluble gas (such as oxygen used in this work) is controlled primarily by the diffusion of the tracer gas in the liquid film because of its significantly lower diffusivity in the liquid as compared to the gas phase. The major resistance for diffusion lies in the liquid side.

The equation governing the transfer velocity is given earlier in Equation (2-3) and repeated here as:

$$V_w \frac{dC}{dt} = K_L A(C_S - C) \,. \tag{4-4}$$

Each symbol has the same meaning as discussed before. Similarly, the overall mean mass transfer velocity over a period of time t_f can be expressed in the following form by integrating Equation (4-4):

$$(\overline{K_L})_{overall\ mean} = \frac{V_w}{At_f} \ln \frac{(C_s - C_i)}{(C_s - C_f)} \,, \tag{4-5}$$

where the area A is taken to be a flat surface equal to the thin film flow in the test section (measuring 8cm (W) × 25cm (L)). Here C_s is the concentration at the interface, C_i and C_f are the concentrations in the bulk liquid at $t = 0$ and $t = t_f$, respectively. In this work, t_f typically ranged from 20 minutes to 30 minutes, and at

least 5 data points were sampled to obtain the representative average value. The total volume of water in the system is measured accurately via calibration flask before introducing into the system. In this work, about nominally 2.0 liter of water was utilized. It may be noted that the mass transfer experiments were carried out separately from the experiments for surface field velocity measurement. Precautions were taken to keep the water and the surface clean.

Along the film surface, the concentration of oxygen C_s is constant and in equilibrium with the partial pressure of oxygen in the gas phase. The concentration of the dissolved oxygen in the water is measured with a DO probe (HACH HQ30d) with an instrument accuracy of 99%. This is a different measuring probe from the earlier experiments in Chapter 2, since this one provide a quicker response time and so more accurate results compared to the previous one. The probe is put in a closed tank located in the downstream of the test section (as shown in Figure 4.2). The probe is factory calibrated and works in the range of 0—20ppm. Its accuracy is confirmed with some standard prepared samples as discussed earlier. Limited by the working range of this probe, only oxygen evasion experiments were carried out in this part of work. As before, for the oxygen evasion experiments, carbon dioxide was also introduced initially for a period of at least 5 minutes. The gas (carbon dioxide) was supplied from a cylinder to the test system. Its flow rate and pressure were controlled so that the pressure did not exceed 20psi (around 1.38bar) and the flow rate did not exceed 10cfh (around 78.7 ml/s).

Chapter 5 Experimental Results of the Thin Falling Film

5.1 Surface Velocity Distribution

Figure 5.1 shows the typical image captured in the experiments. It was taken along the central line in the wide direction. The image is consisted of 1024 × 1024 pixels. The coordinate originates from the left lower corner with the positive x-direction along the flow direction from left to right, and the positive z- direction points from bottom to top. Taking account of the main flow direction lying in the x-direction, the integration window used in the analysis process is 16(x-) × 32(z-) pixels with 25% overlap. The whole field of view for the image is about 3.3cm × 3.3cm, so each integration window area is about 0.5mm × 1mm. Two successive images were compared and the velocity field was obtained by adopting the adaptive correlation algorithm, which have been discussed before in Section 2.3.

Figure 5.2 to Figure 5.7 show the typical velocity distributions for the film surface under different flow conditions. From these figures, it can be seen that the velocity vectors have main components in the streamwise direction. And it is quite clear that the velocities increase with the inclined angle and the flow rate.

Figure 5.8 to Figure 5.13 show the variation of surface mean u velocity along the centerline in the x- direction. The mean u velocity is firstly averaged over a spatial domain 5mm (x- direction) and 33mm (z- direction) with 25% overlap pertaining to each x position eventually distributed in the streamwise direction, then an ensemble

averaging operation is carried out for all of the captured images. The coordinates in the plot have been made dimensionless according to the flat film thickness (h_0) and average velocity (u_0) estimated from Nusselt's theory (see also Gao et al. (2003)):

$$h_0 = \left(\frac{3\,\mathrm{Re}\,\nu^2}{g \sin\theta} \right)^{1/3}, \tag{5-1}$$

$$u_0 = \frac{g h_0^2 \sin\theta}{3\nu}. \tag{5-2}$$

Here θ is the inclined angle and Re is the nominal Reynolds number defined as

$$\mathrm{Re} = \frac{u_0 h_0}{\nu} = \frac{Q}{W\nu}, \tag{5-3}$$

where W is the width of the test plate. Based on these equations, the nominal Reynolds numbers for the studied cases were estimated as:

Re (Case I) = Re (Case IV) ≈ 166,

Re (Case II) = Re (Case V) ≈ 249,

Re (Case III) = Re (Case VI) ≈ 332.

The x- direction is considered to be the wave evolution direction where the major velocity changes occur in this direction. It is unfortunate that there is much less pertinent experimental data from the literature for our direct comparison. Most of the experimental works were obtained under fixed frequency disturbance and the focus is on the time evolution characteristics which is dissimilar to the flow conditions in our experiments. Portalski and Clegg (1972), however, presented the variation of the mean film thickness with distance with naturally occurring waves (similar to us). From their figures, it is possible to deduce the evolution of the surface velocity variation for comparison. According to Nusselt's theory, the u velocity has the

following profile:

$$u = \frac{3}{2}u_0\left[2\left(\frac{y}{\delta}\right)-\left(\frac{y}{\delta}\right)^2\right]. \tag{5-4}$$

From this equation, the surface velocity (where y=δ) is given as 1.5 times the averaged velocity. From Equation (5-2), one knows the relationship between the averaged velocity and the film thickness. The results deduced from Portalski and Clegg (1972) are also shown in Figure 5.8 to Figure 5.13. The Reynolds numbers in Portalski and Clegg (1972) are in the similar range as this work and it provides a near comparison to validate our measurements. There is general concurrence of magnitude for the distributions. Our results also show that the mean u velocity distribution indicates a somewhat decreasing trend fairly similar to Portalski and Clegg (1972). Taking into account the differences in experimental conditions (vertical glass sheet was used in the work of Portalski and Clegg) and the entry conditions, the deviation observed is considered to be acceptable.

Figure 5.8 to 5.13 for the u- distribution also show the non-uniqueness of using only Re to characterize the thin film flow. The intent for these plots serves primarily to provide some validations of the experimental set-up and quantitative measurements versus published work like Portalski and Clegg.

5.2 Surface Divergence

The surface divergence is calculated by the sum of the second order of velocity gradient for u and w. Since the surface divergence is also related to β (Equation

(1-11)), and β has been used to characterize near surface turbulence in Chapter 3, we shall revert to the use of β henceforth in the below discussion.

Figure 5.14 to Figure 5.19 present the variation of surface divergence or β in the streamwise direction. More specifically, the evolution is for

$$(\beta_{rms})^{1/2}{}_{time\ average} \equiv (\overline{\beta^2})^{1/4}{}_{time\ average} = \left[\frac{1}{T}\int_0^T \beta^2 dt\right]^{1/4} \tag{5-5}$$

along the centerline of the thin film flow section as a function of x. Here T=0.25s. β is firstly obtained in each integration area (16 pixel (x- direction) × 32 pixel (z- direction) measuring around 0.5mm × 1mm) with 25% overlap, and $\overline{\beta^2}$ is the average taken over several integration areas (5mm in x- direction and 33mm in z- direction) spanning the transverse extent of each image. These figures clearly show that $(\beta_{rms})^{1/2}{}_{time\ average}$ is not a constant, but is a function along the streamwise direction. It also indicates the mass transfer velocity is not a constant in the flow field. It is consistent with the evolution characteristic of the falling films.

Figure 5.20 shows the effect of observation areas for $(\beta_{rms})^{1/2}{}_{time\ average}$ evaluated along an axis parallel to the centerline but offset by around 1cm in the z- direction. The purpose of this plot is to examine the variation of β in the spanwise (z-) direction. The horizontal lines provided indicate the overall averaged values of $(\beta_{rms})^{1/2}{}_{time\ average}$ taken across the length of the test section given as $(\beta_{rms})^{1/2}{}_{overall\ average}$. Firstly it can be seen that the two distributions in Figure 5.20 follows similar trend with some limited offset variation, and the deviation for the $(\beta_{rms})^{1/2}{}_{overall\ average}$ is below 10%; these features are common for all the other studied cases (not shown). By taking $(\beta_{rms})^{1/2}{}_{time\ average}$ along the centerline as representative

of β distribution over the extent of the thin film test section to minimize the side wall effect, one may expect to incur an error limited to about 10% or so.

Figure 5.21 shows the variation of $(\beta_{rms})^{1/2}_{overall\ average}$ with different flow rates. It is clear to see that $(\beta_{rms})^{1/2}_{overall\ average}$ increases with the flow rate and inclined angle. The increase of $(\beta_{rms})^{1/2}_{overall\ average}$ with inclined angles and flow rates can be regarded logically as indicators for increase of turbulence activities in the flow and especially at/near the interface. Such observations are consistent with the findings in circular wind wave tunnel (like Law & Khoo (2002)). It also demonstrates a possible monotonic relationship between the key parameter β and the studied flow parametric conditions. Though at the same flow rate under two inclined angles have the same nominal Reynolds number, the distribution of $(\beta_{rms})^{1/2}_{overall\ average}$ which indicates an increase with the inclined angle may suggest that β is perhaps a more suitable single parameter to characterize the near surface turbulent conditions than just the Reynolds number.

5.3 Mass Transfer Velocity

Figure 5.22 presents the variation of overall mass transfer velocity $(\overline{K_L})_{overall\ mean}$ with the flow rate at different inclined angles. It is observed that the mass transfer velocity increases with both the flow rates and inclined angles; this behavior is identical to that of the $(\beta_{rms})^{1/2}_{overall\ average}$ distribution. Figure 5.22 clearly shows that the mass transfer velocity is not a unique function of the nominal Reynolds number

and would certainly require other(s) to ensure a 1-1 functional relationship. On the other hand, the possibility exists that the mass transfer velocity can be made related to $(\beta_{rms})^{1/2}{}_{overall\ average}$. The potential of β is evident since it characterizes the near surface turbulent conditions and the scalar transport across the interface is definitely affected by the hydrodynamic conditions right at the interface within the mass concentration boundary layer.

Figure 5.23 presents the variation of overall mean mass transfer velocity $(\overline{K_L})_{overall\ mean}$ with $(\beta_{rms})^{1/2}{}_{overall\ average}$. This figure shows a distinct feature of monotonic trend between these two parameters. This figure gives us more confidence to use β as the key/crucial parameter affecting the mass transfer across the thin film flow. Several of the mass transfer experimental works (for falling films) presented the empirical correlation between the mass transfer velocity and the nominal Reynolds number (such as Miller & Keyhani (2001)). Nosoko et al. (1996) had included the effect of forcing disturbance frequency as an additional parameter. Invariably more than one governing parameter is involved and deemed necessary to describe (indirectly) the surface flow condition, which affect directly the mass transfer across the interface. Our finding of β as a single hydrodynamic parameter relating to the scalar transport for the thin film flow is probably carried out for the first time; it presents an opportunity to relate to a previously obtained empirical relation based on vastly different non-thin film flow configurations/arrangements where β is involved and given in Equation (3-2).

5.4 Mass Transfer Model Validation

Figure 5.24 shows the results expressed in terms of $K_{L-mean}Sc^{0.5}/(\beta_{rms}\upsilon)^{0.5}$ vs. $(\beta_{rms})^{1/2}$ for the studied cases. The horizontal line indicates the mean value of the ratio for all of the studied cases. It is remarkable that the distribution of $K_{L-mean}Sc^{0.5}/(\beta_{rms}\upsilon)^{0.5}$ for the present experiment takes on a constant of about 0.55 (or at most a slow-varying function with β_{rms}) which still corresponds reasonably in the same order of magnitude to the constant quantity of 0.2 given in Equation (3-2) (reported in Xu et al. (2006) and Law & Khoo (2002)). As already noted by Xu et al. (2006), the larger magnitude of $K_{L-mean}Sc^{0.5}/(\beta_{rms}\upsilon)^{0.5}$ attained in McKenna and McGillis (2004) can be possibly attributed to the large uncertainty in the DPIV measurement of roughly 10-30% and spatial resolution issue of which are likely to lead to an underestimation of the flow dynamic parameters like β.

There are several other contributing factors leading to the observed discrepancy between our experiments and Equation (3-2). One is related to the surface area A taken to be the region of the thin film flow in the test section for the evaluation of K_{L-mean} in Equation (4-5). Ideally, though precautions have already been adopted to reduce the exposed water surface to the tracer gas except in the test section, it is inevitable that there are still considerable exposed areas upstream and downstream of the inclined plane test section. The nominal test section (pertaining to the thin film flow and where β was quantified) was measured as 8cm×25cm; both the upstream and downstream regions have exposed areas constituting about more than 50% of the test section. Experimentally, it is not feasible to cover up these upstream and downstream

areas such that there is no exposure to the tracer gas. Even if one can find a means to do so, the near surface turbulence intensity in the test section and especially β would be unclearly affected. Since this is perhaps the first time measurement of β has been attempted for the falling film flow configuration, we believe the present preliminary finding can serve the all-important purpose to ascertain broadly if β is indeed truly a critical parameter to consider affecting the scalar transport across the interface. In essence, we are looking for whether there is a broad agreement of the measurements from the falling film flow experiments and Equation (3-2) in both magnitude and trend. Let's bear in mind that if the increased surface areas for the scalar transport were properly accounted for, the mentioned agreement in terms of magnitude would be even better. Other possible error may arise from the determination of the scaling factor, which was used to estimate the surface velocity. The scaling factor was determined by capturing a scaled ruler and estimate the pixel distance for a known length. Another source of major error/uncertainty comes from the evaluation of the surface velocity derivatives to obtain the surface divergence and hence β. It is estimated the uncertainty associated is around 10%. All in all, in the midst of the errors incurred, our preliminary results for the falling film flow experiments have clearly shown broad agreement with the scalar correlation given in Equation (3-2). One can hardly say that the present finding is simply just fortuitous to concur well with Equation (3-2) since both experiment and numerical simulation (Chapter 6) were attempted. Of course, more works need to be done to increase the range of flow conditions with wider variations of β. and this we hope to do so in the near future.

Chapter 6 Numerical Simulation in Falling Film

6.1 Introduction

Numerical study can offer further insights into the film hydrodynamics that are not easily obtained from experiments. Nusselt (1916) was probably the first to develop solutions for the falling film hydrodynamics on a vertical flat plate. For a steady, uniform, fully developed one-dimensional flow (Figure 6.1), the Navier-stokes equations reduce to:

$$\frac{d^2u}{dy^2}+\frac{g}{\nu}=0, \tag{6-1}$$

and

$$\frac{dP}{dy}=0. \tag{6-2}$$

Nusselt used the no-slip boundary conditions at the wall and assumed that the shear at the liquid-gas interface was negligible. Equation (6-1) was solved and a parabolic velocity profile was given as:

$$u(y)=\frac{g\Delta^2}{\nu}\left(\frac{y}{\Delta}-\frac{y^2}{2\Delta^2}\right), \tag{6-3}$$

where Δ is the nominal thickness of falling film, y- is the direction perpendicular to the interface, and u is the streamwise velocity (x- direction). By integrating the velocity profile over the film thickness, the averaged velocity can be obtained as:

$$\overline{U}=\frac{g\Delta^2}{3\nu}. \tag{6-4}$$

Usually, Equation (6-4) is substituted into Equation (6-3) to simplify the velocity

profile as:

$$u(y) = \frac{3}{2}\overline{U}\left[2\frac{y}{\Delta} - (\frac{y}{\Delta})^2\right]. \tag{6-5}$$

Several analytical models on film hydrodynamics extend the idea as seen in Kapitza and Kapitza (1949) which is based on the parabolic velocity profile and assuming that the streamwise hydrodynamic variables scale with the wavelength. In examining various models developed to that date, Dukler (1972) concluded that all failed to accurately represent any measured characteristics of the wave except at Reynolds numbers well below those of industrial interest.

In a different approach, Brauner & Maron (1983) and Maron et al. (1985) treated isolated waves as a series of segments (Figure 6.2 where the velocity vector is indicated as relative to the interface velocity), each having a different type of velocity distribution depending on the physics of the region. In the so-called substrate region, a parabolic velocity profile was adequate, while the flow under the front of the wave was assumed to be fully mixed. The slowly varying wave back was described with a boundary layer model. Upon matching these solutions at the segment boundaries, it was possible to predict wave mean characteristics (such as film thickness, wave length and phase velocity) in reasonable agreement with the values measured. The model was fitted with a limited amount of data from experimental measurements and it failed to explain the large variation observed in individual wave amplitudes and lengths.

Wavy film flow is a challenge both for experimental measurements and for numerical simulations due to the typical length scales involved: a few millimeters

thickness, but tens to hundreds centimeters running length to exhibit wave characters. Modeling the wavy film flow by a direct solution of the Navier-Stokes equation is hampered by numerical stiffness imposed by the stress free interface, resulting in convergence difficulties except at lower Reynolds Numbers. Bach and Villadsen (1984) explored the application of a finite-element scheme to the unsteady problem of waves developing from initial perturbations on the smooth film for Reynolds numbers up to 100. Kheshgi and Scriven (1987) applied a finite-element technique to problems with periodic boundary conditions in the flow direction, and verified the evolution of infinitesimal disturbances as predicted by Orr-Sommerfeld analyses. Their work was limited to low flow rates, and failed to generate waveforms comparable to those observed experimentally for fully developed flow. Recently, some pertinent works have been carried out using finite element methods, such as Ho & Patera (1990), Malamataris & Papanastasiou (1990), Salamon et al. (1994), and Ramaswamy et al. (1996). Malamataris & Papanastasiou focused on a modified outflow boundary condition by calculating traveling waves in truncated domains. Salamon et al. assumed an initial sinusoidal waveform, and solved the governing equations in a reference frame moving with the wave. Ramaswamy et al. used the so-called Arbitrary Lagrangian-Eulerian (ALE) method, where the grid velocity must be judiciously selected in order to handle very large deformations. The moving surface was captured by a Lagrangian type method. Their simulation work introduced spatial waves on the initial film and used periodic boundary conditions with the constraint that the mean film thickness is conserved. This is not compatible with the

experimental conditions corresponding obviously to open flow conditions where the flow rate is conserved. Gao et al. (2003) used the Volume of Fluid (VOF) surface tracking method based on the finite volume idea, and the Continuum Surface Force (CSF) model to account for the surface tension effect. They succeeded in simulating the thin film flow subjected to an inlet flow rate perturbation and investigated the downstream response to the small monochromatic forcing disturbance. This method does not need to assume a prior waveform and velocity.

The falling film flow used in industries mostly operates in the wavy-laminar flow regime. However, because of its complexity, research has been limited until recently, with the advent of powerful computational tools. The wavy-laminar flow regime is considerably more dynamic than the smooth laminar flow and requires either considerable computational effort or excellent physical insight to simplify and solve. Morioka & Kiyota (1991), Yang & Jou (1993), and Patnaik & Perez-Blanco (1996) numerically solved the wavy-laminar flow problems for absorption of water vapor into a film of aqueous LiBr. In their studies, the velocity profile was assumed as prior and was used as input for solving the energy and diffusion equations. Morioka and Kiyota assumed a parabolic velocity profile and solved the energy and diffusion equations for a periodic, sinusoidal wave motion. Their results showed that the averaged mass flux increase 1.7 to 2.4 times that of laminar flow. In order to avoid modeling the wave structure that accompanies falling film flow, Wasden and Dukler (1989, 1990) applied a semi-empirical method in which the flow was calculated for experimentally measured wave shapes and velocities. Subsequent solution of the

diffusion equation in a coordinate system moving with the wave demonstrated enhancement of the mass transfer rate by a factor of 1.5 to 2.5 times in comparison with the smooth film case.

An accurate or at least reasonable determination of the film hydrodynamics is of paramount importance since it directly affects the mass transfer across the interface. In this study, we adopted the familiar and well-established VOF method (as used in Gao et al.) provided by the Fluent software package to determine the hydrodynamics of the falling film flow, and the mass transfer computation was added in through a user defined scalar (UDS) function and started after the flow field has reached a quasi-steady state.

6.2 Numerical Methods

6.2.1 Governing Equation

The VOF method relies on the fact that the two (or more) considered fluids are not interpenetrating. For each phase, a new variable is introduced: the volume fraction of the phase in the computational cell (α). In each control volume, the volume fractions of all phases sum to unity. The fields for all variables and properties are shared by the phases and represented by volume-averaged values, as long as the volume fraction of each phase is known at each location. Thus the variables and properties in any given cell are either purely representative of one of the phases, or representative of a mixture of the phases, depending upon the volume fraction values.

We consider a two-dimensional vertical thin film flow on a flat plane. The x- axis is oriented the streamwise direction along the plane, and the y- axis is perpendicular to the plane in the film thickness direction with the origin at the plate. Two different Reynolds numbers under various disturbance frequency cases were considered in this study. Taking account of the low Reynolds number and no heat transfer included, the flow is considered to be a laminar incompressible Newtonian and isothermal flow. The governing equation is given as:

$$\frac{\partial \rho}{\partial t} + \nabla \cdot (\rho \vec{v}) = 0 , \tag{6-6}$$

$$\frac{\partial}{\partial t}(\rho \vec{v}) + \nabla \cdot (\rho \vec{v}\vec{v}) = -\nabla p + \nabla \cdot \left[\mu(\nabla \vec{v} + \nabla \vec{v}^{T})\right] + \rho \vec{g} + F_{vol} , \tag{6-7}$$

$$\frac{\partial}{\partial t}(\alpha_W \rho_W) + \nabla \cdot (\alpha_W \rho_W \vec{v}_W) = 0 , \tag{6-8}$$

Here $\vec{v} = (u, v)$, where u and v are the streamwise and perpendicular velocities respectively, and all the other variables and symbols carry the usual meanings. F_{vol} is the additional volume force. The subscript w denotes the properties related to the water phase. Equation (6-8) is the volume fraction equation for water phase. For the gas-phase (denoted by subscript g), the volume faction (α_g) will be computed based on the following relationship:

$$\alpha_W + \alpha_g = 1 . \tag{6-9}$$

The volume-fraction-averaged density and viscosity take on the following form as:

$$\rho = \alpha_W \rho_W + (1 - \alpha_W)\rho_g , \tag{6-10}$$

$$\mu = \alpha_W \mu_W + (1 - \alpha_W)\mu_g . \tag{6-11}$$

The governing equation for mass transport is given as:

$$\frac{\partial \alpha_W \rho_W \phi}{\partial t} + \nabla \cdot (\alpha_W \rho_W \vec{v} \phi - \alpha_W \rho_W D \nabla \phi) = 0 , \tag{6-12}$$

where $\phi = c / \rho_w$. Here c is the concentration of tracer gas dissolved in the liquid side, and D is the corresponding liquid side diffusion coefficient.

The momentum and mass transfer equations are discretized by the second-order upwind scheme. PRESTO! (Pressure Staggering Option) scheme is adopted for the pressure interpolation. Pressure-velocity coupling is achieved by the PISO (Pressure-Implicit with Splitting of Operators) scheme.

6.2.2 Surface Tension

As discussed before, the surface tension plays an important role in the thin film flows. The surface tension is taken into account through the Continuum Surface Force (CSF) model proposed by Brackbill et al. (1992), where the surface tension is transformed to a volume force F_{vol}. The addition of surface tension to the VOF calculation results in a source term in the momentum equation. The localized volume force F_{vol} is calculated from the volume fraction data by

$$F_{vol} = \sigma \frac{\rho \kappa \nabla \alpha_W}{\frac{1}{2}\left(\rho_W + \rho_g\right)}, \tag{6-13}$$

where κ is the curvature of surface, and calculated from the local gradients in the surface normal at the interface. Let n be the outward surface normal vector and is given as:

$$n = (n_x, n_y) = -\nabla \alpha_W, \qquad \hat{n} = n / |n|. \tag{6-14}$$

The curvature κ is thus defined in the terms of the divergence of the unit normal $\hat{n}$:

$$\kappa = \nabla \cdot \hat{n} . \tag{6-15}$$

6.2.3 Interface Reconstruction and Face Flux Interpolation

The standard interpolation schemes are used to obtain the face fluxes whenever a cell is completely filled with one phase or another. When the cell is near the interface between two phases, a special method called geometric reconstruction scheme is adopted.

The geometric reconstruction scheme represents the interface between fluids using a piecewise-linear approach. The geometric reconstruction scheme is generalized for unstructured meshes from the work of Youngs (1982). It assumes that the interface between two fluids has a linear slope within each cell, and uses this linear shape for calculation of the advection of fluid through the cell faces. Figure 6.3 gives out the actual interface shape and the interface shape represented by the geometric reconstruction scheme.

The first step in this reconstruction scheme is calculating the position of the linear interface relative to the center of each partially-filled cell, based on information about the volume fraction and its derivatives in the cell. Figure 6.4 shows an example for the interface reconstruction. For the cell (i, j), the surface is represented by the line function as:

$$y = k_{i,j} x + d_{i,j} . \tag{6-16}$$

The slope $k_{i,j}$ is obtained from the volume fraction derivative in the cell and given

as:

$$k_{i,j} = -[n_x / n_y]_{i,j} . \tag{6-17}$$

The intersection point of the line with the local y- axis is determined by the liquid volume fraction in the cell and the slope. Specifically for the case of $0 < k_{i,j} < \Delta y_j / \Delta x_i$ and $V_{i,j} < \left|k_{i,j}\right| \Delta x_i^2 / 2$, the value $d_{i,j}$ is given by:

$$d_{i,j} = -\left[\Delta y_j / 2) - (2kV)_{i,j}^{1/2} + k_{i,j} \Delta x_i / 2\right], \tag{6-18}$$

where $V_{i,j}$ is the fluid volume in the cell (i, j). Other cases at the different fluid occupation conditions can be computed in a similar way.

The second step is calculating the amount of advection fluid through each face using the computed linear interface representation and information about the normal and tangential velocity distribution on the face. The third step is calculating the volume fraction in each cell using the balance of fluxed calculated during the previous step.

6.2.4 Boundary Conditions

For the VOF method based on a fixed rectangular grid, since the free surface is no longer the real computational boundary, the boundary conditions for the extended computation domain take on a relatively simpler form.

For the bottom wall, non-slip boundary condition and zero scalar flux condition are adopted and given as:

$$u = v = 0 \quad \text{and} \quad \frac{\partial \phi}{\partial x_i} \cdot \vec{n} = 0 . \tag{6-19}$$

For the top side, the inlet gas velocity and the saturated concentration are given as:

$$u = v = 0 \quad \text{and} \quad \phi = c_{sat} / \rho_w . \tag{6-20}$$

where ρ_w is the density of water. For the inlet conditions, gas and liquid inlet are treated separately based on the estimated film thickness h_*. The dimensionless parameter Reynolds (Re) number is defined as:

$$\mathrm{Re} = \frac{u_0 h_0 \rho_w}{\mu}, \tag{6-21}$$

where u_* is the estimated film average velocity. Based on Nusselt's theory, u_* is given as:

$$u_* = \frac{\rho_w g h_*^2}{3\mu}. \tag{6-22}$$

From Equations (6-21) and (6-22), for a given Reynolds number, the characteristic length and velocity can be expressed as:

$$u_* = \left(\frac{\mathrm{Re}^2 \mu g}{3\rho_w} \right)^{1/3} \quad \text{and} \quad h_* = \left(\frac{3\,\mathrm{Re}\,\mu^2}{\rho_w^{\,2} g} \right)^{1/3}. \tag{6-23}$$

To allow the inlet disturbance to evolve into steady-state periodic waves, the film running length needs to be quite long. In this work, the computation domain is 500h_* in the x- direction and 2.5h_* in the y- direction. The mesh size is 0.4h_* in the x-direction and 0.1h_* in the y- direction. The time step is fixed as 2×10^{-5} s for all the computed cases (i.e. $\Delta t = 0.01 \sim 0.02 h_* / u_*$). It may be noted that much smaller mesh sizes especially in the y- direction and time steps were implemented for several selected configurations to ensure grid invariance of computed results. The gas is 'induced' above the nominal liquid film thickness of h_* (i.e. in the range of h_* to

$2.5h_*$). The inlet gas velocity and the saturated concentration are given as:

$$u = v = 0 \quad \text{and} \quad \phi = c_{sat} / \rho_w . \tag{6-24}$$

Liquid is 'induced' below the height of h_* (i.e. in the range of 0 to h_*). The inlet liquid velocity is given as the Nusselt's theory predicted parabolic velocity profile:

$$u_{in} = \frac{3}{2}\left[2\left(\frac{y}{h_*}\right) - \left(\frac{y}{h_*}\right)^2\right]\left[1 + \varepsilon \sin(2\pi Ft)\right]u_*, \tag{6-25}$$

$$\phi_{in} = 0 . \tag{6-26}$$

The forcing perturbation is included in Equation (6-25). F is the frequency of the forcing disturbance and ε is the disturbance magnitude. As discussed in Gao et al. (2003), the disturbance magnitude has negligible effect on the wavy characteristics at the steady state. In fact, for the previous experimental works, such as Liu & Gollub (1994), Alekseenko et al. (1985) and Nosoko et al. (1996), all have reported that the steady-state wave shape is sensitive to the forcing frequency but remains fairly independent of the forcing strength. This kind of perturbation introduced as initial/boundary conditions by Gao et al. (2003) is compatible with the disturbance introduction methods used in experiments, and as such is adopted in the present work.

For the outlet conditions, the type of outflow boundary condition is adopted, where the exit flow is assumed to be close to a fully developed condition. The scalar flux is given to be zero. The same exit boundary condition was adopted as in Gao et al. (2003):

$$\frac{\partial u}{\partial x} = \frac{\partial v}{\partial x} = 0 \quad \text{and} \quad \frac{\partial \phi}{\partial x_i} \cdot \vec{n} = 0 . \tag{6-27}$$

6.3 Results and Discussion

We computed for two flow conditions with different Reynolds numbers and under four different frequencies imposed. The present preliminary work covered representative small-amplitude nearly sinusoidal type wave and high amplitude teardrop type wave. The mass transfer simulation was started after reaching quasi-steady wave shape, and the mass transfer associated parameters (such as β and K_L) were measured after the concentration profile has reached quasi-steady state. In our implementation, the mass transfer measurement commenced around $35000 \sim 45000\Delta t$ after the simulation started, depending on the case studied. The water properties were given as:

$\rho = 998.2\ kg/m^3, \quad g = 9.78\ m/s^2, \quad \mu = 0.001003\ kg/(m \cdot s), \quad \sigma = 0.073\ N/m.$

Other simulation conditions were given as:

1) Re=20.1, f=27 Hz (Case A);
2) Re= 20.1, f=45 Hz (Case B);
3) Re=69, f=30 Hz (Case C);
4) Re=69, f=70 Hz (Case D).

6.3.1 Wave Shapes

As studied by Gao et al. (2003), we also selected Case A to validate the present simulation result. This Case A corresponds to the experimental case of No.11 of PLATE 41 reported in the Kapitza study (1949). Kapitza and Kapitza did not provide

explicitly the forcing frequency, but reported the steady-state wavelength λ and wave velocity u_w. Following Gao et al. (2003), we estimated the inlet forcing frequency through the relation $F = u_w / \lambda$ with the assumption that the waves inherit the perturbation frequency.

Figure 6.5 shows the comparison of the calculated almost stationary sinusoidal type wave shape for Case A. The shadowgraph provided by Kapitza and Kapitza (1949) and the simulated wave shape calculated by Gao et al. (2003) are also presented for comparison. Figure 6.5(a) is the experiment via shadowgraph; Figure 6.5 (b) is the calculation by Gao et al. (2003); Figure 6.5 (c) is the results calculated in this work. From this figure, it can be seen that the calculated waveform and the experiment are very similar. Gao et al. overestimated the wave length on comparison with the experiment and our work. Overall, the wave shape exhibits a slightly steep front and gentle tail. The curvature of the wave surface is larger at the wave trough and smaller at the wave crest and tailing slope.

Figure 6.6 shows the evolution of the studied film flows under the inlet forcing disturbance. The coordinates in these figures are made dimensionless by the corresponding characteristic film thickness estimated by Equation (6-23). Same operations are done for all of the figures in this work. It can be seen that the small capillary ripples rapidly spread over the whole length and grow into larger amplitude waves in the downstream direction. For the smaller Reynolds number cases (Case A and Case B), the small inlet waves grow into nearly sinusoidal type waves. The semi-stationary waves have nearly the same shape and amplitude, and they travel at

nearly the same speed. However, they are not exactly stationary. On close examination of these figures, it can be found that the wavelength and amplitude slightly increase in the streamwise direction. This behavior is consistent with the finding of Kapitza (1949) and Alekseenko (1985). Such behavior also has been summarized by Chang (1994). The wave length and the wave amplitude decrease with the increasing of disturbance frequency. This trend is validated by the experimental works of Nosoko et al. (1996). For the mid Reynolds number cases (Case C and Case D), such trend is also observed with the increasing of disturbance frequency. At low frequency, the small inlet waves grow into solitary type waves with capillary wave ahead.

These four cases cover the regular wave shapes from small amplitude capillary wave (Case B), sinusoidal type wave (Case A and Case D), and solitary type wave (Case C). These four typical types of flow were chosen to further our understanding on mass transfer model application in the thin film flows.

6.3.2 Vector Plots

Figure 6.7 shows the typical velocity vector plots for the studied cases with stationary wave shapes. The vector plots are expressed with the reference coordinates moving with the respective wave velocities. For all of the studied cases, much change occurs at the trough region. The largest velocity variations occur at the two sides of the trough region. For Case C, with the interaction of the successive solitary wave and

capillary, the largest variation occurs in the front of the large solitary waves. Such interaction effects can also be seen in Case A and Case D. For these two cases, the velocity variation at the front of the wave is slightly larger than the tail region of the wave. Such trend seems to bear some relationships to the relative ratio of the wave amplitude and wave separation. With the increase of such ratio (wave amplitude/wave separation), the variation in the front becomes more significant compared with the tail region of the wave. For the studied four cases, Case B have the smallest ratio; the velocity variation on the two sides of the trough have the almost same magnitude.

From these figures, it also can be seen that a circulation region exists for Case A, Case C and Case D, which have relatively high amplitudes compared to Case B. With the increasing of the amplitude, the circulation region becomes larger and larger. It is noted that the circulation region is restricted to the peak region of the waves. No circulation is found at the residual layer. Such behaviors is also revealed by Gao et al. (2003) and Wasden & Dukler (1989, 1990). The existence of these circulation regions is thought to be helpful for mass transfer process, since they will take the materials from the surface to the substrate region and refresh the surface with fluid from the substrate.

6.3.3 Streamwise Velocity Profiles in the Normal Direction

Figure 6.8(b) to Figure 6.11(b) and Figure 6.10(c) show the x- velocity profiles for various parts along the wave flow direction. The coordinates in the velocity

profiles are made dimensionless according to normalization by the corresponding maximum velocity and film thickness at the respective location, so that the velocity profiles at various position can be drawn in one plot. The positions where the velocity profiles are taken are indicated and numbered by vertical lines shown in the respective Figure 6.8(a) to Figure 6.11(a). In each Figure 6.8(b) to Figure 6.11(b) and including Figure 6.10(c), the black solid line corresponds to the parabolic velocity profile estimated by the flat film theory. From these figures, it can be seen that the velocity profiles generally fit well with the parabolic profile predicted. The largest deviations came from the trough region in Case A and the front wave region in Case C. For Case C, the experimental results of Alekseenko et al. (1985) are provided for comparison. Figure 6.12 shows the comparison between the experimental study carried out by Alekseenko et al. (1985) and the simulation result (Case C) in this work (the taken points are shown in Figure 6.10(a)). Case C is chosen since it has fairly similar wave shape as in Alekseenko et al.'s work. It fits rather well with our simulated results in these regions (the marked regions in Alekseenko et al.'s result are shown in Figure 12(a)), where regions I, II and III broadly correspond to stations 2, 1, and 3, respectively.

Generally, the smaller wave amplitude, the less deviation from the parabolic profile can be observed. Best agreement can be found for Case B. As the amplitude increases, the more obvious deviation from the parabolic profile is observed. These observations are consistent with the prior assumption of parabolic theory.

6.3.4 Other Quantitative Wave Parameters

The wave speeds are calculated by careful examining the magnified two views of waveforms at two close moments as displayed in Figure 6.13 typically. These figures are also made dimensionless and the corresponding time moments are listed in the legend. The wave peak height h_p (the distance between the wave crest and bottom wall), the wave length λ and wave amplitude h_{am} (the distance between the wave crest and wave trough) can also be obtained from the wave evolution figures. Table 6.1 shows the simulated wave parameters for these four studied cases.

Table 6.1: Simulated wave parameters

Flow conditions	Wave speed u_w (m/s)	Wave peak height h_p (m)	Wave length λ (m)	Wave amplitude h_{am} (m)
Case A	0.196	0.00027	0.0072	0.00019
Case B	0.255	0.0002	0.0057	0.000022
Case C	0.378	0.00046	0.01248	0.00037
Case D	0.375	0.00039	0.0054	0.000275

Nosoko et al. (1996) carried out many experiments on falling film characteristics with Reynolds numbers ranging from 14 to 90. Wave velocity, wave peak height and wave length were measured in their experiments. Based on their experimental works, two correlations are presented as:

$$N_{uw} = 1.13 K_F^{0.02} N_\lambda^{0.31} \mathrm{Re}^{0.37}, \tag{6-28}$$

$$N_{hp} = 0.49 K_F^{0.044} N_\lambda^{0.39} \mathrm{Re}^{0.46}. \tag{6-29}$$

where K_F is defined as dimensionless physical properties group parameter ($K_F = \rho^3 \nu^4 g / \sigma^3$), N_λ is the dimensionless wave separation ($N_\lambda = \lambda (g/\nu^2)^{1/3}$), N_{uw} is the dimensionless wave velocity ($N_{uw} = u_w /(\nu g)^{1/3}$), and N_{hp} is the dimensionless wave peak height ($N_{hp} = h_p (g/\nu^2)^{1/3}$).

Figure 6.14 and Figure 6.15 show the comparison of the calculated dimensionless wave velocity and wave peak height with the empirical relations (6-28) and (6-29), respectively. The lines indicate the predictions by the empirical relationships (6-28) and (6-29). The marked points are the corresponding dimensionless parameters obtained from the simulated results. Generally, the simulated results concur reasonably in magnitude and trend with the empirical relation. Taking note that the VOF method essentially tracks VOF data in each computational cell, the wave surface is reconstructed based on given VOF value (in this work, we have regarded VOF=0.5 as the surface position). Such deviation is considered to be acceptable in the midst of experimental uncertainty associated with the two correlations. Now that the results for the wave dynamics are established and compared reasonably with published works, we next proceed to the mass transfer results.

6.3.5 Concentration Profiles

Figure 6.16 shows the instantaneous concentration contours for the studied four cases. Generally, the concentration contour ‘bends’ with the same trend as the wave surface. A closer observation reveals that the circulation motion which occurred in

Cases A, C and D causes the concentration contour in the wave crest region gradually bends towards the wave trough and finally forms an enclosed shape. The concentration gradient at the wave rear region is stepper than the wave front region

In the substrate region, the concentration contours gradually bend towards the bulk region. This is the direct result of mass diffusion motion in the fluid phase. It has been found that the largest velocity variation lies on the two sides of trough region (see Figure 6.7). As it is, the contours of concentration are indeed closest in the vicinity of the trough region; this suggests that there is likely a close relation between the near surface hydrodynamic activities and the associated mass transfer at the interface.

6.3.6 Instantaneous Bulk Concentration Profiles

The instantaneous local bulk concentration is given by the following expression:

$$C_b = \frac{\int_0^{\delta} c dy}{\delta}, \tag{6-30}$$

where δ is the local film thickness, c is the local concentration value.

Figure 6.17 to Figure 6.20 show the typical bulk concentration variations along the wave flow direction. All of these figures plotted are at the same time moment t=0.09s after starting the mass transfer simulation. These figures indicate that the bulk concentration also changes with the surface wave shape. The bulk concentration gradually increases in the downstream direction and remains semi-stationary close to the exit region. This is because the effects from the surface and upstream have

reached the region near the bottom wall. By taking a comparison of the bulk concentration in the further downstream regions, it can be found that the bulk concentration has the following relationship:

C_b (Case D) > C_b (Case C) > C_b (Case A) > C_b (Case B). (6-31)

Such trend indicates the relative mass transfer velocity relationship for the studied four cases. It is known that rapid mass transfer speed will cause the bulk concentration to increase rapidly.

6.3.7 Mass Transfer Velocity Variations

The mass transfer velocity across the interface is calculated as:

$$K_L = \frac{Flux}{C_{i/f} - C_b} = \frac{-D\frac{\partial c}{\partial y}\Big|_{y=i/f}}{C_{i/f} - C_b}, \quad (6\text{-}32)$$

where $y = i/f$ indicates the interface position. Figure 6.21 to Figure 6.24 show the mass transfer velocity variations along the wave flow direction at a particular instance in time. The bulk concentration profile and the wave shape are also included to demonstrate the variation of K_L with the wavy surface. From these figures, it can be seen that the maximal and minimal of mass transfer velocities are located near the troughs and crests of the wave profile, respectively. Close inspection of these figures, it can be found that the maximum value of mass transfer velocity is located in the vicinity of the trough while the minimum value of mass transfer velocity lies slightly ahead of the film crest. Such characteristics were also observed by Sisoev et al. (2005).

Sisoev et al. explained these phenomena from the points of view of the concentration gradient. In Figure 6.16(a) on the instantaneous concentration profile, it is clear that the concentration contours at the trough of each wave are much closer compared to any other regions. As such, one would logically expect the largest mass transfer across the interface to occur at these regions of steep concentration contours. On the other hand, the contours at the wave crest and the region slightly ahead are relatively more spaced out and probably lead to lower value of mass transfer velocity in the mentioned associated regions.

6.3.8 Results

Figure 6.25 to Figure 6.28 show the variation of $(\beta_{rms})^{1/2}{}_{time\ average}$ (where $\beta_{rms} = (\overline{\beta^2})^{1/2}$) along the wave flow direction for studied cases. The value of β^2 at each spatial location is averaged over the computation time of $T = 0.2s$, i.e.:

$$(\beta_{rms})^{1/2}{}_{time\ average} \equiv (\overline{\beta^2})^{1/4}{}_{time\ average} = \left[\frac{1}{T}\int_0^T \beta^2 dt\right]^{1/4}. \tag{6-33}$$

From these figures, it can be seen that $(\beta_{rms})^{1/2}{}_{time\ average}$ increases along the wave evolution direction before reaching the steady-state value corresponding to the quasi-steady condition of the propagating waves further downstream.

On the other hand, by first averaging β^2 spatially across the whole computation length L and then taking the square root, we obtain $(\beta_{rms})^{1/2}{}_{mean}$ (spatial averaging) which varies with time. That is,

$$(\beta_{rms})^{1/2}{}_{mean} \equiv (\overline{\beta^2})^{1/4}{}_{mean} = \left[\frac{\int_0^L \beta^2 dx}{L} \right]^{1/4}, \tag{6-34}$$

where L is the whole length of the computation domain in the x- direction. Figure 6.29 shows the variations of $(\beta_{rms})^{1/2}{}_{mean}$ for the studied four cases. Since the mass transfer simulation is started after the waves have reached semi-stationary (or quasi-steady) state, $(\beta_{rms})^{1/2}{}_{mean}$ should also depict the characteristic of the semi-stationary state affecting the mentioned mass transfer. At different moment in time, $(\beta_{rms})^{1/2}{}_{mean}$ does not change much or there is limited variation about a mean value. It is clear that the variation of $(\beta_{rms})^{1/2}{}_{mean}$ with time about a mean value is found to be higher for the larger Re with imposed higher disturbance frequency F. A note worth mentioning is that from Figure 6.29, the mean value of $(\beta_{rms})^{1/2}{}_{mean}$ generally increases rather monotonically with Re. But it is obvious that the disturbance frequency F has significant effect on $(\beta_{rms})^{1/2}{}_{mean}$ and the Reynolds number is not the sole determining parameter affecting $(\beta_{rms})^{1/2}{}_{mean}$. On stand-alone amplitudes of the waves (see Table 6.1), there is no clear trend between $(\beta_{rms})^{1/2}{}_{mean}$ and the wave amplitude. Neither is there a clear trend or monotonic relation between the wavelength λ (see Table 6.1) and $(\beta_{rms})^{1/2}{}_{mean}$. As such, a combination of wave parameters may be necessary to relate to $(\beta_{rms})^{1/2}{}_{mean}$ (and subsequently the mass transfer velocity K_{L-mean}, see below and Figure 6.30) in a consistent monotonic behavior. This may partly explain why it is so much harder to reach a general grouping of wave/hydrodynamic parameters to relate consistently to the mass transfer velocity across the interface of thin film flow represented by K_{L-mean}.

Figure 6.30 shows the variation of the mean mass transfer velocity (K_L) taken over the computation domain with time, which is calculated as:

$$K_{L-mean} = \frac{\int_0^L K_L dx}{L}. \tag{6-35}$$

It may be noted that long time computation has been adopted for the wave propagation downstream to have reached quasi-steady condition and likewise mass transfer across the interface has similarly obtained quasi-steady condition before the evaluation of K_{L-mean}. From Figure 6.30, it is clear that:

$$K_{L-mean}\text{(Case D)} > K_{L-mean}\text{(Case C)} > K_{L-mean}\text{(Case A)} > K_{L-mean}\text{(Case B)} \tag{6-36}$$

follows faithfully the monotonic behavior of

$$(\beta_{rms})^{1/2}{}_{mean}\text{(Case D)} > (\beta_{rms})^{1/2}{}_{mean}\text{(Case C)} > (\beta_{rms})^{1/2}{}_{mean}\text{(Case A)} > (\beta_{rms})^{1/2}{}_{mean}\text{(Case B)}$$

which gives us hope that the functional form of Equation (3-2) may yet be applicable for the thin film flow.

Figure 6.31 presents the variation of the ratio $K_{L-mean} Sc^{0.5} / \left[(\beta_{rms})_{mean} \nu\right]^{0.5}$ with time. For all of the studied cases, an overall mean linear fit can be obtained giving rise to a constant C=0.14. This correlation deduced is indeed close to the constant coefficient of C=0.2 as presented in Xu et al. (2006) or Equation (3-2). Not only is the functional form between K_{L-mean} and $(\beta_{rms})^{1/2}{}_{mean}$ consistent with Equation (3-2) but the coefficient obtained is of the same order of magnitude, all of which portents well that the correlation relation of Equation (3-2) may truly possess universal property. Of course, this is just the first step in the preliminary tests of mass transfer across thin film flow. More tests of vastly different wave conditions for the thin film flow are needed to further substantiate or otherwise.

Chapter 7 Concluding Summary and Future Work

An objective of this study is to investigate the correlation between the interfacial mass transfer velocity and the near interface turbulence parameters. It is increasingly clear that the employment of bulk turbulence is unable to provide a unique relationship between the turbulent hydrodynamics and the scalar transfer velocity. It is also widely acknowledged that the flow hydrodynamics in the immediate vicinity of the interface like the vertical velocity gradient (β or the surface divergence) play an important role in determining the transport process which is fairly independent of the means of turbulence generation. To reveal the flow hydrodynamics in the immediate vicinity of the interface, a reliable improved measurement method was developed for the circular wind wave channel setup. Two independent camera systems were used to observe the flow field beneath the interface and the liquid surface. Compared with the previous works reported by other researchers (Jahne & Wierzimok (1990), and Law & Khoo (2002)), this measurement method has a higher spatial resolution up to 20μm, enabling it to reveal the near interface region. Another feature of this measurement method is that the interface position can be precisely determined by an local adaptive image processing technique developed. Based on the improved measurement method presented in this work, quantification of the vertical velocity with respect to the fluctuating interface and evaluation of the associated velocity gradient in the vicinity of the interface were carried out. The critical parameter β was obtained under vastly different and distinct flow conditions. These flow conditions included turbulence

induced by wind shear from above, turbulence generated and diffused to the free surface from beneath the interface, and turbulence generated under a combination of contributing conditions from above and beneath the gas-liquid interface simultaneously. All of them can be regarded as simplifications of real life complex turbulence generation methods.

Mass transfer experiments were also carried out to provide the scalar transfer velocity information. In this work, the mass transfer velocity was determined by measuring the evasion rate and the absorption rate of dissolved oxygen. These two rates were employed as a self-consistent check and were used to demonstrate that the correlation relationship obtained is independent of the direction of scalar transport. Results from the mass transfer experiments suggest that the relationship between the interfacial hydrodynamic parameters and the mass transfer velocity can be expressed in the following relationship:

$$\frac{K_L}{(\beta_{rms}\nu)^{0.5}} Sc^{0.5} = 0.20 . \tag{7-1}$$

In industrial applications, falling film setups are widely used and mass or heat transfer phenomena are most important processes in such setups. Numerical simulations and experimental works were also carried out for this kind of flow type—falling film—in the present work.

An inclined plate falling film setup was designed for the experimental work. The setup is highly compact and suitable for falling film experiments. Several flow conditions under different inclined angles and flow rates were tested. The surface velocity variations and the surface divergence were analyzed and correlated with the

mass transfer velocity. This is perhaps the first time that an attempt is made to correlate the selected parameter β with the mass transfer velocity in such conditions. Most of the prior works tried to correlate the mass transfer velocity with some characteristic flow parameters such as Reynolds number or wave velocity or others; all with varying degree of universality. The present (preliminary) results from the falling film experiments, which generally fit rather well with the correlation expression of (7-1) obtained from non-falling film experimental setups, give us hope on the generality of the proposed mass transfer model based on β .

For the numerical simulation of falling film, Volume of Fraction (VOF) method was adopted to track the wavy surface, and a User Defined Function (UDF) was added in the FLUENT software to provide a forcing disturbance boundary conditions. A User Defined Scalar (UDS) function was added to perform the mass transfer simulation. Several vertical types of falling film flow conditions under various Reynolds numbers with different forcing disturbance frequencies were analyzed. The wave shapes, velocity distribution profiles and concentration profiles were discussed. The selected parameter β was deduced from the vertical velocity profile, and its relationship with the mass transfer velocity was explored again. The simulation results show reasonable concurrence with the correlation relationship of (7-1).

Finally, Figure 7.1 shows the various experimental results from Chapter 3 (based on co-current and counter-current shear flow at the gas-water interface), Law & Khoo (2002) (based on deeply submerged jet and wind induced shear flow at the gas-water interface), McKenna & McGillis (2004) (based on oscillating grid-stirred turbulence

beneath the free surface), Tamburrino & Gulliver (2002) (based on moving-bed flume in open channel flow), the numerical simulations of McCready et al. (1986) (based on a simple liquid flow beneath a mobile interface next to gaseous medium), and the present numerical simulation and experimental results based on falling thin film arrangement for comparison. Generally, these data depict similar trend and same order of magnitude. This observation suggests that the selected key parameter β (the gradient of the vertical fluctuating velocity at the interface or surface divergence) likely plays an important role in determining the transport process, which is fairly independent of the turbulence generation methods. A possible general relationship can be presented as:

$$\frac{K_{L-mean} Sc^{0.5}}{(\beta_{rms}\nu)^{0.5}} = C \sim \text{O}(1.0). \tag{7-2}$$

The ability of Equation (7-2) to predict mass transfer rates under different conditions using a single model based on β_{rms}, highlights the significance of β as the primary governing hydrodynamic parameter controlling the scalar transport rate.

It should be noted that the sparingly soluble gases were used as the scalar tracer in this study. Under such conditions, the major resistance for transporting lies in the liquid phase and the transport is determined predominantly by the liquid side hydrodynamics. The situation is completely different for the other gases with large solubility such as NH_3. For such gases, the major resistance for transporting shifts to the gas phase. As a result, the present scalar transfer model may not be applicable (However, one may yet define an equivalent β applicable to the gaseous phase and perhaps a similar expression to (7-2) is still relevant). In addition, as we have pointed

out earlier, the interfacial scalar transfer velocity is also affected by other factors. In addition to the liquid hydrodynamics (characterized by β_{rms}) and the liquid properties (characterized by Sc), the liquid surface conditions (such as contamination conditions) also have a significant effect on the transfer velocity. How these factors contribute to the mass transfer rate and how their effects can be included in the transfer model are interesting topics for future work.

Lastly, the present mass transfer model based on β was generalized from many different types of experiments. For wider applications, it may be expedient to relate β to the more easily measurable/quantifiable parameter(s) pertaining to each particular application. This opens up a wide scope for future work.

References:

Alekseenko S V, Nakoryakov V Ye, Pokusaev B G. Wave formation on a vertical falling liquid film. AIChE Journal, 1985; 31: 1446-1460.

Bach P, Villadse N J. Simulation of the vertical flow of a thin, wavy film using a finite-element method. International Journal of Heat and Mass Transfer, 1984; 27(5): 815-827.

Banerjee S, Lakehal D, Fulgosi M. Surface divergence models for scalar exchange between turbulent streams. International Journal of Multiphase Flow, 2004; 30: 963-977.

Baumann K H, Muhlfriedel K. Mass transfer and concentration profiles near phase boundaries. International Journal of Thermal Science, 2001; 40: 425-436.

Brackbill J U, Kothe D B, Zemach C. A continuum method for modeling surface tension. Journal of Computational Physics, 1992; 100: 335-354.

Brauner N, Maron D M. Modelling of wavy flow in inclined thin films. Chemical Engineering Science, 1983; 38: 775-788.

Brauner N. Modelling of wavy flow in turbulent free falling films. International Journal of Multiphase Flow, 1989; 15(4): 505-520.

Brumley B H, Jirka G H. Air-water transfer of slightly soluble gases: turbulence. Interfacial processes and conceptual models. Physicochemical Hydrodynamics, 1988; 10: 295-319.

Change H C. Wave evolution on a falling film. Annual Review of Fluid Mechanics, 1994; 26:103-136.

Cussler E L. Diffusion, Mass Transfer in Fluid Systems. Cambridge University Press, New York, 1984; 282.

Davies J T, Rideal E K. Interfacial phenomena. Academic Press, New York, NY, 1963.

Danckwerts P V. Significance of liquid-film coefficients in gas absorption. Industrial and Engineering Chemistry Research, 1951; 43(6):1460-1467.

Duke S R, Wolff L M, Hanratty T J. Slope of small scale wind waves and their relation to mass transfer rates. Experiments in Fluids, 1995; 19: 280-292.

Dukler A E. Characterization, effects and modeling of the wavy gas-liquid interface. Progress in Heat and Mass Transfer, 1972; 6:207-234.

Fortescue G E, Pearson J R A. On gas absorption into turbulent liquid. Chemical Engineering Science, 1967; 22: 1163-1176.

Gao D, Morley N B, Dhir V. Numerical simulation of wavy falling film flow using VOF method. Journal of Computational Physics, 2003; 192: 624-642.

George J, Minel F, Grisenti M. Physical and hydrodynamical parameters controlling gas-liquid mass transfer. International Journal of Heat and Mass Transfer, 1994; 37: 1569-1578.

Grossman G.. Heat and mass transfer in film absorptions. In: The Handbook for Heat and Mass Transfer Operations, Cheremisinoff N P (Eds.), Gulf, 1984.

Gulliver J S. Introduction to gas-liquid mass transfer. In: Gas-liquid mass transfer. Wilhelm S C and Gulliver J S (Eds.), 1990; 1-7.

Gulliver J S, Halverson M J. Air-water gas transfer in open channels. Water Resource Research, 1989; 25: 1783-1793.

Hanratty T J. Effect of gas flow on physical adsorption. In: Air-water mass transfer. Wilhelm S C, Gulliver J S(Eds.), New York: ASCE, 1991: 10-33.

Hassan Y A, Okamoto K, Philip O G. Investigation of the interaction between a fluid flow and the fluid's free surface using particle image velocimetry. In the Ninth International Symposium on Transport Phenomena in Thermal-Fluids Engineering (ISTP-9),1996: 566-574.

Higbie R. The rate of absorption of a pure gas into a still liquid during short periods of exposure. Trans. AIChE, 1935; 31: 365-388.

Ho F C K, Hummel R L. Average velocity distributions within falling liquid films. Chemical Engineering Science, 1970; 25: 1225-1237.

Ho L W, Patera A T. A legendre spectral element method for simulation of unsteady incompressible viscous free-surface flows. Computer Methods in Applied Mechanics and Engineering, 1990; 80: 355-366.

Hunt J C R, Graham J M R. Free stream turbulence near plane boundaries. Journal of Fluid Mechanics, 1978; 84: 209-235.

Jahne B, Huber W, Dutzi A, Wais T, Ilmberger J. Wind/wave-tunnel experiments on the Schmidt number and wave field dependence of air-water gas exchange. in: Gas Transfer at Water Surfaces, Brutsaert W & Jirka G H (Eds.). 1984; 303-309.

Jahne B, Munnich K O, Bosinger B, Dutzi A, Huber W, Libner, P. On the parameters influencing gas-liquid gas transfer. Journal of Geophysical Research, 1987; 92(c2). 1937-1949.

Jahne B, Munnich K O, Siegenthaler U. Measurements of gas exchange and

momentum transfer in a circular wind-water tunnel. Tellus. 1979; 31: 321-329.

Jahne B, Reimer K S. Two-dimensional wave number spectra of small-scale water surface waves. Journal of Geophysical Research, 1990; 95: 11531-11546.

Jahne B, Wierzimok D. Measurement of wave-induced turbulent flow structures using digital image sequence analysis. In: Gas-liquid mass transfer. Wilhelm S C and Gulliver J S (Eds.). 1990; 200-209.

Kapitza P L, Kapitza S P. Wave flow of thin layers of a viscous liquid. Zh. Eksp. Teor. Fiz.1949; 19:105-120; also seen in Collected papers of P.L.Kapitza(vol II), the Macmillant company, New York,1964.

Karapantsios T D, Karabelas A J. Surface characteristics of roll waves on free falling films. International Journal of Multiphase Flow, 1990; 16: 835-852.

Karapantsios T D,Paras S V, Karabelas A J. Statistical characteristics of free falling films at high Reynolds number. International Journal of Multiphase Flow, 1989; 15(1):1-21.

Katznelson R. DQM standard operating procedure (SOP) 9.2.1.2(v3); 2004. http://www.swrcb.ca.gov/nps/docs/cwtguidance/9212sop.pdf.

Kawaji M. Two-phase flow measurements using a photochromic dye activation technique. Nuclear Engineering and Design. 1998; 184: 379-392.

Kheshgi H S, Scriven L E. Disturbed film flow on a vertical plate. Physics of Fluids, 1987; 30(4): 990-997.

Khoo B C, Sonin A A. Scalar rate correlation at a turbulent water free surface: a two-regime correlation for high Schmidt number. International Journal of Heat

and Mass Transfer, 1992; 35: 2233-2244.

Komori S, Murakami Y, Ueda H. The relationship between surface renewal and bursting motions in an open channel flow. Journal of Fluid Mechanics, 1989; 203: 103-123.

Lamont J C, Scott D S. An eddy cell model of mass transfer into surface of a turbulent liquid. AICHE Journal, 1970; 16: 513-519.

Lau Y L. An experimental investigation of reaeration in open channel flow. Progress in Water Technology, 1975; 7(3/4): 519-530.

Law C N S, Khoo B C, Chew, T C, Turbulence structure in the immediate vicinity of the shear-free air-water interface induced by a deeply submerged jet. Experiments in Fluids, 1999; 27: 321-331.

Law C N S, Khoo B C. Transport across a Turbulent Gas-liquid Interface. AIChE. Journal, 2002; 48(9): 1856-1868.

Law C N S. Turbulence and mass transfer at the air-water interface. Ph.D thesis. National University of Singapore. 2002.

Lel V V, Al-Sibai F, Leefken A, Renz U. Local thickness and wave velocity measurement of wavy films with a chromatic confocal imaging method and a fluorescence intensity technique. Experiments in Fluids, 2005; 39: 856-864.

Li B Y, Liu N S, Lu X Y. Direct numerical simulation of vertical rotating turbulent open-channel flow with heat transfer. Communications in Computational Physics, 2006; 1: 336-361.

Lin H J, Perlin M. Improved methods for thin surface boundary layer investigations.

Experiments in Fluids,1998; 25: 431-444.

Liu J, Gollub J P. Solitary wave dynamics on films flows. Physics of Fluids, 1994; 6(5): 1702-1712.

Lorencez C, Nasr-Esfahany M, Kawaji M. Turbulence structure and prediction of interfacial heat and mass transfer in wavy-stratified flow. AICHE Journal. 1997: 43: 1426-1435.

Lyu T H, Mudawar I. statistical investigation of the relationship between interfacial waviness and sensible heat transfer to a falling liquid film. International Journal of Heat and Mass Transfer, 1991; 34(5): 1451-1464.

Malamataris N T, Papanastasiou T C. Unsteady free surface flows on truncated domains. Industrial and Engineering Chemistry Research, 1990; 30: 2211-2219.

Maron D M, Brauner N, Dukler A E. Interfacial structure of thin falling films: piecewise modeling of the waves. Physicochemical Hydrodynamics, 1985; 6: 87-113.

McCready M J, Vassihadou E, Hanratty T J. Computer simulation of turbulent mass transfer at a mobile interface. AIChE Journal, 1986; 32: 1108-1115.

McKenna S P, McGillis W R. The role of free-surface turbulence and surfactants in gas-water gas transfer. International Journal of Heat and Mass transfer, 2004; 47: 539-553.

Mckenna S P. Free-surface turbulence and air-water gas exchange. Ph.D. Thesis. MIT, Cambridge, MA. 2000.

Miller W A, Keyhani M. The correlation of simultaneous heat and mass transfer

experimental data for aqueous lithium bromide vertical falling film absorption. Journal of Solar Energy Engineering, 2001; 123: 30-42.

Miller W A. Experimental and analytical study of aqueous LiBr falling film absorption. Ph.D thesis. University of Tennessee, USA. 1992.

Mills A F. Mass transfer. Prentice-Hall, Inc. Upper Saddle River, New Jersey, 2001; 392-393.

Molder E, Tenno T, Mashirin A. The effect of surfactants on oxygen mass-transfer through the gas-water interface. Environmental Science and Pollution Research, 2002; Special Issue 1: 39–42.

Moran K, Inumaru J, Kawaji M. Instantaneous hydrodynamics of a laminar wavy liquid film. International Journal of Multiphase Flow, 2002; 28:731-755.

Morioka I, Kiyota M, Nakao R. Absorption of water vapor into a film of aqueous solution of LiBr falling along a vertical pipe. JSME International Journal, 1993; series B; 36(2): 351-356.

Morioka I, Kiyota M. Absorption of water vapor into a wavy film of an aqueous solution of LiBr. JSME International Journal, 1991; series II 34(2):183-188.

Munsterer T, Jahne B. LIF measurements of concentration profiles in the aqueous mass boundary layer. Experiments in Fluids, 1998; 25: 190-196.

Nosoko T, Yoshimura P N, Nagata T, Oyakawa K. Characteristics of two-dimensional waves on a falling liquid film. Chemical Engineering Science, 1996; 51(5): 725-732.

Nusselt W. Die oberflachenkondensation des wasserdampfes (in German). Zeitschrift

VDI, 1916; 60:541-546.

Patnaik V, Perez-Blanco H. A study of absorption enhancement by wavy film flows. International Journal of Heat and Fluid Flow, 1996; 17: 71-77.

Peirson W L. Measurement of surface velocities and shears at a wavy gas-water interface using particle image velocimetry. Experiments in Fluids, 1997; 23: 427-437.

Portalski A, Clegg A J. An experimental study of wave inception on falling liquid films. Chemical Engineering Science, 1972; 27: 1257-1265.

Raffel M, Willert C, Kompenhans J. Particle Image Velocimetry, a Practical Guide. Springer, Berlin. 1998; 59-60.

Ramaswamy B, Chippada S, Joo S W. A full-scale numerical study of interfacial instabilities in thin-film flows. Journal of Fluid Mechanics, 1996; 325: 163-194.

Ridler T W, Calvard S. Picture thresholding using an iterative selection method. IEEE Transactions.System Man.Cybern, 1978; 8(8):630-632.

Salamon T R, Armstrong R C, Brown R A. Traveling waves on vertical films: numerical analysis using the finite element methods. Physics of Fluids, 1994; 6: 2202-2220.

Saylor J R, Handler R A. Gas transport across an air-water interface populated with capillary waves. Physics of Fluids, 1997; 9: 2529-2541.

Sisoev G M, Matar O K, Lawrence C J. Absorption of gas into a wavy falling film. Chemical Engineering Science, 2005; 60: 827-838.

Tamburrino A, Gulliver J S. Free surface turbulence and mass transfer in a channel

flow. AIChE Journal, 2002; 48: 2732-2743.

Tamburrino A. Free-surface kinematics: Measurement and relation to the mass transfer coefficient in open channel flow. Ph.D. Thesis. University of Minnesota. Minnesota. 1994.

Theofanous T G. Conceptual models of Gas Exchange. In: Gas transfer at water surfaces. Brutsaert W, Jirka GH. (Eds.), Dordrecht, Holland: D. Reidel Publishing company, 1984: 271-281.

Vasconcelos J M T, Rodrigues J M L, Orvalho S C P, Alves S S, Mendes R L, Reis A. Effect of contaminants on mass transfer coefficients in bubble column and airlift contactors. Chemical Engineering Science, 2003; 58: 1431–1440.

Vikas P, Horacio P B. Roll waves in falling films: an approximate treatment of the velocity field. International Journal of Heat and Fluid Flow, 1996; 17(1):63-70.

Wasden F K, Dukler A E. A numerical study of mass transfer in free falling wavy films. AIChE Journal, 1990; 36(9): 1379-1390.

Wasden F K, Dukler A E. Insights into the hydrodynamics of free falling wavy films. AIChE Journal, 1989; 35(2):187-195.

Weitbrecht V, Kühn G, Jirka G H Large scale PIV-measurements at the surface of shallow water flows. Flow Measurement and Instrumentation, 2002; 13 (5-6): 237-245.

Xu Z F, Khoo B C, Carpenter K. Mass transfer across the turbulence gas-water interface. AIChE Journal, 2006; 52: 3363-3374.

Yang R, Jou D. Heat and mass transfer on the wavy film absorption process. Canadian

Journal of Chemical Engineering, 1993; 69:723-728.

Yoshimura P N, Nosoko T, Nagata T. Enhancement of mass transfer into a falling laminar liquid film by two-dimensional surface waves—some experimental observations and modeling. Chemical Engineering Science, 1996; 51(8): 1231-1240.

Youngs D L. Time-dependent multi-material flow with large fluid distortion. In Morton K W and Baines M J, editors, Numerical method for fluid dynamics, Academic Press. 1982.

Zhang X, Cox C S. Measuring the two-dimensional structure of a wavy surface optically: a surface gradient detector. Experiments in Fluids, 1994; 17: 225-237.

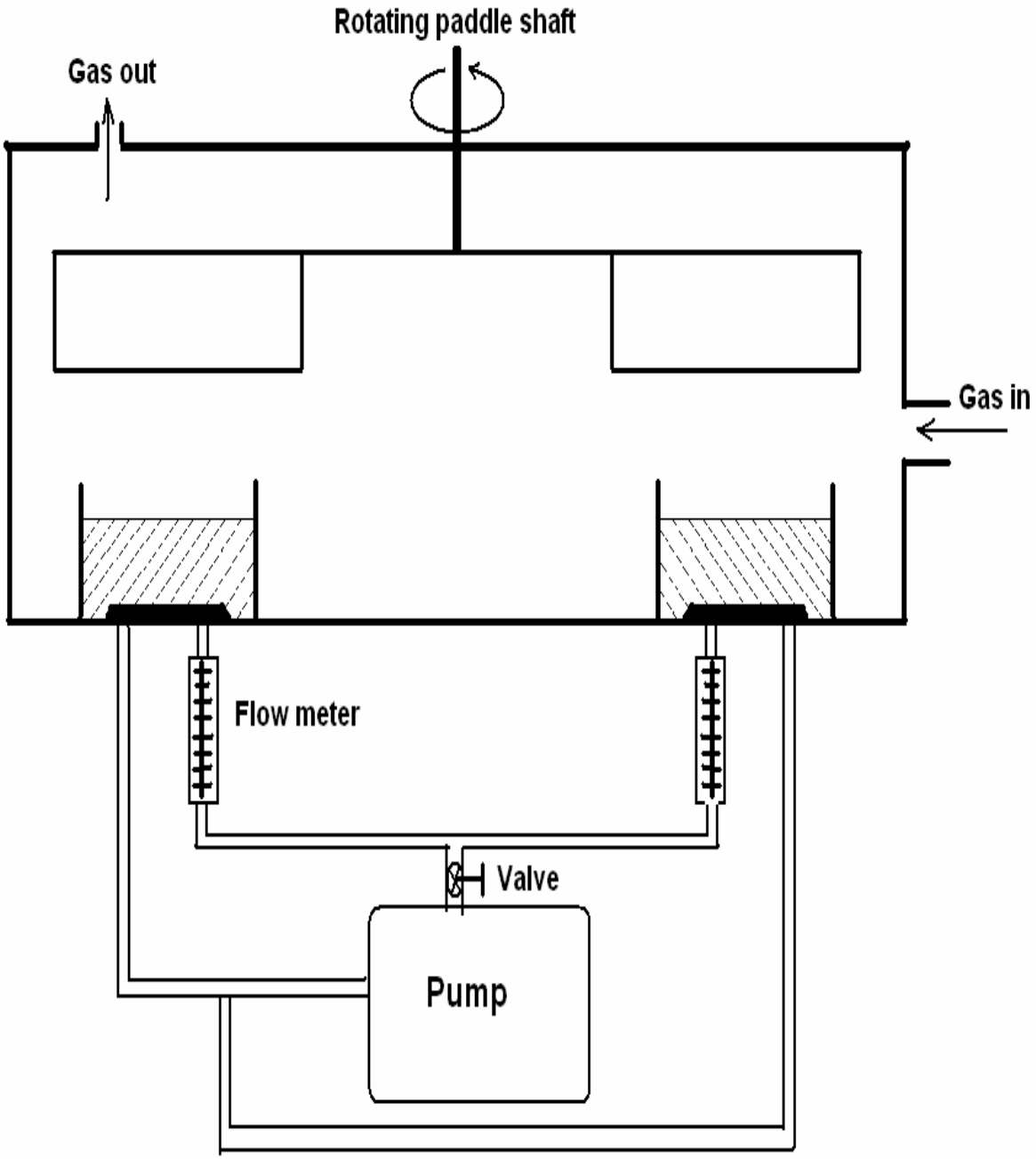

Figure 2.1: Schematic diagram of the circular water tank (not to scale)

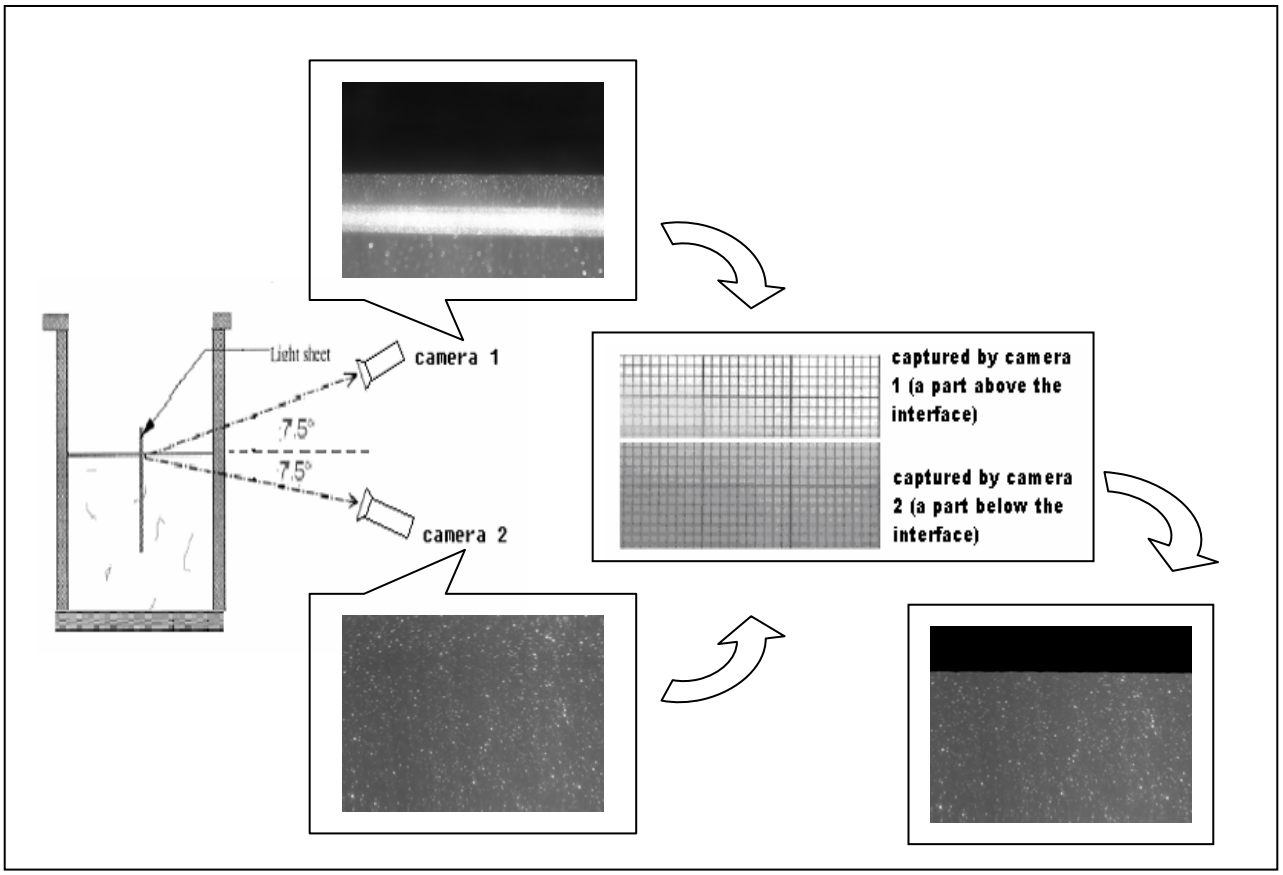

Figure 2.2: Schematic diagram of the observing angles and interface detection

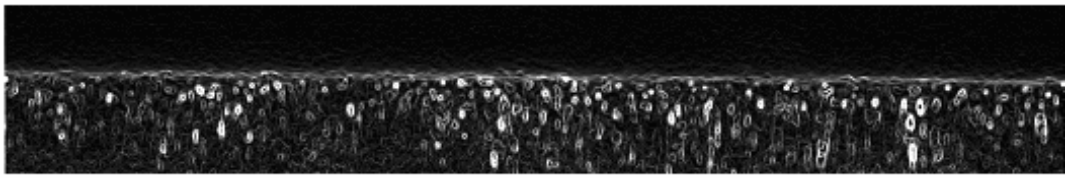

Figure 2.3: Edge detection worked on the near surface region (gray image)

Figure 2.4: Edge detection worked on the near surface region (binary image)

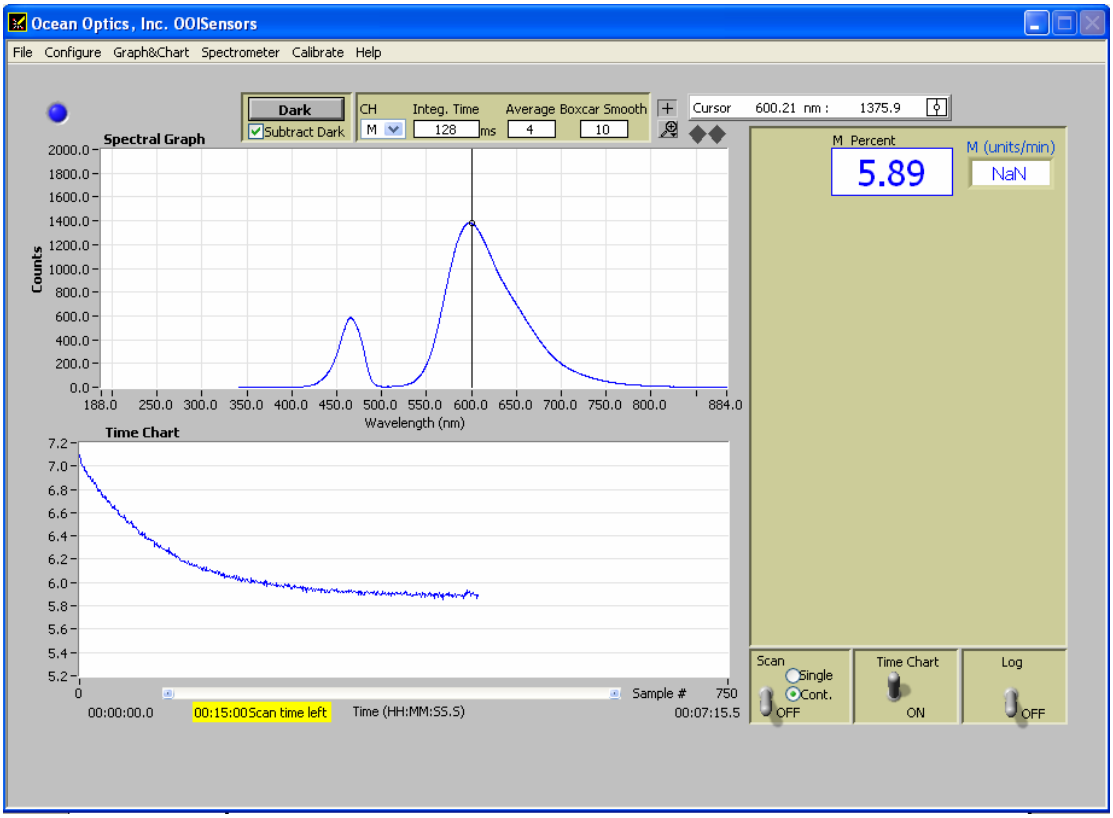

Figure 2.5: Measurement of dissolved oxygen concentration

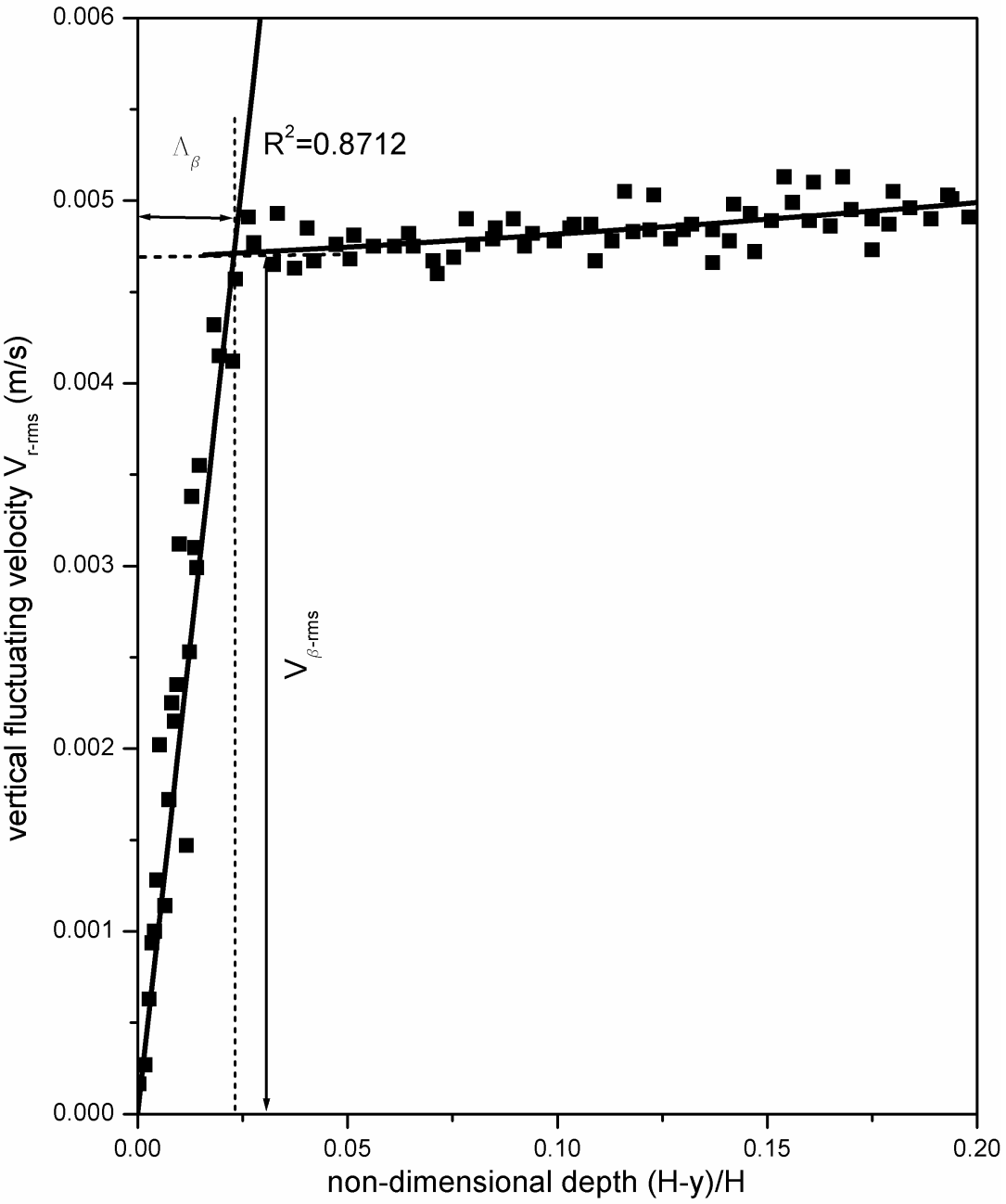

Figure 3.1: Typical Variation of $V_{r\text{-}rms}$ with non-dimensional depth

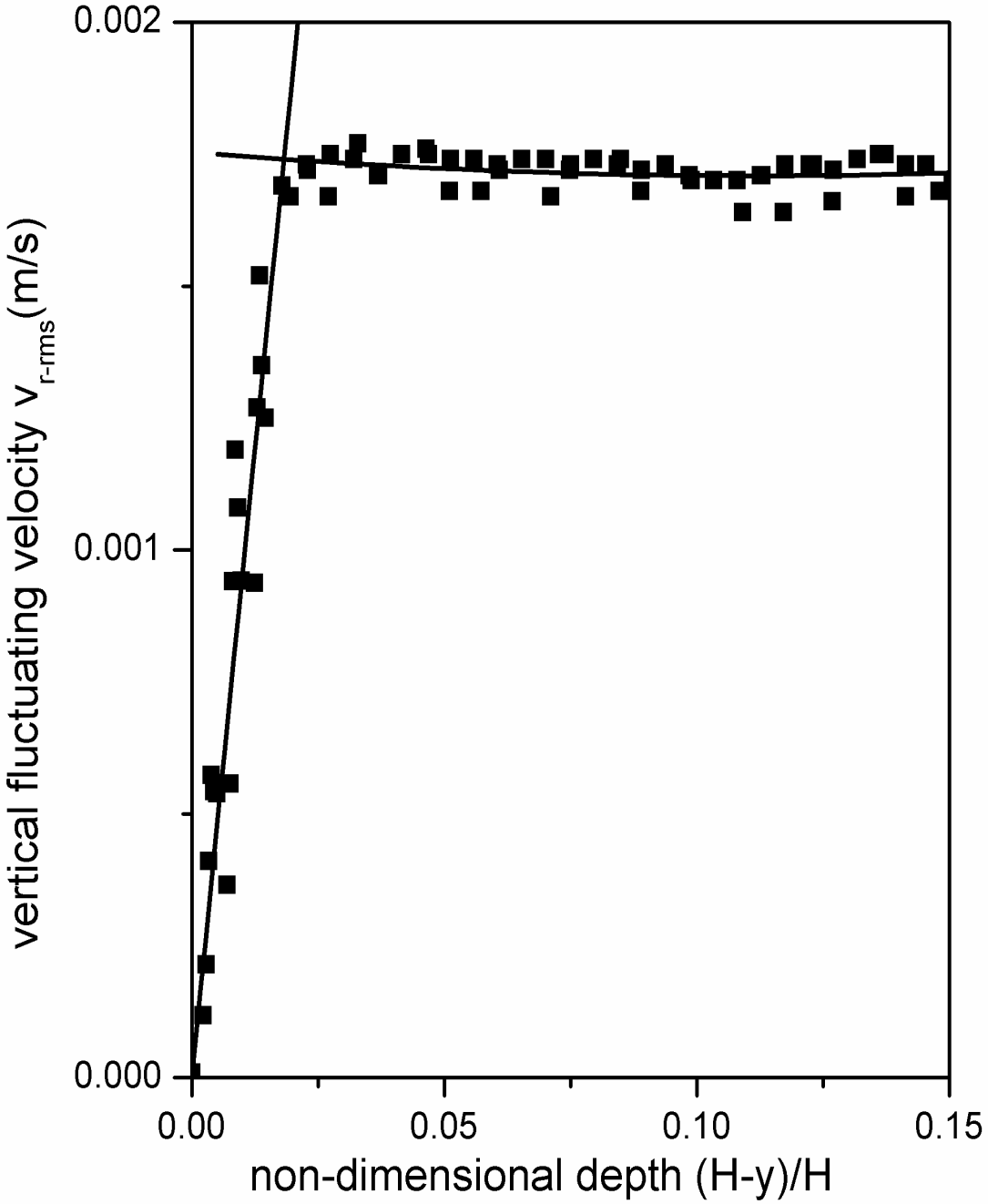

Figure 3.2: Variation of Vr-rms with non-dimensional depth from the interface. Turbulence generated from above the interface only, Wind speed=3m/s

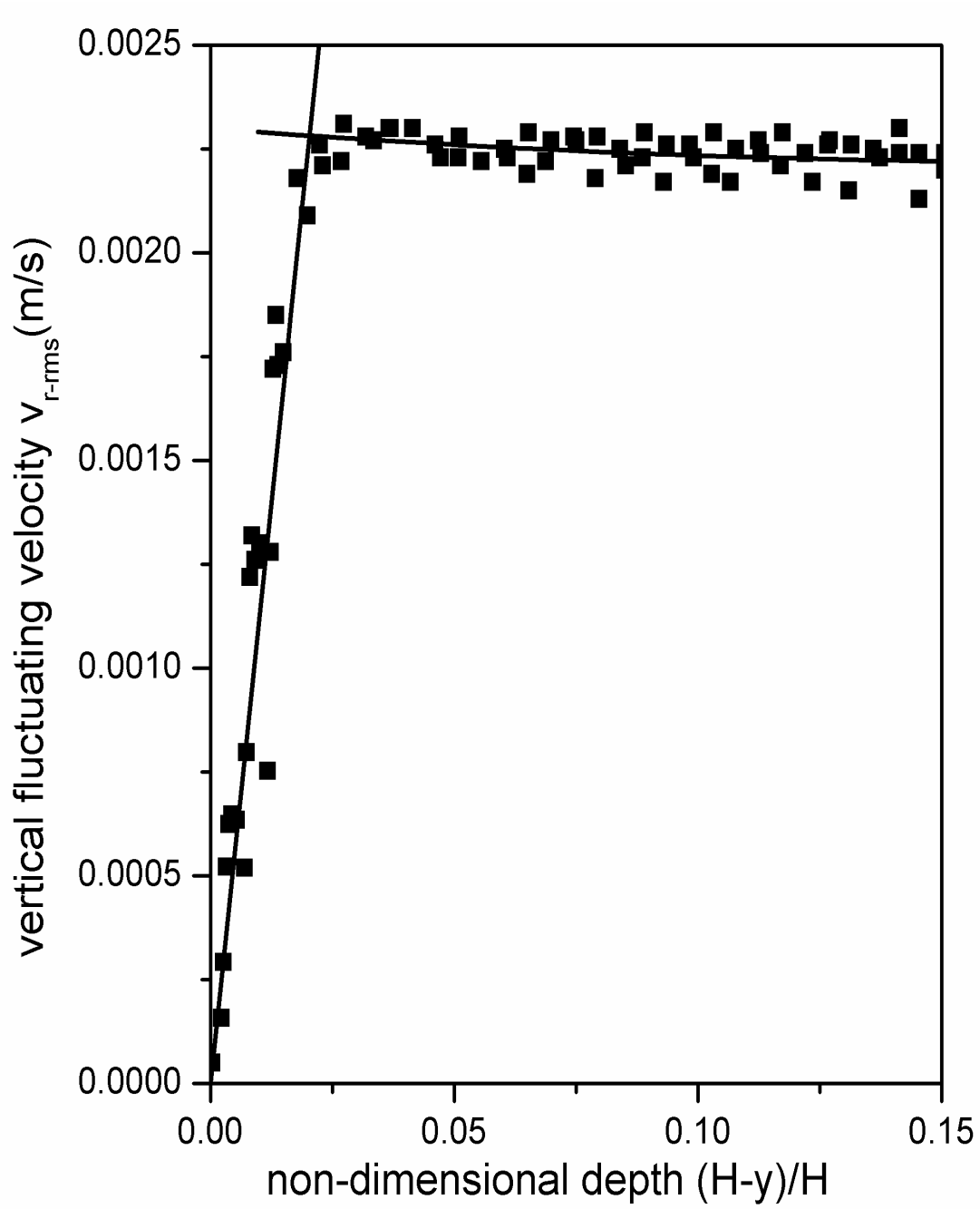

Figure 3.3: Variation of Vr-rms with non-dimensional depth from the interface. Turbulence generated from above the interface only, Wind speed=3.5m/s

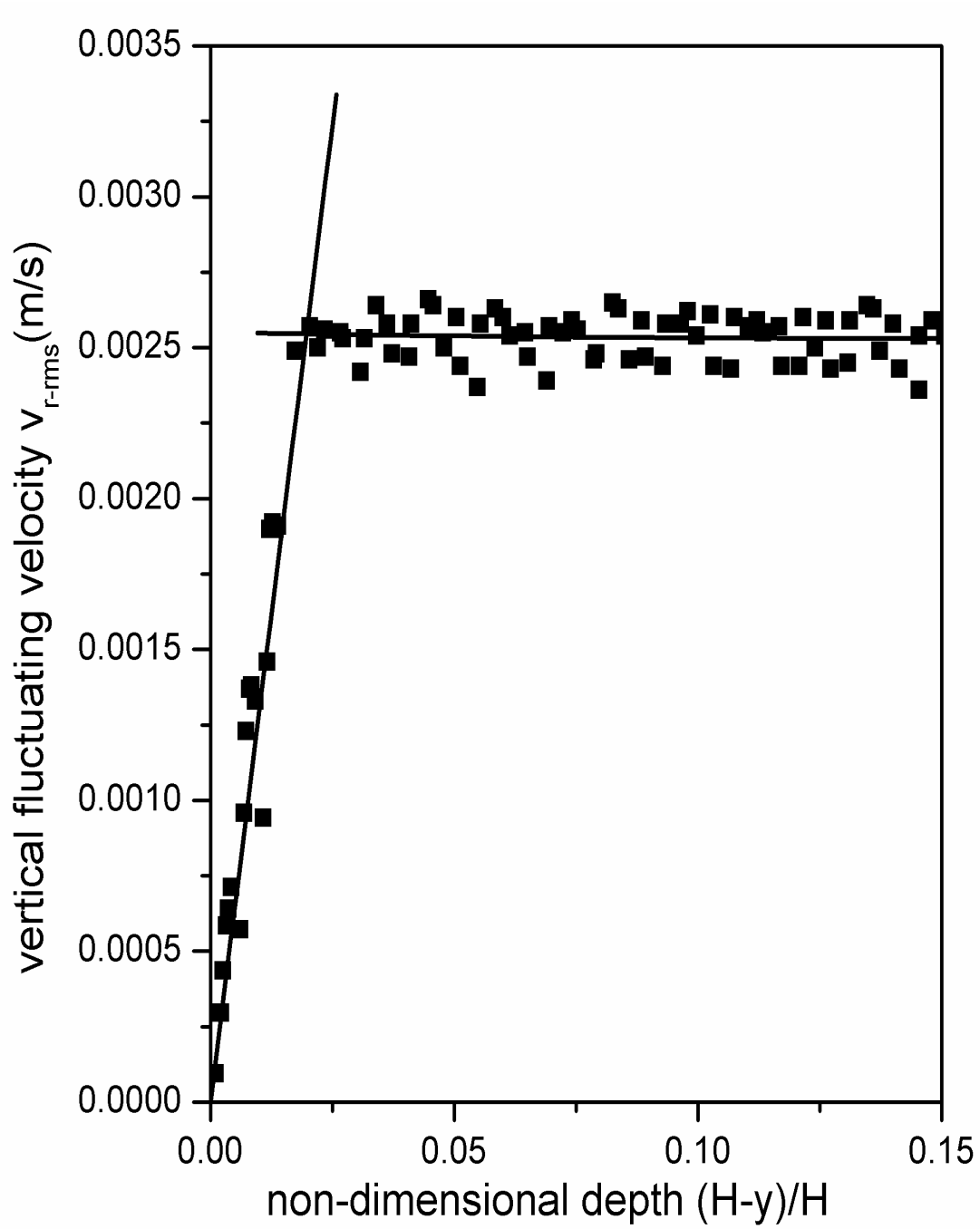

Figure 3.4: Variation of Vr-rms with non-dimensional depth from the interface. Turbulence generated from above the interface only, Wind speed=4m/s

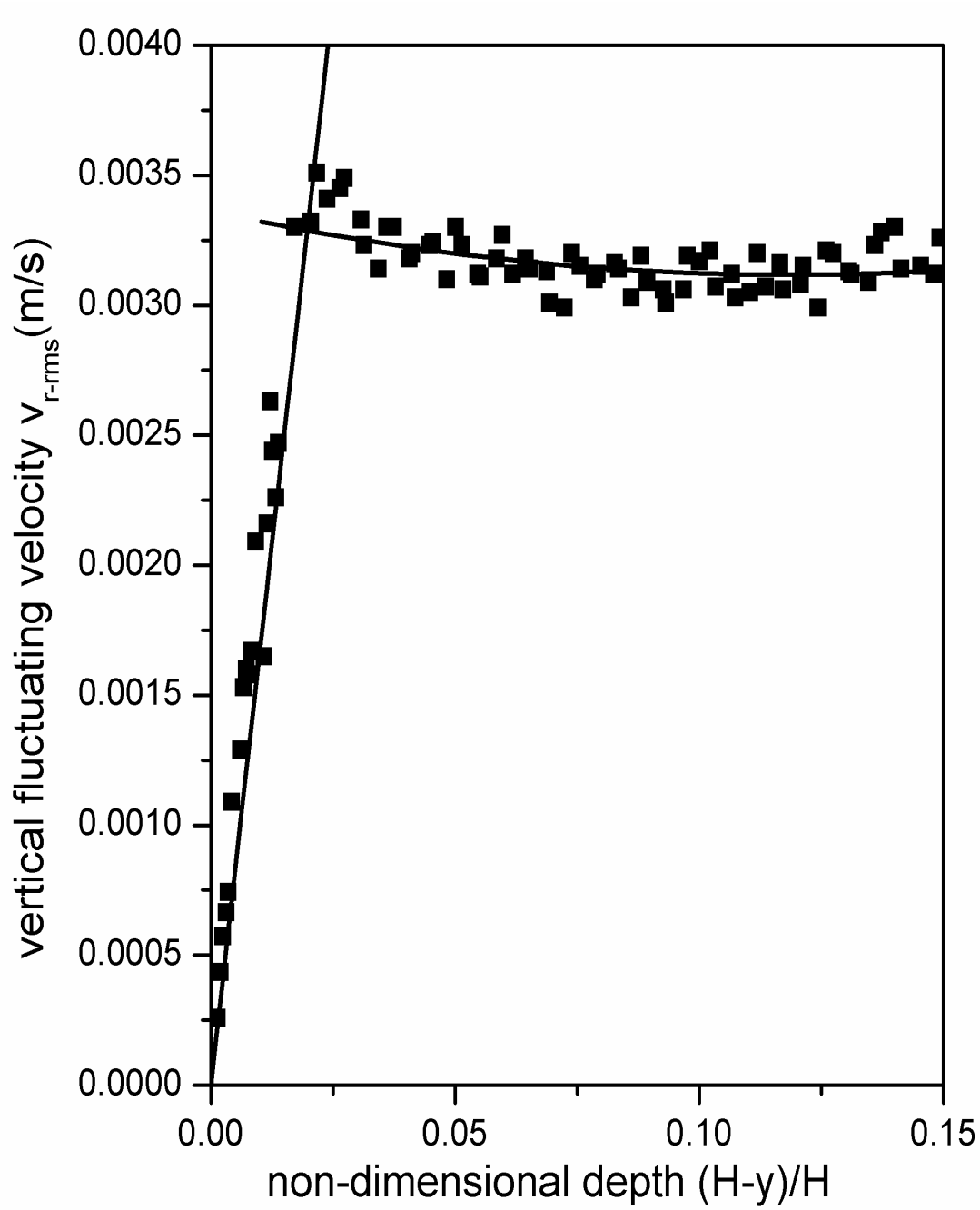

Figure 3.5: Variation of Vr-rms with non-dimensional depth from the interface.

Turbulence generated from above the interface only, Wind speed=4.5m/s

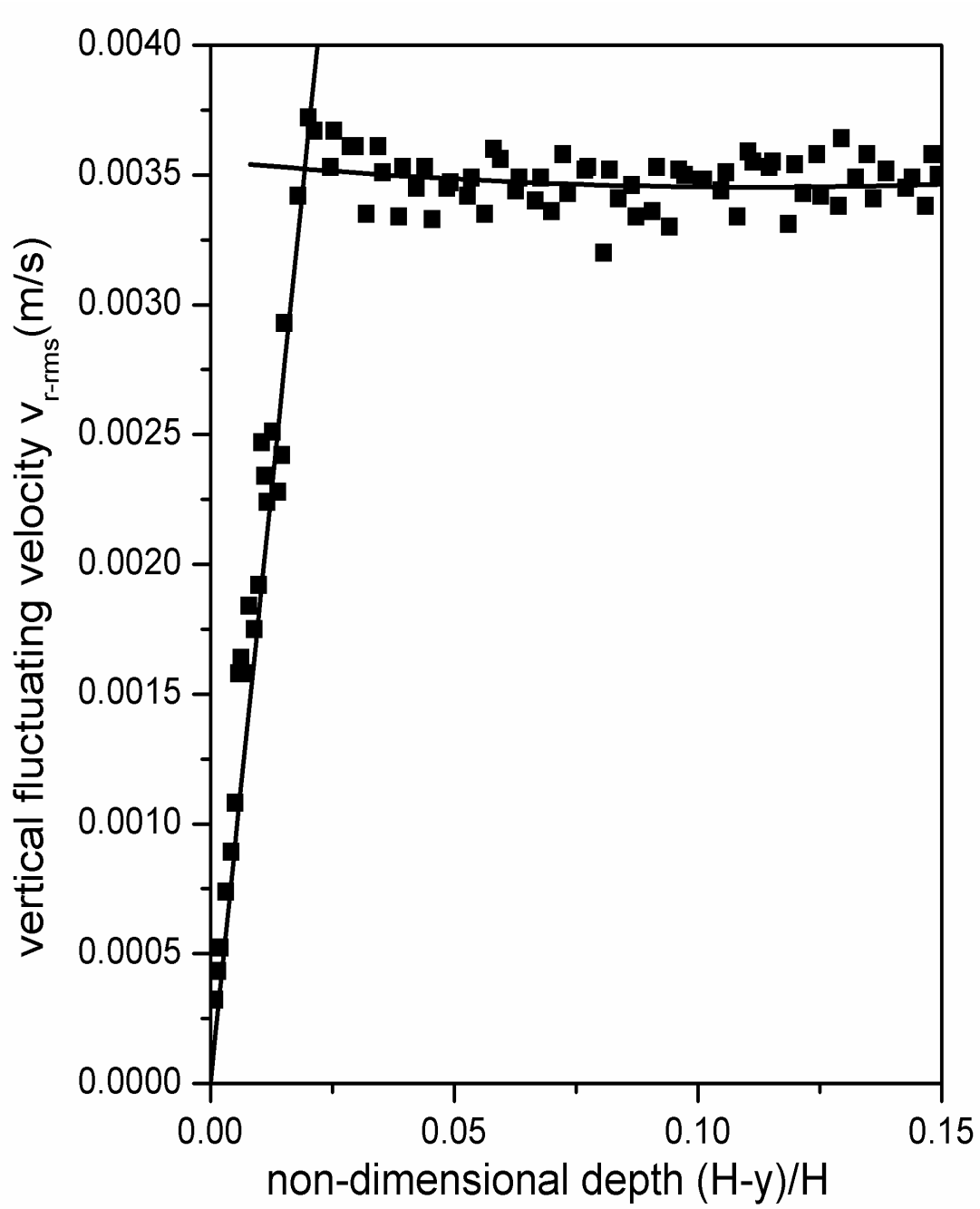

Figure 3.6: Variation of Vr-rms with non-dimensional depth from the interface. Turbulence generated from above the interface only, Wind speed=5m/s

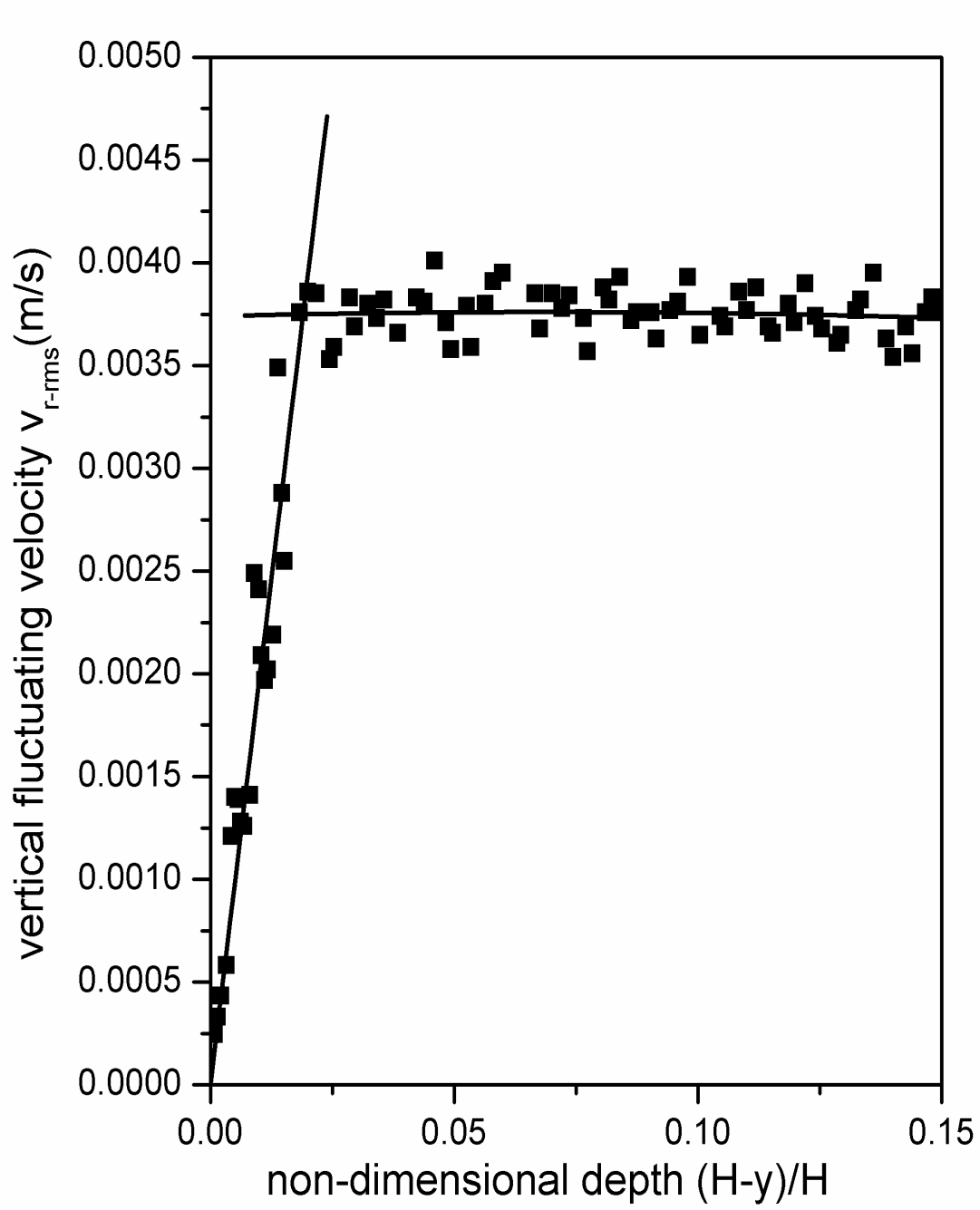

Figure 3.7: Variation of Vr-rms with non-dimensional depth from the interface. Turbulence generated from above the interface only, Wind speed=5.5m/s

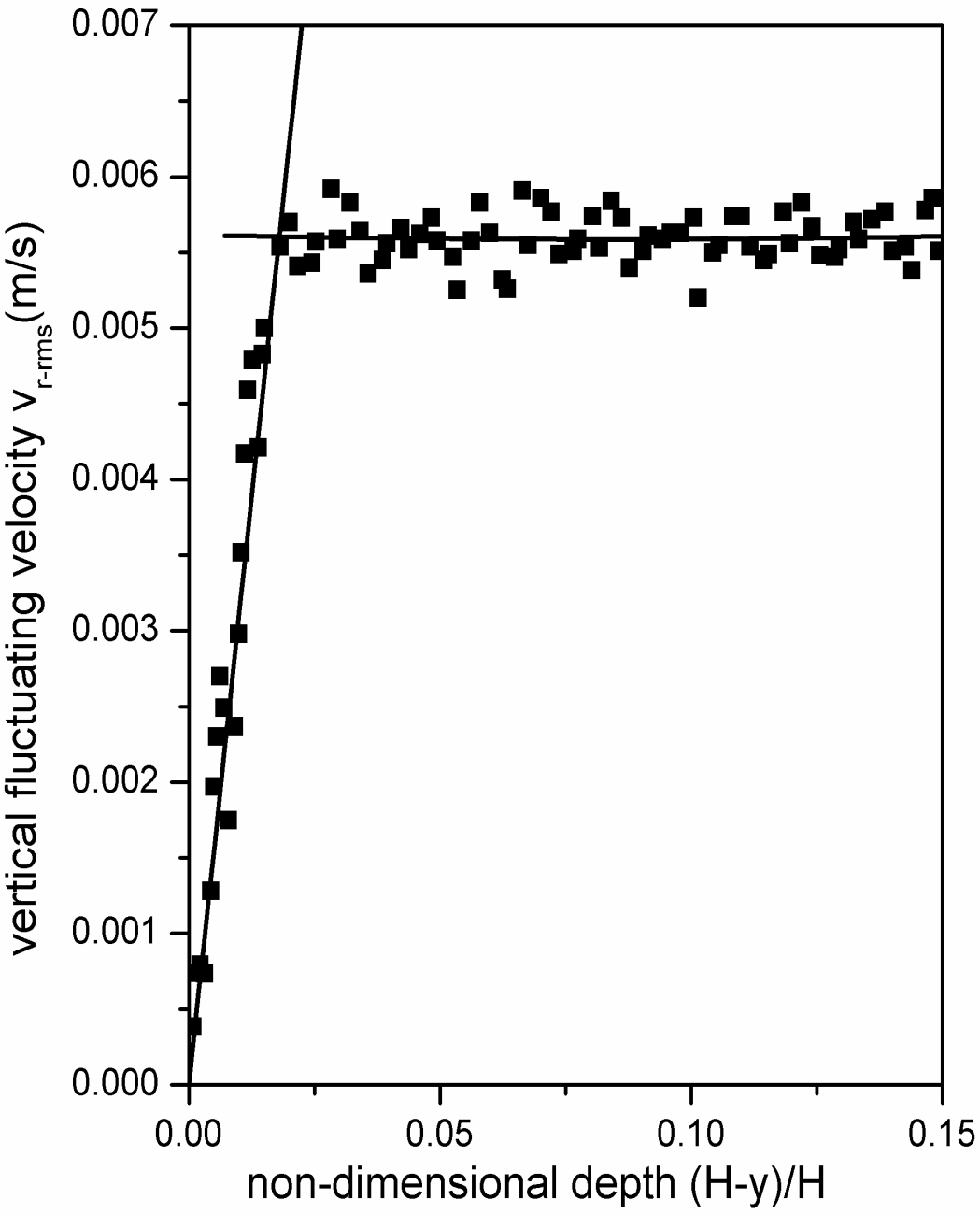

Figure 3.8: Variation of Vr-rms with non-dimensional depth from the interface. Turbulence generated from above the interface only, Wind speed=6m/s

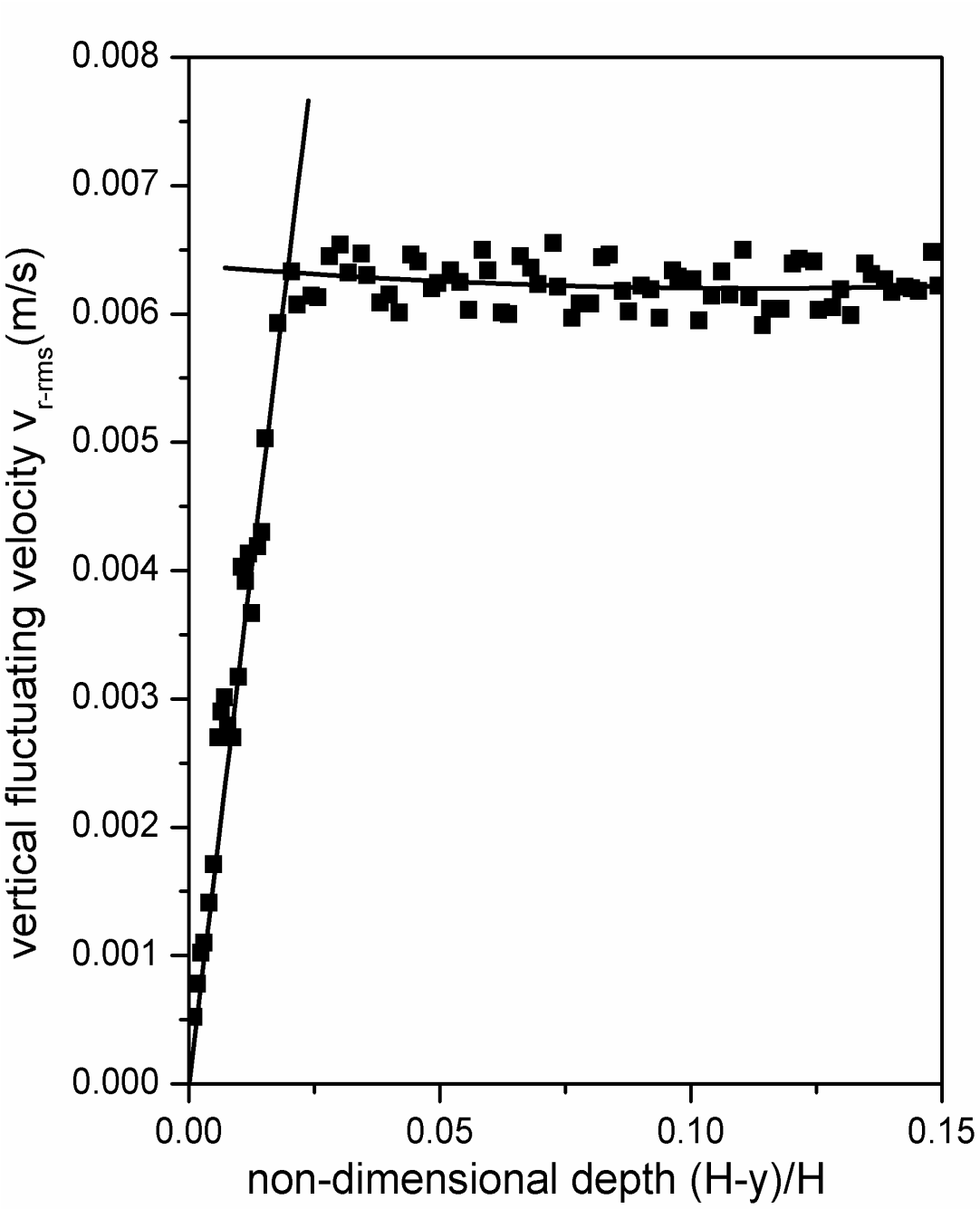

Figure 3.9: Variation of Vr-rms with non-dimensional depth from the interface. Turbulence generated from above the interface only, Wind speed=6.5m/s

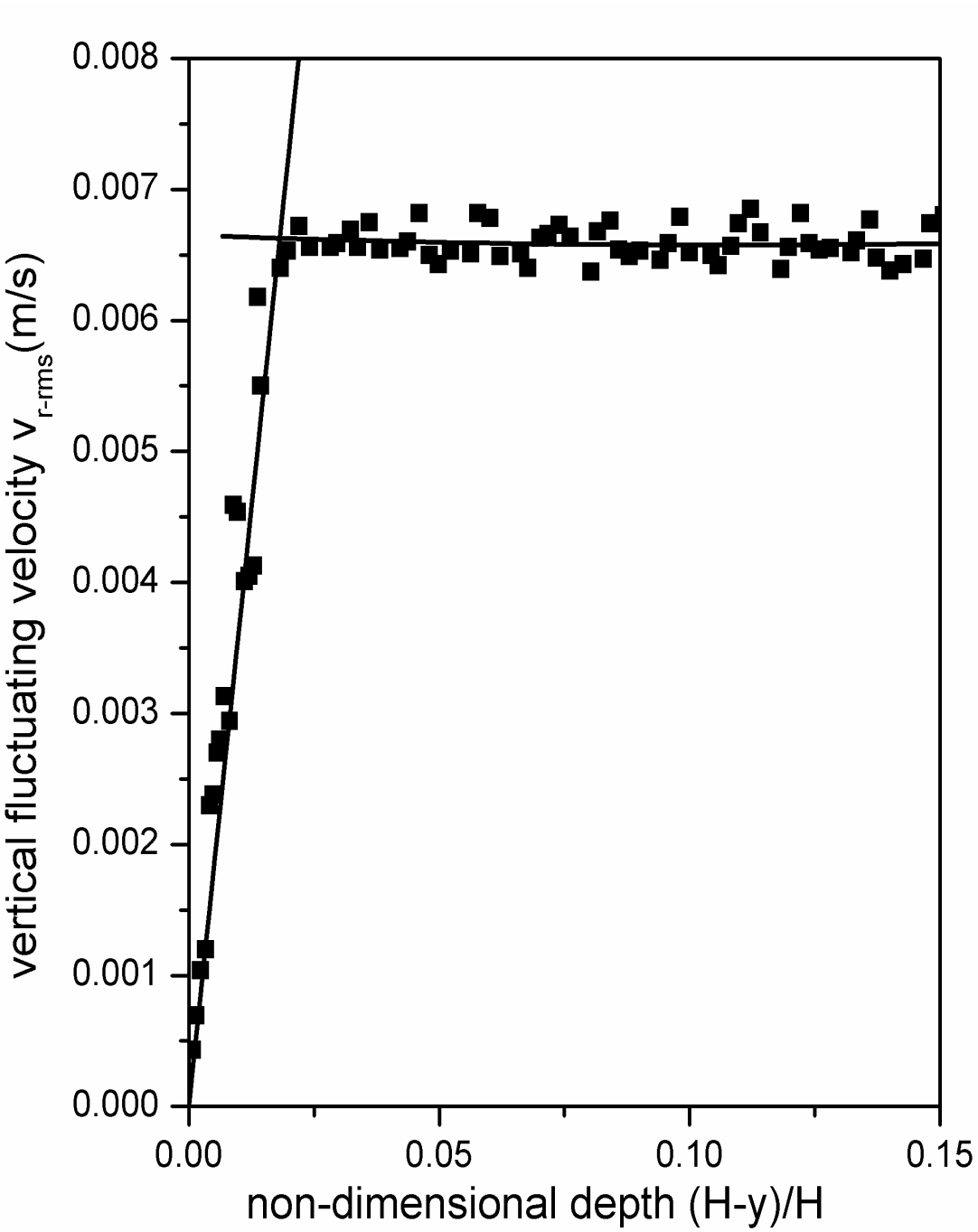

Figure 3.10: Variation of Vr-rms with non-dimensional depth from the interface. Turbulence generated from above the interface only, Wind speed=7m/s

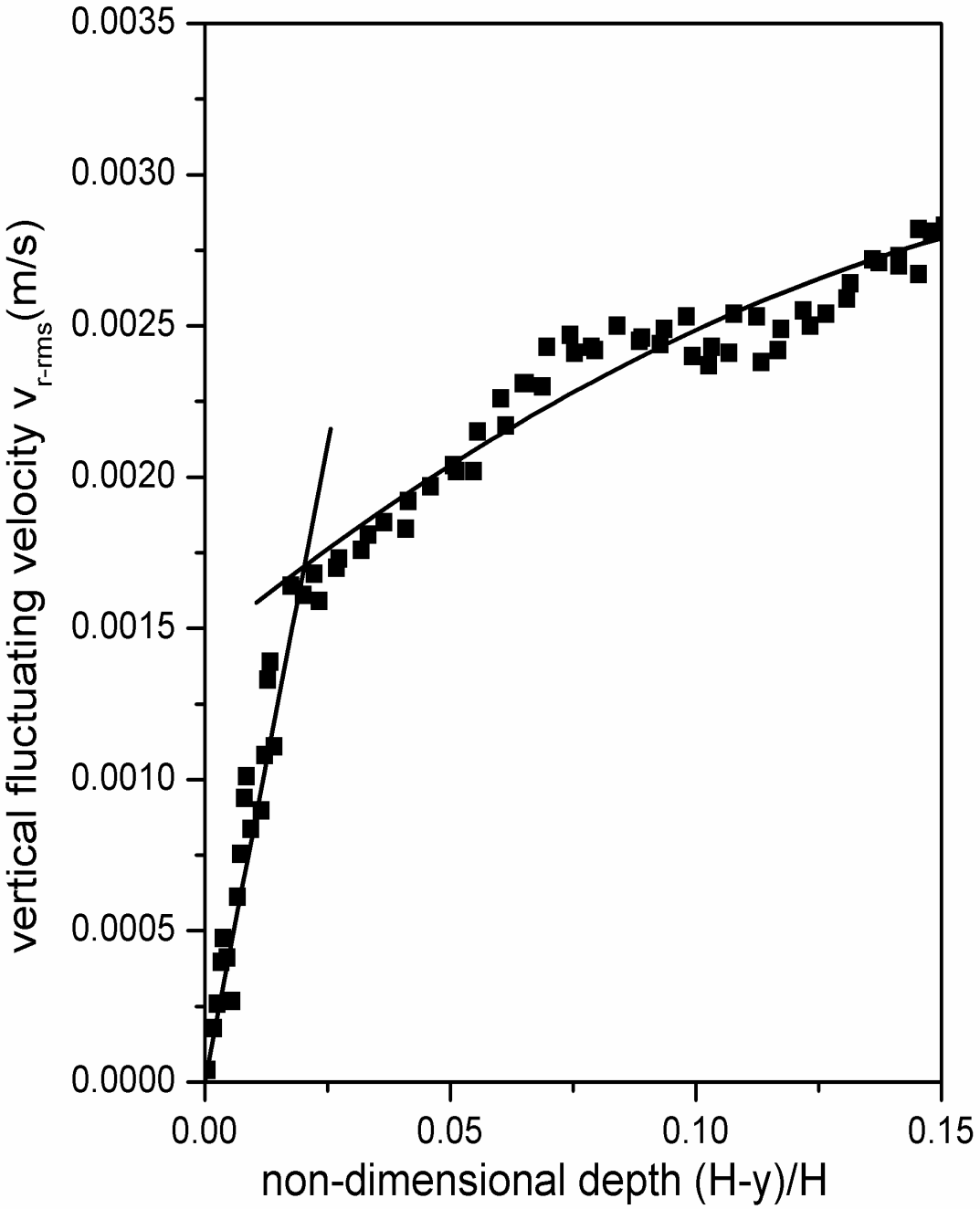

Figure 3.11: Variation of Vr-rms with non-dimensional depth from the interface. Turbulence generated from above and below in the opposite direction, Wind speed=3m/s, pump flow rate=6.3ml/s

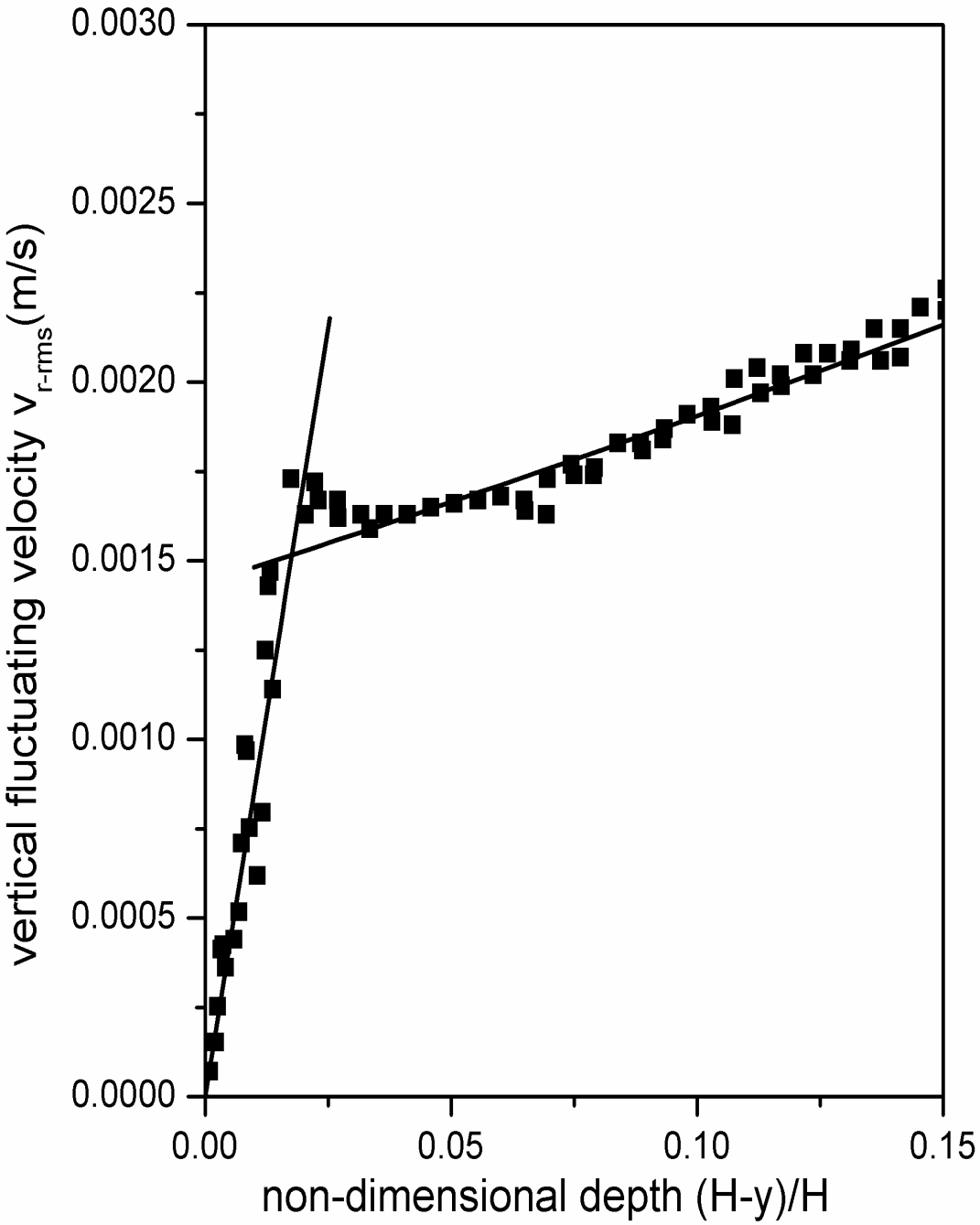

Figure 3.12: Variation of Vr-rms with non-dimensional depth from the interface.
Turbulence generated from above and below in the opposite direction,
Wind speed=3.5m/s, pump flow rate=6.3ml/s

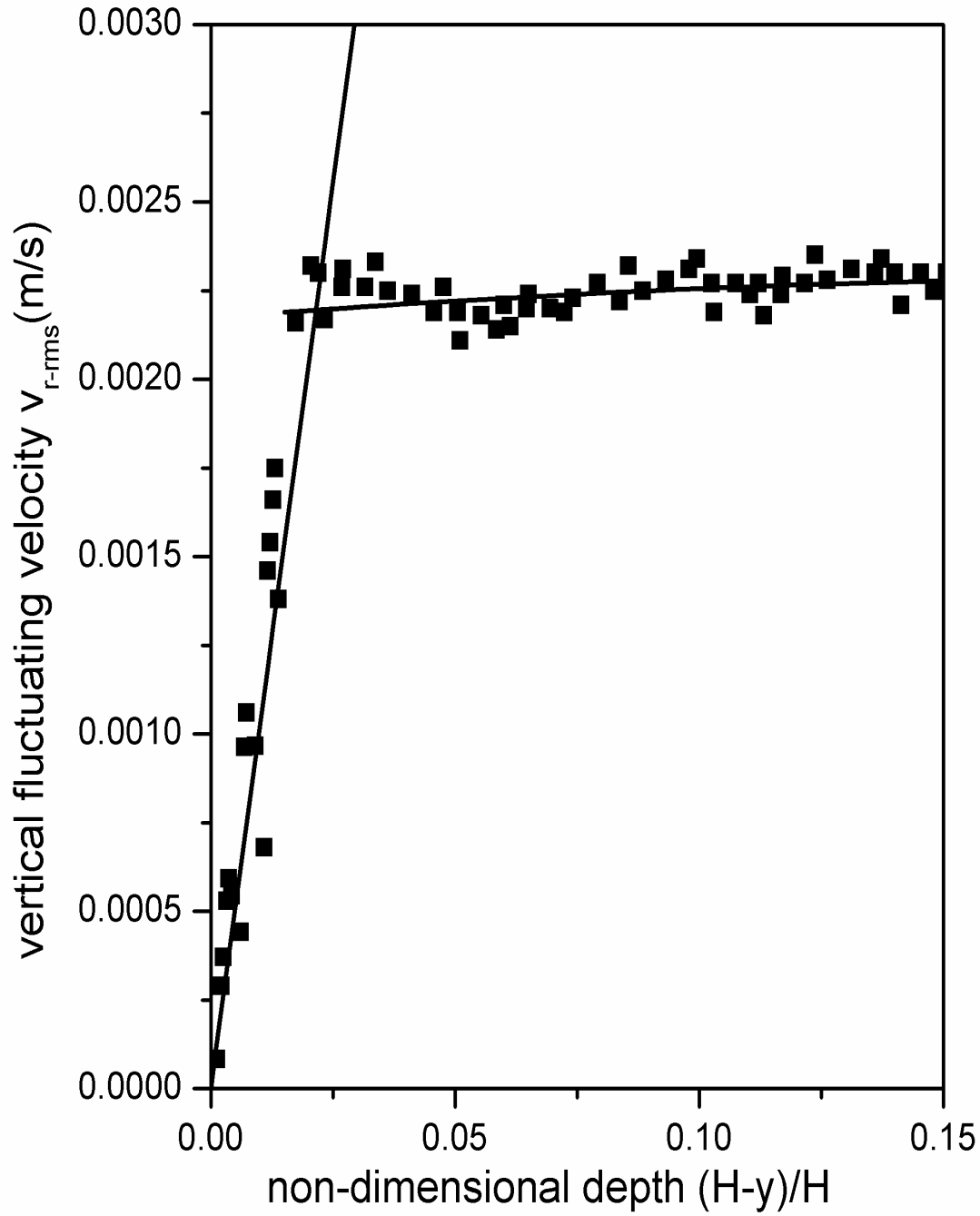

Figure 3.13: Variation of $V_{r\text{-}r}$ms with non-dimensional depth from the interface. Turbulence generated from above and below in the opposite direction, Wind speed=4m/s, pump flow rate=6.3ml/s

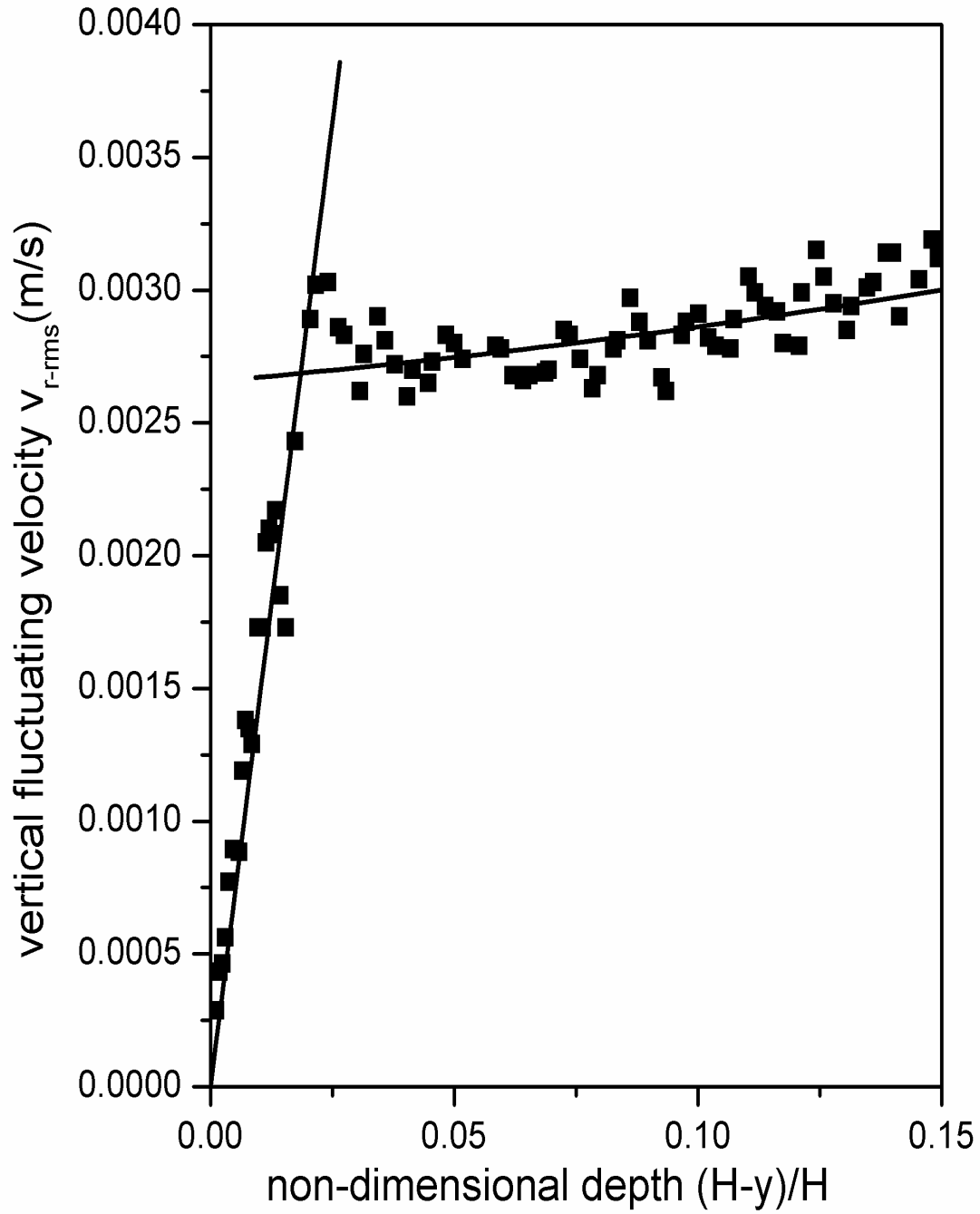

Figure 3.14: Variation of Vr-rms with non-dimensional depth from the interface.
Turbulence generated from above and below in the opposite direction,
Wind speed=4.5m/s, pump flow rate=6.3ml/s

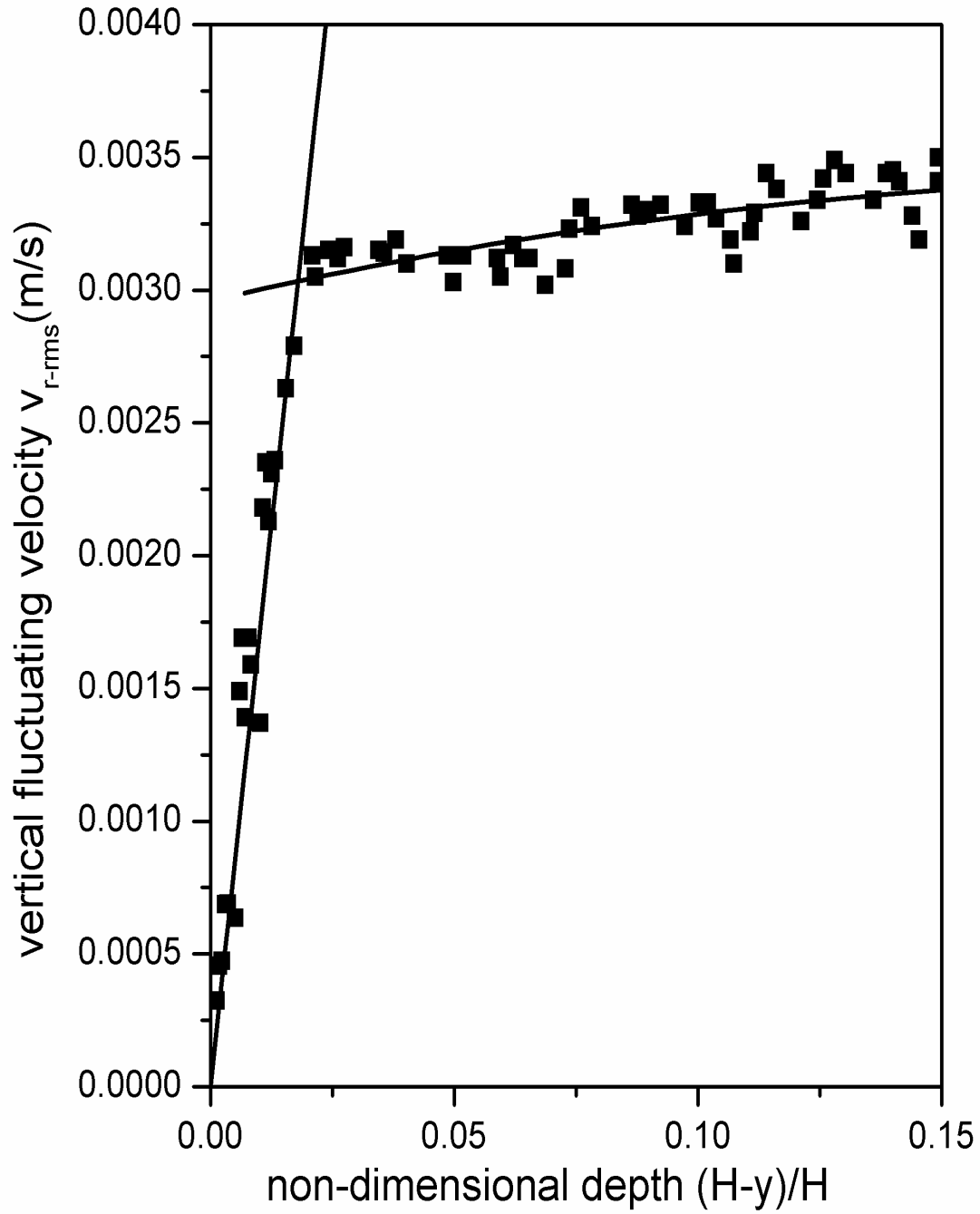

Figure 3.15: Variation of Vr-rms with non-dimensional depth from the interface.
Turbulence generated from above and below in the opposite direction,
Wind speed=5m/s, pump flow rate=6.3ml/s

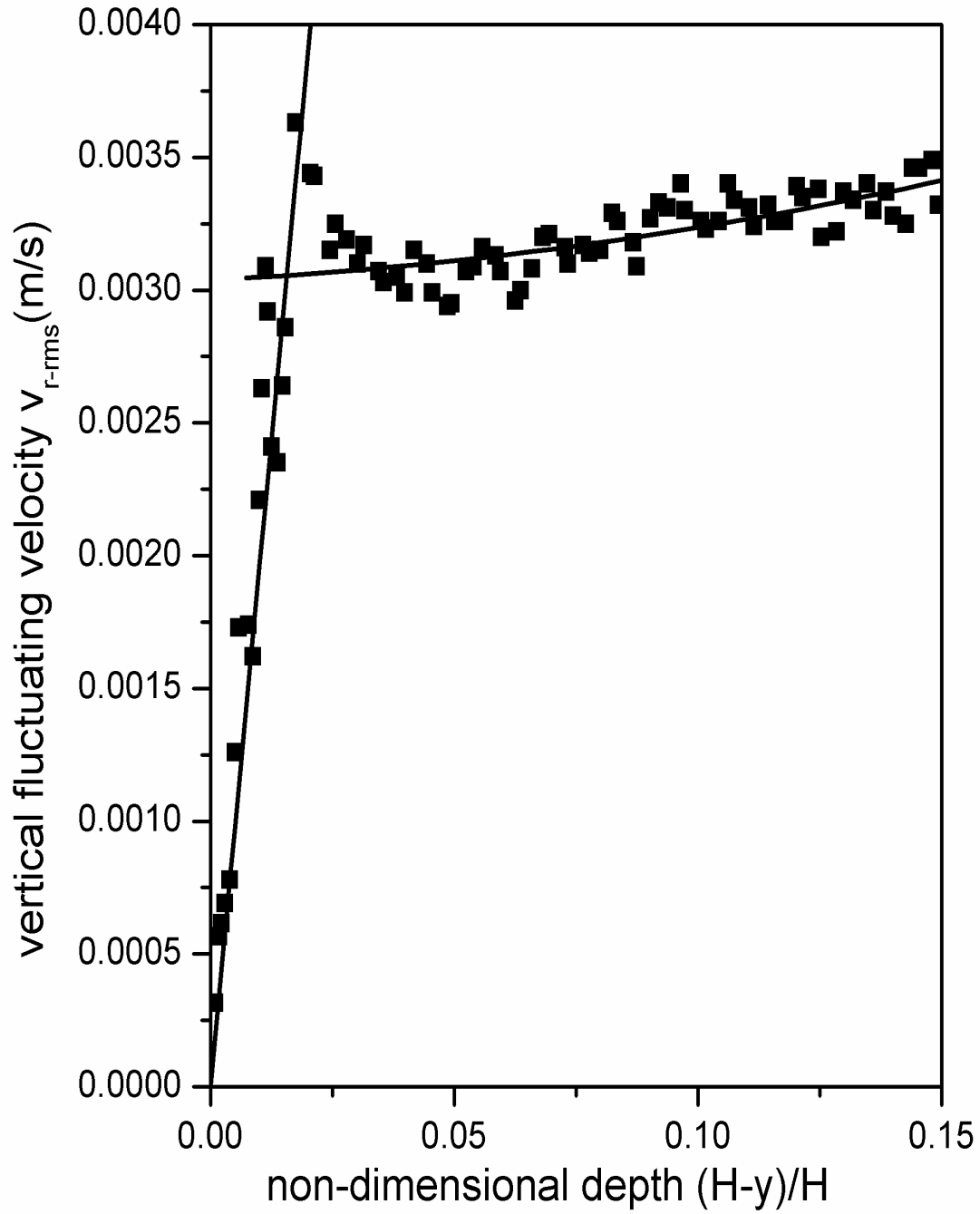

Figure 3.16: Variation of Vr-rms with non-dimensional depth from the interface.
Turbulence generated from above and below in the opposite direction,
Wind speed=5.5m/s, pump flow rate=6.3ml/s

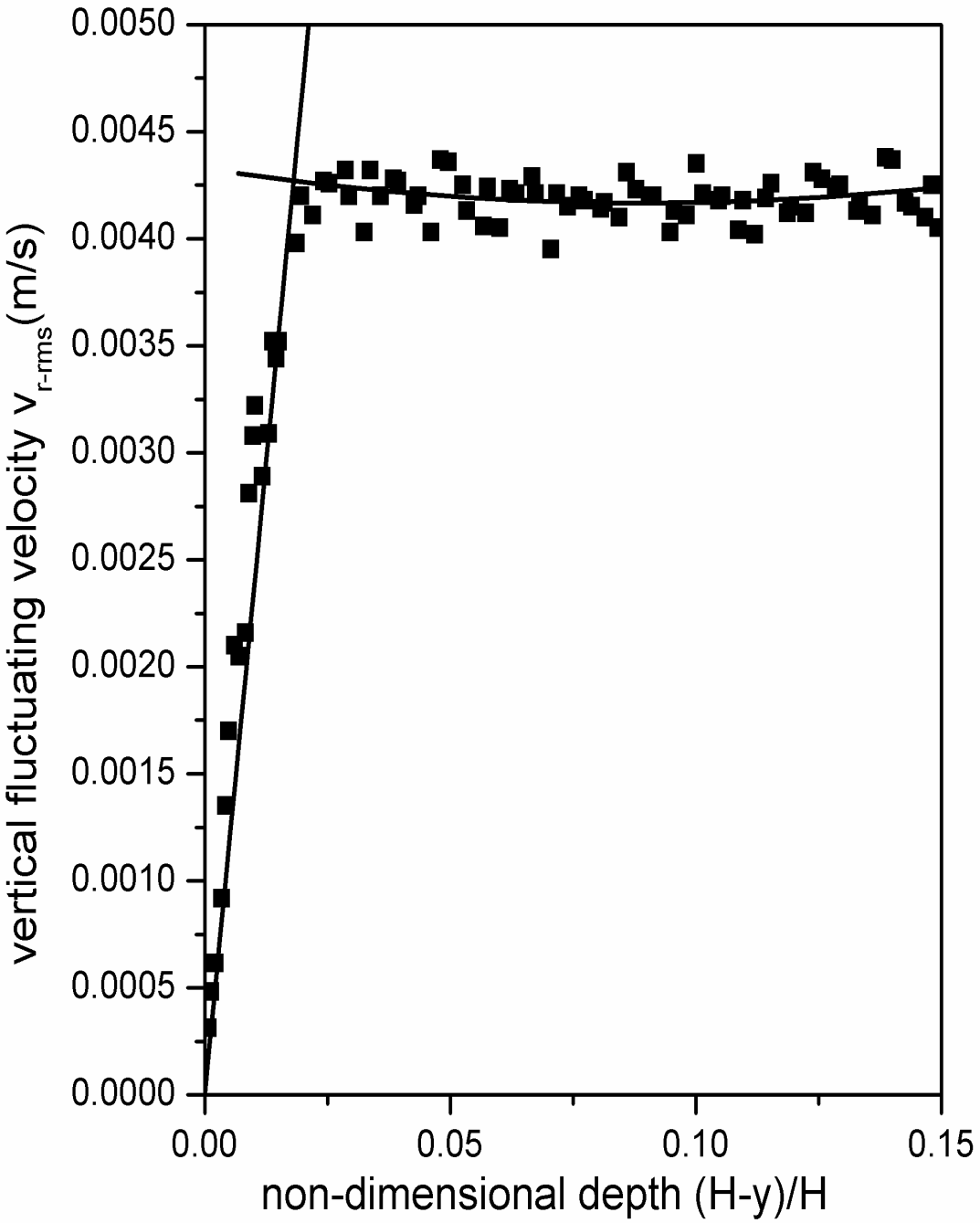

Figure 3.17: Variation of $V_{r\text{-}rms}$ with non-dimensional depth from the interface. Turbulence generated from above and below in the opposite direction, Wind speed=6m/s, pump flow rate=6.3ml/s

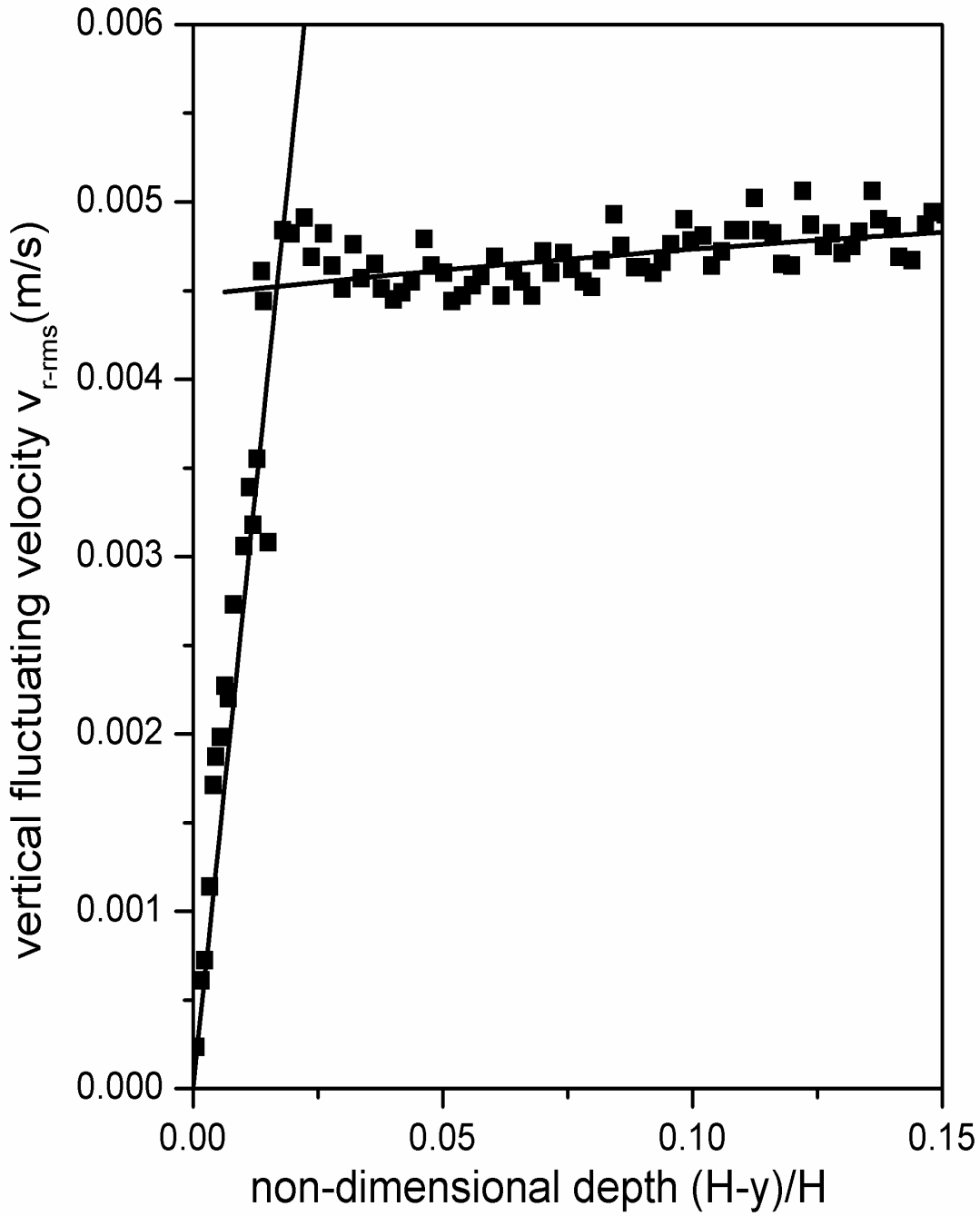

Figure 3.18: Variation of Vr-rms with non-dimensional depth from the interface.
Turbulence generated from above and below in the opposite direction,
Wind speed=6.5m/s, pump flow rate=6.3ml/s

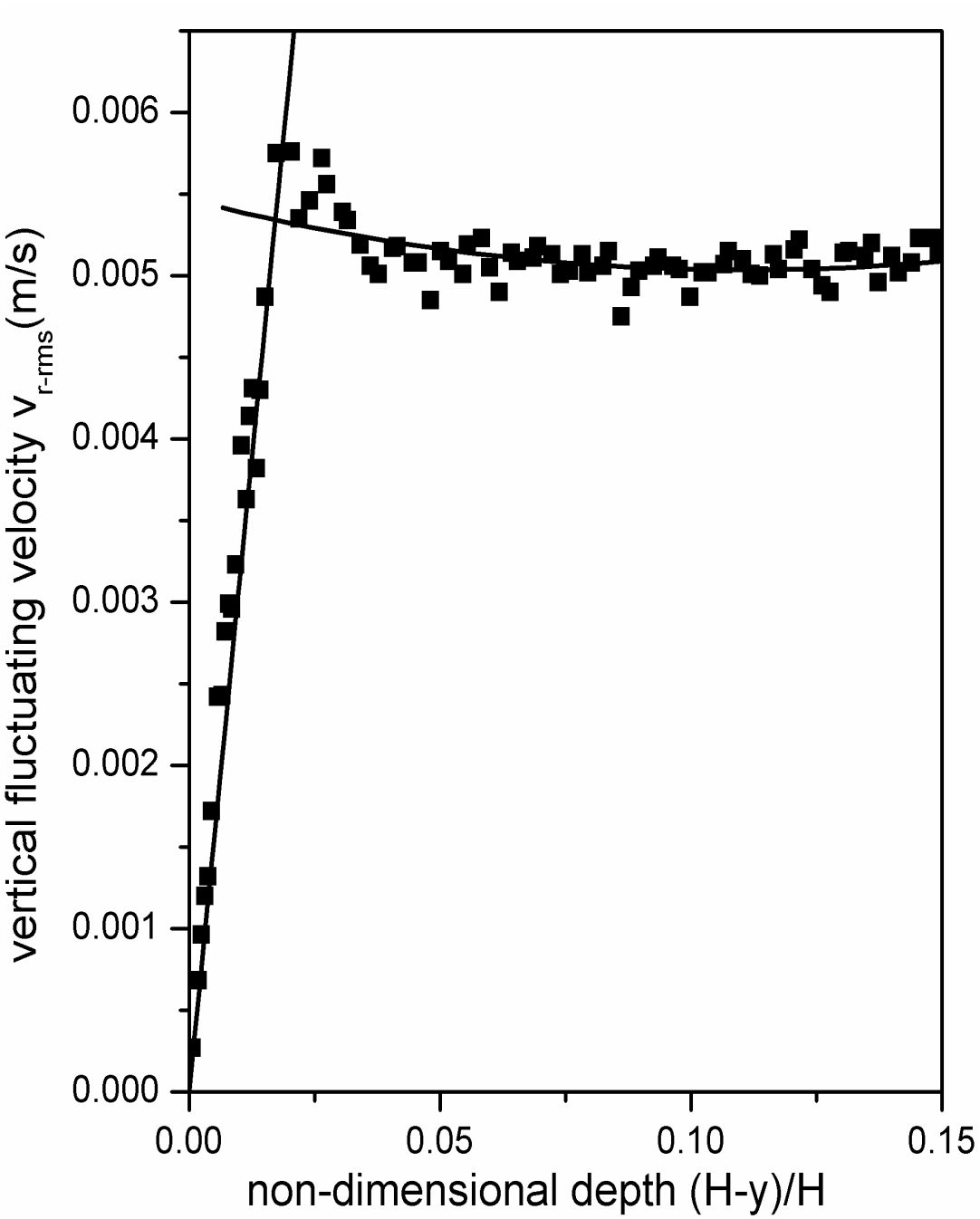

Figure 3.19: Variation of Vr-rms with non-dimensional depth from the interface.
Turbulence generated from above and below in the opposite direction,
Wind speed=7m/s, pump flow rate=6.3ml/s

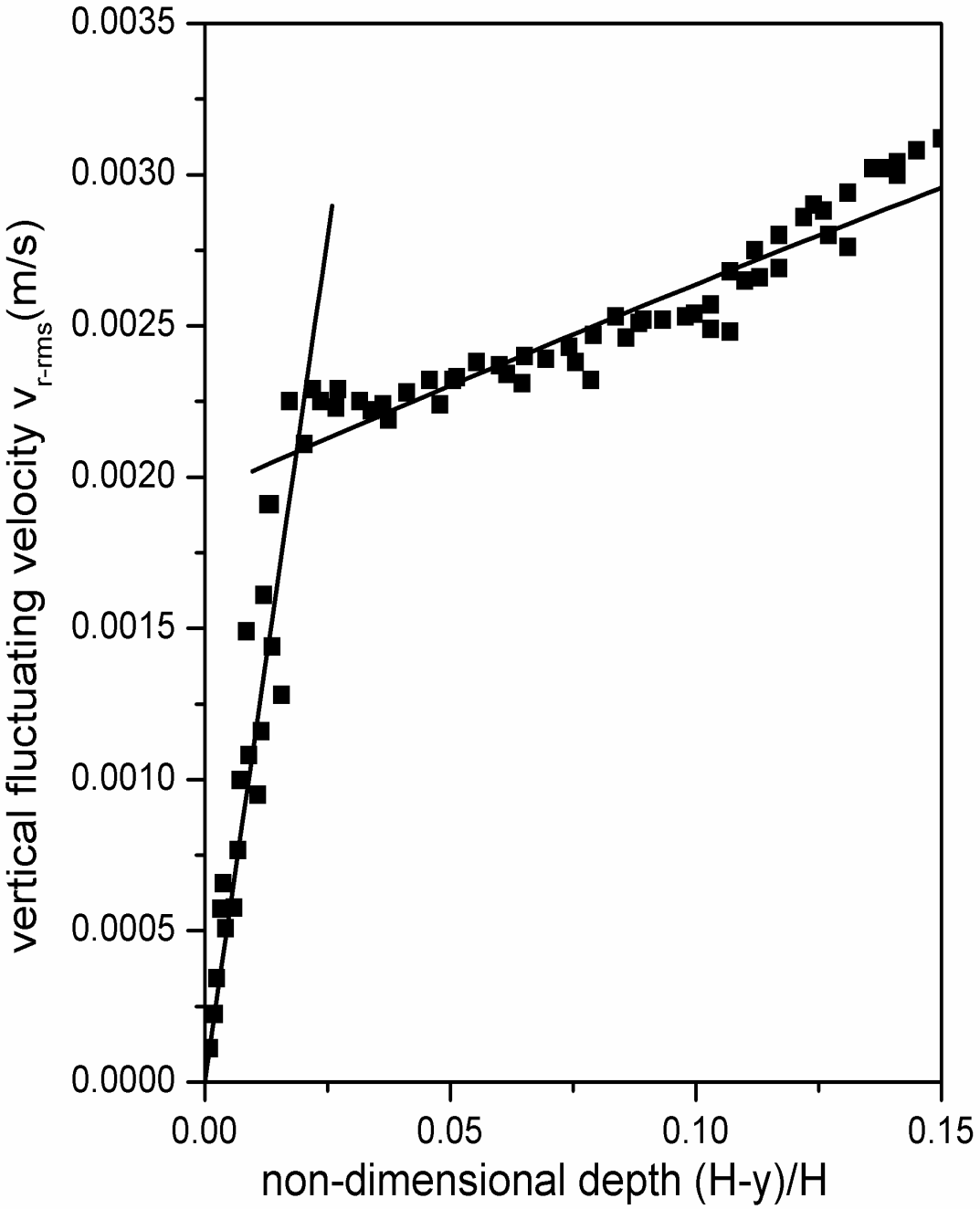

Figure 3.20: Variation of $V_{r\text{-}rms}$ with non-dimensional depth from the interface.
Turbulence generated from above and below in the same direction,
Wind speed=3m/s, pump flow rate=6.3ml/s

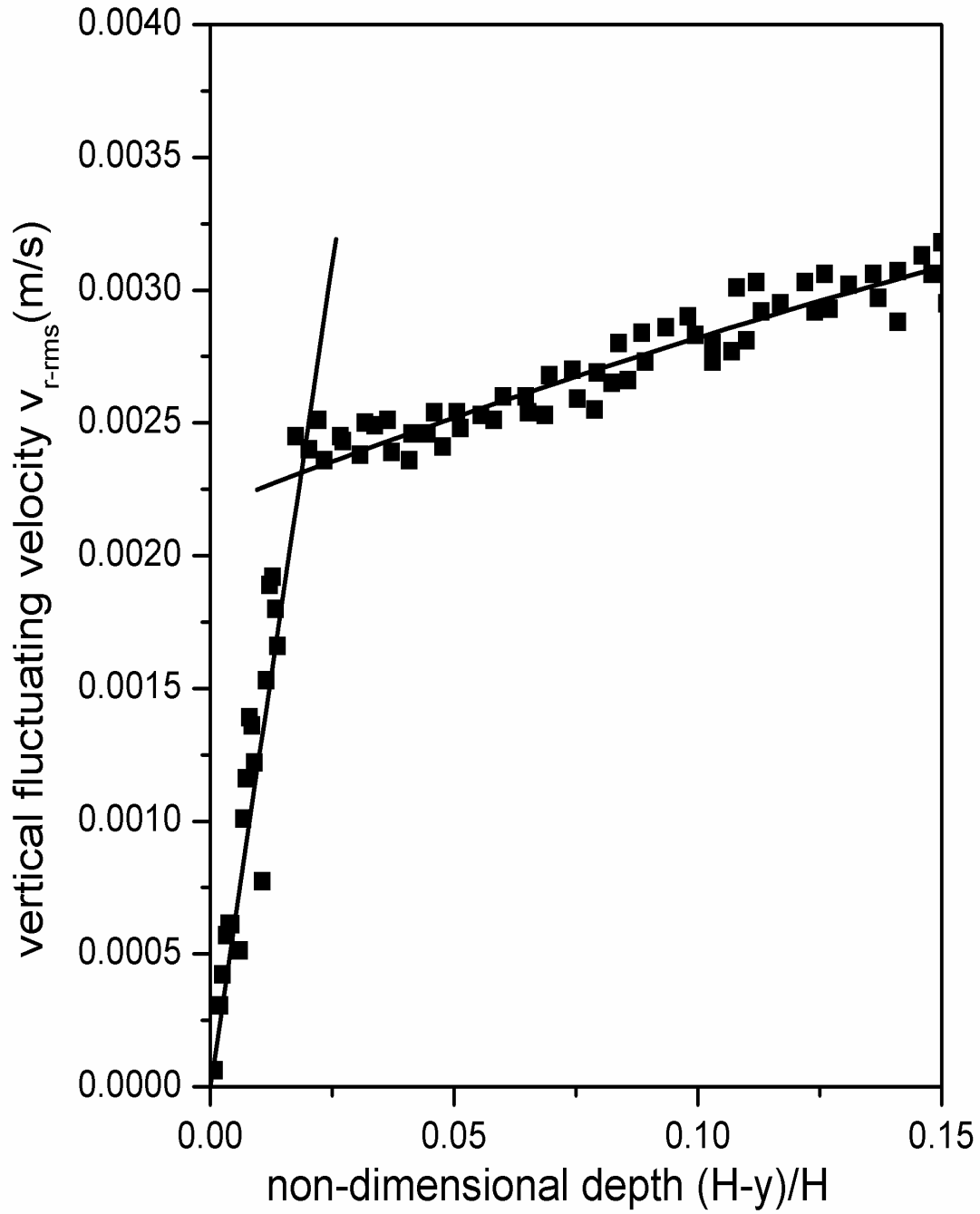

Figure 3.21: Variation of Vr-rms with non-dimensional depth from the interface.
Turbulence generated from above and below in the same direction,
Wind speed=3.5m/s, pump flow rate=6.3ml/s

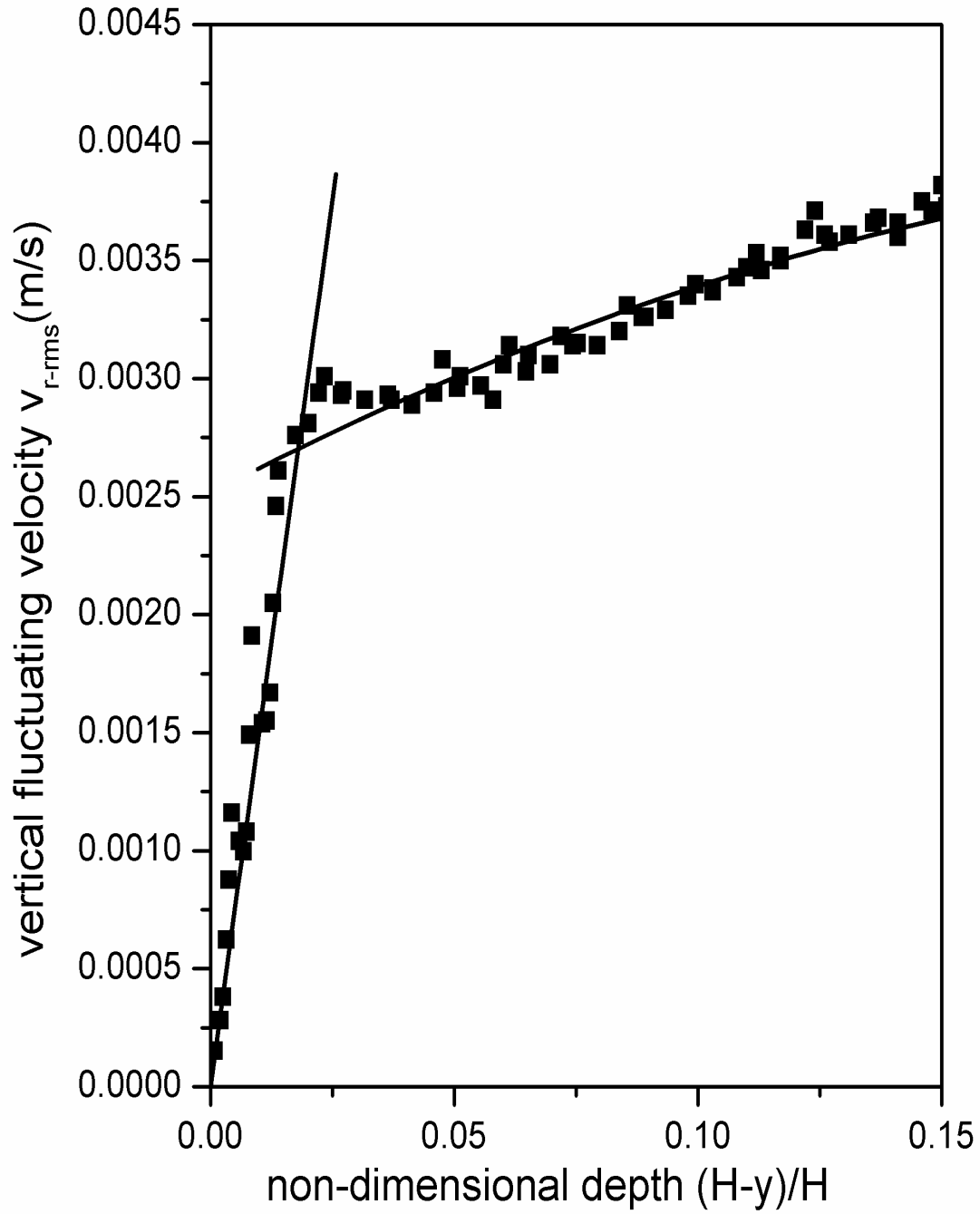

Figure 3.22: Variation of Vr-rms with non-dimensional depth from the interface.
Turbulence generated from above and below in the same direction,
Wind speed=4m/s, pump flow rate=6.3ml/s

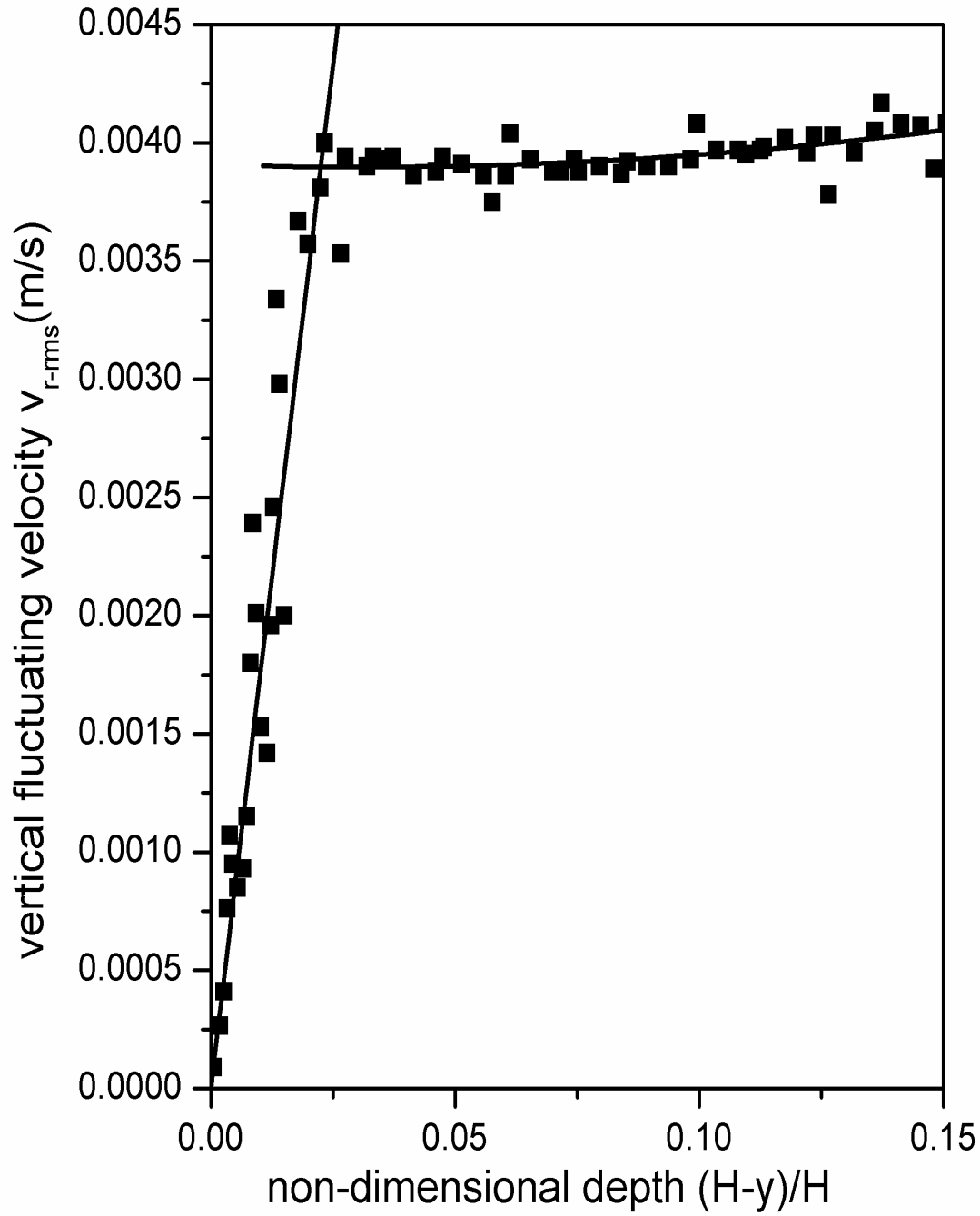

Figure 3.23: Variation of Vr-rms with non-dimensional depth from the interface.
Turbulence generated from above and below in the same direction,
Wind speed=4.5m/s, pump flow rate=6.3ml/s

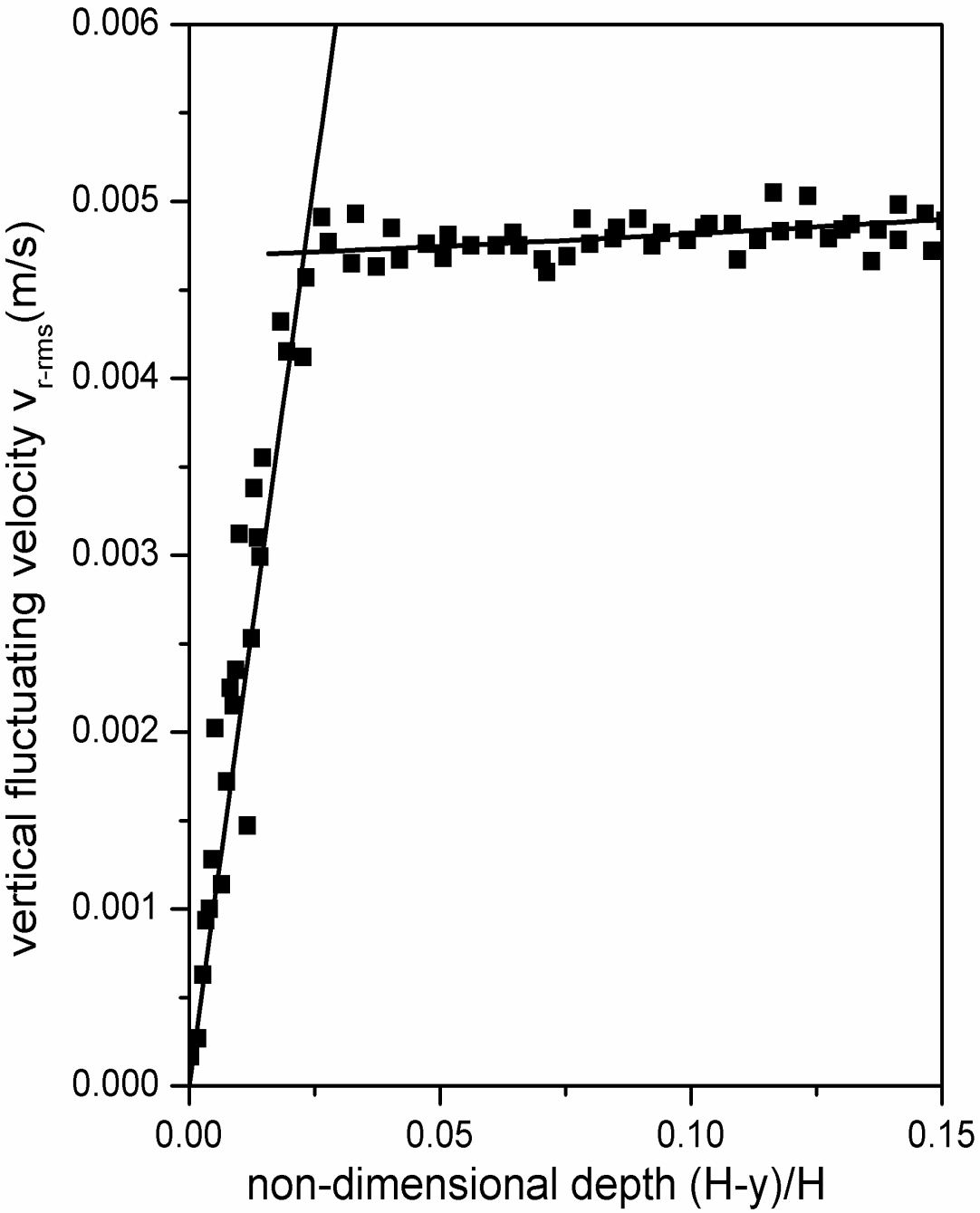

Figure 3.24: Variation of Vr-rms with non-dimensional depth from the interface.
Turbulence generated from above and below in the same direction,
Wind speed=5m/s, pump flow rate=6.3ml/s

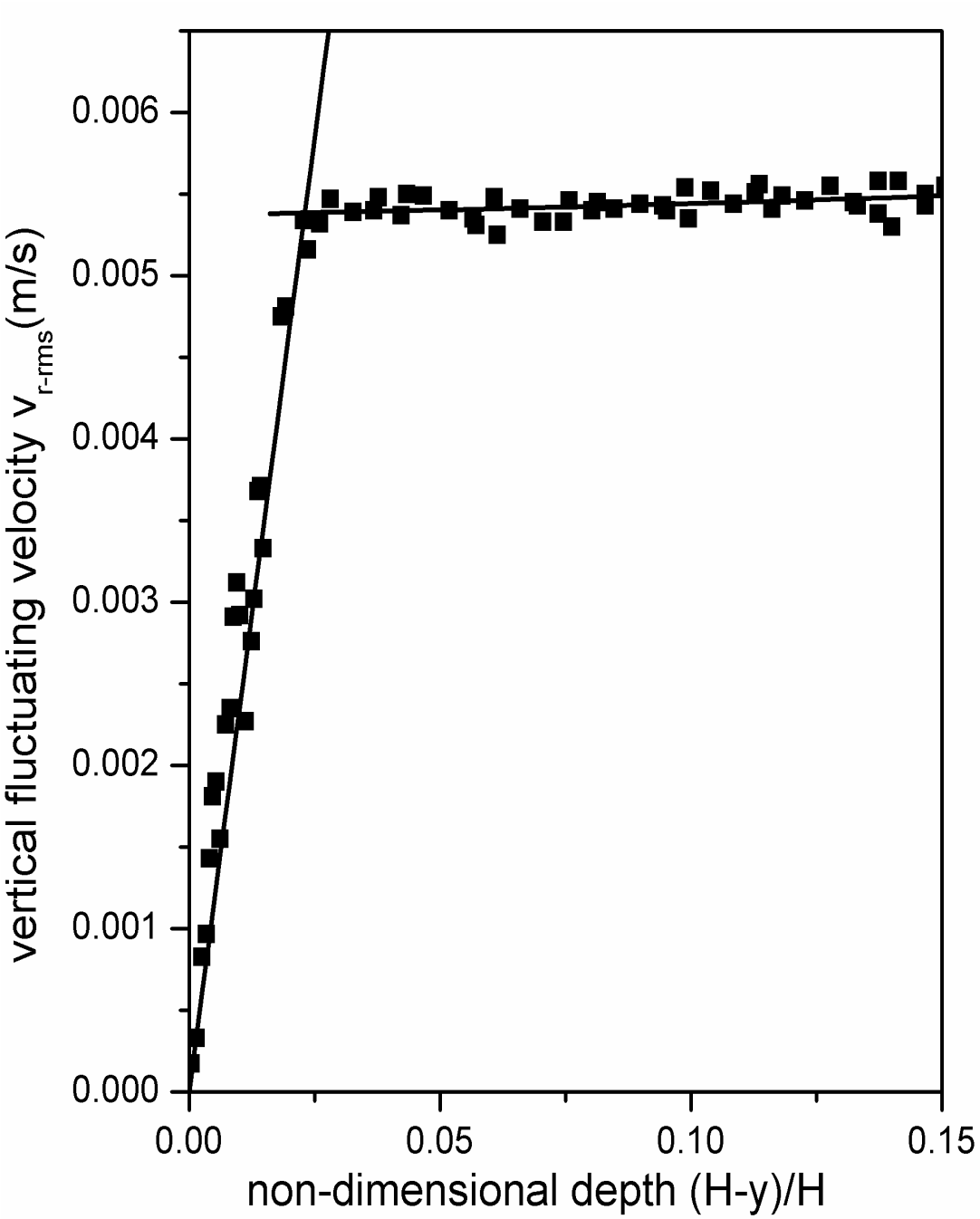

Figure 3.25: Variation of Vr-rms with non-dimensional depth from the interface.
Turbulence generated from above and below in the same direction,
Wind speed=5.5m/s, pump flow rate=6.3ml/s

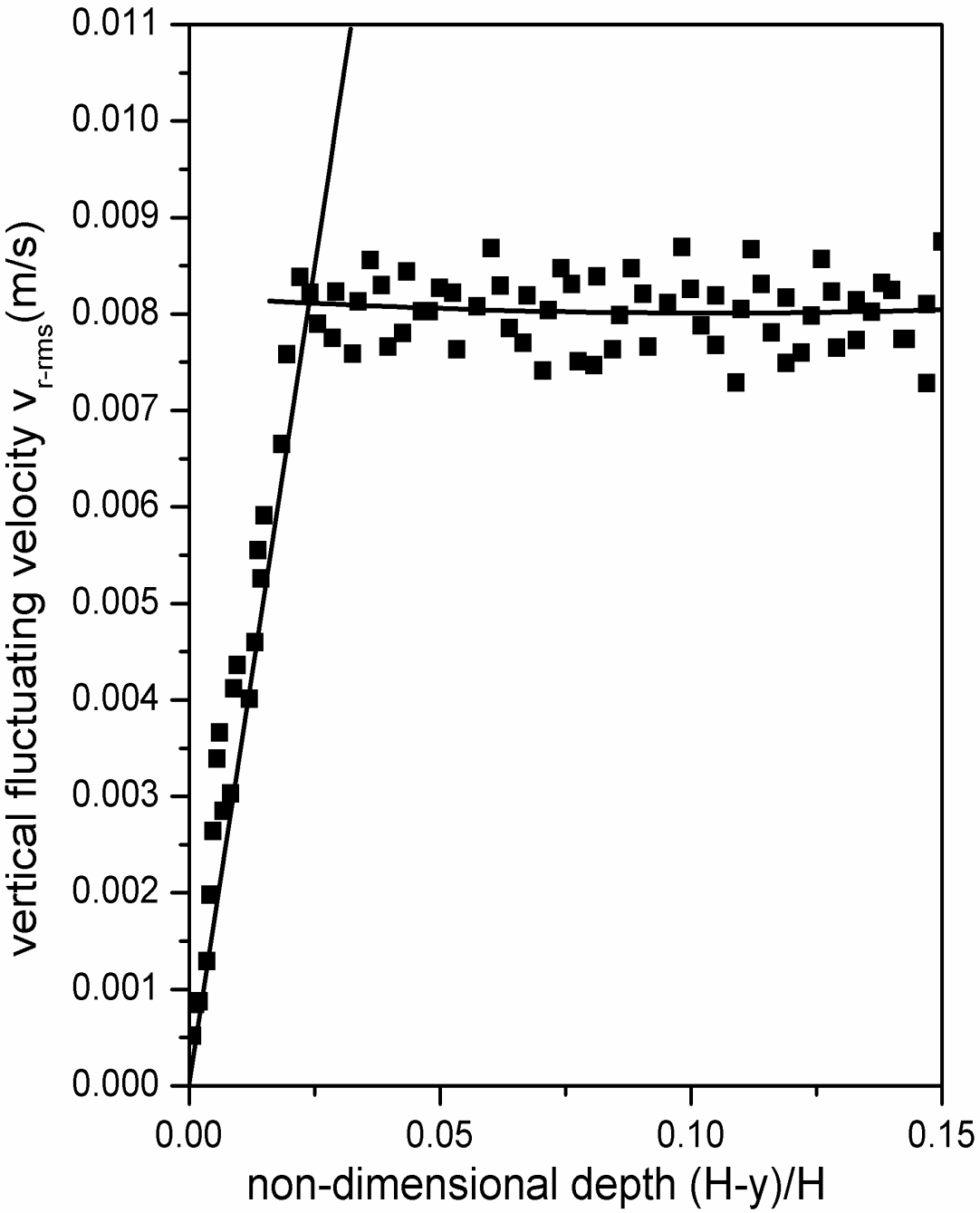

Figure 3.26: Variation of Vr-rms with non-dimensional depth from the interface.
Turbulence generated from above and below in the same direction,
Wind speed=6m/s, pump flow rate=6.3ml/s

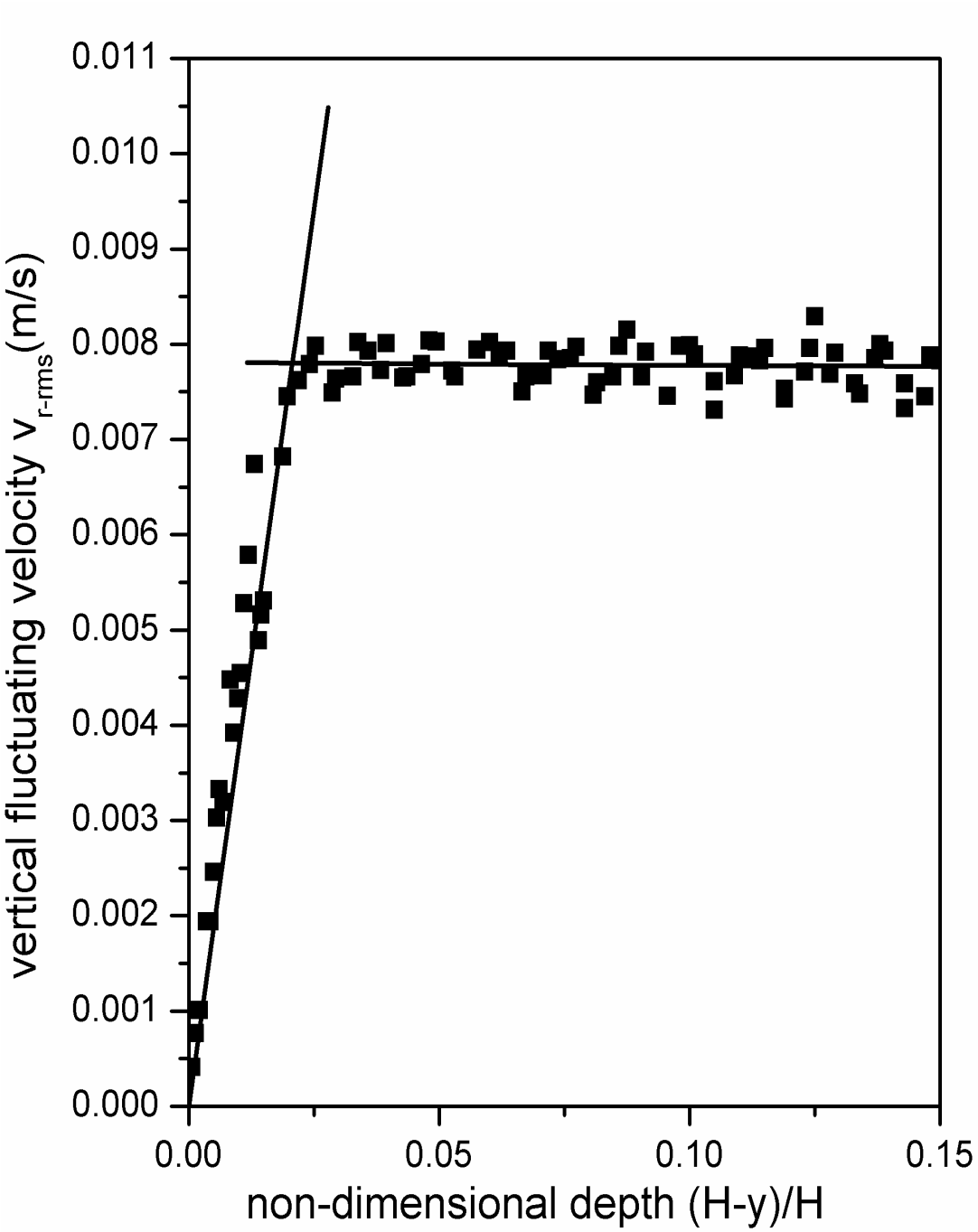

Figure 3.27: Variation of Vr-rms with non-dimensional depth from the interface.
Turbulence generated from above and below in the same direction,
Wind speed=6.5m/s, pump flow rate=6.3ml/s

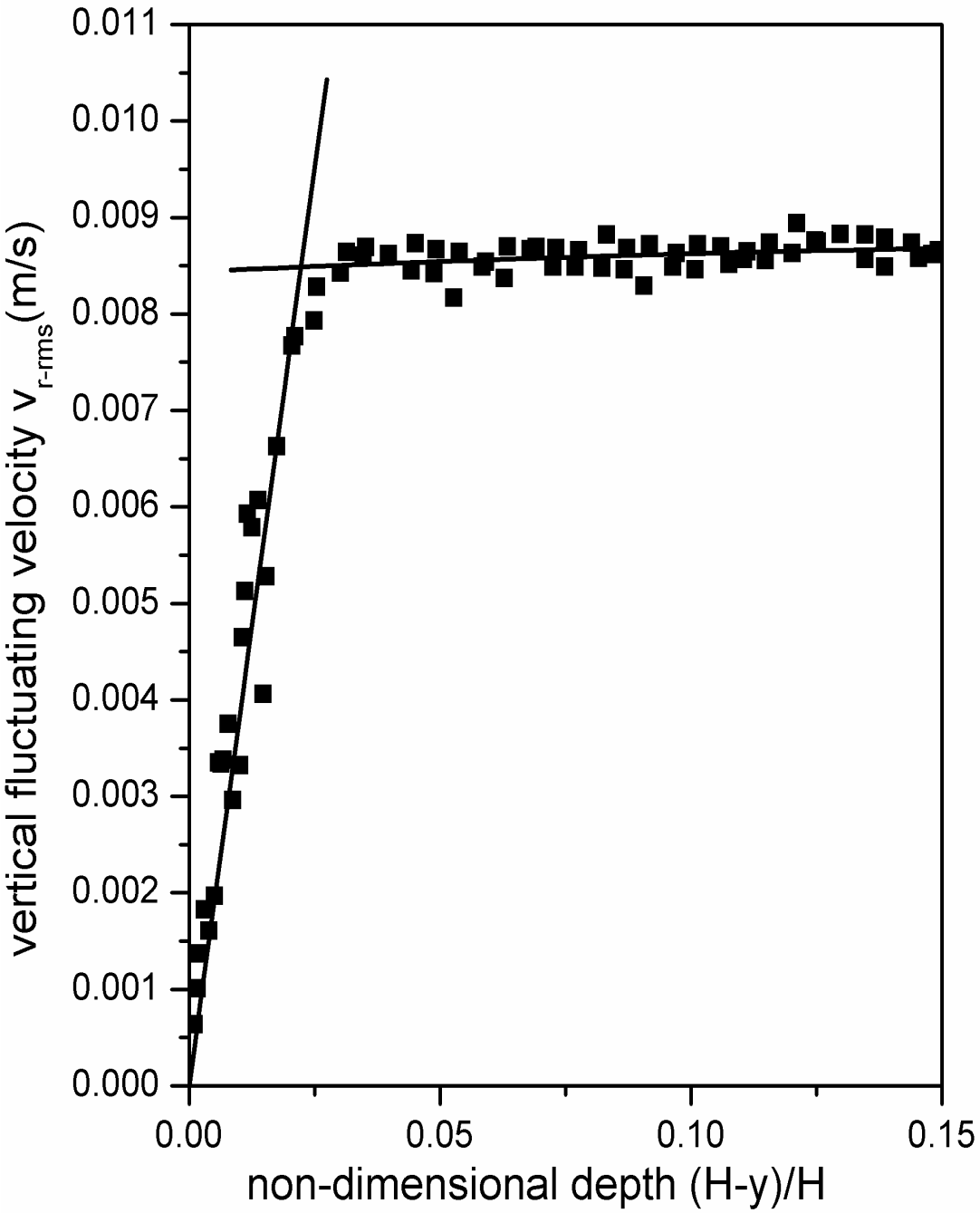

Figure 3.28: Variation of Vr-rms with non-dimensional depth from the interface.
Turbulence generated from above and below in the same direction,
Wind speed=7m/s, pump flow rate=6.3ml/s

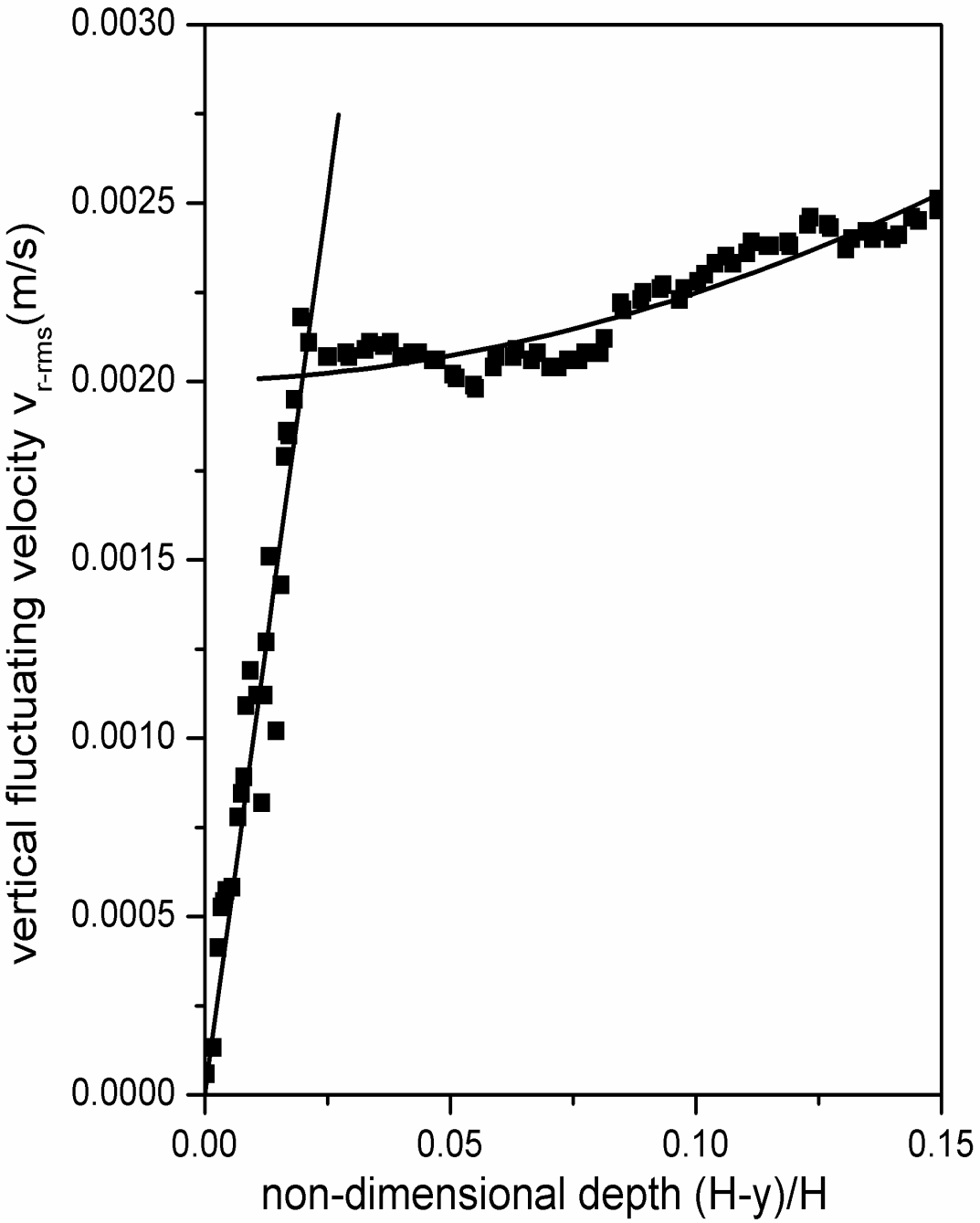

Figure 3.29: Variation of Vr-rms with non-dimensional depth from the interface.
Turbulence generated from above and below in the opposite direction,
Wind speed=3.5m/s, pump flow rate=3.2ml/s

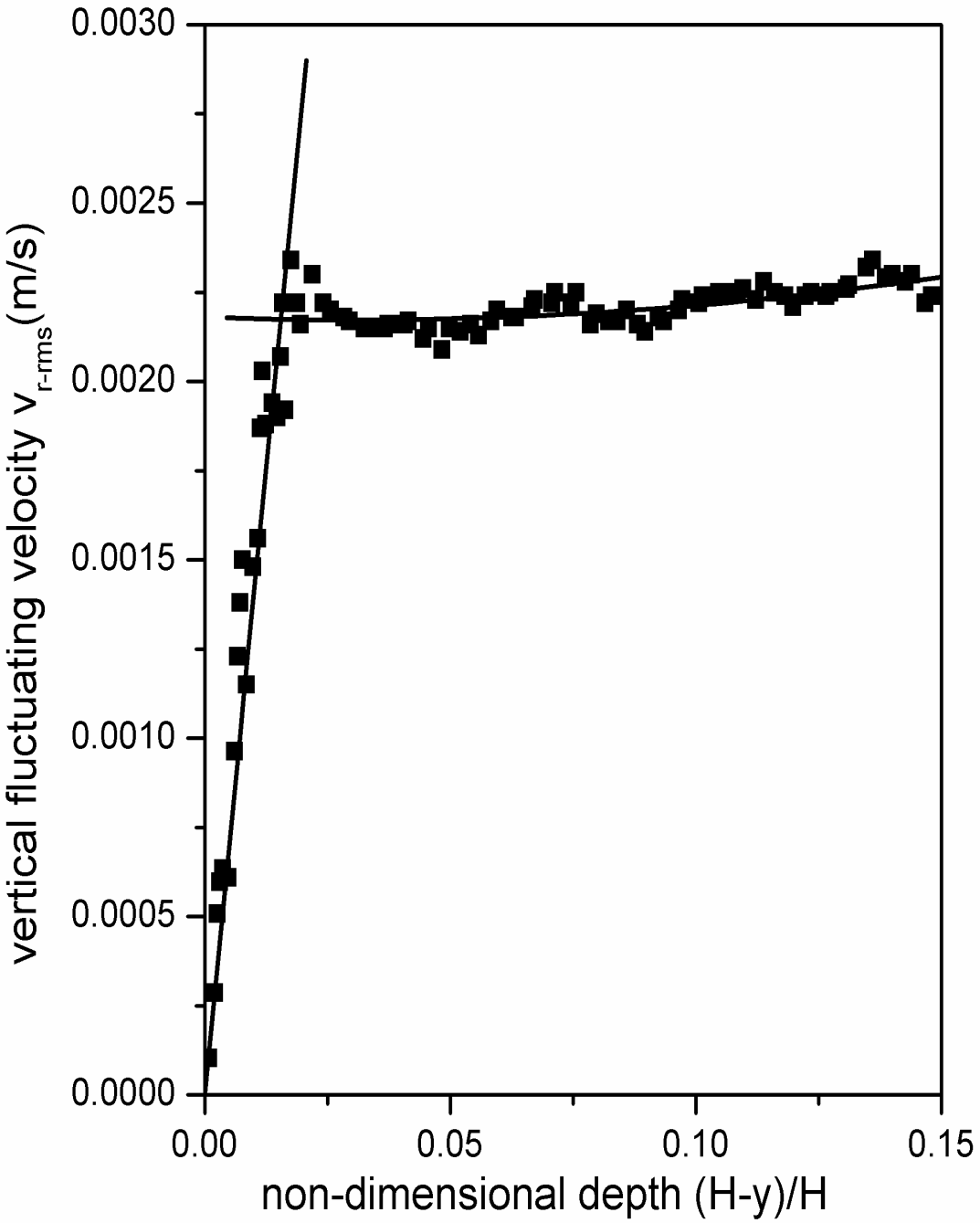

Figure 3.30: Variation of Vr-rms with non-dimensional depth from the interface.
Turbulence generated from above and below in the opposite direction,
Wind speed=4.5m/s, pump flow rate=3.2ml/s

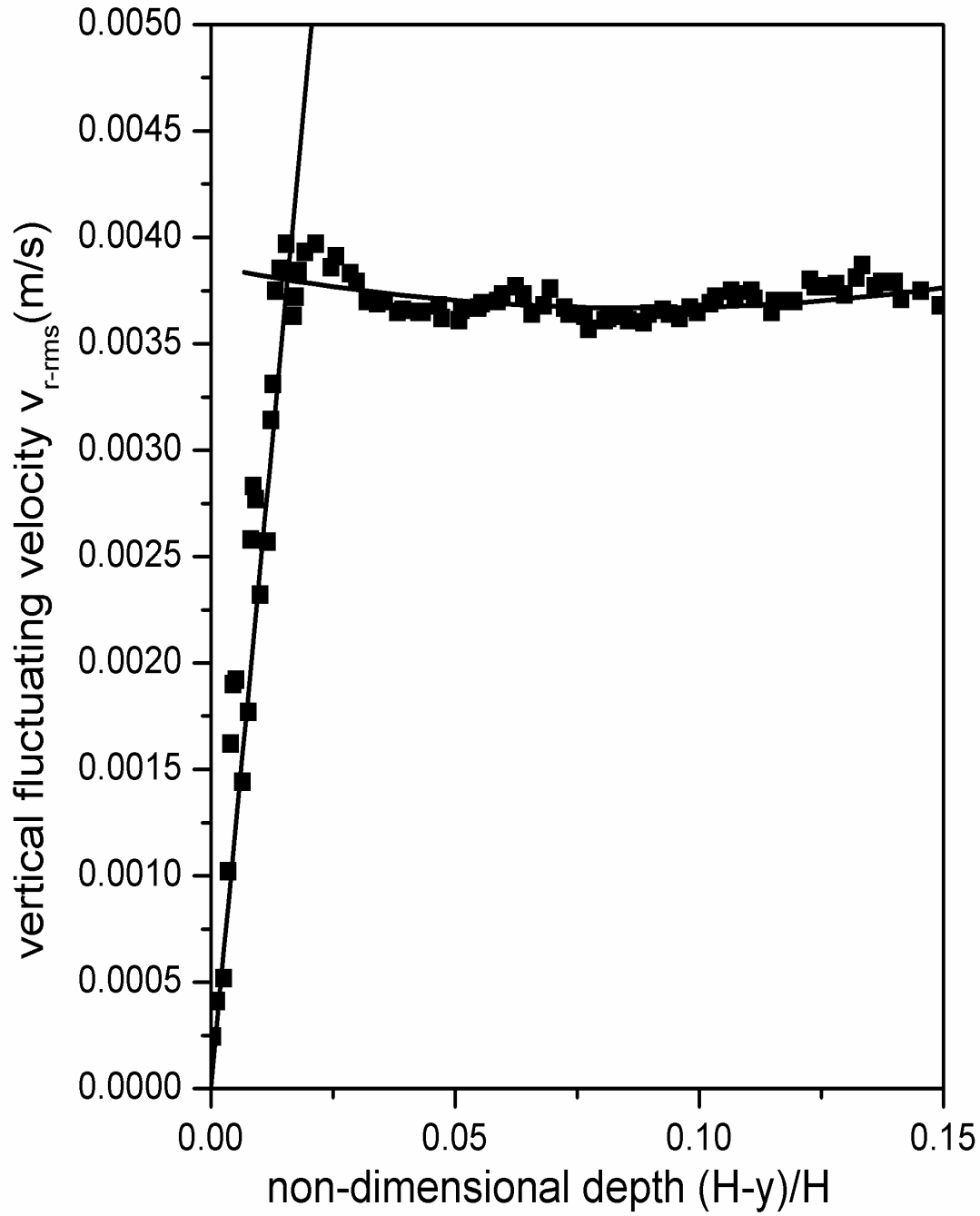

Figure 3.31: Variation of Vr-rms with non-dimensional depth from the interface.
Turbulence generated from above and below in the opposite direction,
Wind speed=6m/s, pump flow rate=3.2ml/s

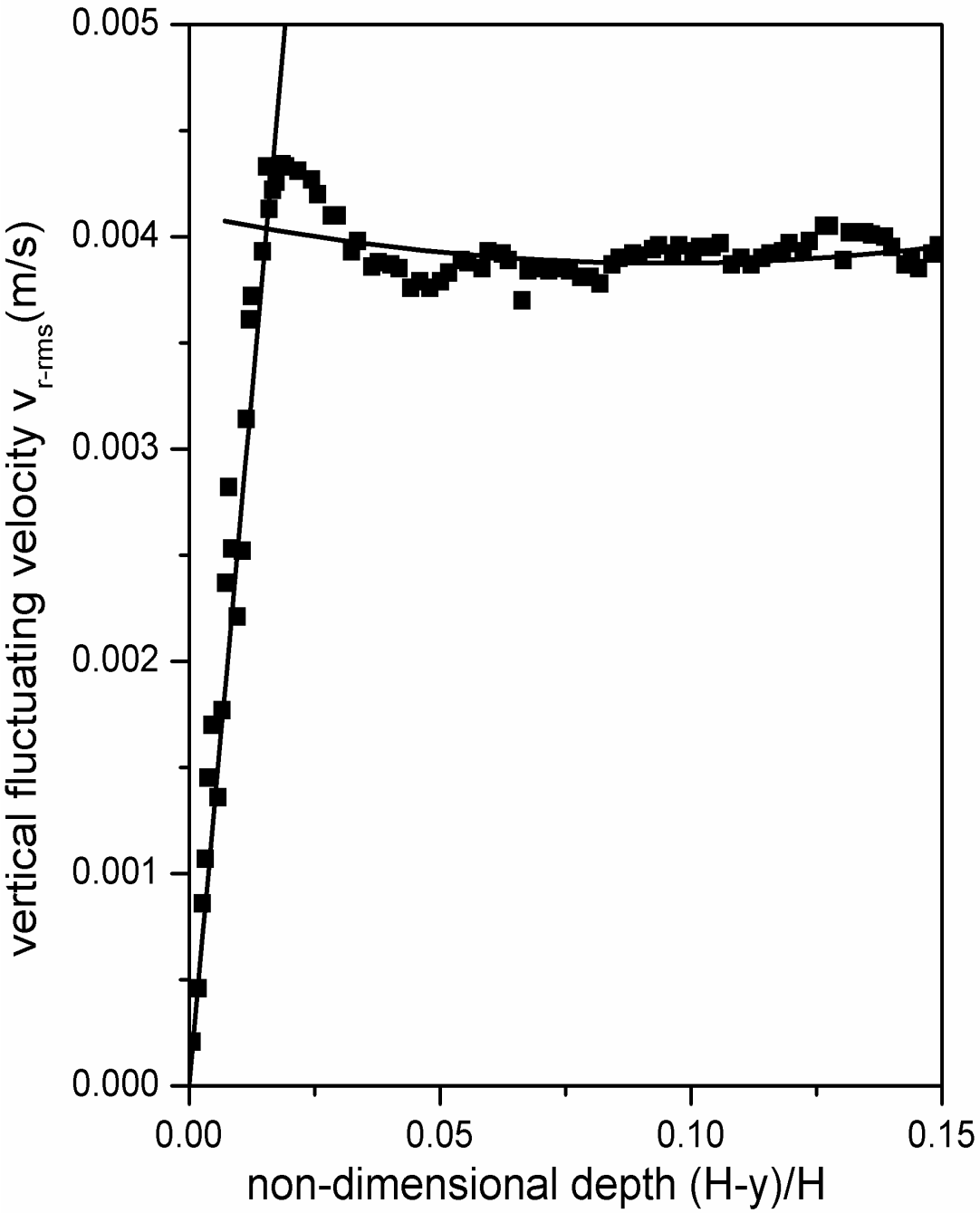

Figure 3.32: Variation of Vr-rms with non-dimensional depth from the interface.
Turbulence generated from above and below in the opposite direction,
Wind speed=6.5m/s, pump flow rate=3.2ml/s

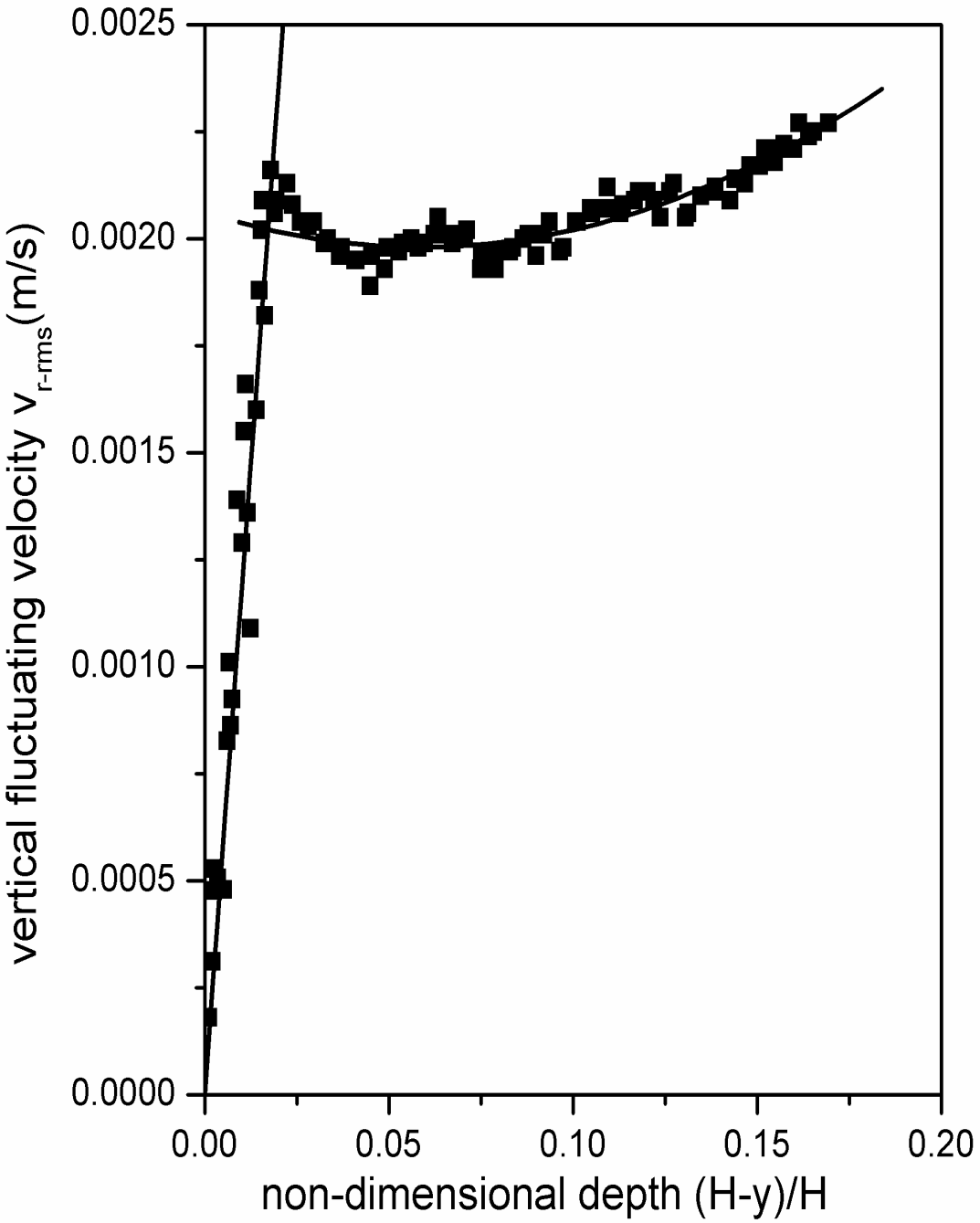

Figure 3.33: Variation of Vr-rms with non-dimensional depth from the interface.
Turbulence generated from above and below in the same direction,
Wind speed=3.5m/s, pump flow rate=3.2ml/s

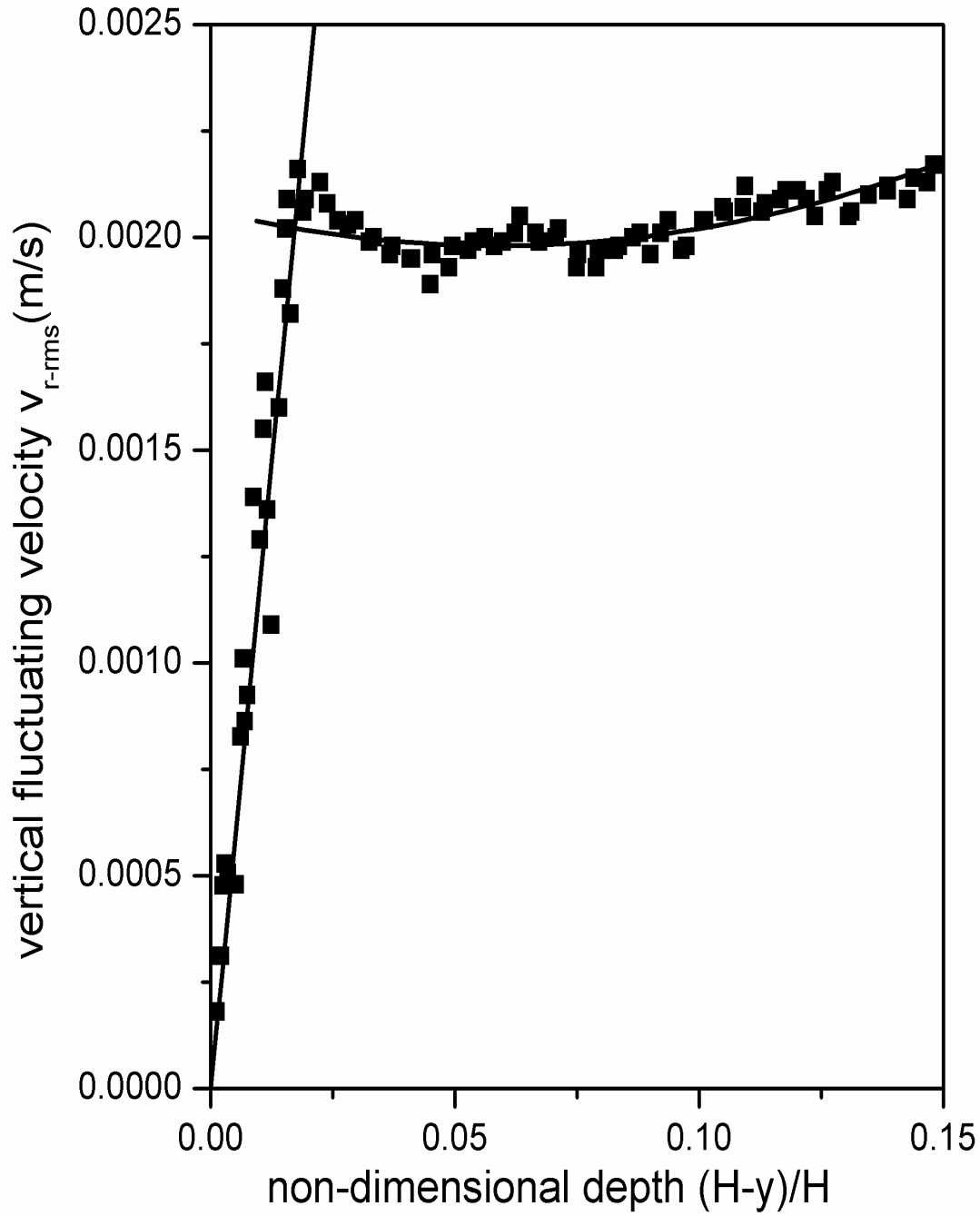

Figure 3.34: Variation of Vr-rms with non-dimensional depth from the interface.
Turbulence generated from above and below in the same direction,
Wind speed=4.5m/s, pump flow rate=3.2ml/s

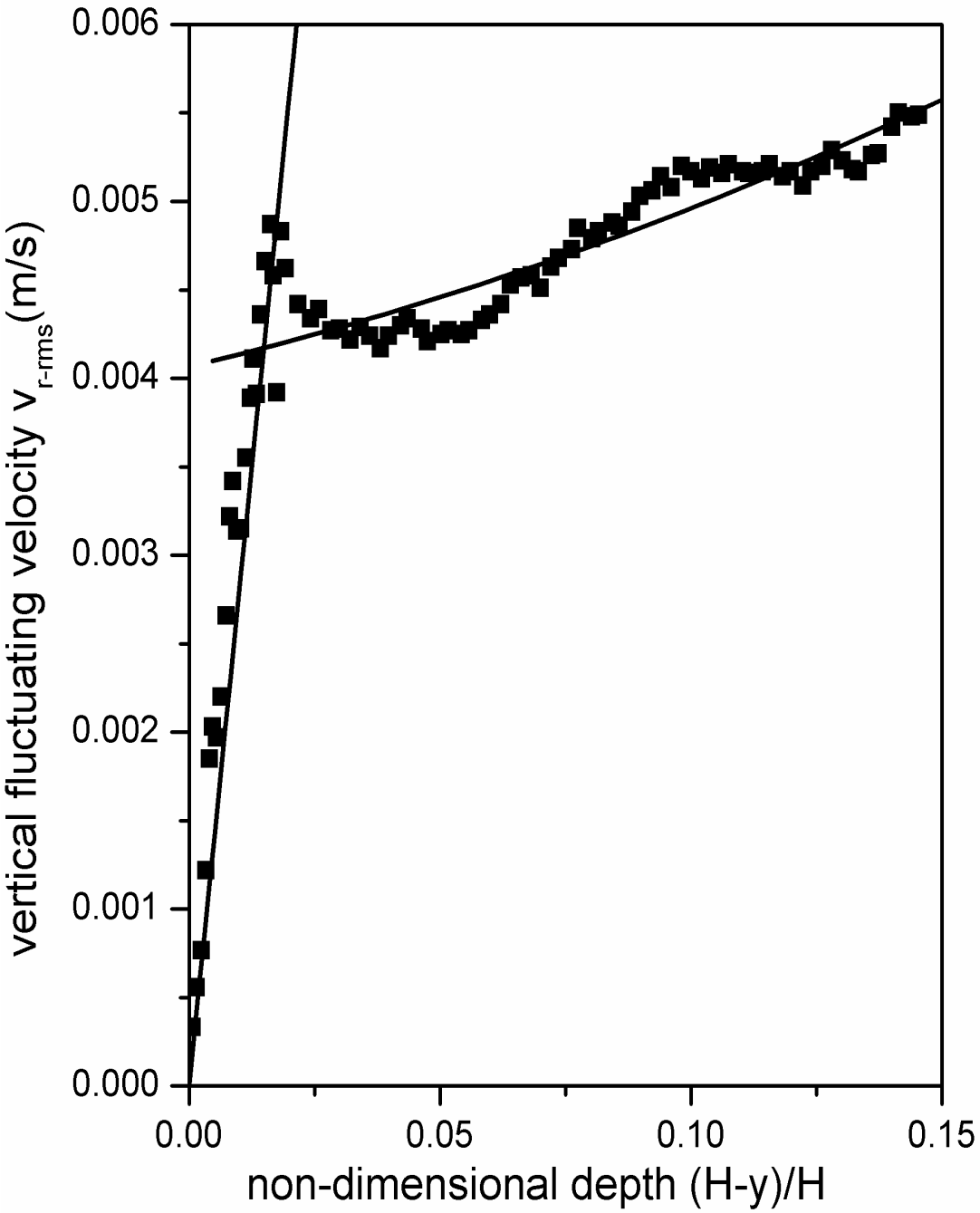

Figure 3.35: Variation of Vr-rms with non-dimensional depth from the interface.
Turbulence generated from above and below in the same direction,
Wind speed=6m/s, pump flow rate=3.2ml/s

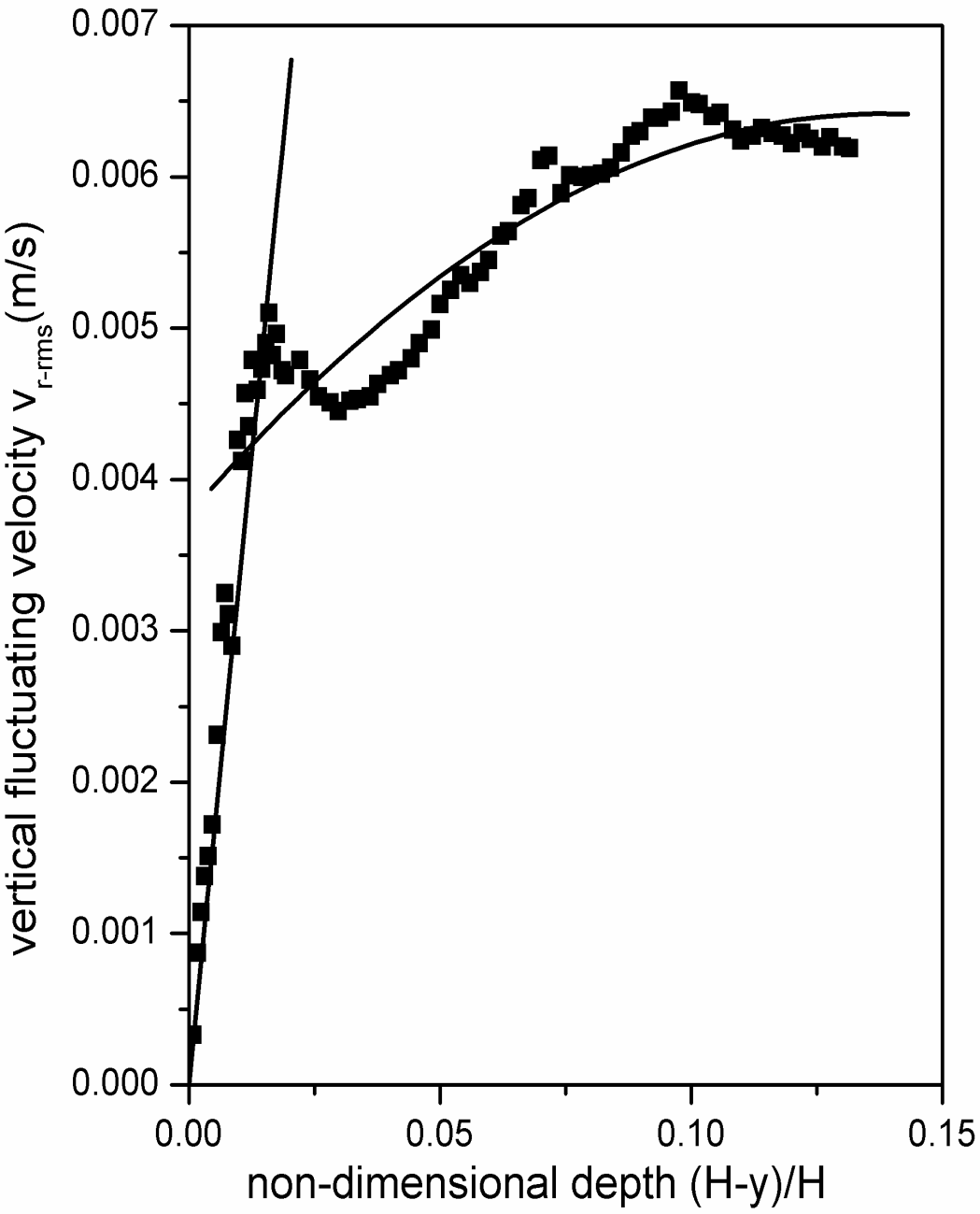

Figure 3.36: Variation of Vr-rms with non-dimensional depth from the interface.
Turbulence generated from above and below in the same direction,
Wind speed=6.5m/s, pump flow rate=3.2ml/s

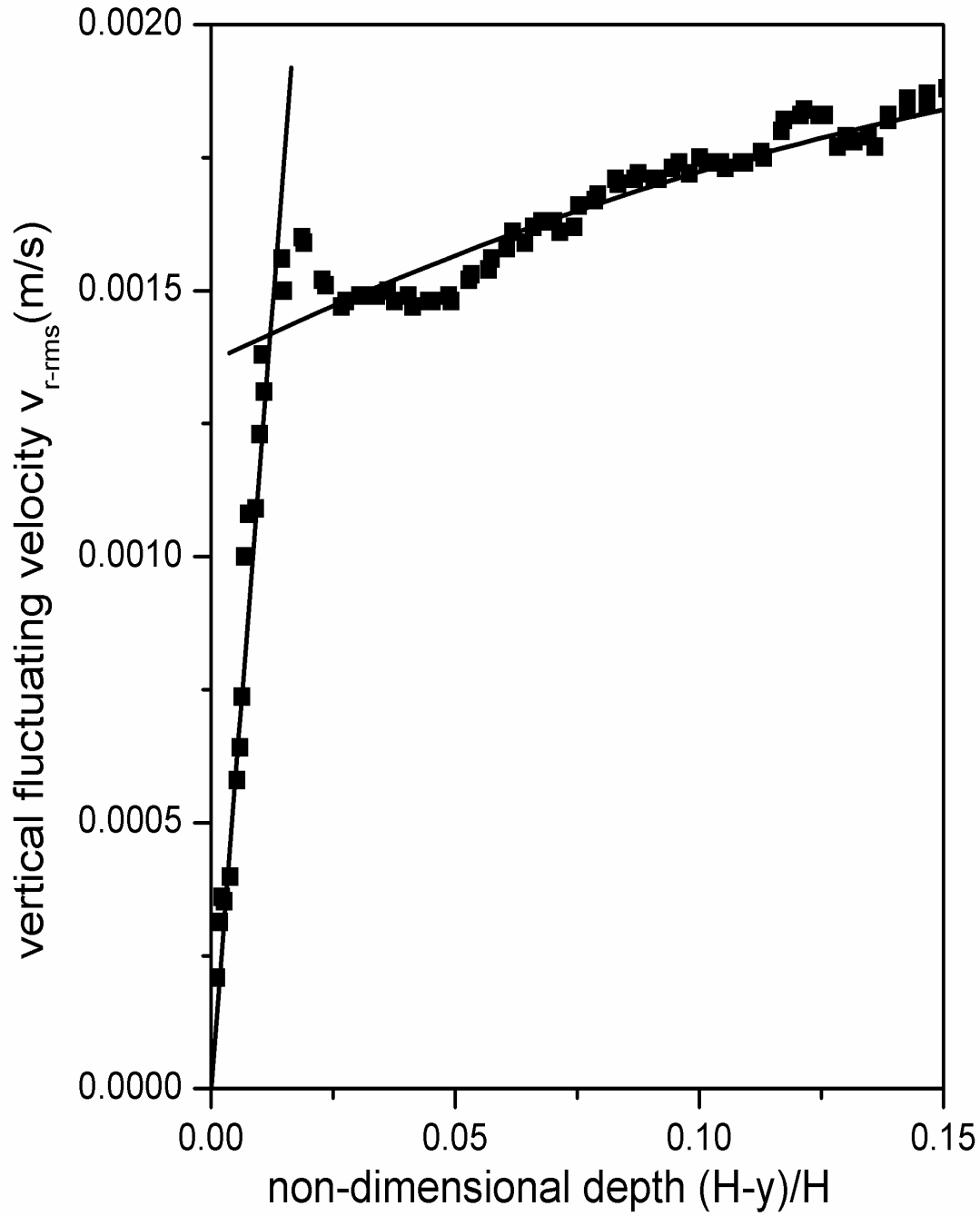

Figure 3.37: Variation of Vr-rms with non-dimensional depth from the interface.
Turbulence generated from above and below in the opposite direction,
Wind speed=3.5m/s, pump flow rate=10.5ml/s

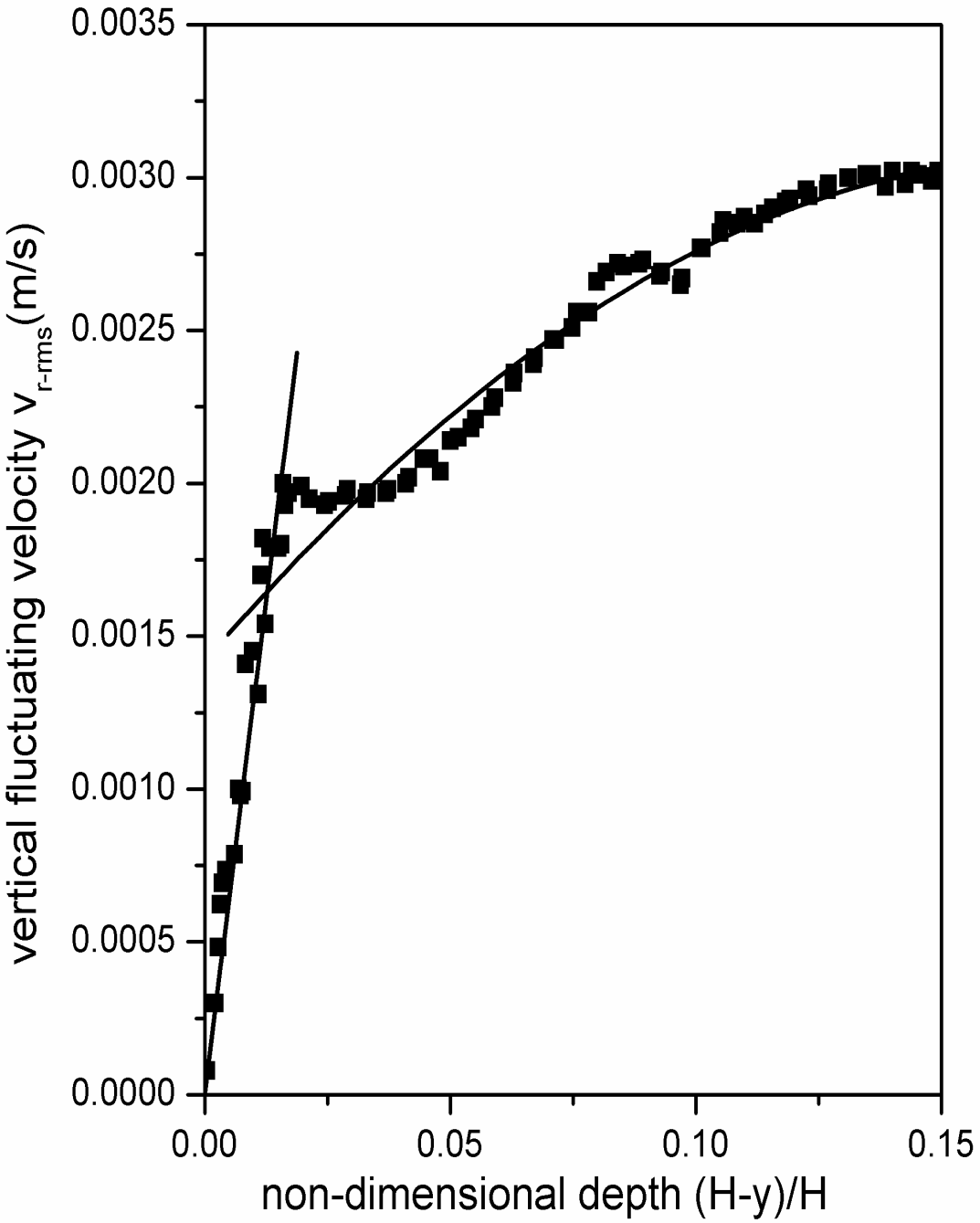

Figure 3.38: Variation of Vr-rms with non-dimensional depth from the interface.
Turbulence generated from above and below in the opposite direction,
Wind speed=4.5m/s, pump flow rate=10.5ml/s

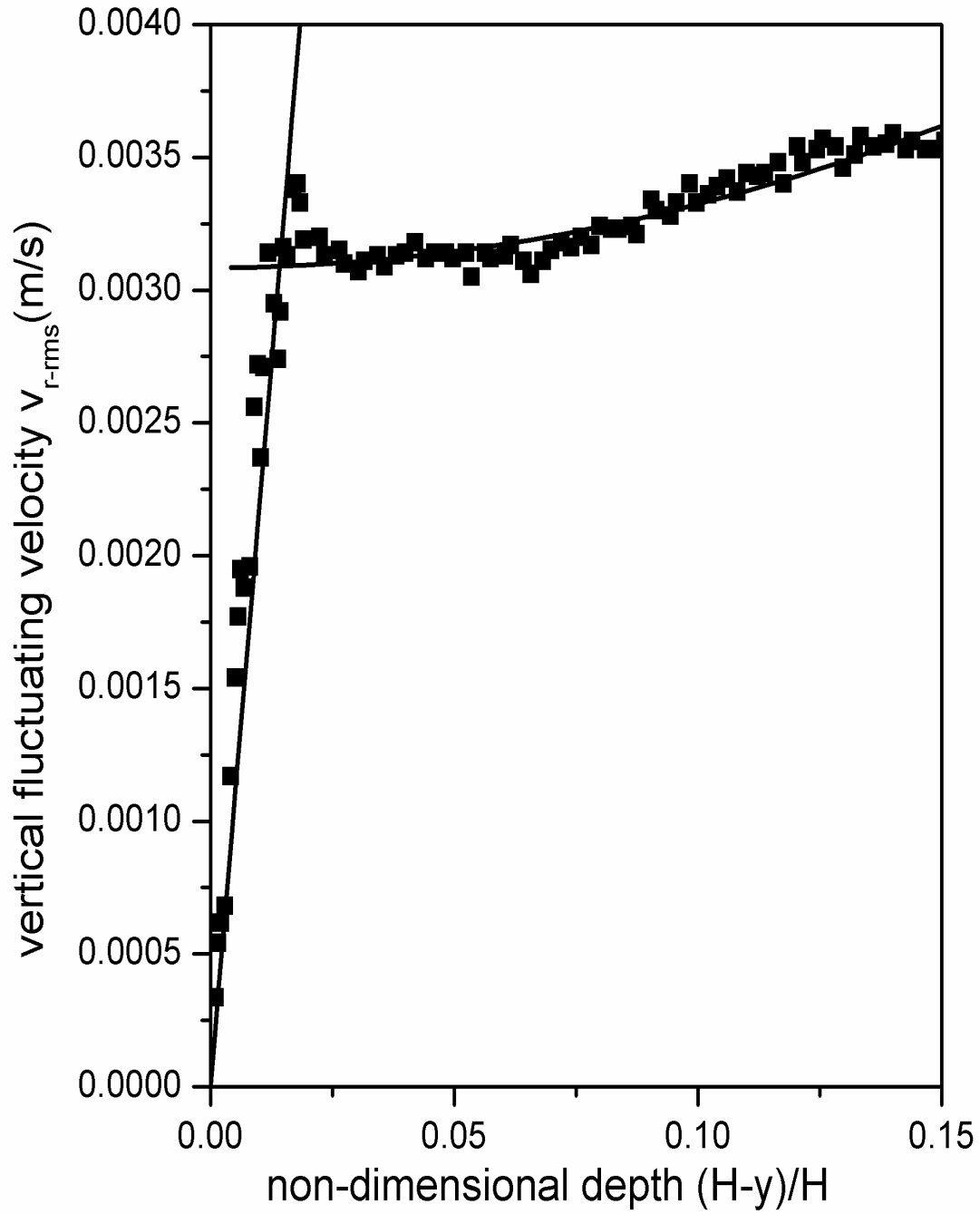

Figure 3.39: Variation of Vr-rms with non-dimensional depth from the interface.
Turbulence generated from above and below in the opposite direction,
Wind speed=6m/s, pump flow rate=10.5ml/s

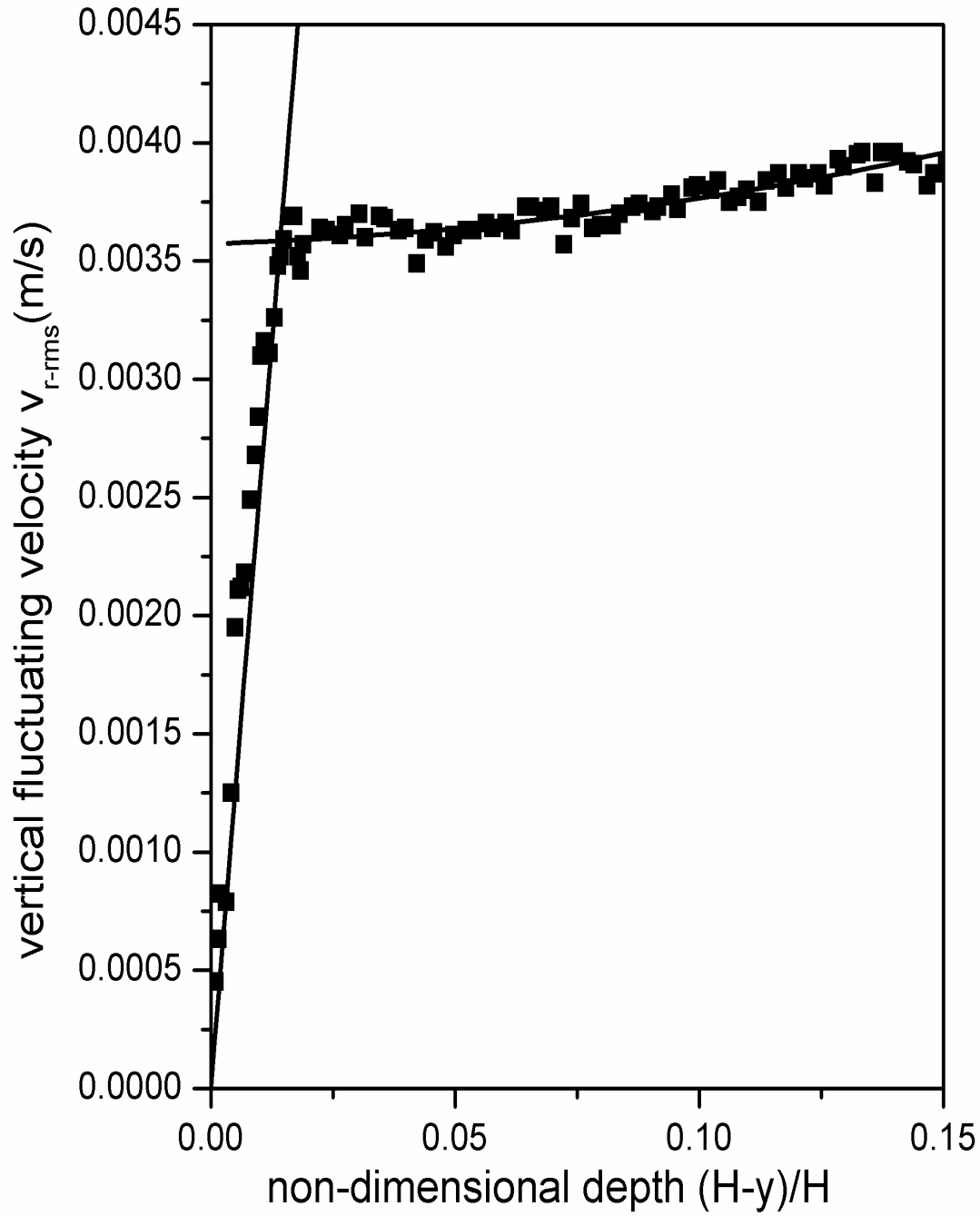

Figure 3.40: Variation of Vr-rms with non-dimensional depth from the interface.
Turbulence generated from above and below in the opposite direction,
Wind speed=6.5m/s, pump flow rate=10.5ml/s

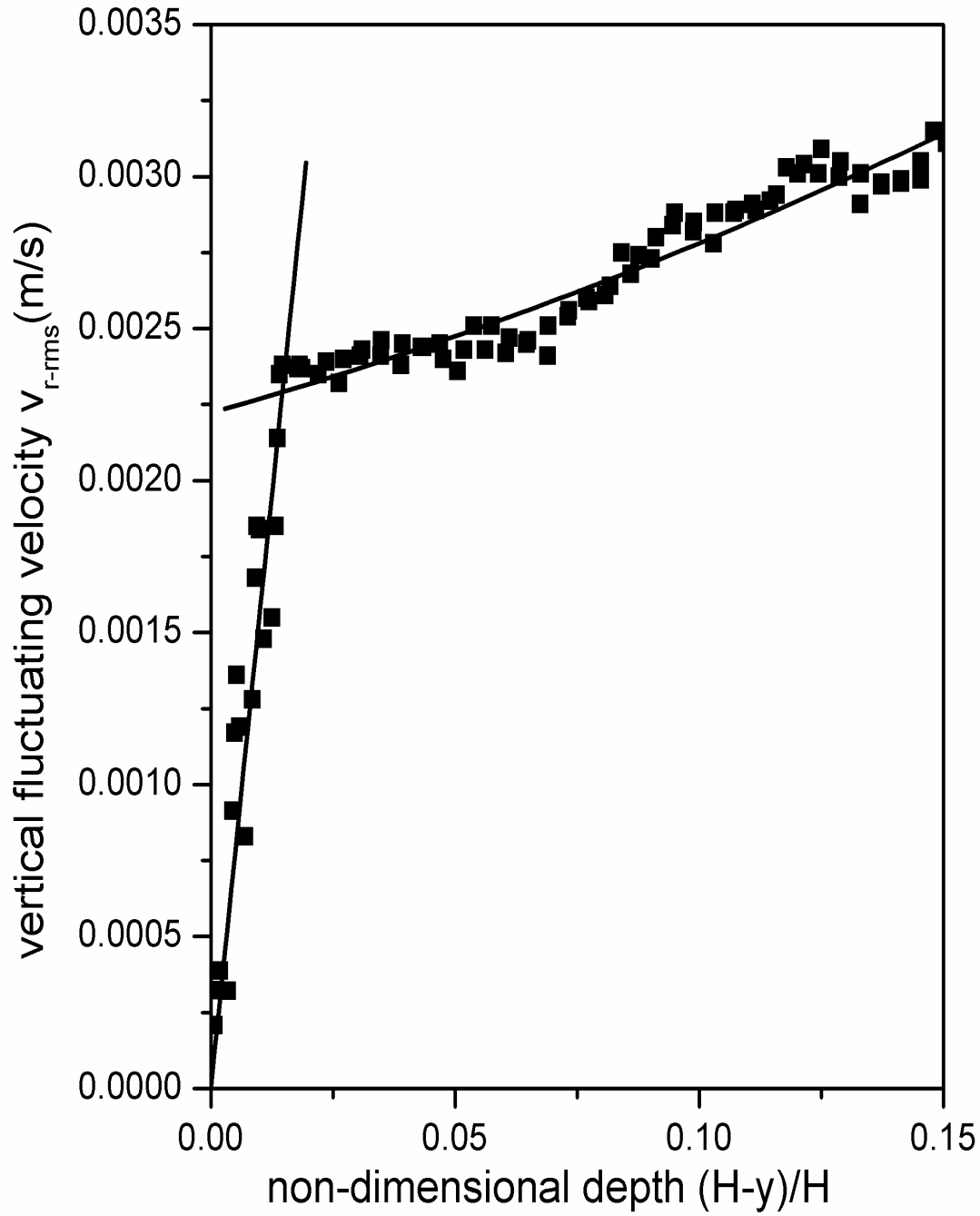

Figure 3.41: Variation of Vr-rms with non-dimensional depth from the interface.
Turbulence generated from above and below in the same direction,
Wind speed=3m/s, pump flow rate=10.5ml/s

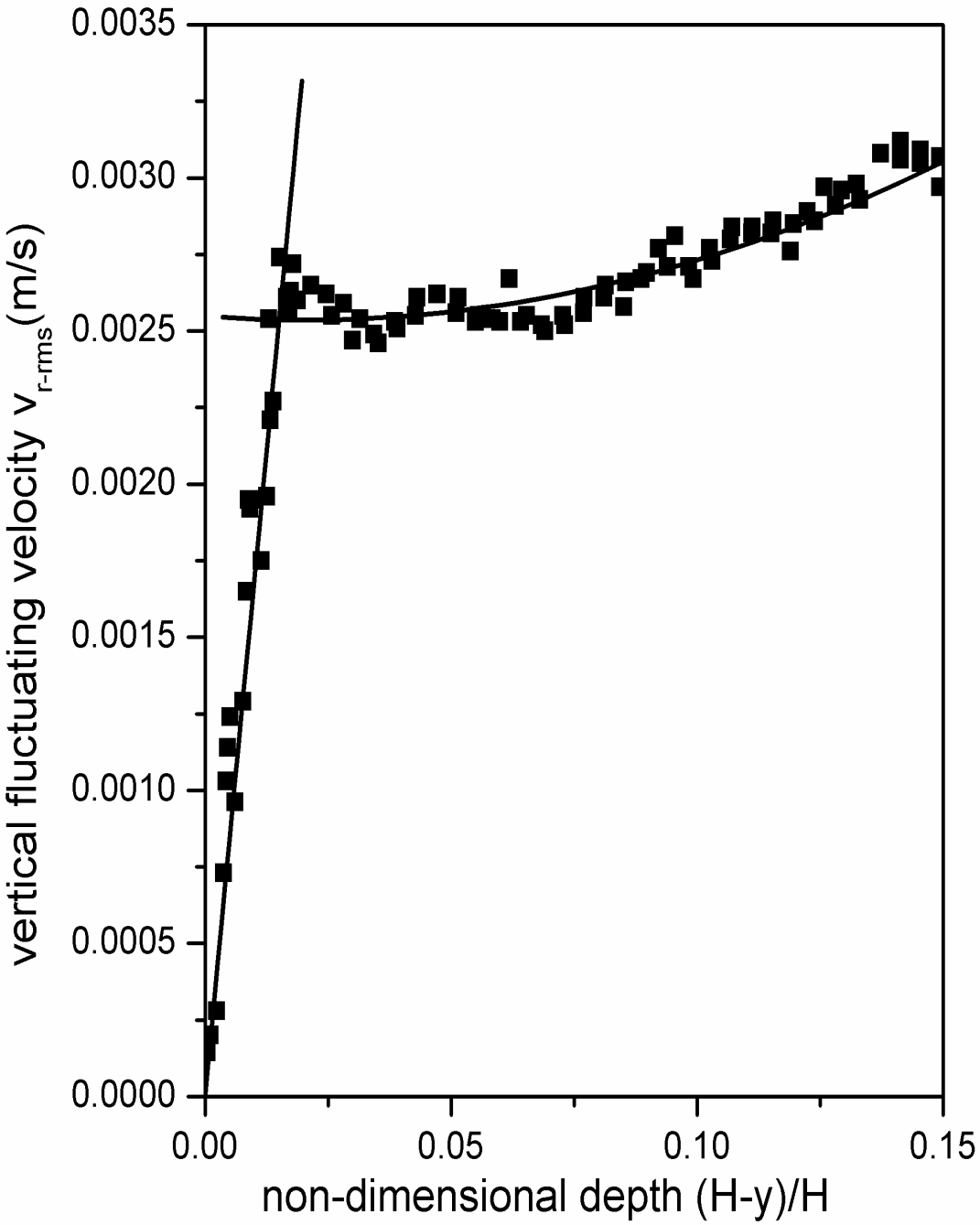

Figure 3.42: Variation of Vr-rms with non-dimensional depth from the interface.
Turbulence generated from above and below in the same direction,
Wind speed=3.5m/s, pump flow rate=10.5ml/s

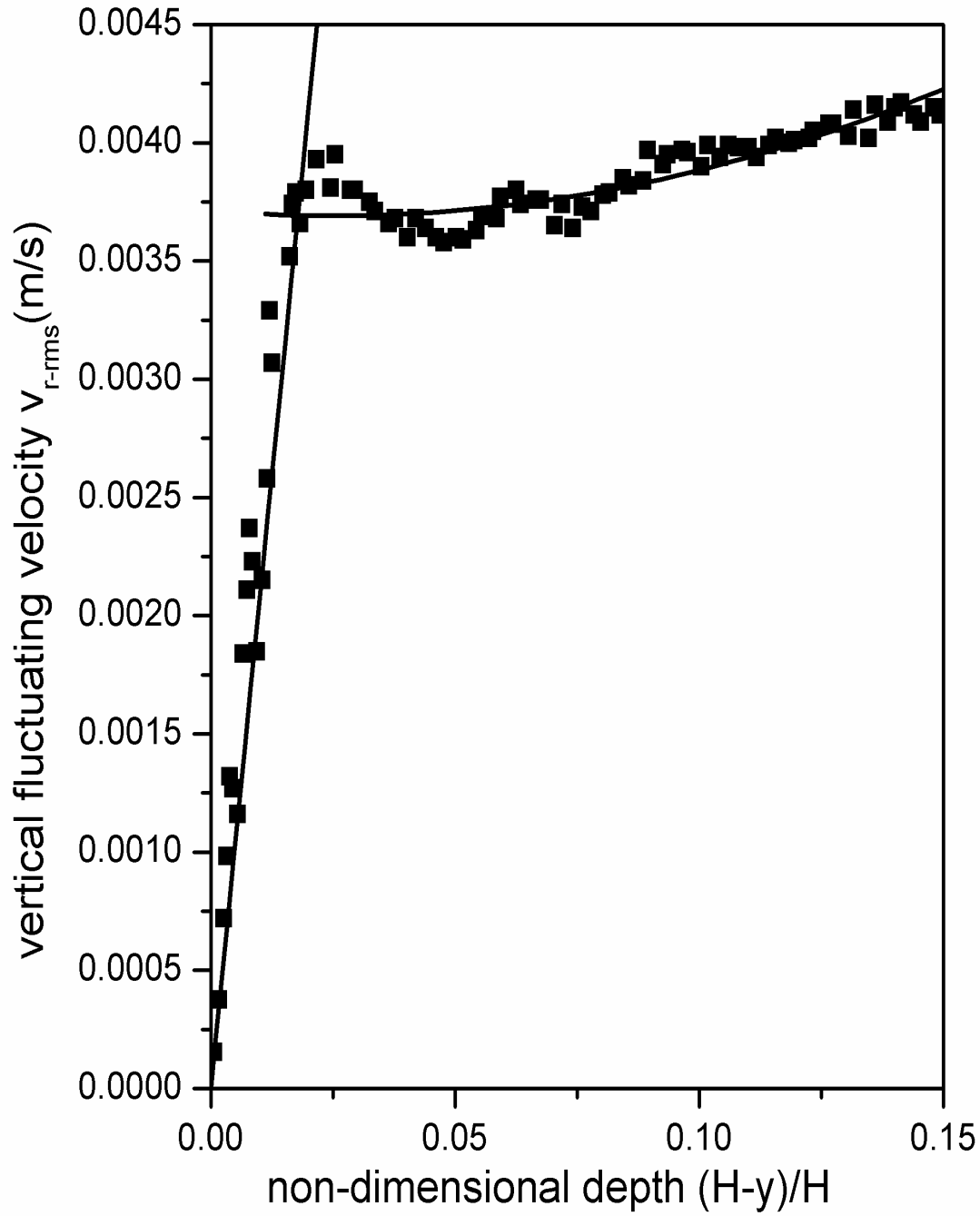

Figure 3.43: Variation of Vr-rms with non-dimensional depth from the interface.
Turbulence generated from above and below in the same direction,
Wind speed=4.5m/s, pump flow rate=10.5ml/s

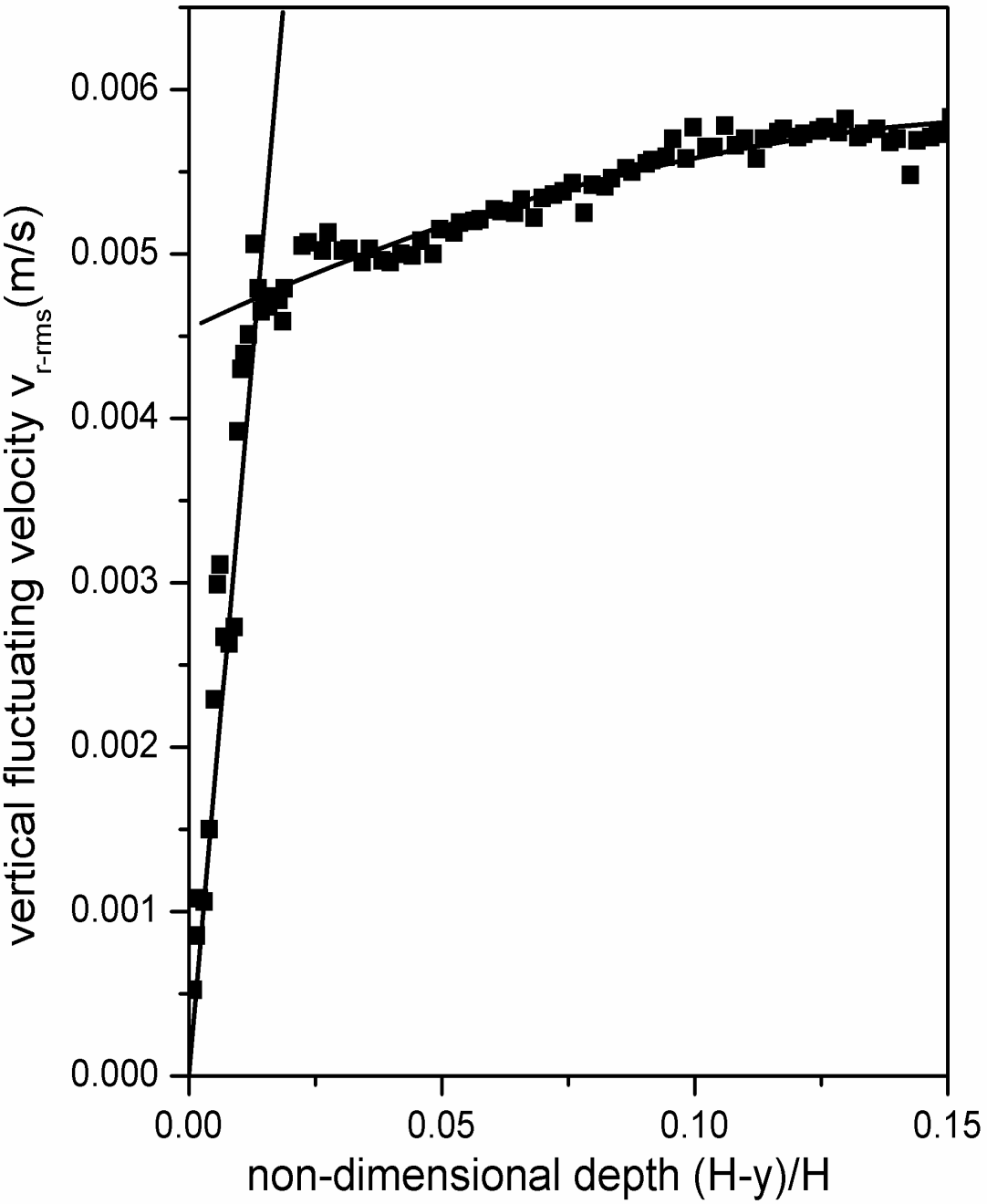

Figure 3.44: Variation of Vr-rms with non-dimensional depth from the interface.
Turbulence generated from above and below in the same direction,
Wind speed=6m/s, pump flow rate=10.5ml/s

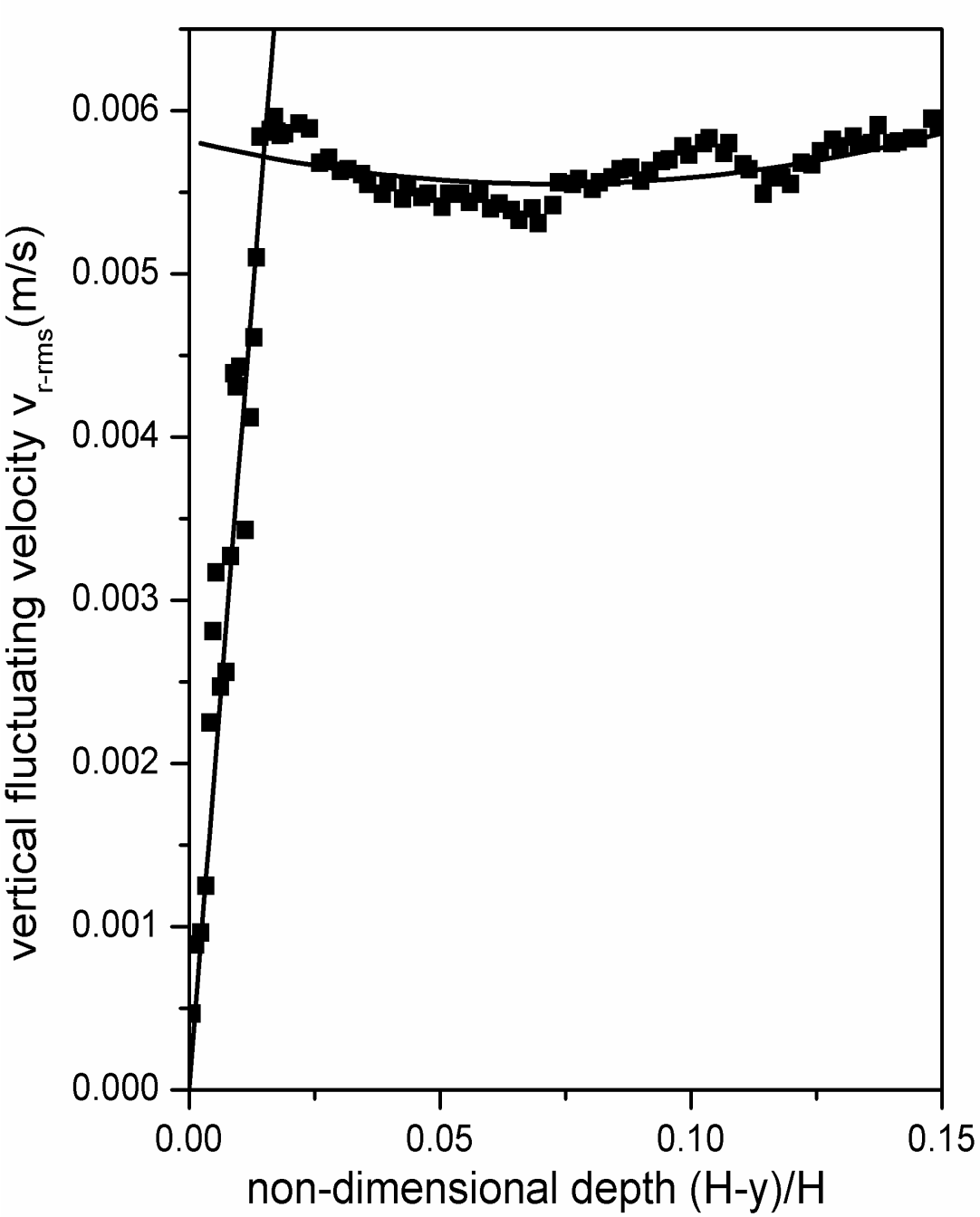

Figure 3.45: Variation of Vr-rms with non-dimensional depth from the interface.
Turbulence generated from above and below in the same direction,
Wind speed=6.5m/s, pump flow rate=10.5ml/s

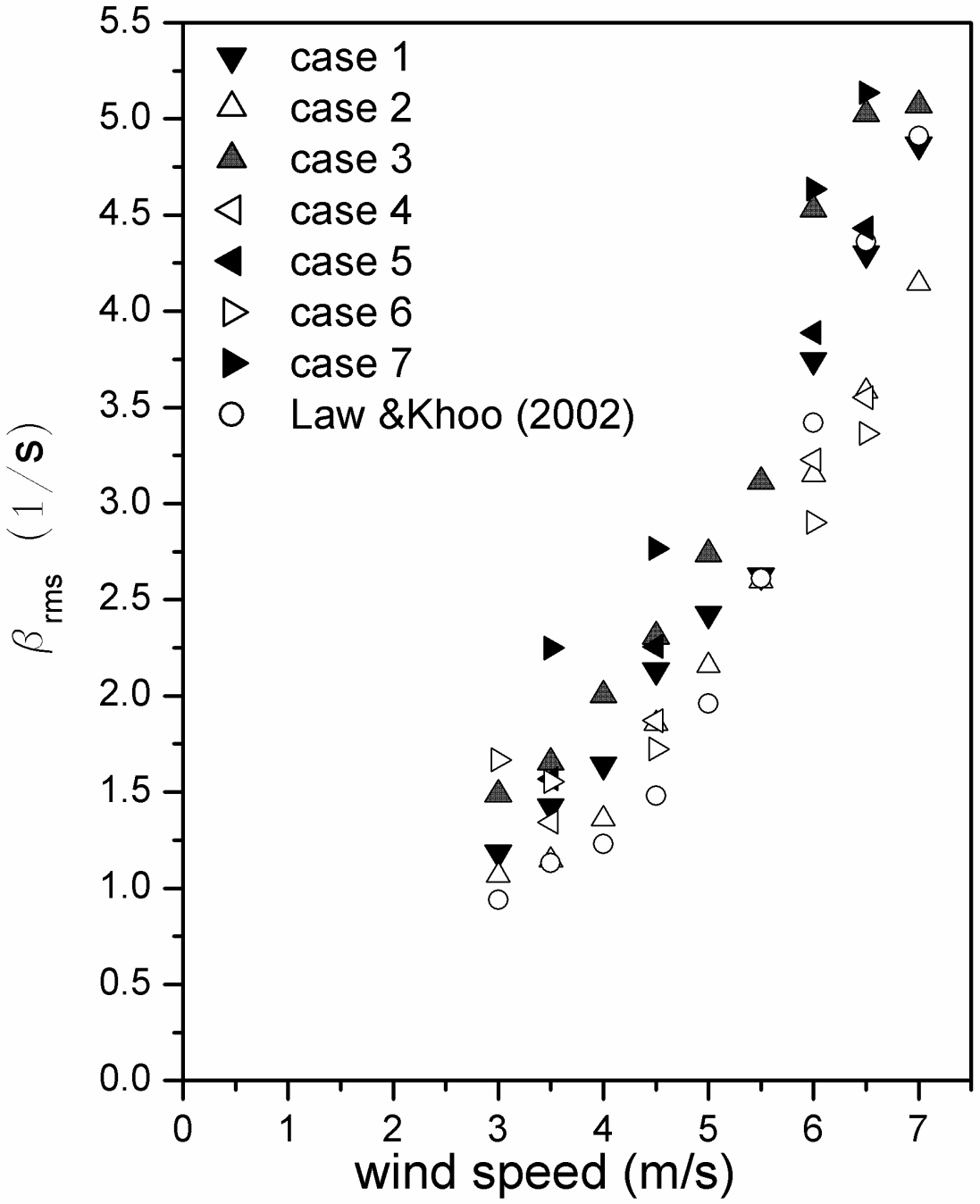

Figure 3.46: Variation of β_{rms} with nominal wind speed for Cases 1-7 (see Table 2.1)

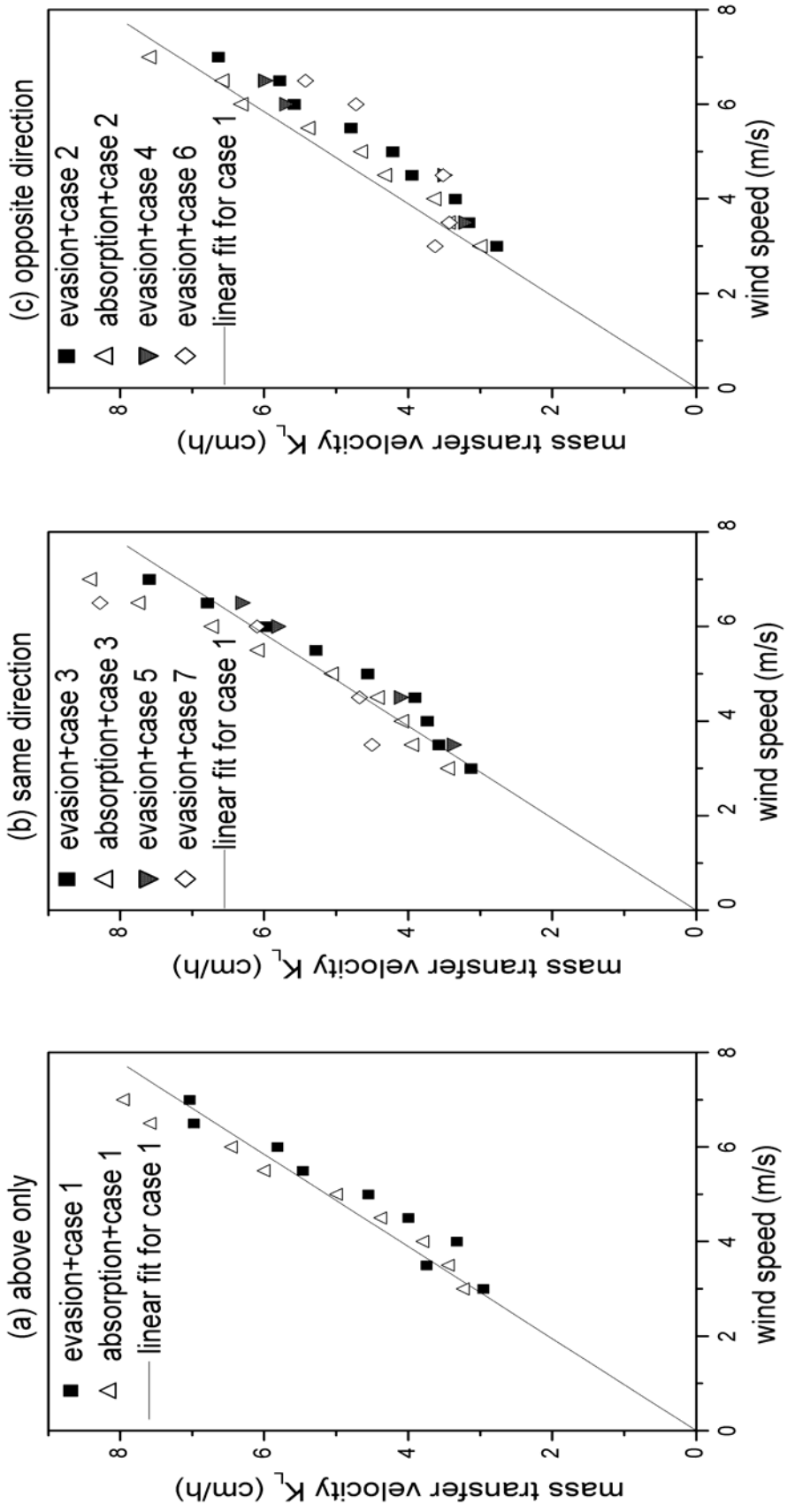

Figure 3.47: Mass transfer velocity versus wind speed

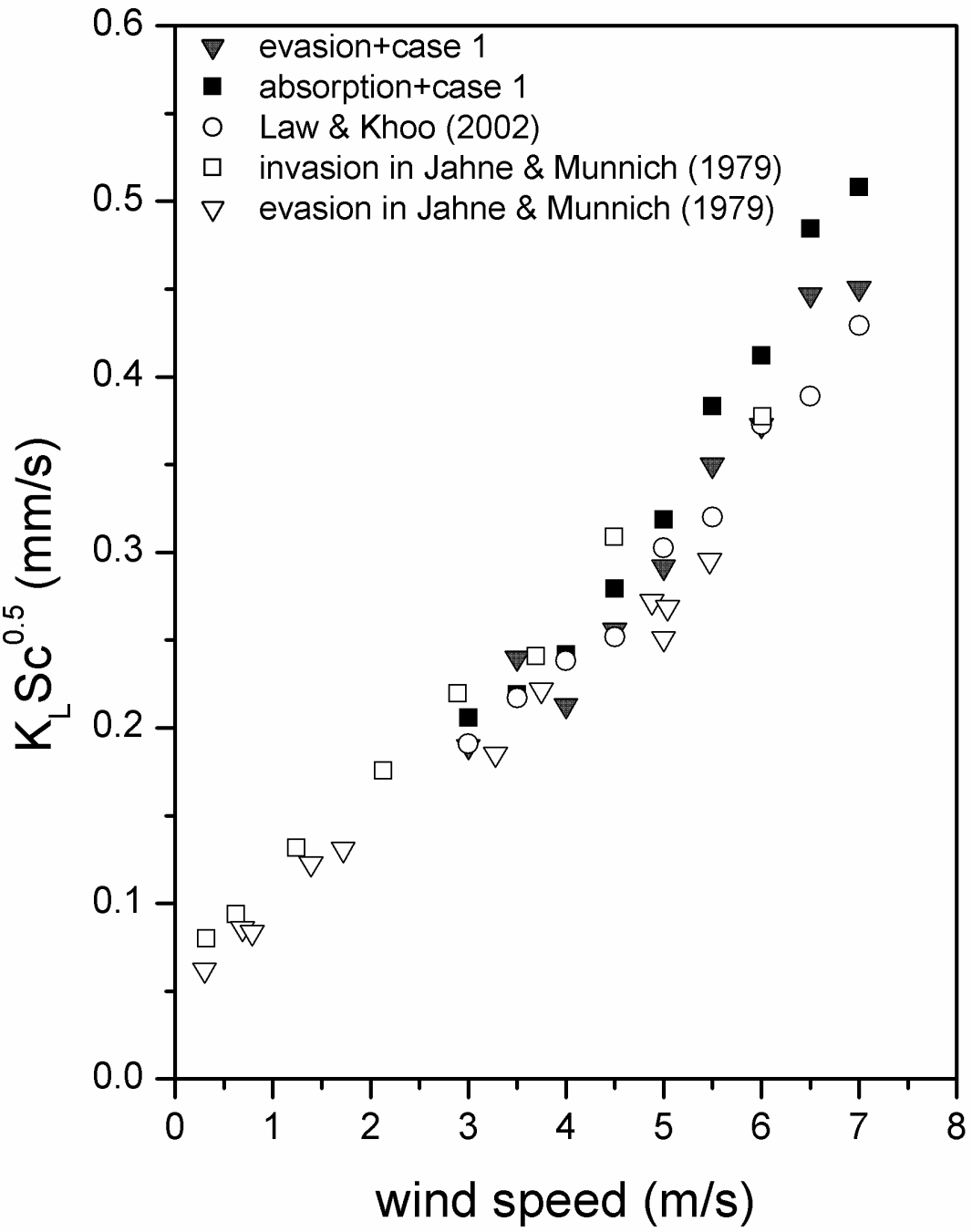

Figure 3.48: Comparison of the mass transfer velocity varying with nominal wind speed

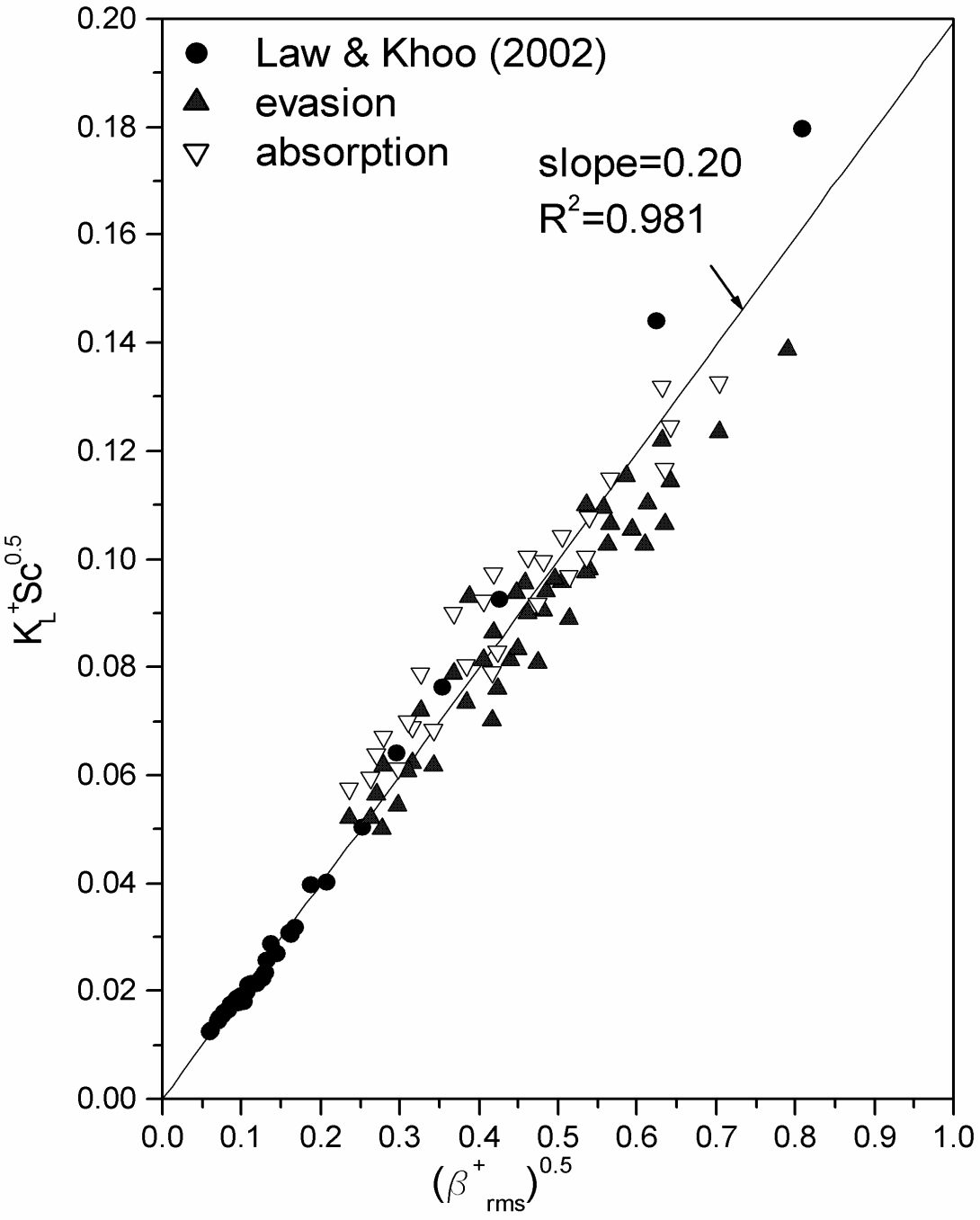

Figure 3.49: $K_L^+ Sc^{0.5}$ versus $(\beta_{rms}^+)^{0.5}$ for all the tested flow conditions

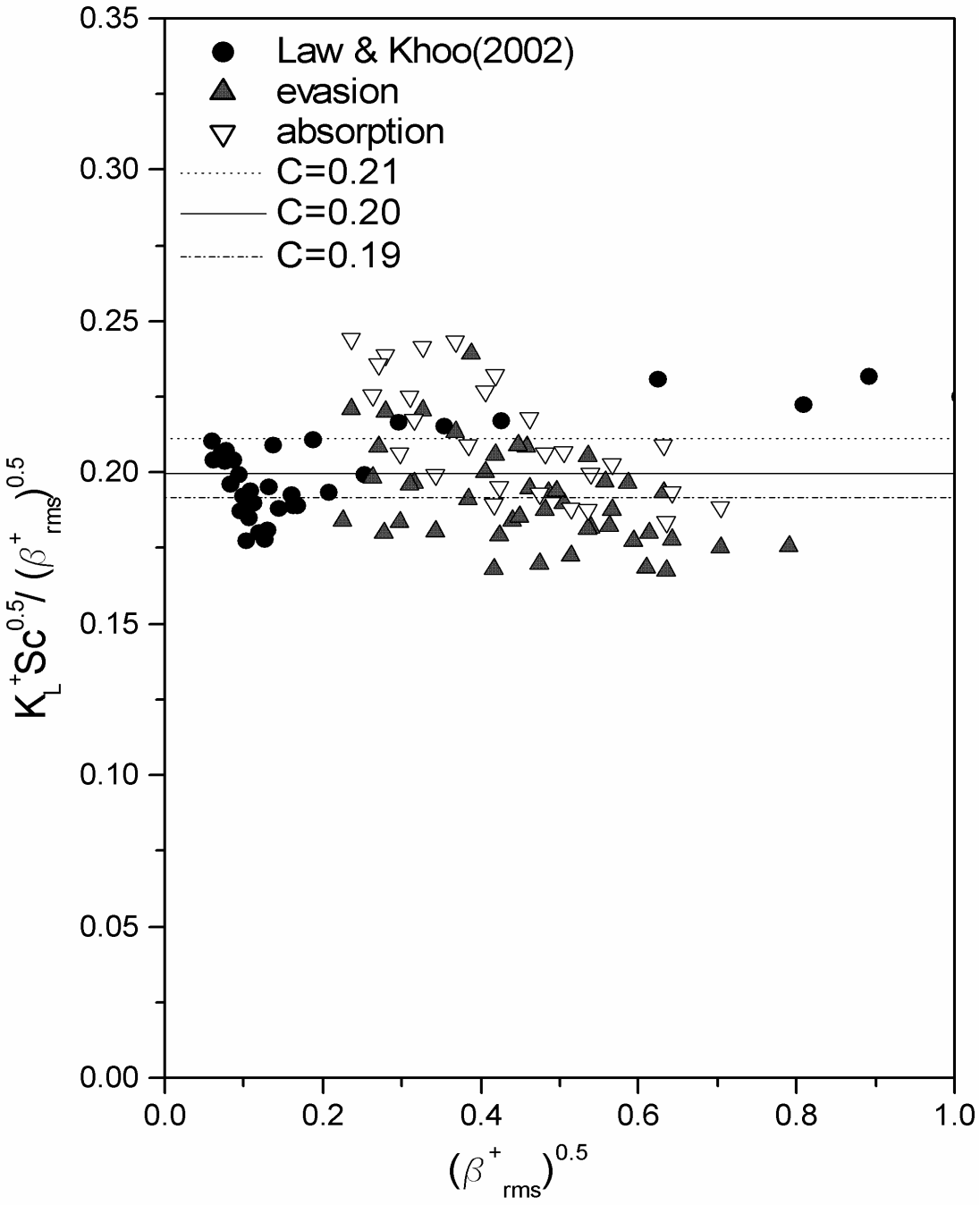

Figure 3.50: $\frac{K_L^+ Sc^{0.5}}{(\beta_{rms}^+)^{0.5}}$ versus $(\beta_{rms}^+)^{0.5}$ for all the tested flow conditions

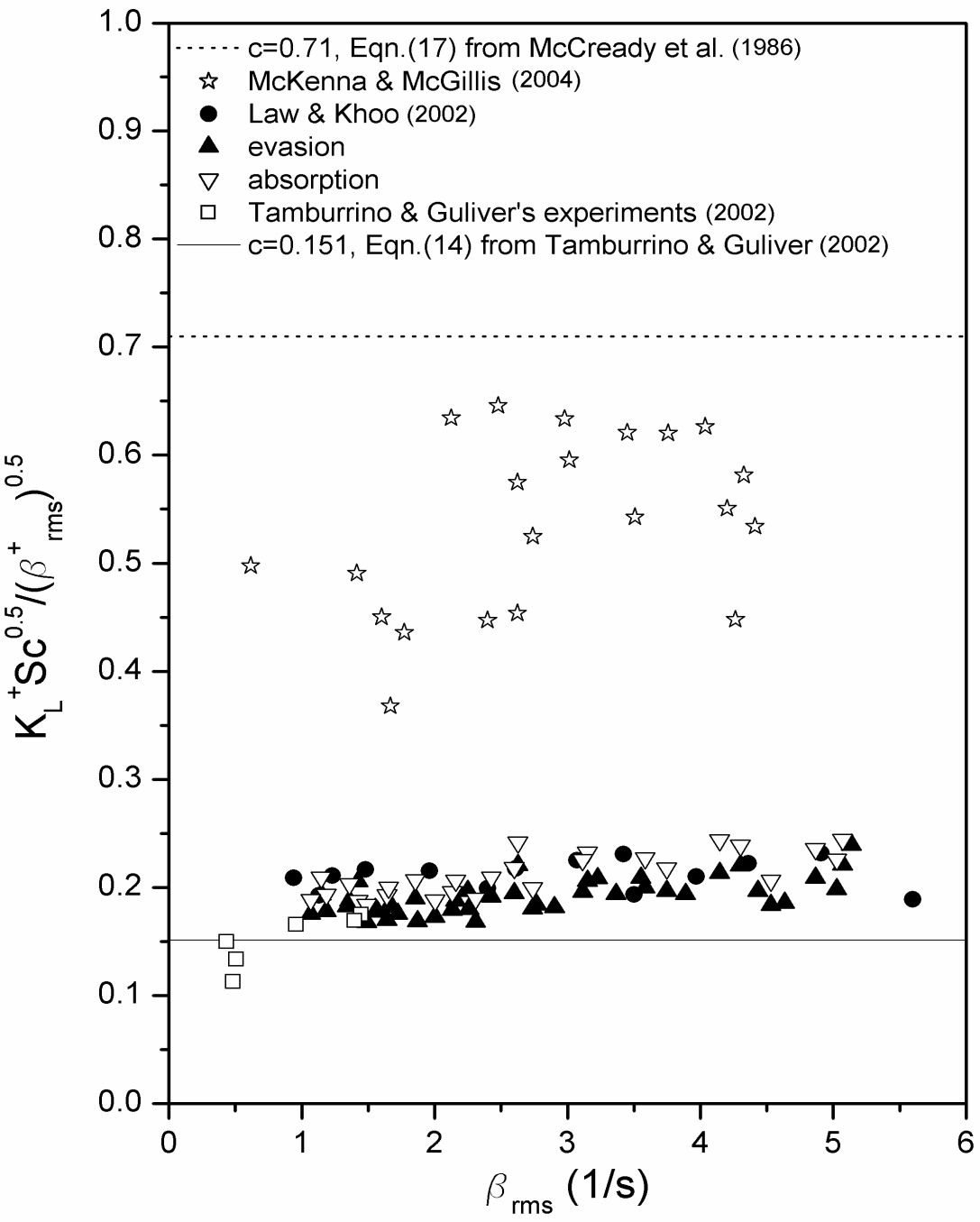

Figure 3.51: Comparison of various works

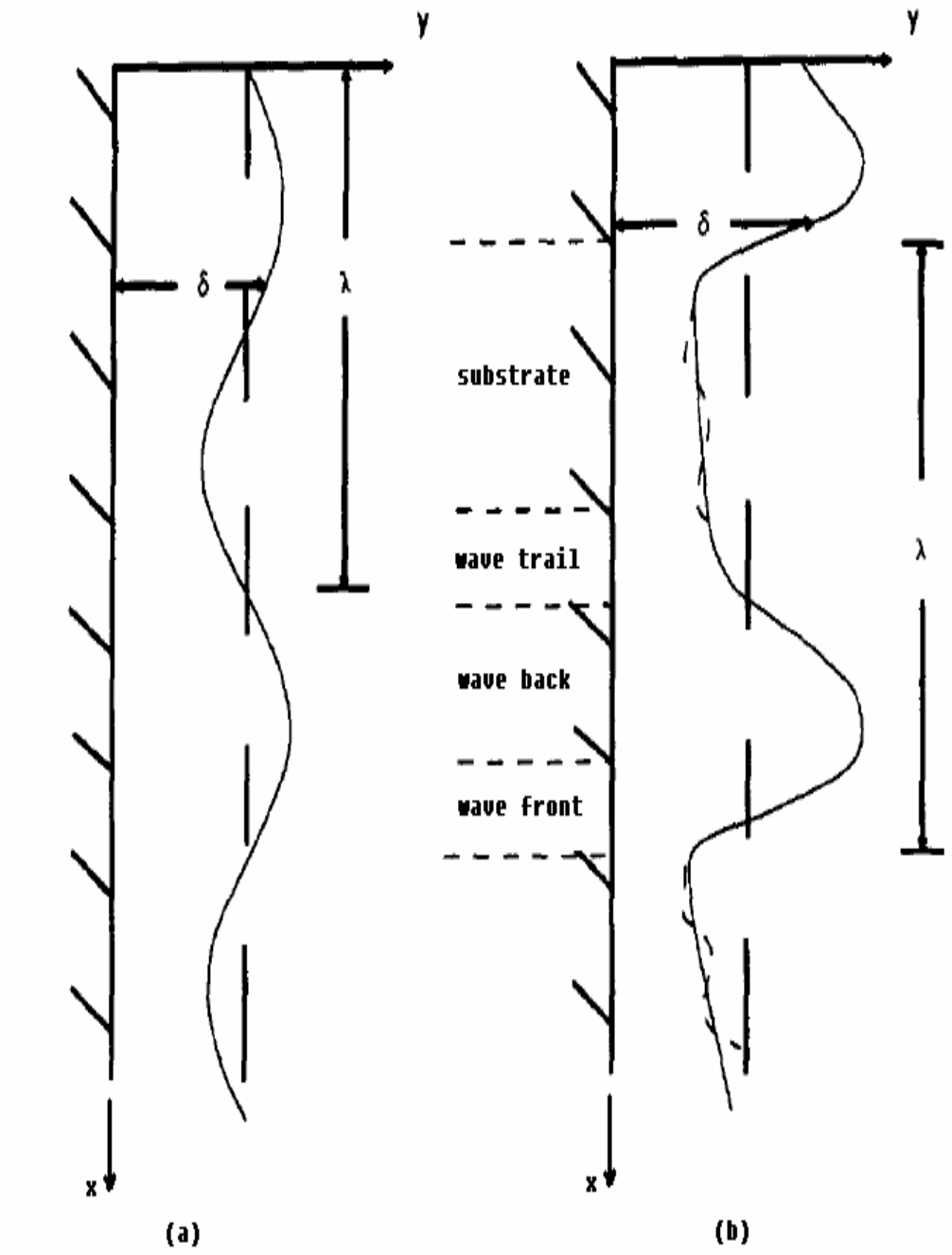

Figure 4.1: Typical wave shapes: (a) capillary waves; (b) roll waves (adopted from Patnaik and Perez-Blanco (1996))

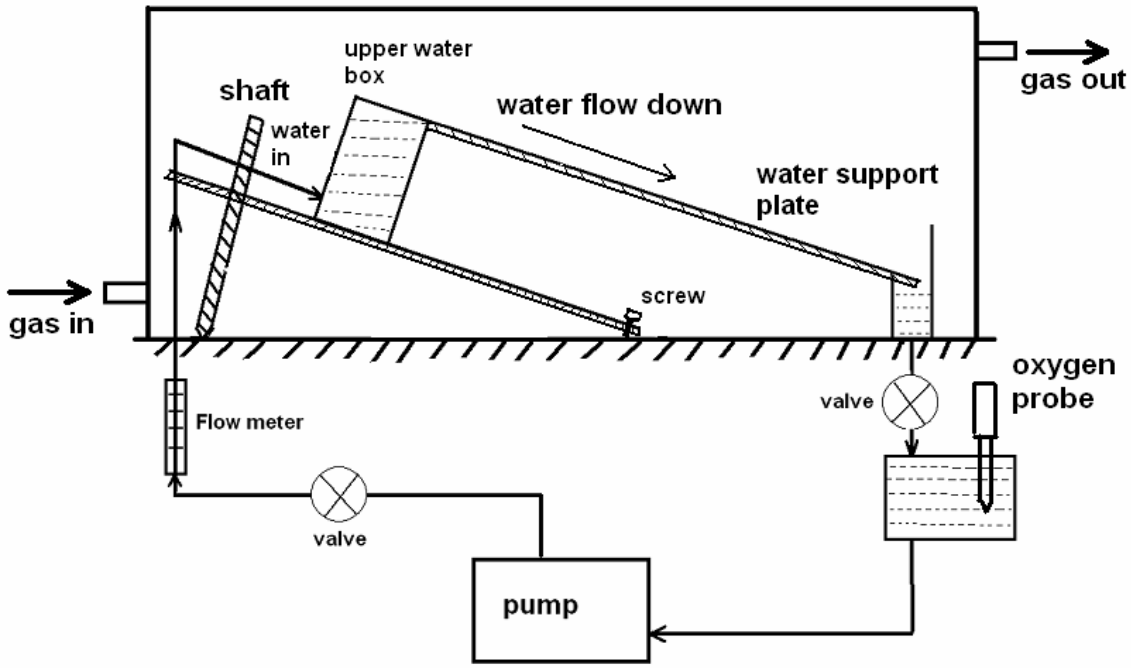

Figure 4.2: Schematic of the falling film setup (not to scale)

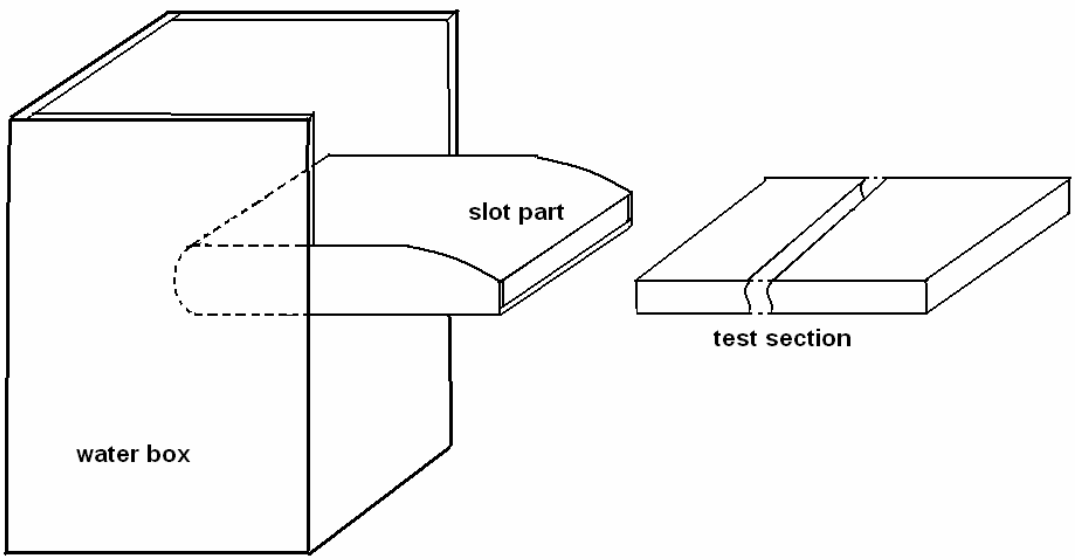

Figure 4.3: Schematic diagram for the slot part (not to scale)

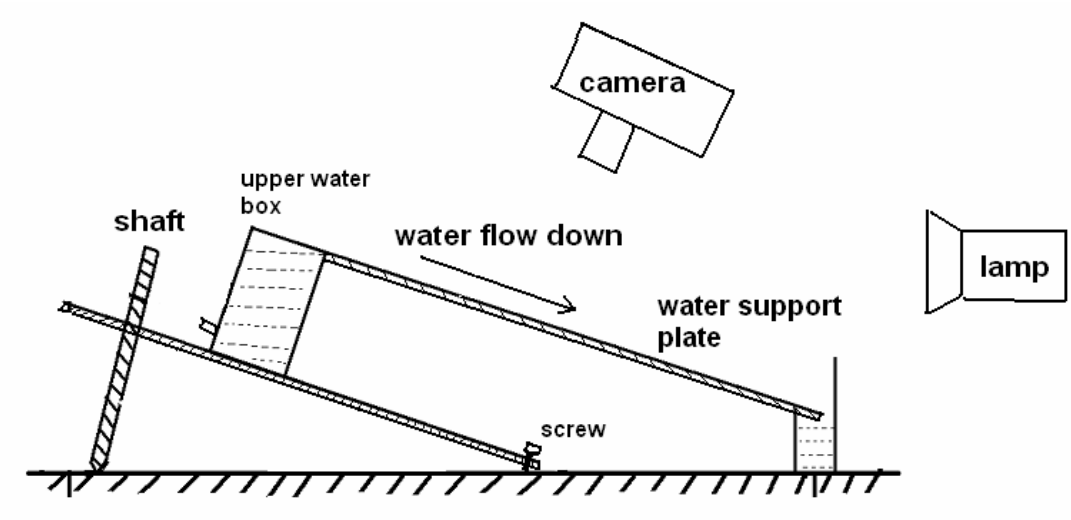

Figure 4.4: Arrangement of the experimental components

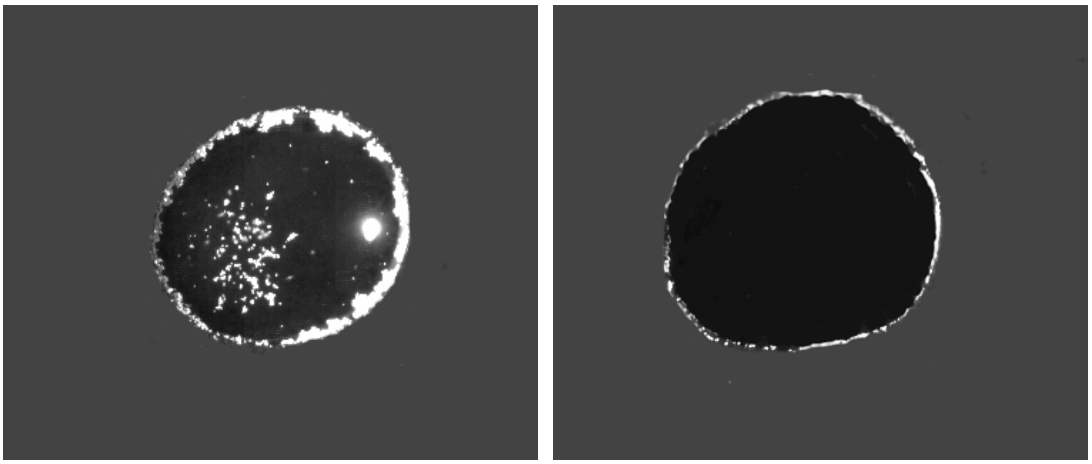

(a) before introducing dye (b) after introducing dye

Figure 4.5: Water drop with particles before and after introducing dye

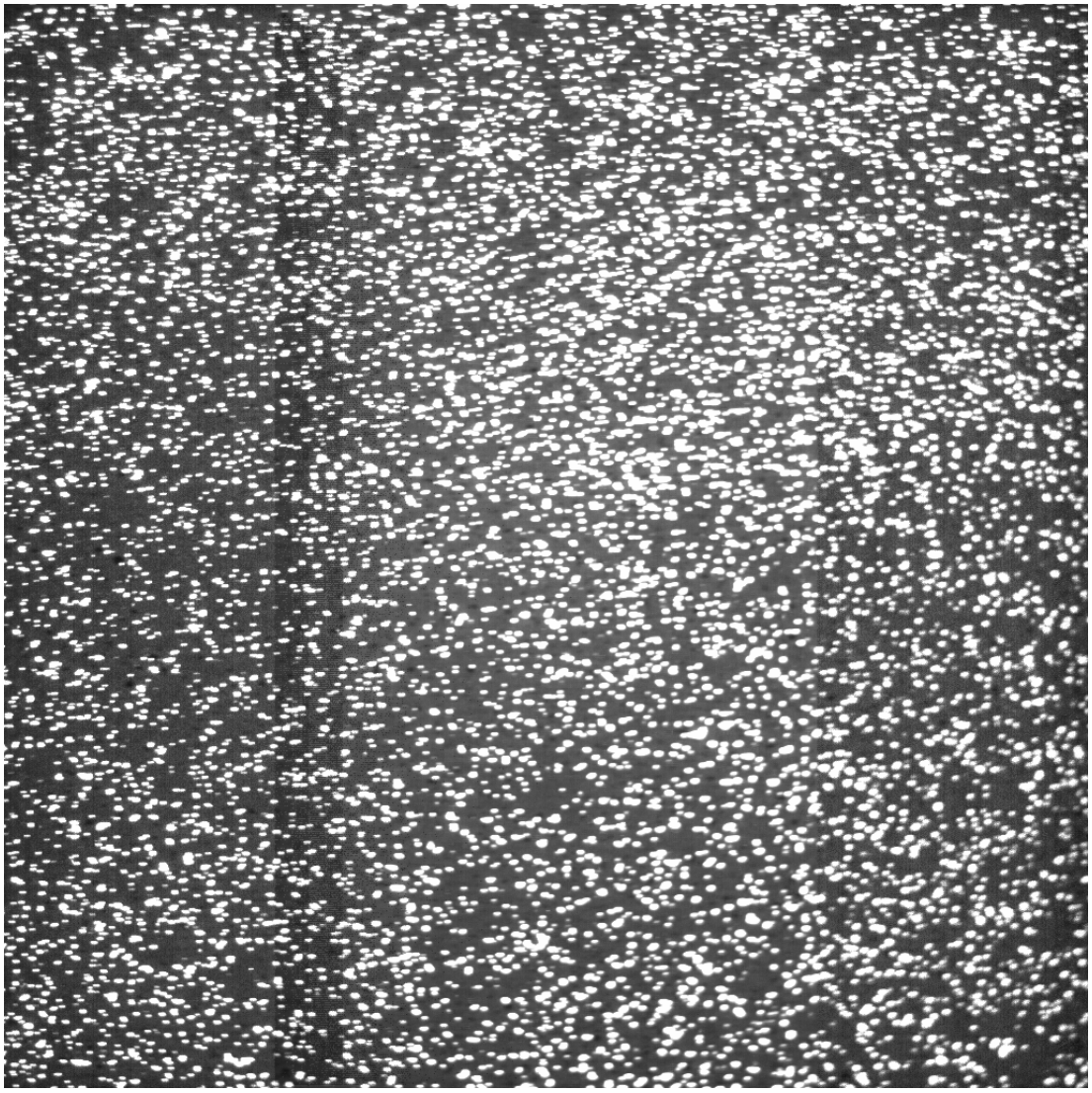

Figure 5.1: Typical image captured in falling film setup (33mm×33mm)

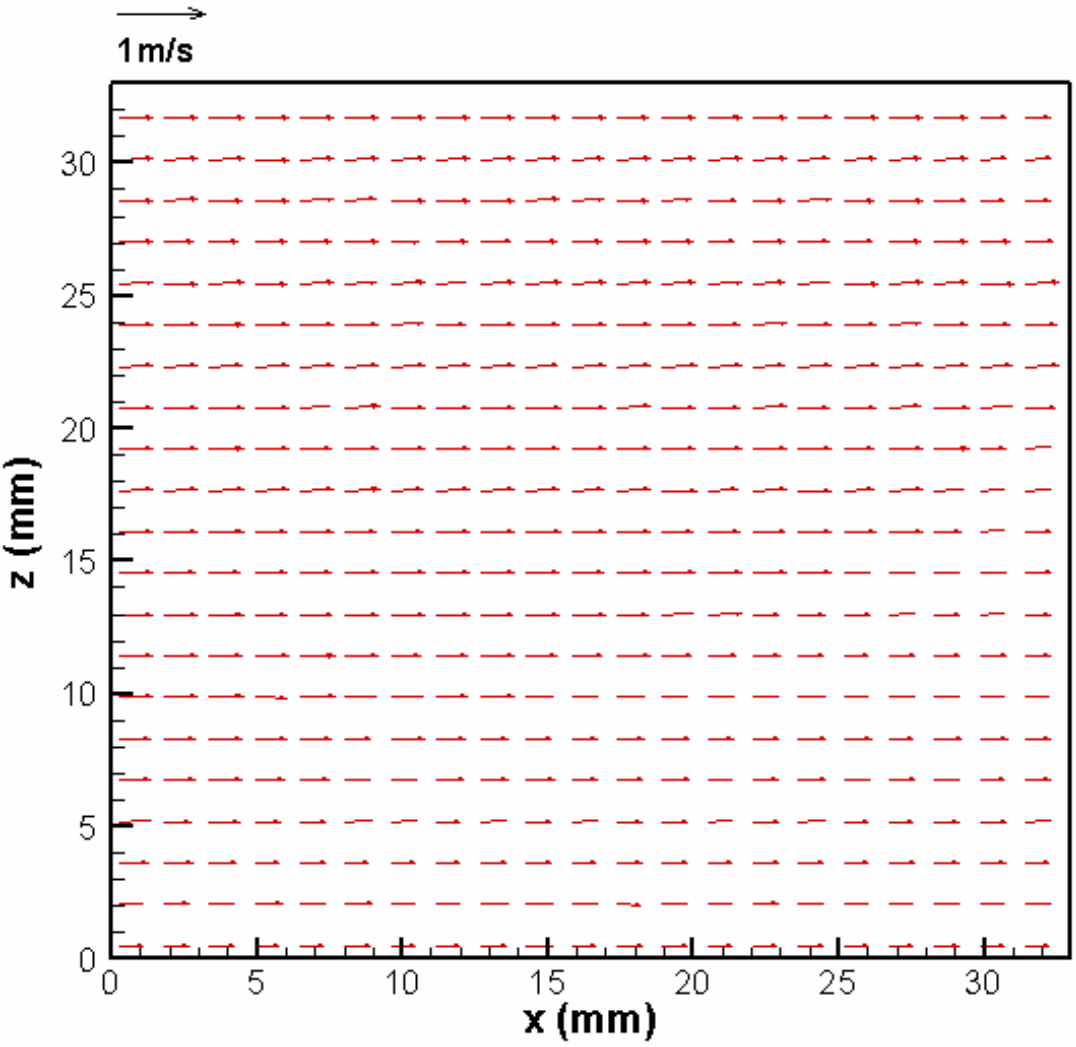

Figure 5.2: Velocity distribution for the case of $\theta = 5$ deg ree, Q=0.8 L/M

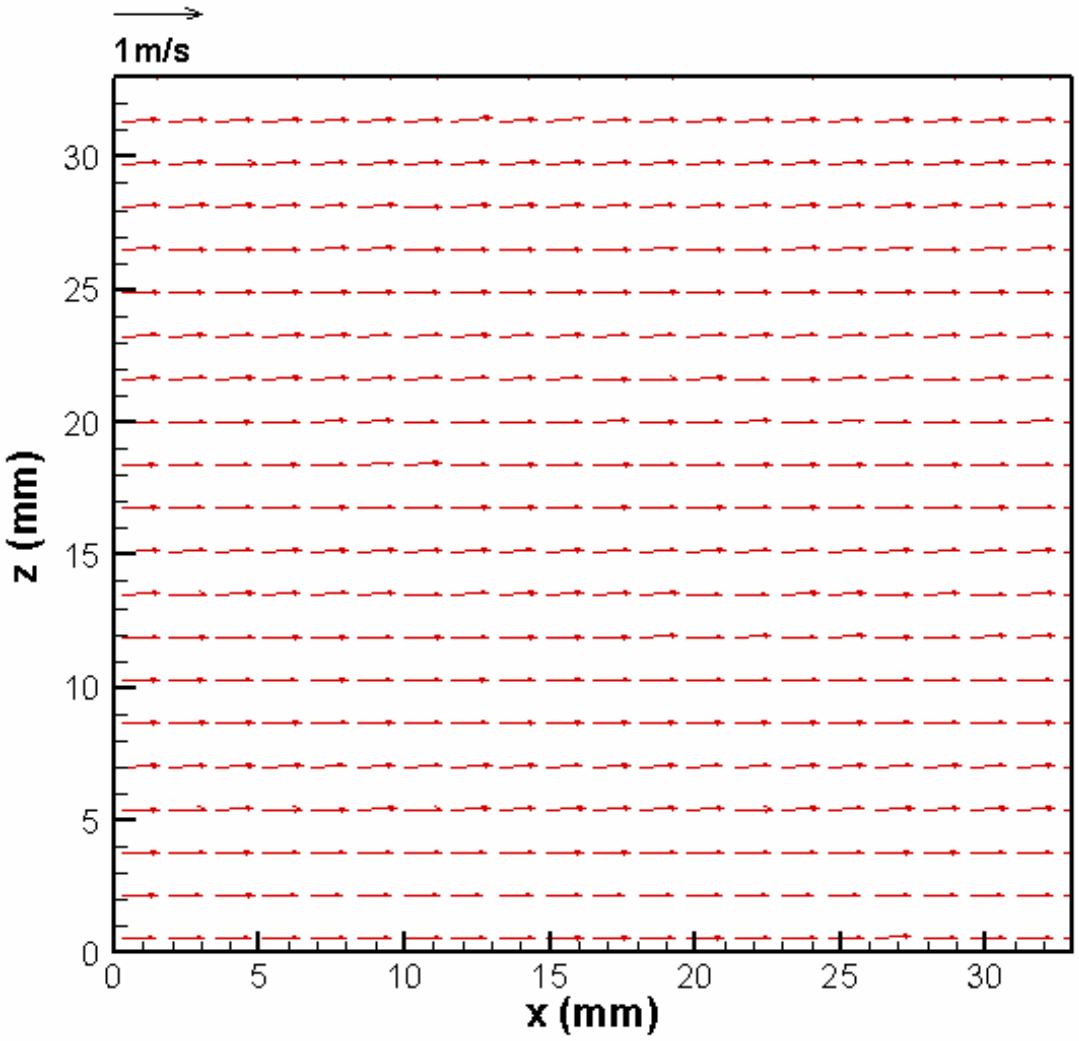

Figure 5.3: Velocity distribution for the case of $\theta = 5$ deg ree, Q= 1.2 L/M

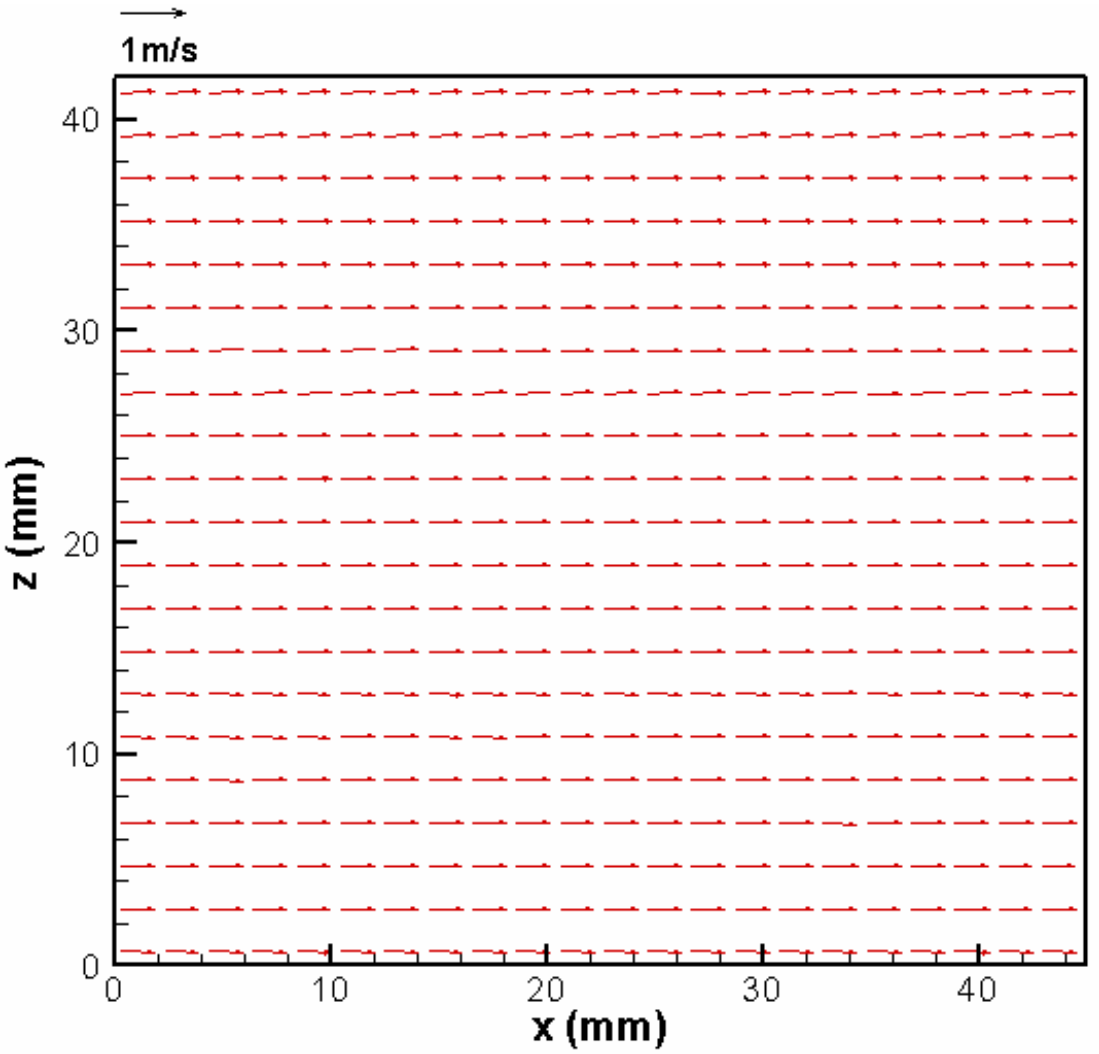

Figure 5.4: Velocity distribution for the case of $\theta = 5$ deg *ree* , Q= 1.6 L/M

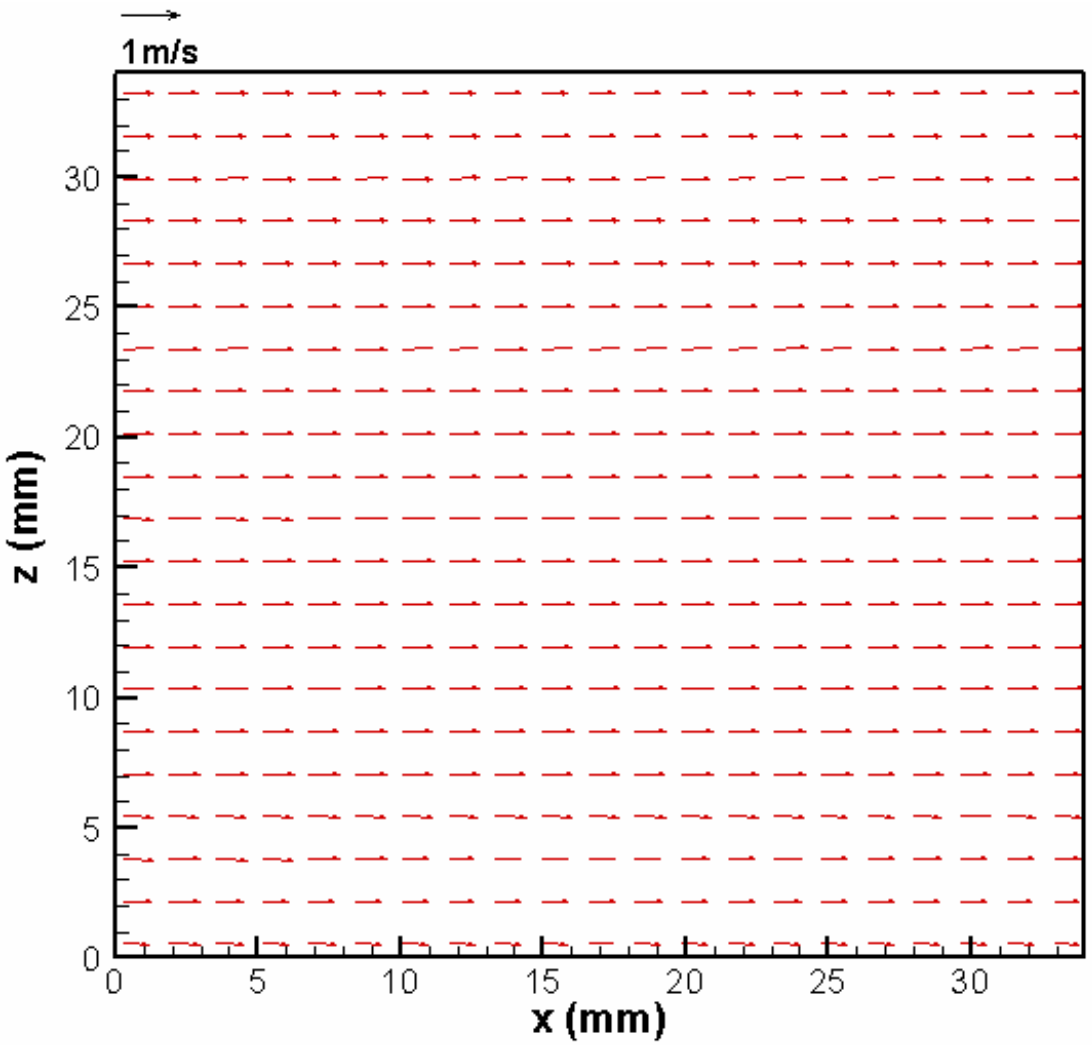

Figure 5.5: Velocity distribution for the case of $\theta = 15$ deg ree, Q= 0.8 L/M

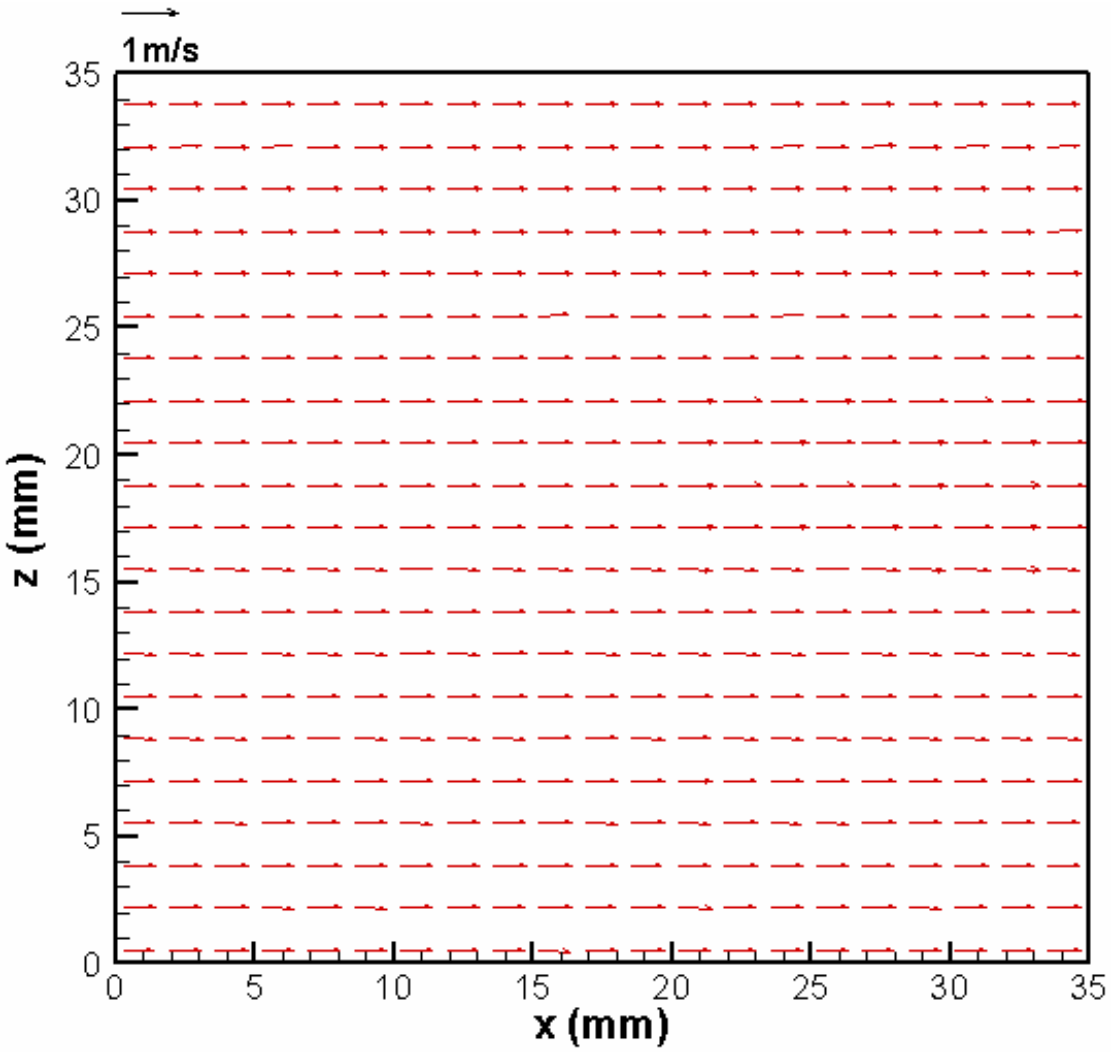

Figure 5.6: Velocity distribution for the case of $\theta = 15$ degree, Q= 1.2 L/M

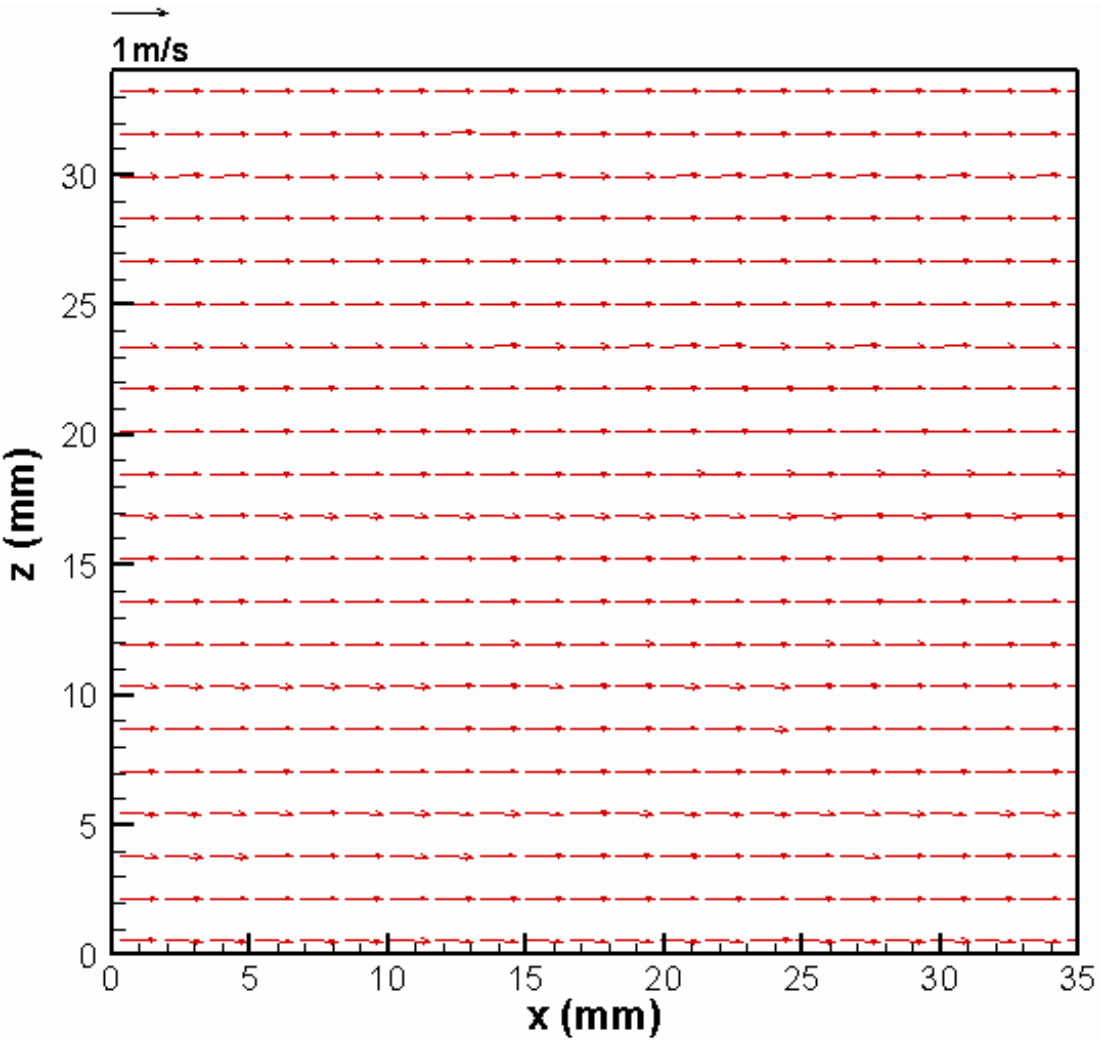

Figure 5.7: Velocity distribution for the case of $\theta = 15$ deg ree, Q= 1.6 L/M

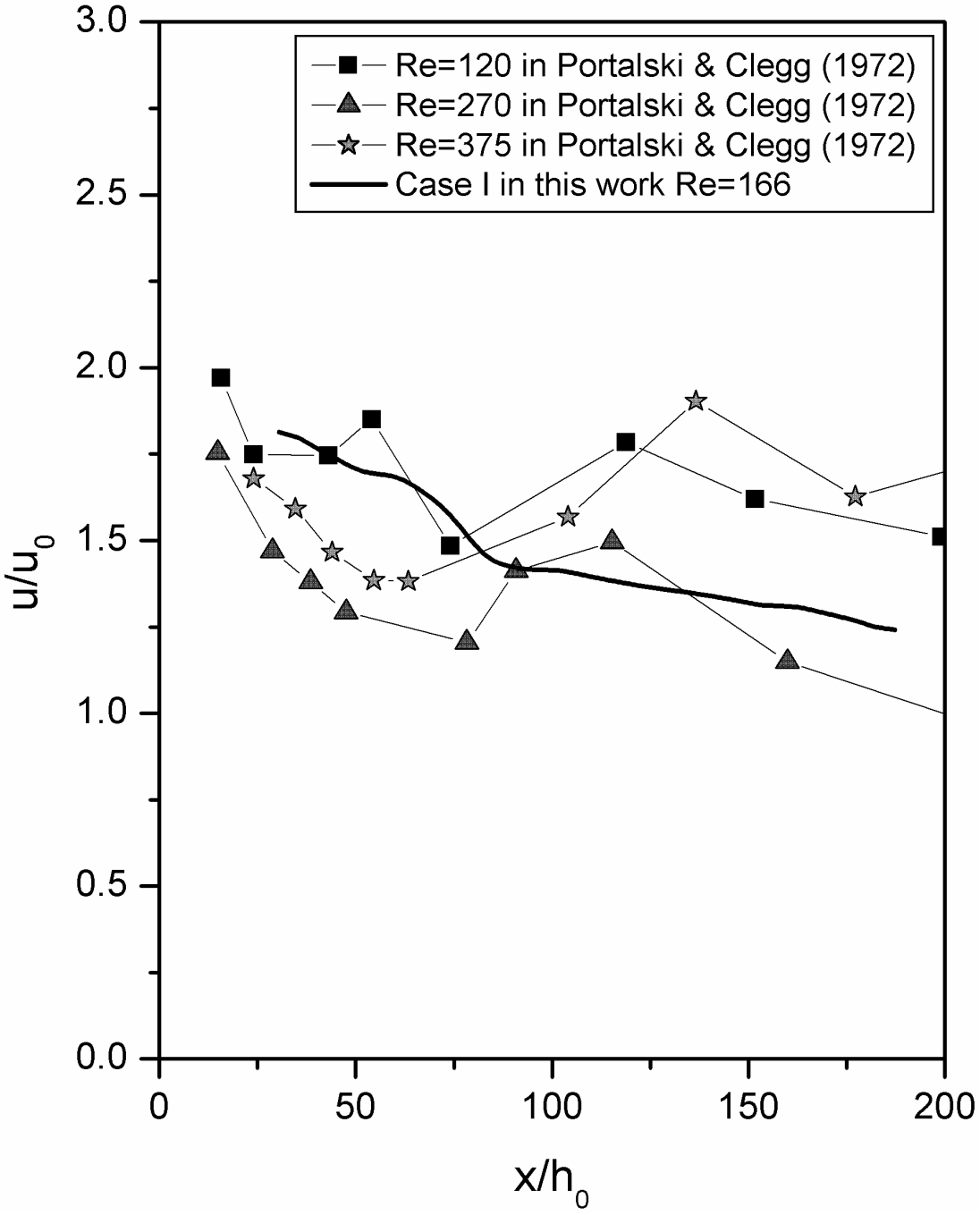

Figure 5.8: Variation of mean u/u_0 velocity with non-dimensional distance for Case I

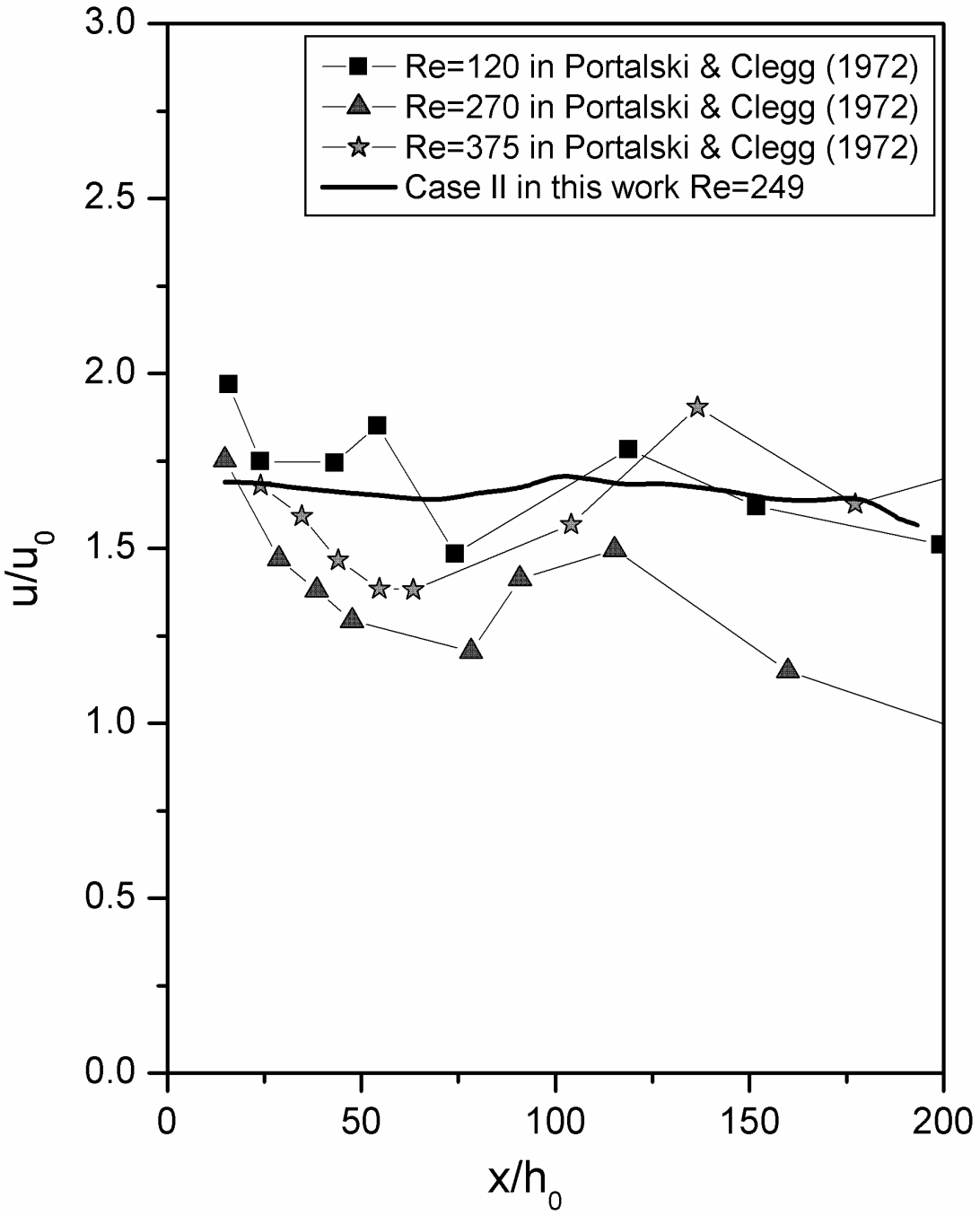

Figure 5.9: Variation of mean u/u_0 velocity with non-dimensional distance for Case II

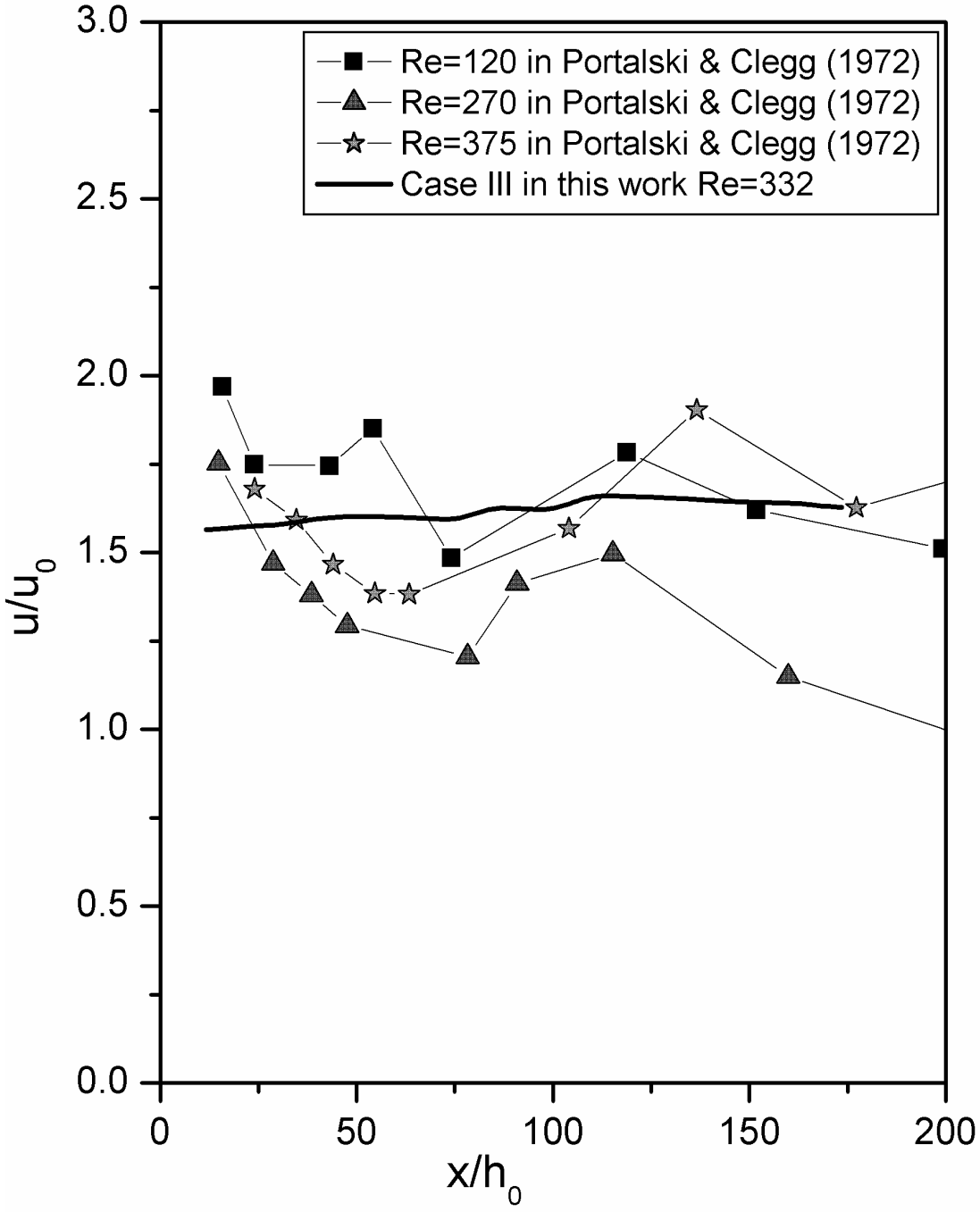

Figure 5.10: Variation of mean u/u_0 velocity with non-dimensional distance for Case III

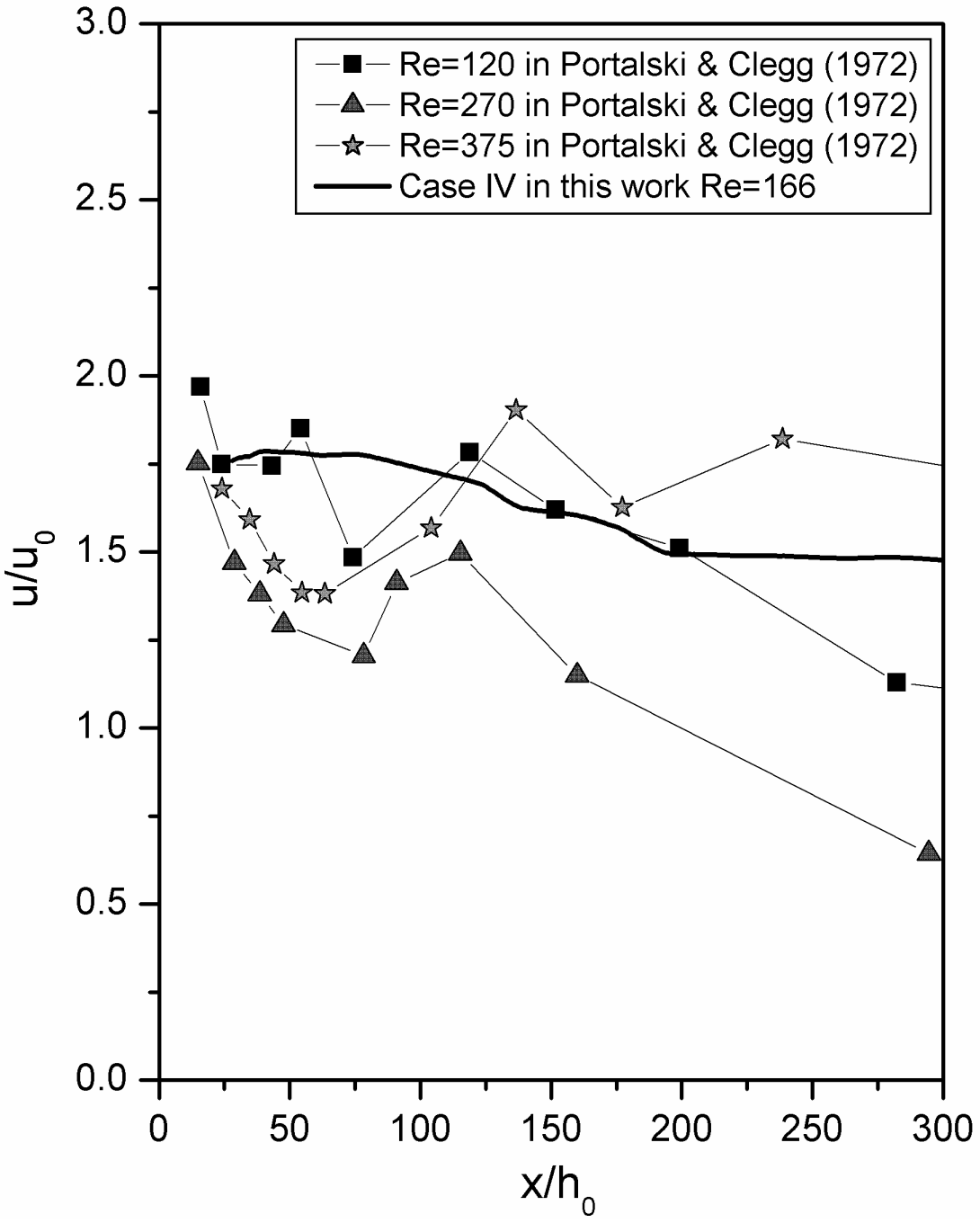

Figure 5.11 Variation of mean u/u_0 velocity with non-dimensional distance for Case IV

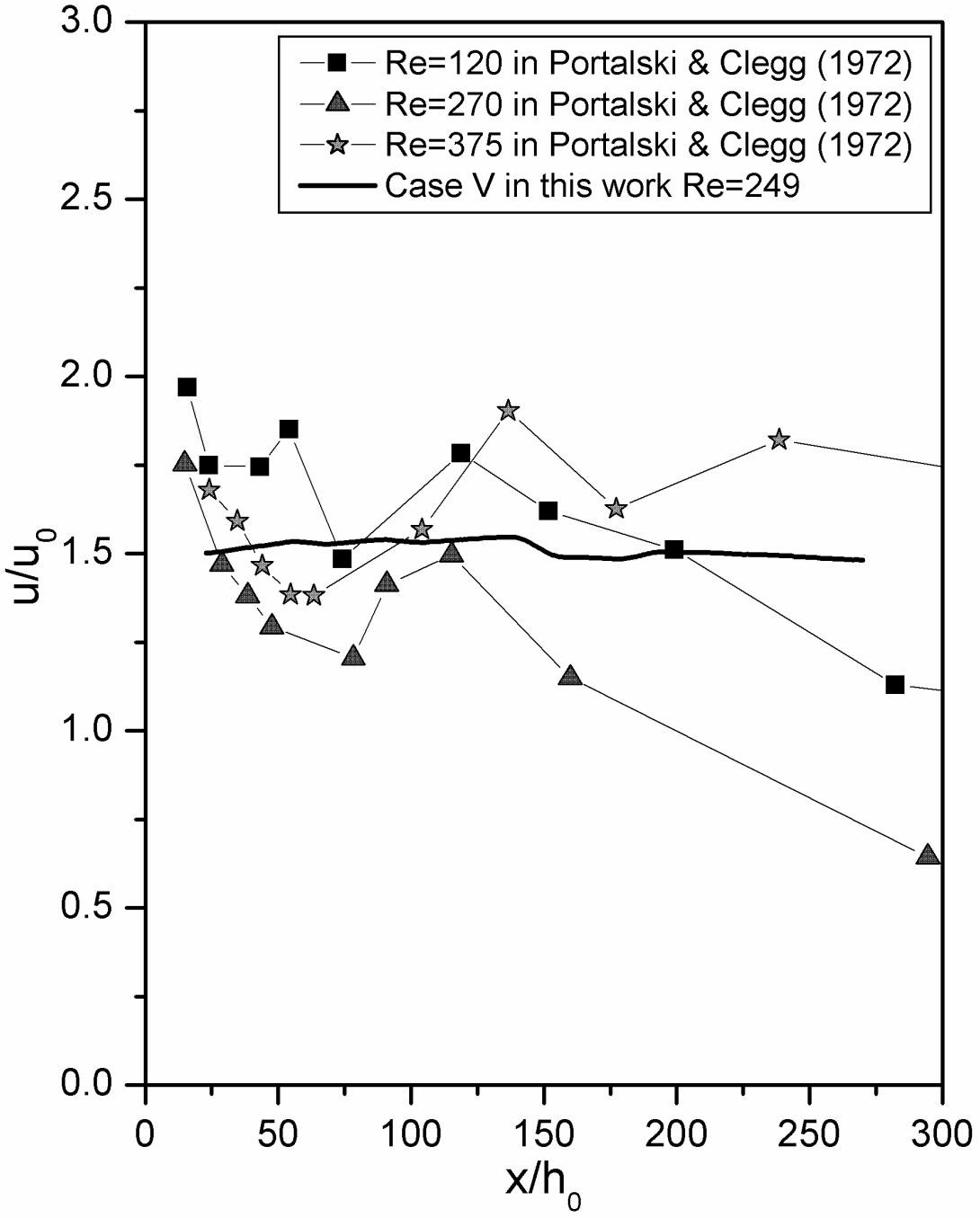

Figure 5.12: Variation of mean u/u_0 velocity with non-dimensional distance for Case V

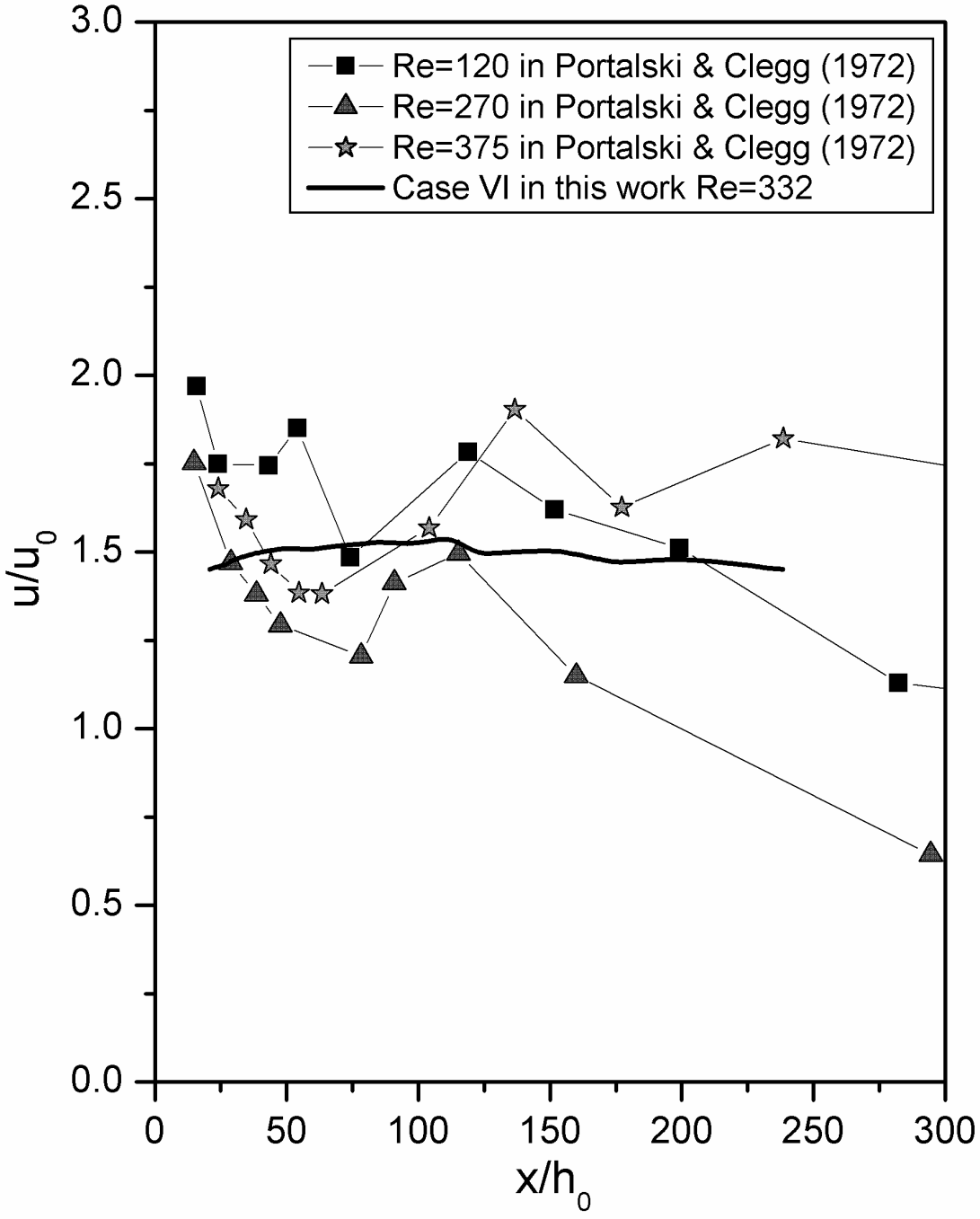

Figure 5.13: Variation of mean u/u_0 velocity with non-dimensional distance for Case VI

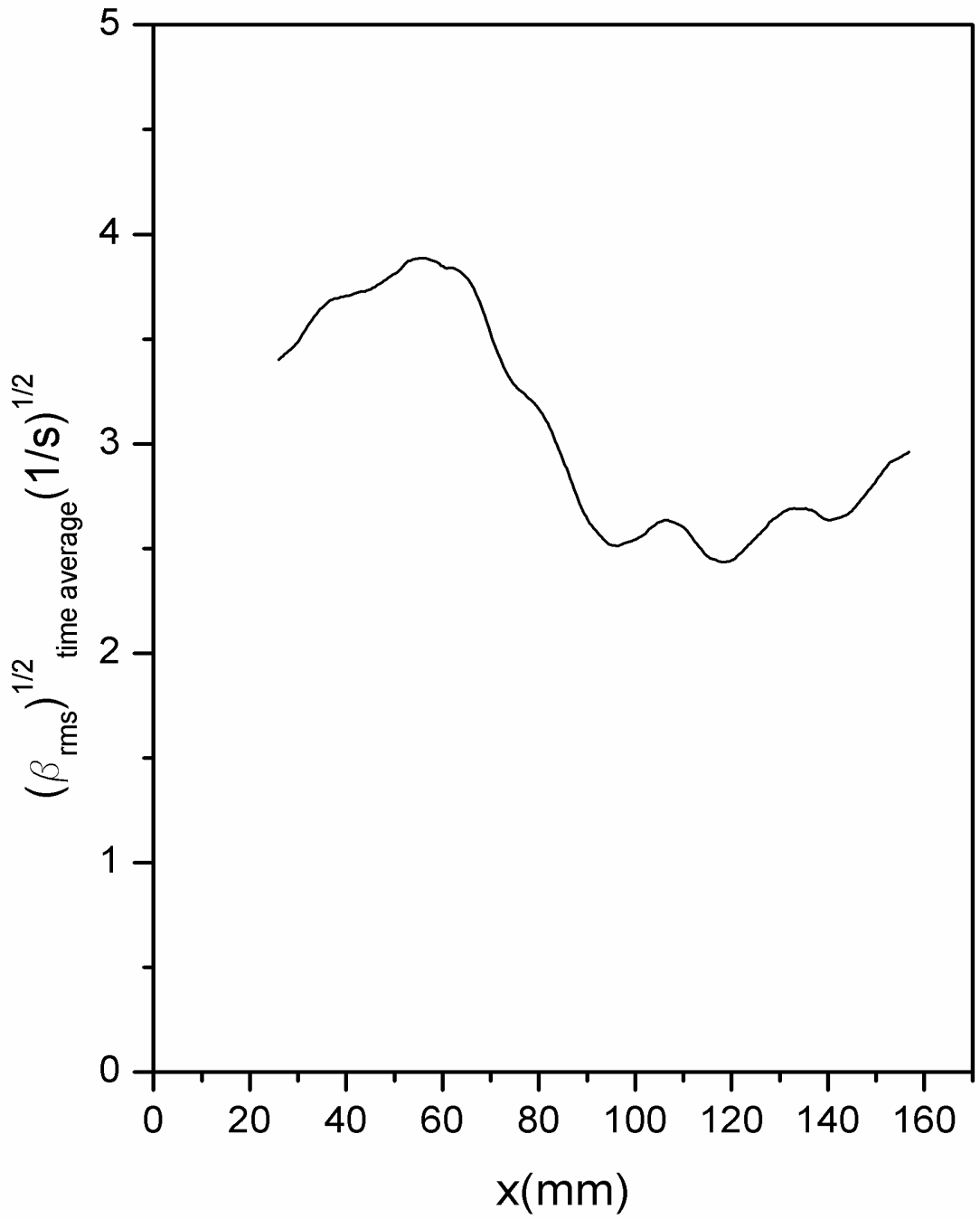

Figure 5.14: Variation of $(\beta_{rms})^{1/2}_{time\ average}$ with x- direction for Case I

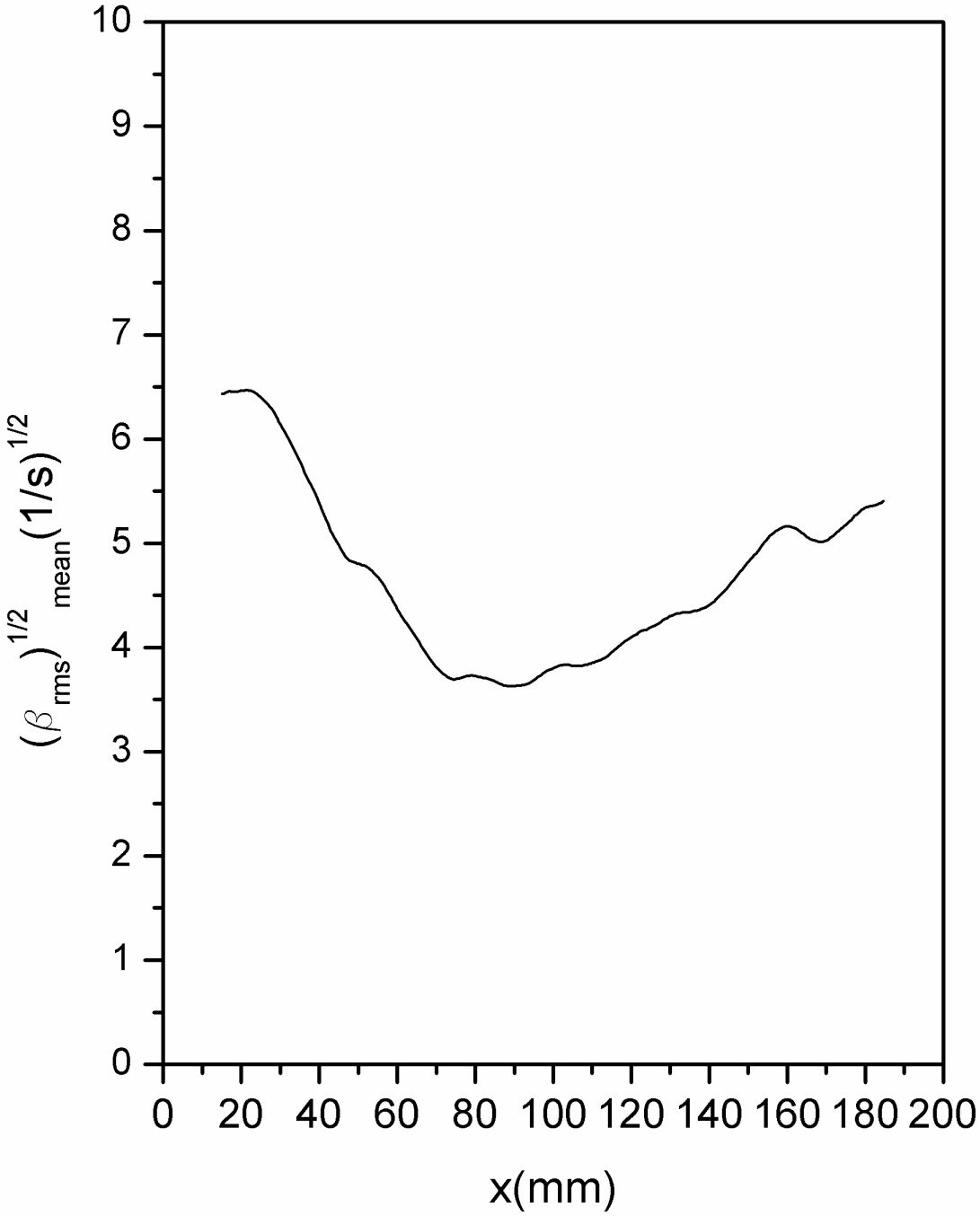

Figure 5.15: Variation of $(\beta_{rms})^{1/2}_{time\ average}$ with x- direction for Case II

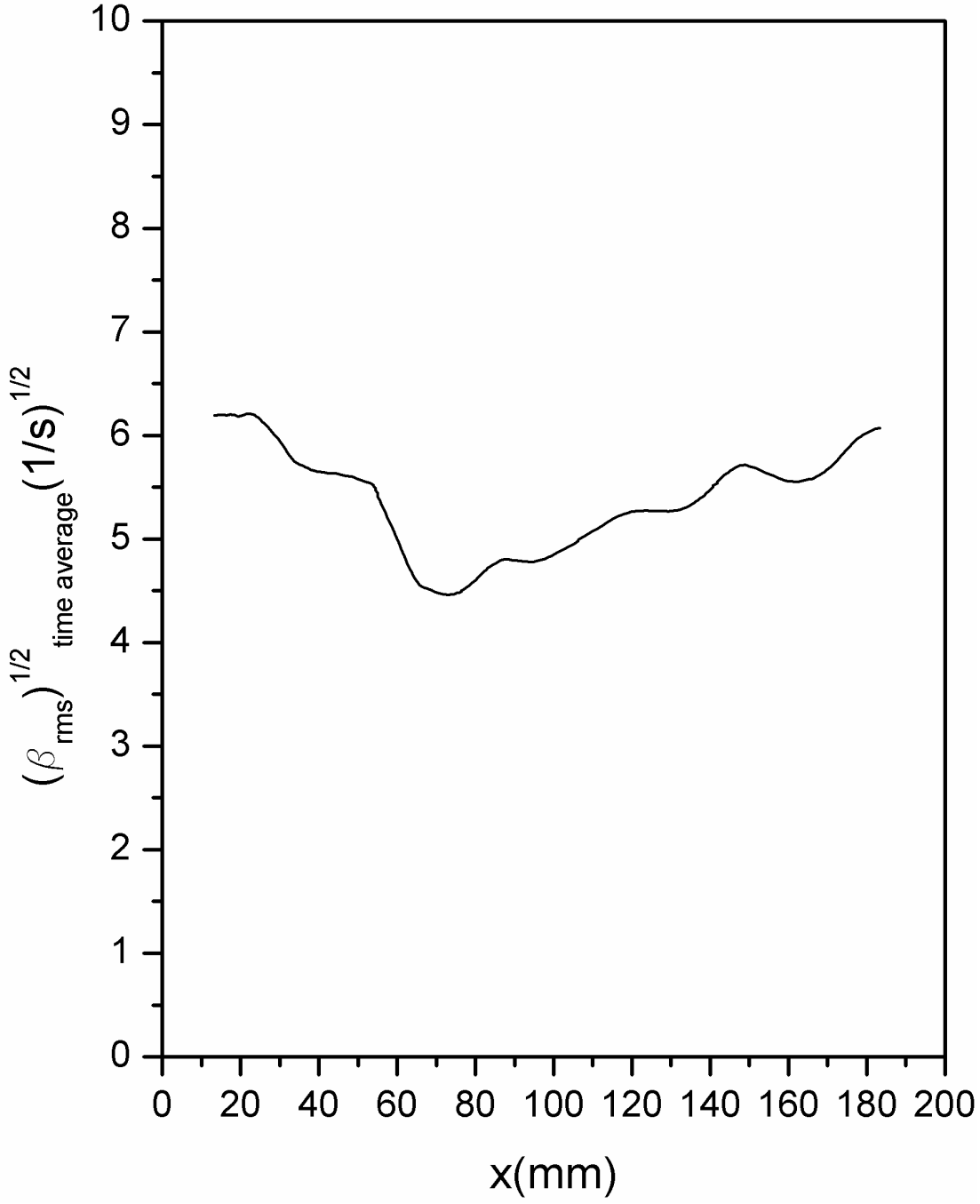

Figure 5.16: Variation of $(\beta_{rms})^{1/2}_{time\ average}$ with x- direction for Case III

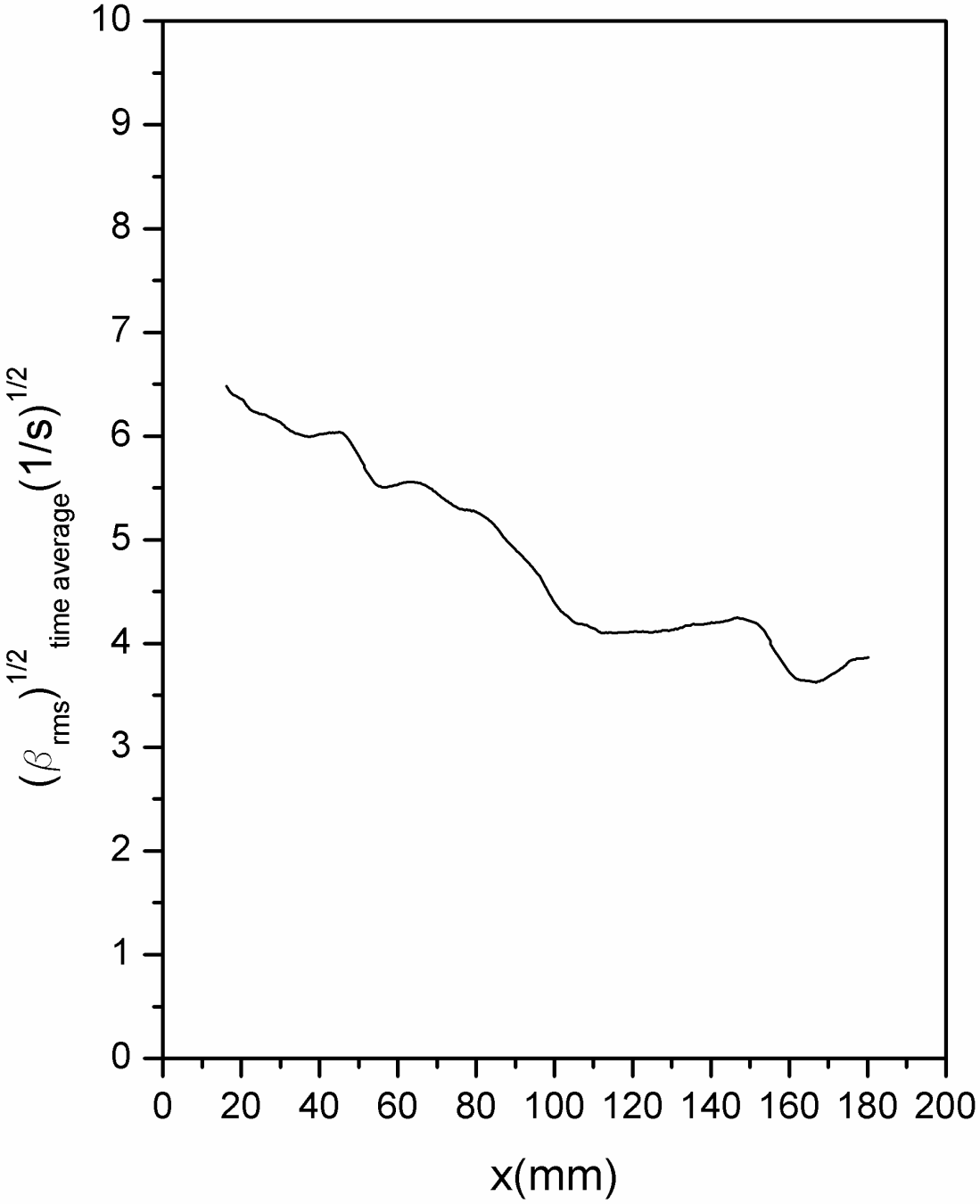

Figure 5.17: Variation of $(\beta_{rms})^{1/2}_{time\ average}$ with x- direction for Case IV

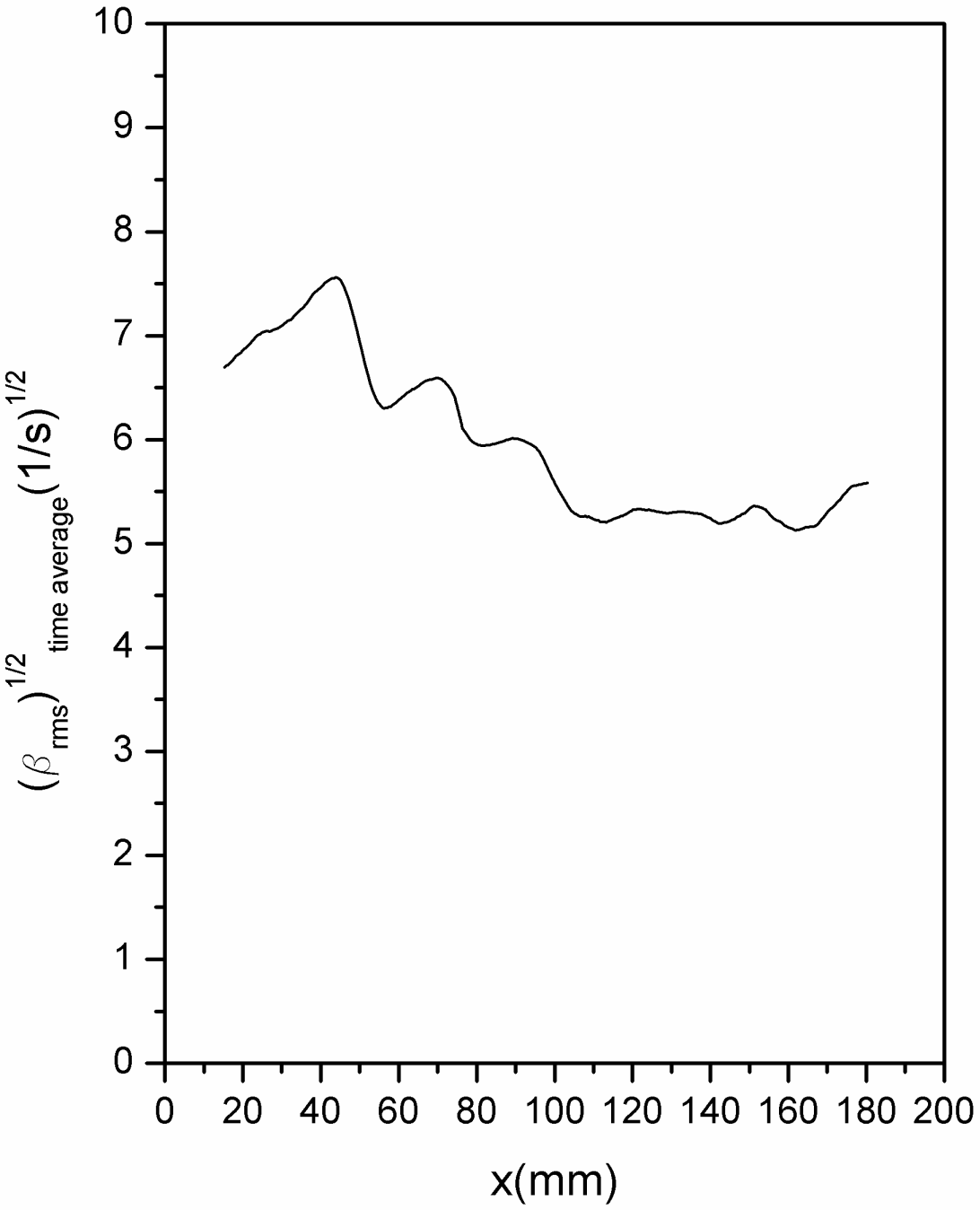

Figure 5.18: Variation of $(\beta_{rms})^{1/2}_{time\ average}$ with x- direction for Case V

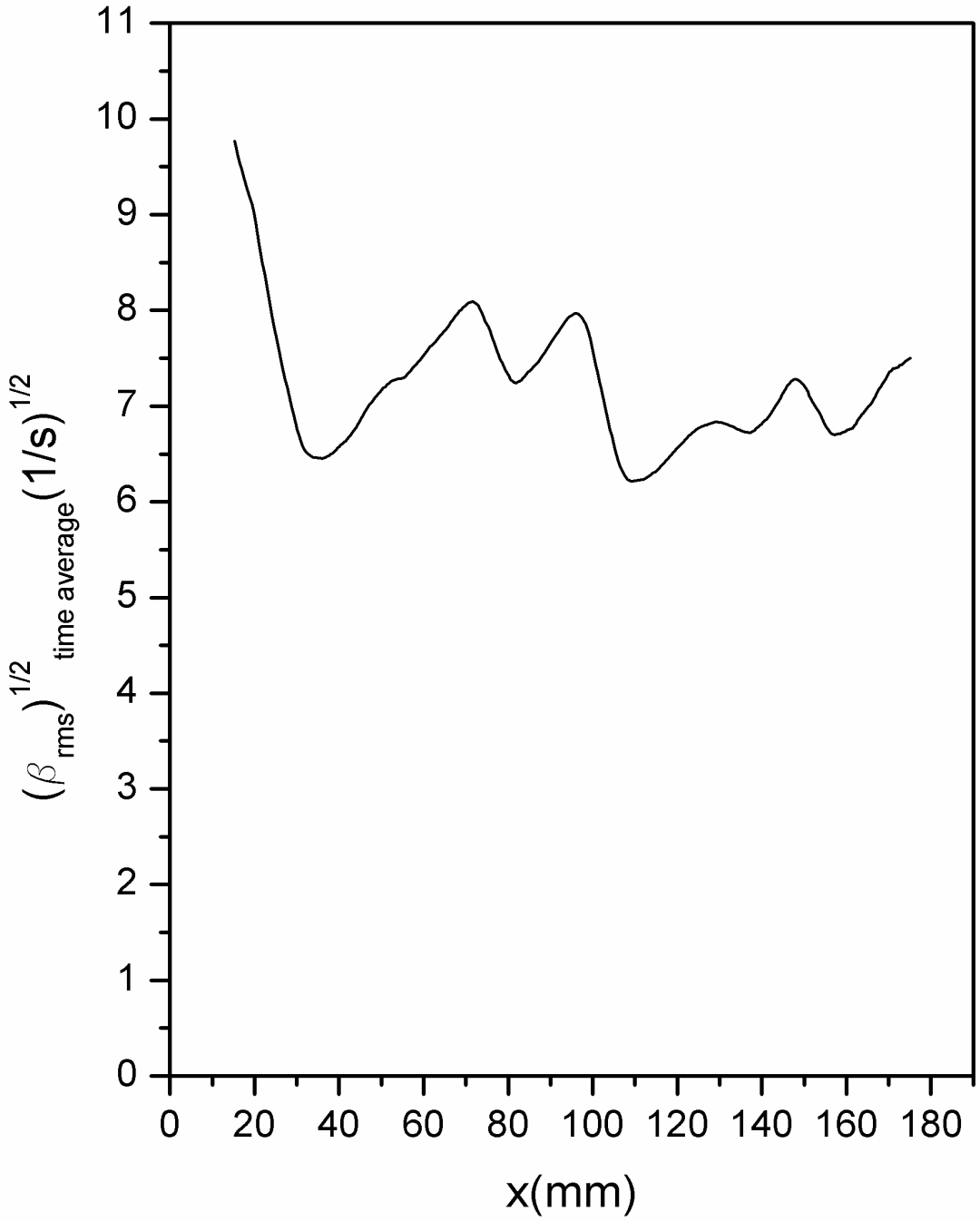

Figure 5.19: Variation of $(\beta_{rms})^{1/2}_{time\ average}$ with x- direction for Case VI

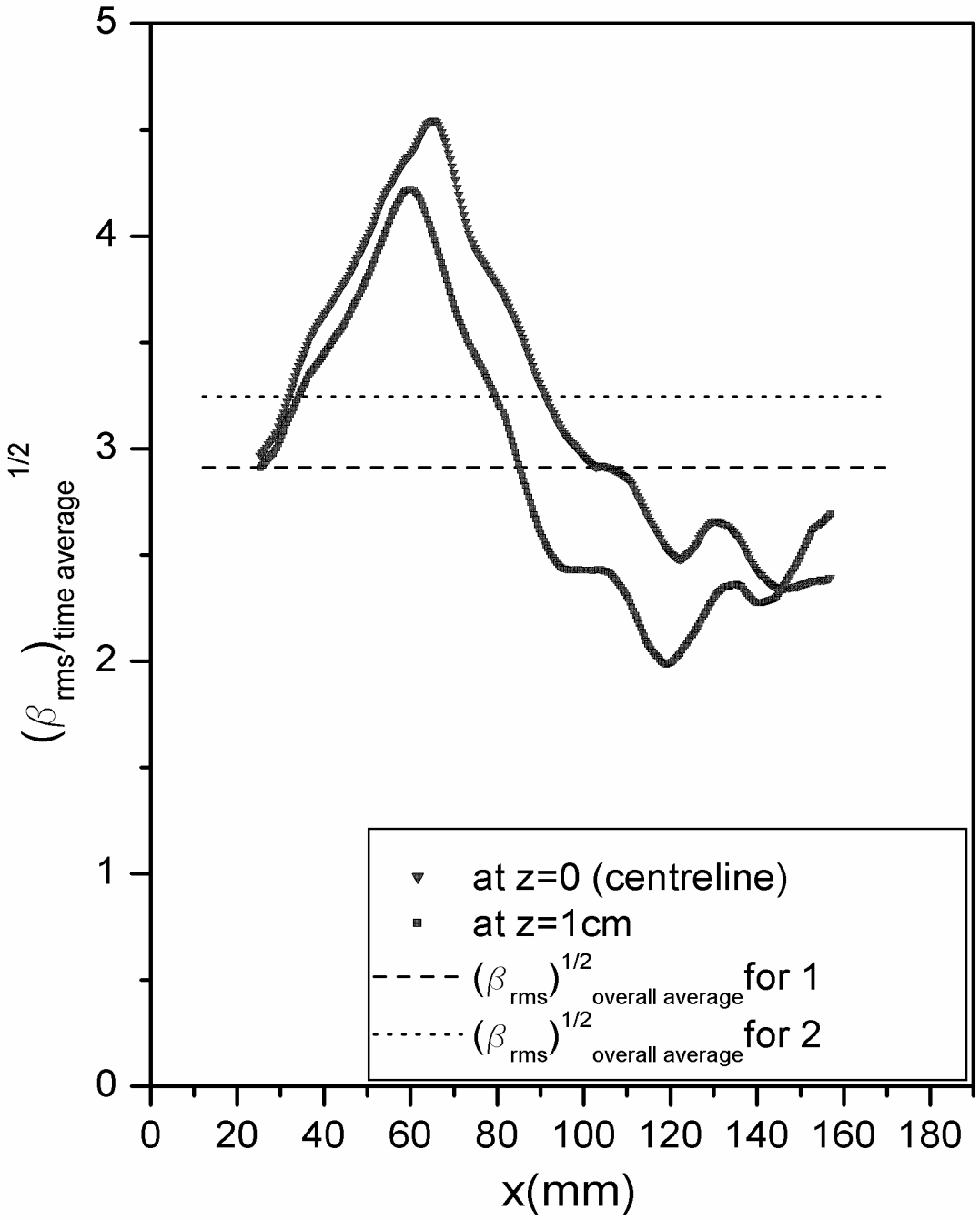

Figure 5.20: Variation of $(\beta_{rms})^{1/2}_{time\ average}$ in both x- and z- direction and $(\beta_{rms})^{1/2}_{overall\ average}$

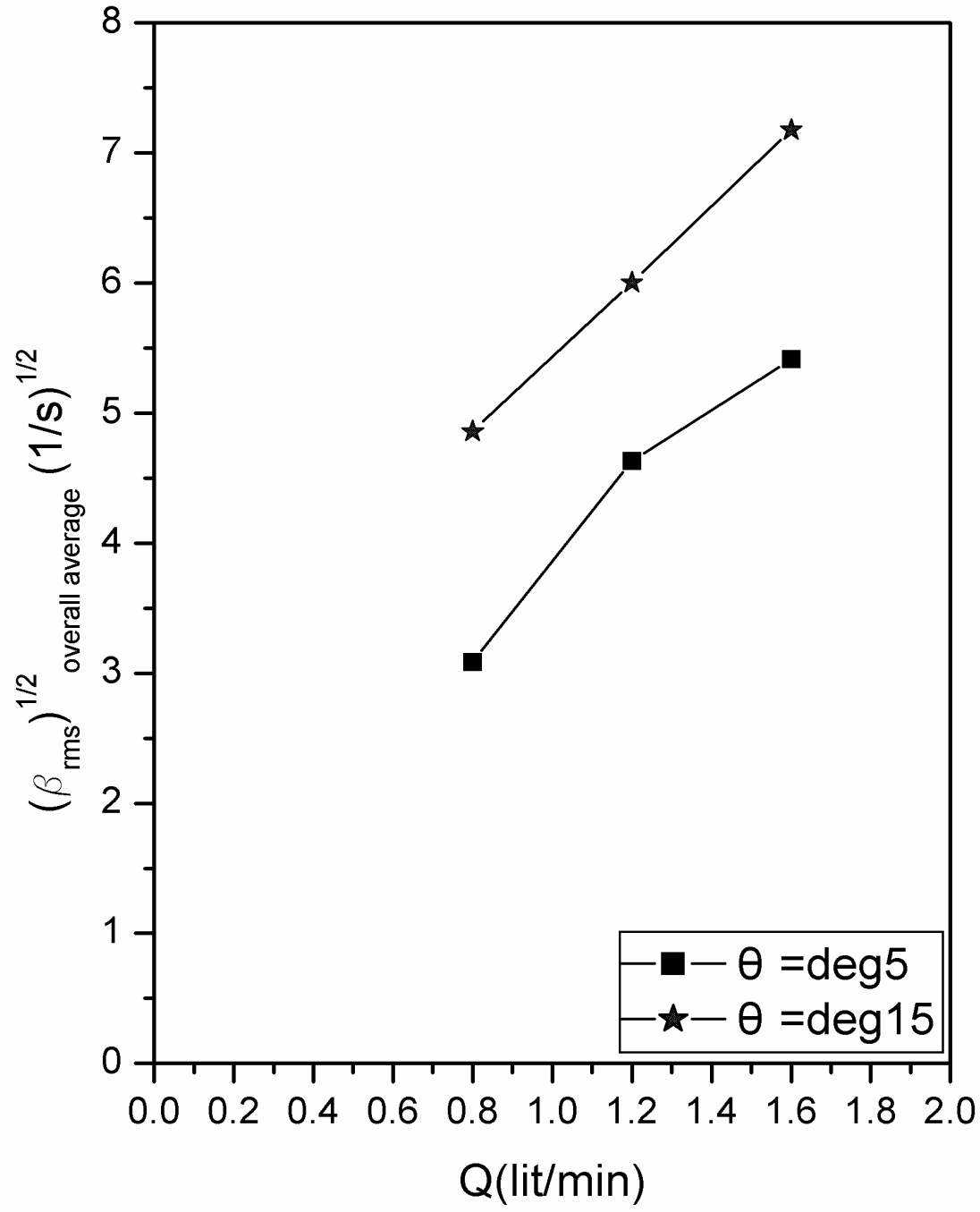

Figure 5.21: Variation of $(\beta_{rms})^{1/2}_{overall\ average}$ with flow rate Q down the inclined plane at angle θ

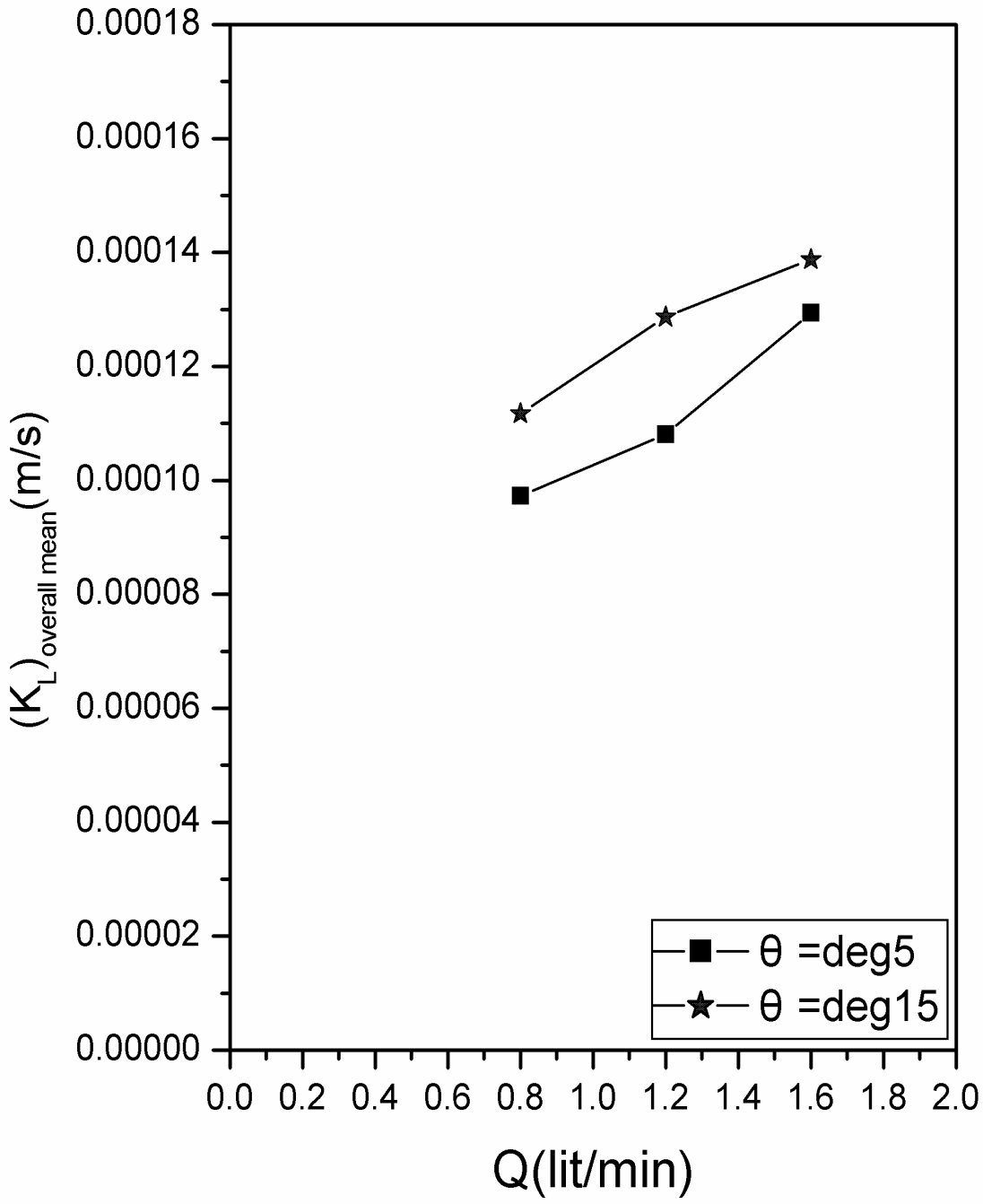

Figure 5.22: Variation of mean mass transfer velocity with flow rate Q down the inclined plane at angle θ

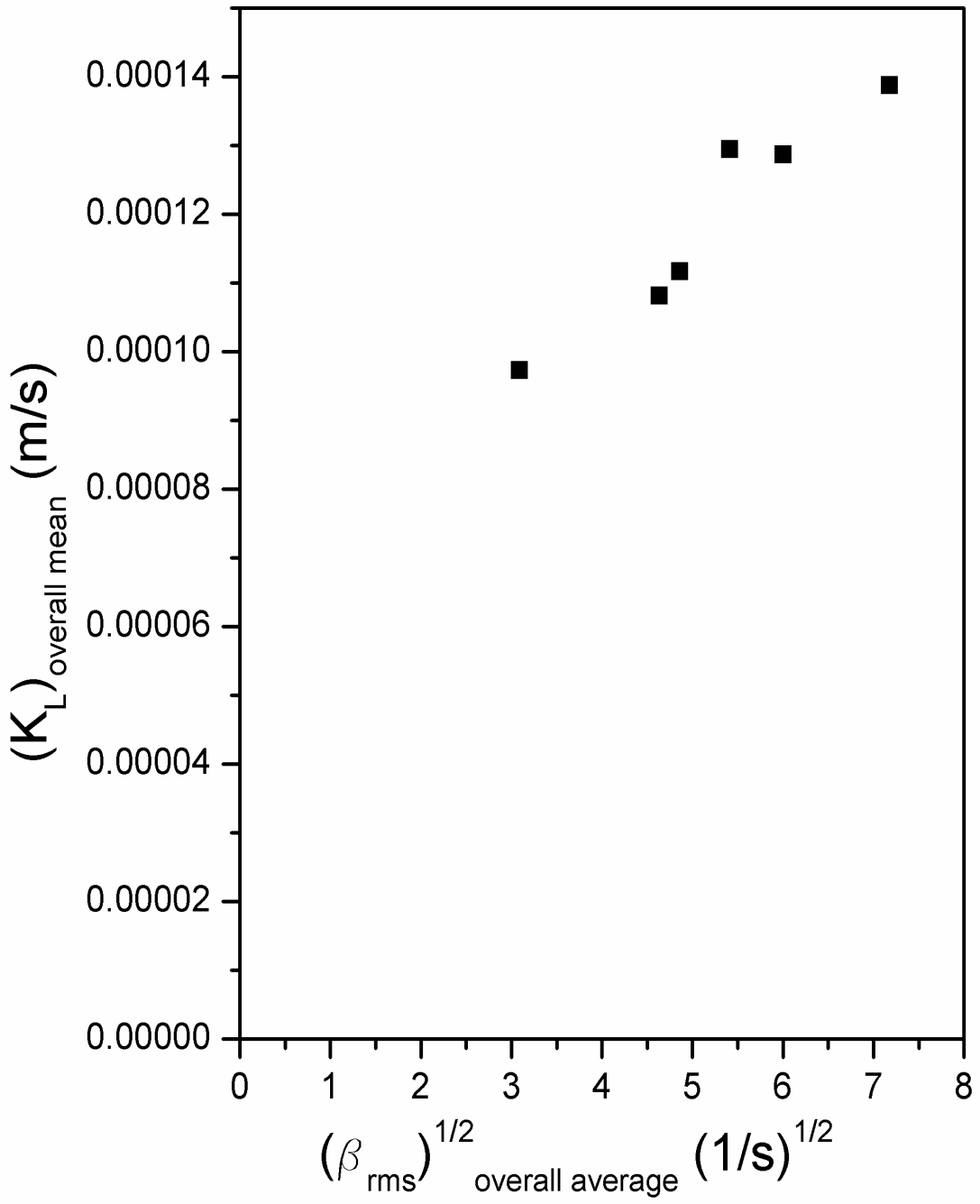

Figure 5.23: Variation of mean mass transfer velocity with $(\beta_{rms})^{1/2}_{overall\ average}$

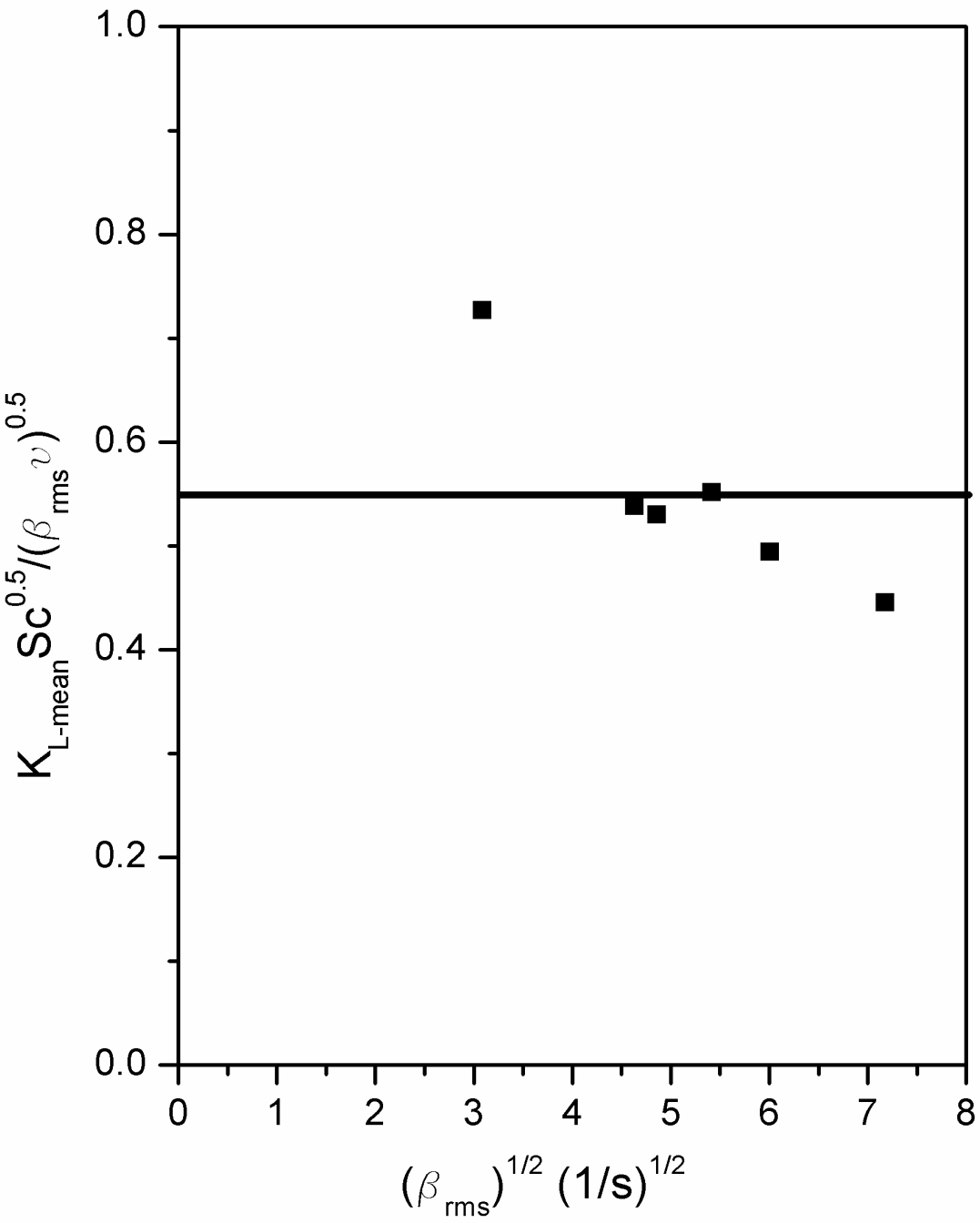

Figure 5.24: $K_{L-mean}Sc^{0.5}/(\beta_{rms}\upsilon)^{0.5}$ vs. $(\beta_{rms})^{1/2}$

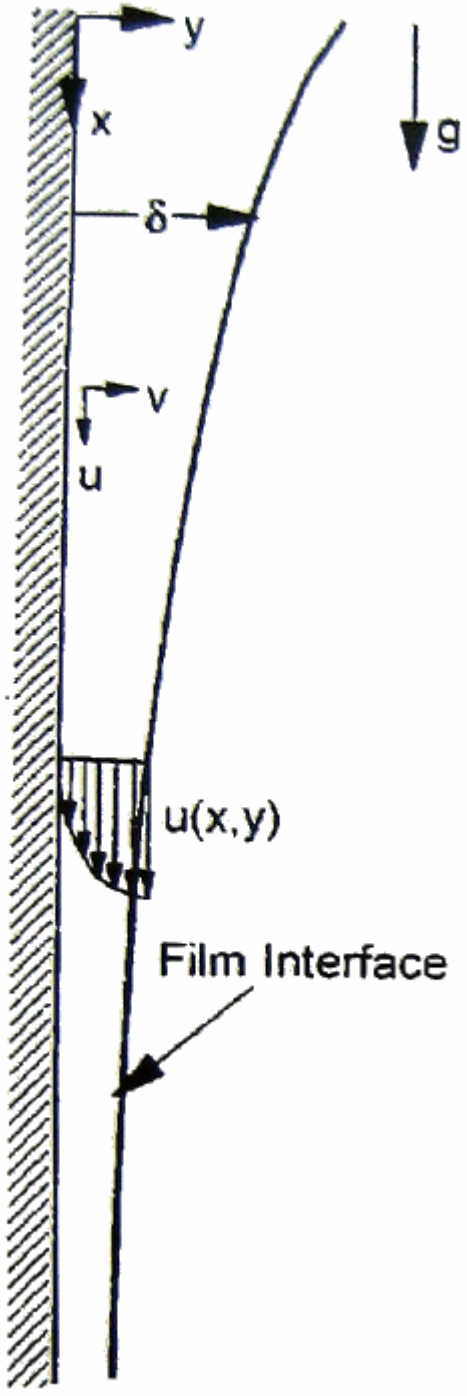

Figure 6.1: Cartesian coordinate system for laminar falling film (two dimensional)

(adopted from Miller's thesis (1992))

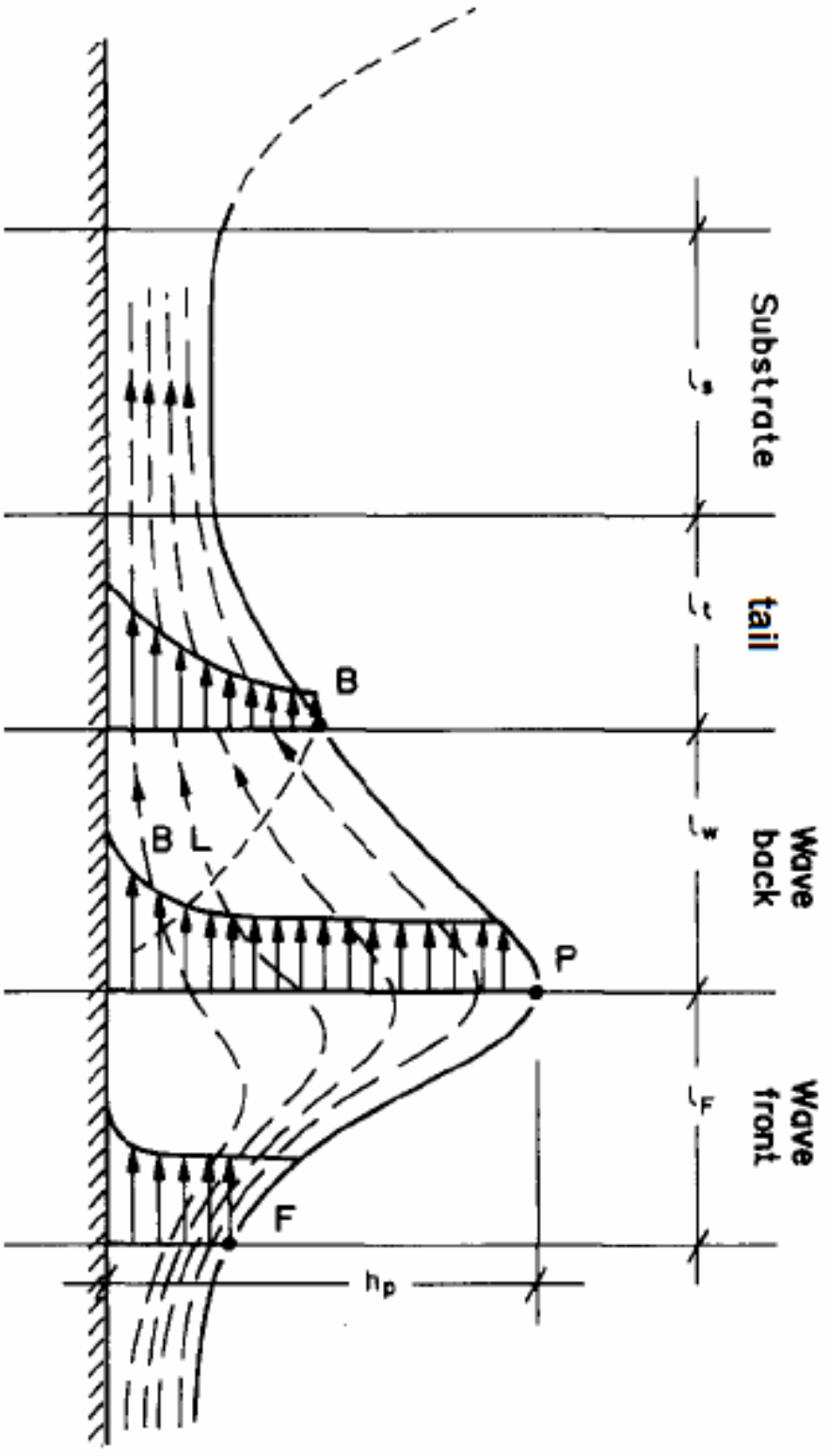

Figure 6.2: The wave segment in Brauner & Maron (1983) and Maron et al. (1985) (adopted from Brauner (1989))

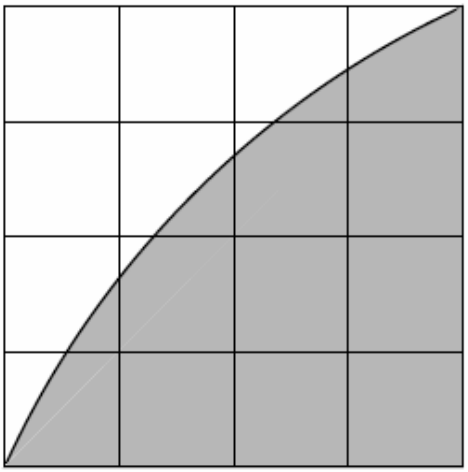

actual interface shape

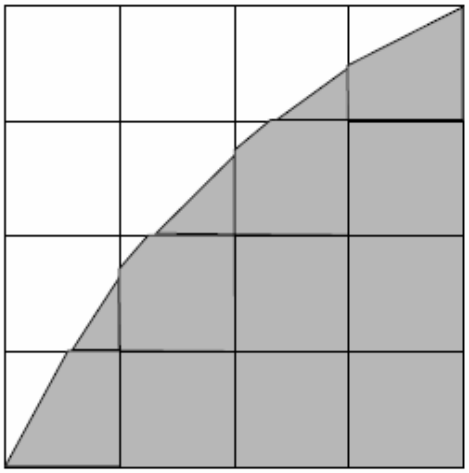

interface shape represented by the geometric reconstruction (piecewise-linear) scheme

Figure 6.3: Interface reconstruction

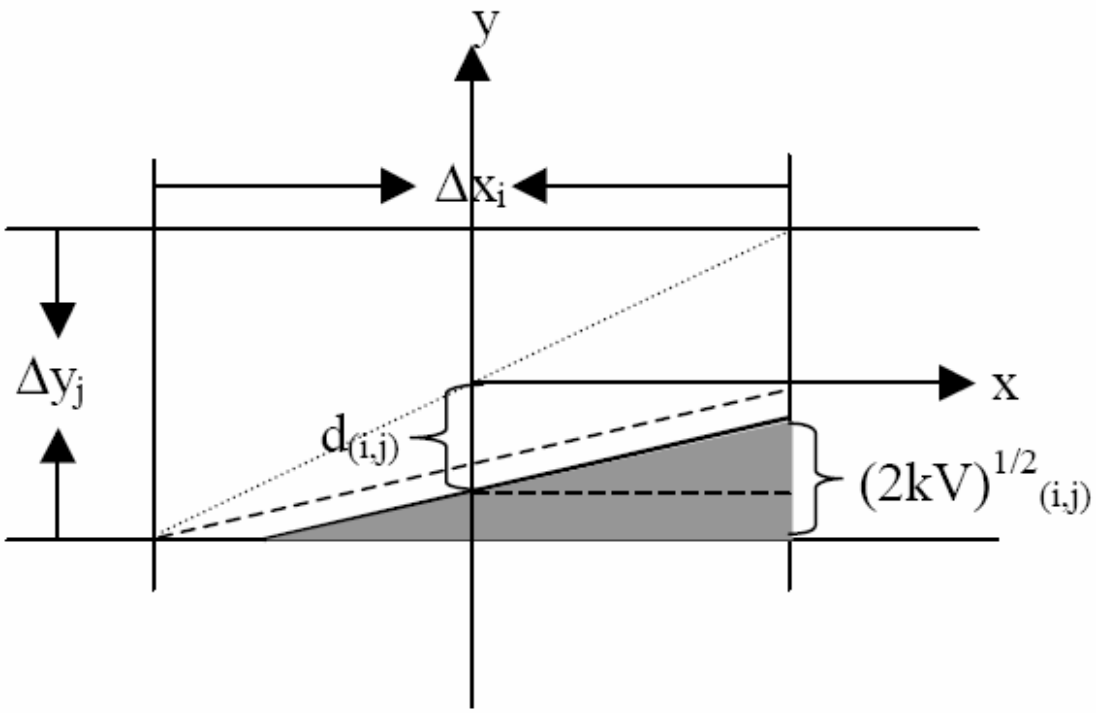

Figure 6.4: An example for interface position determination.
The dark region denotes the volume occupied by water

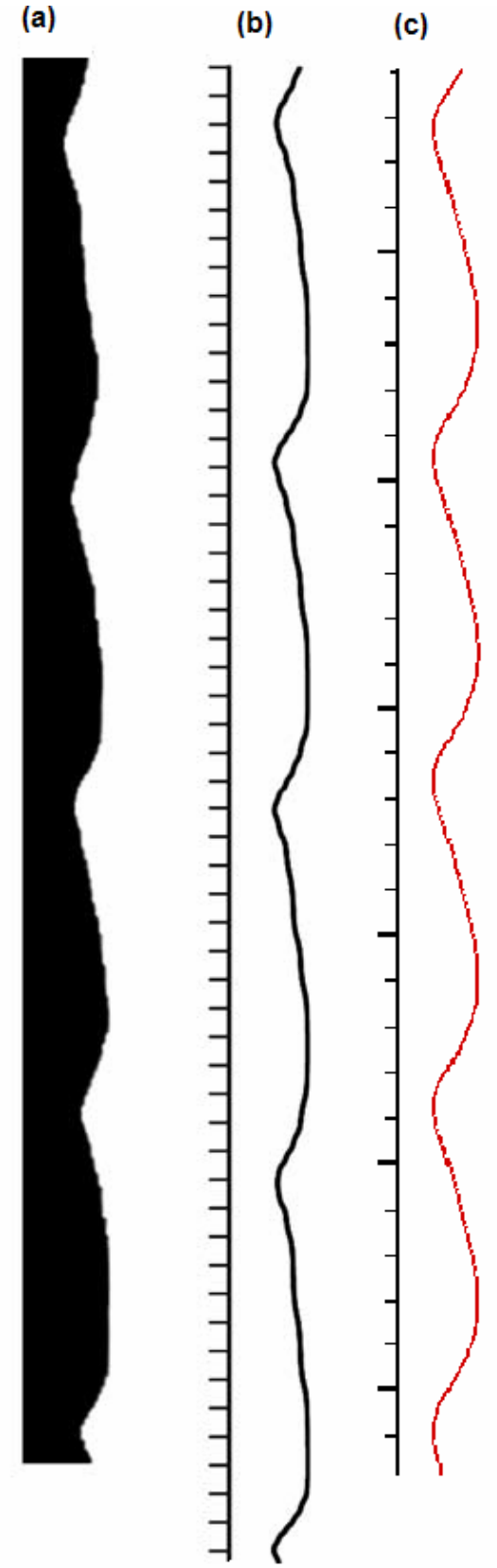

Figure 6.5: Wave shape comparison: (a) Kapitza's shadowgraph; (b) calculated results from Gao et al. (2003); (c) simulated results in this work

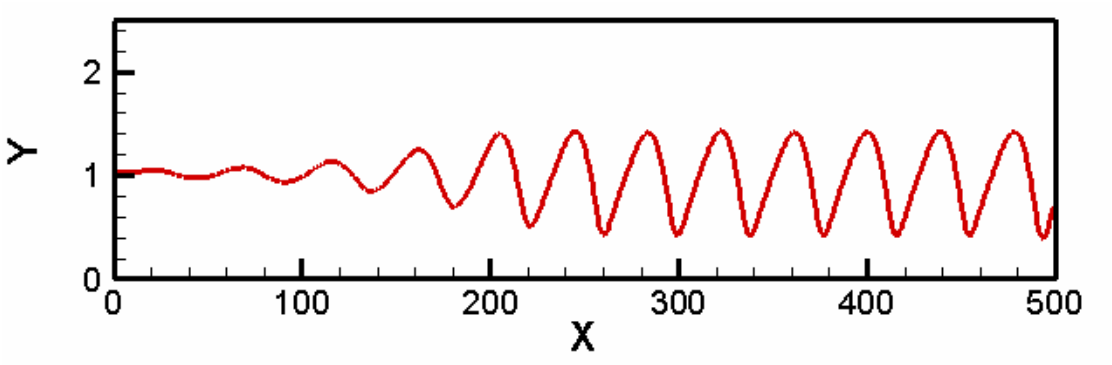

(a) Wave evolution for Case A

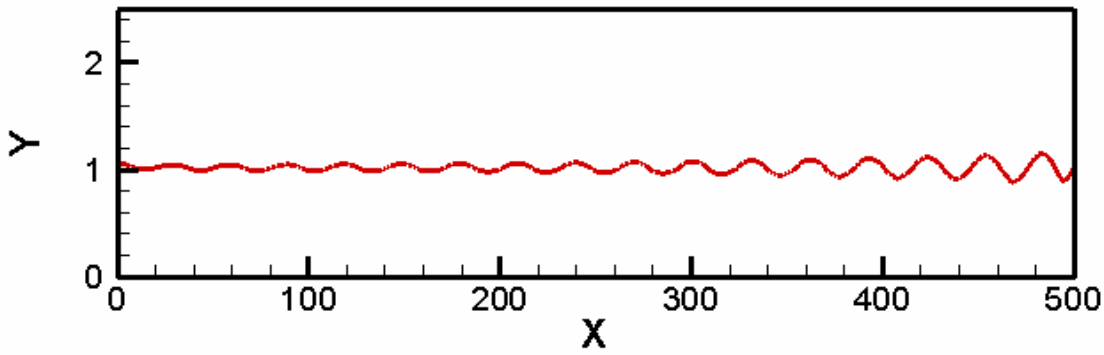

(b) Wave evolution for Case B

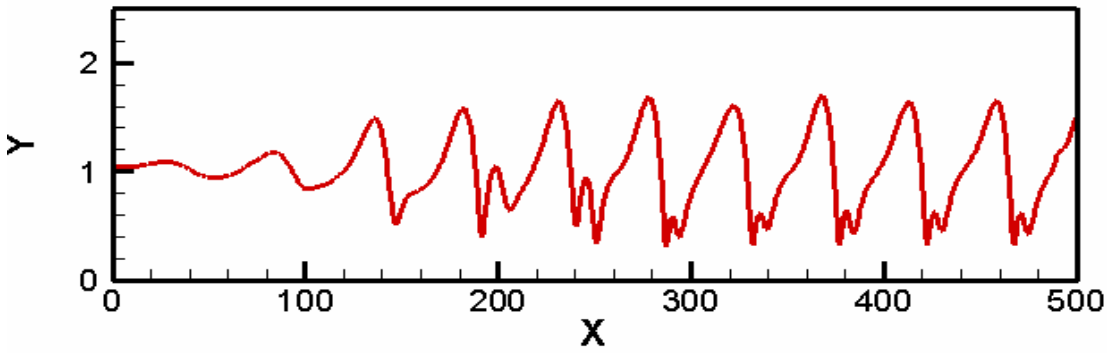

(c) Wave evolution for Case C

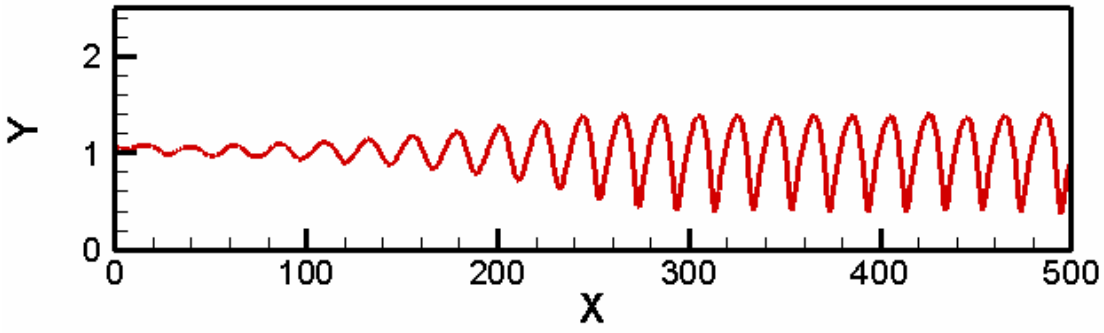

(d) Wave evolution for Case D

Figure 6.6: Wave evolution with distance

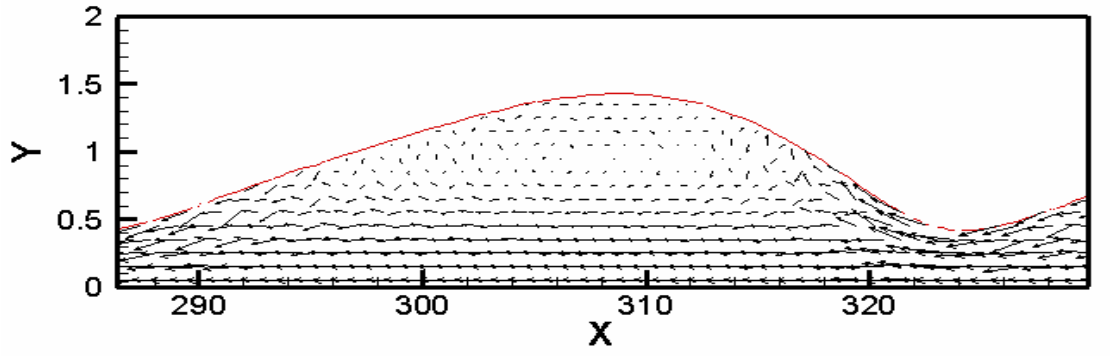

(a) Velocity vector at the wave-phase moving coordinate for Case A

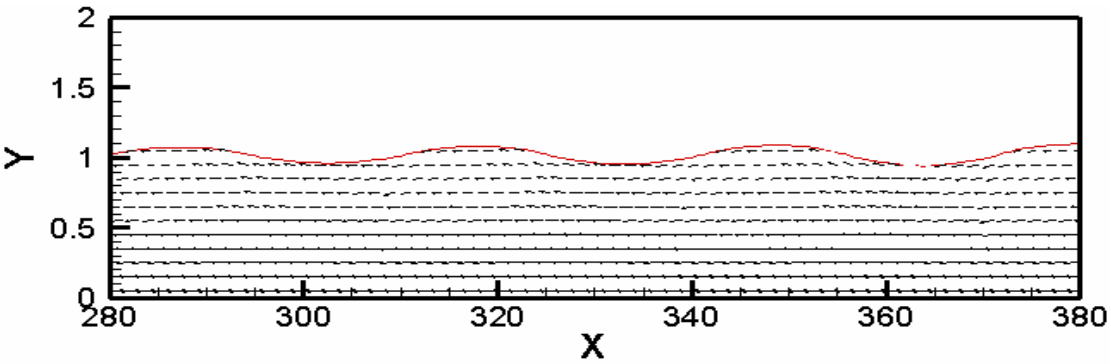

(b) Velocity vector at the wave-phase moving coordinate for Case B

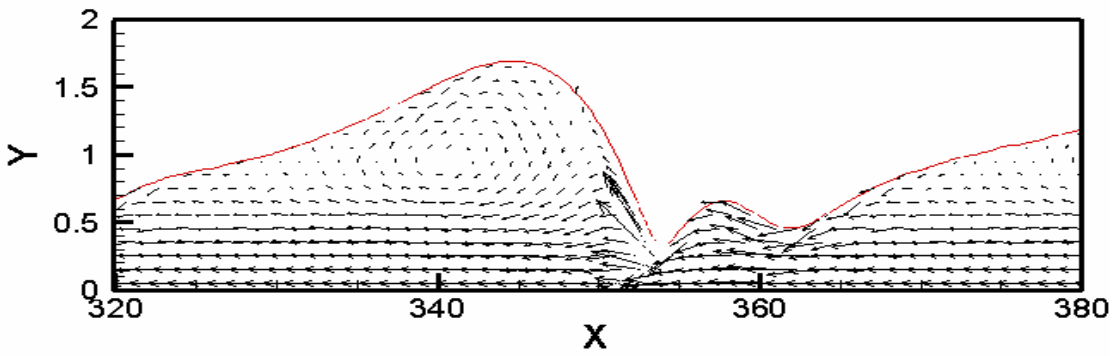

(c) Velocity vector at the wave-phase moving coordinate for Case C

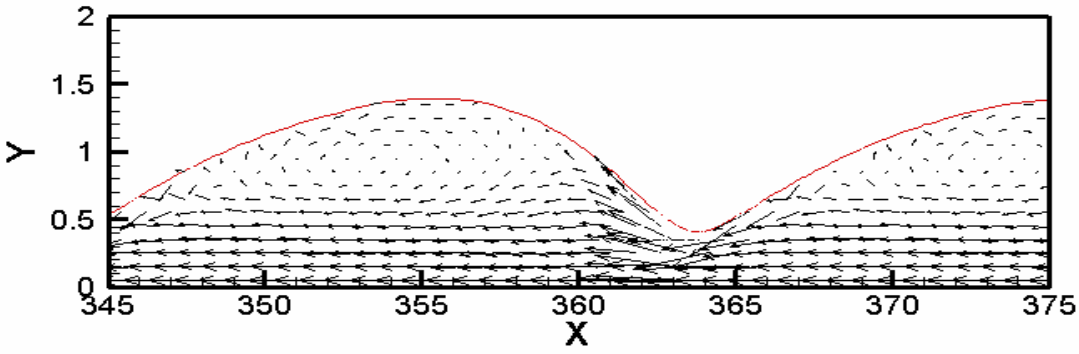

(d) Velocity vector at the wave-phase moving coordinate for Case D

Figure 6.7: Vector plots at the wave-phase moving coordinates

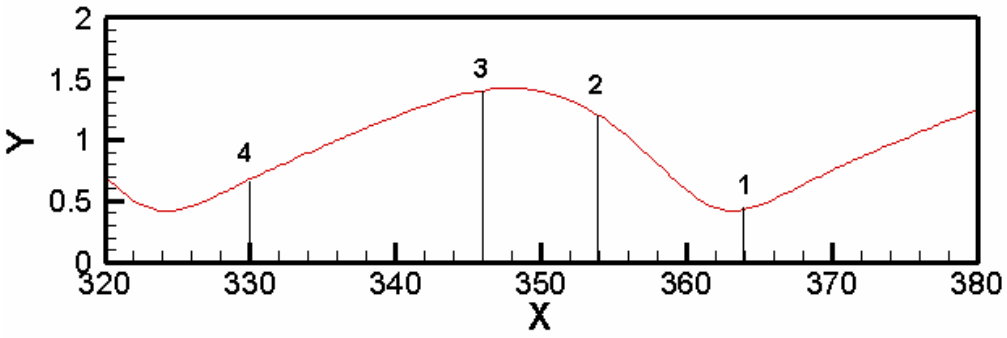

(a) Taken points along the wave

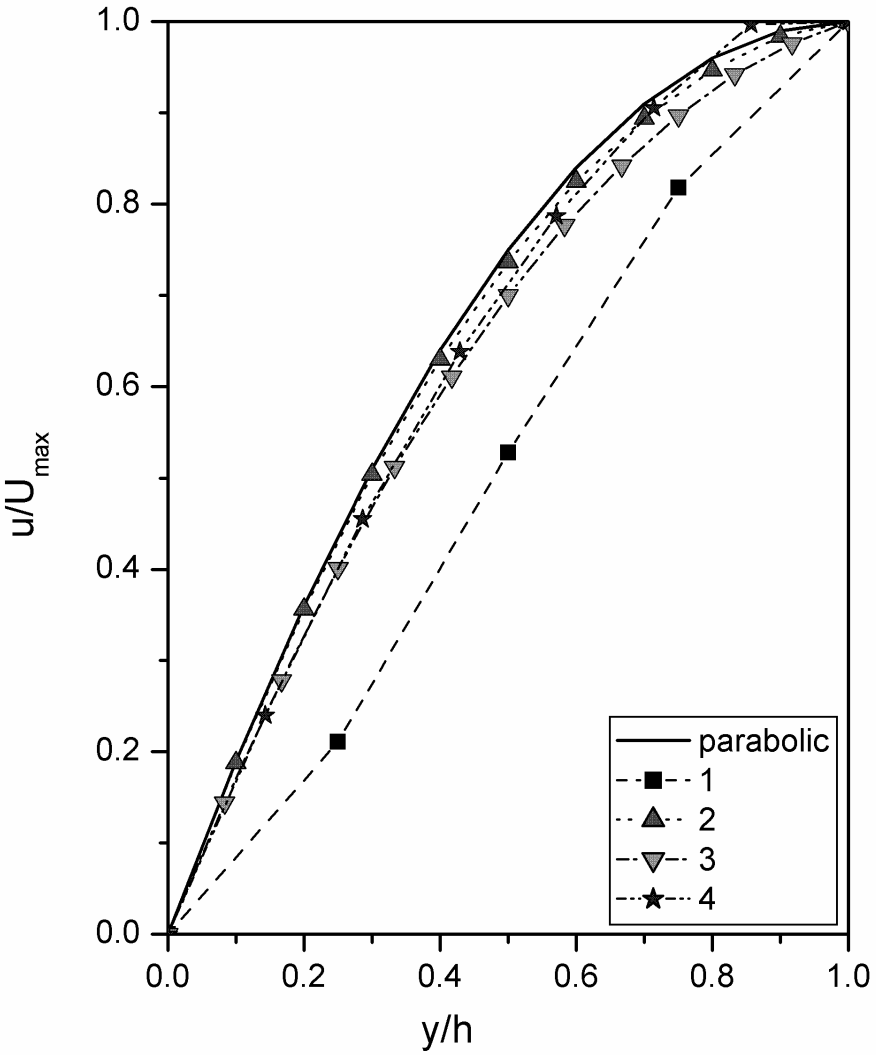

(b) Streamwise velocity profiles in the normal direction for Case A

Figure 6.8: Velocity profiles along the wave for Case A

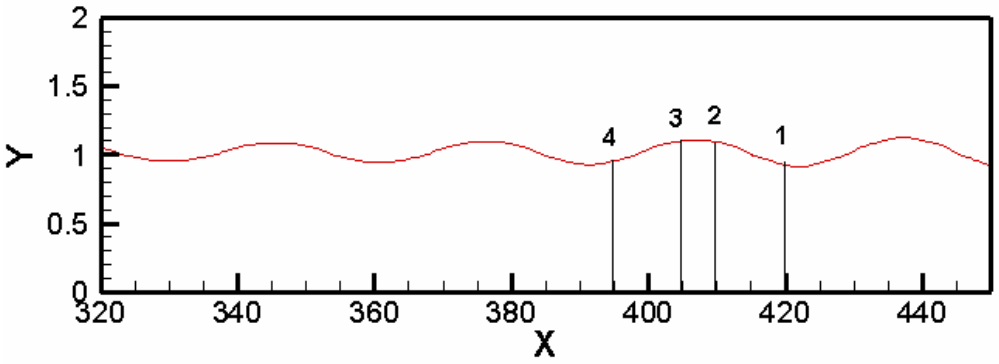

(a) Taken points along the wave

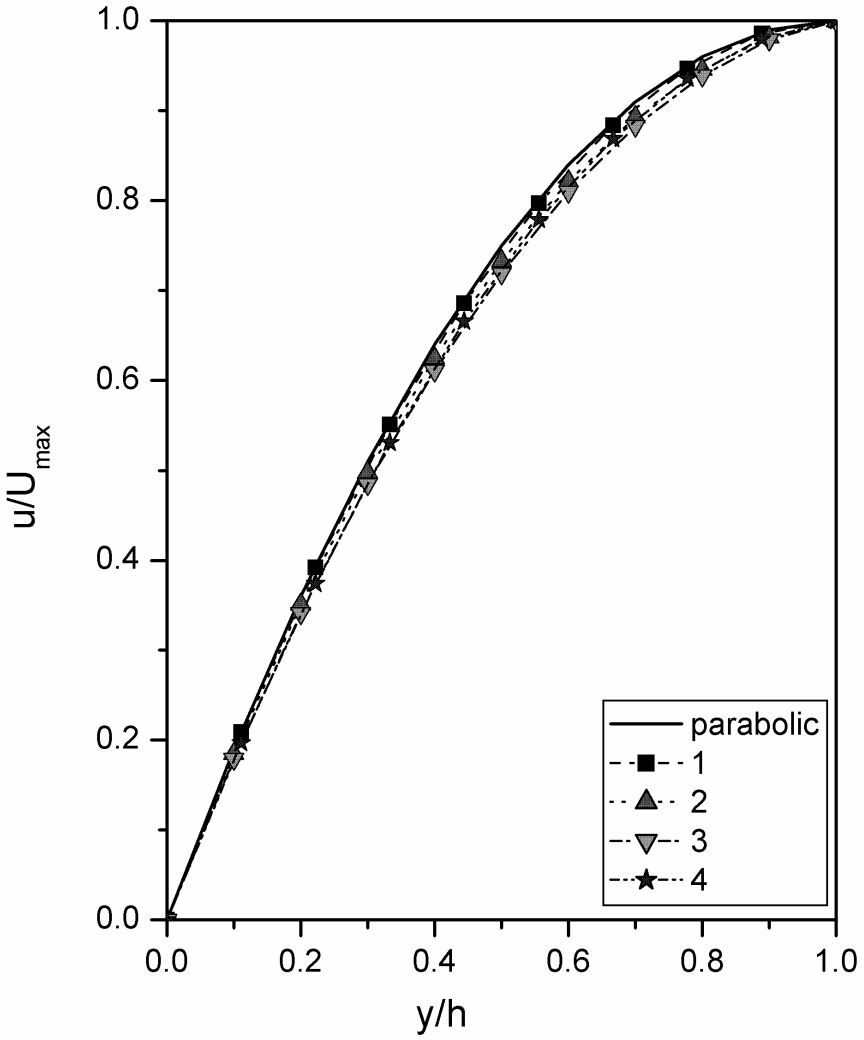

(b) Streamwise velocity profiles in the normal direction for Case B

Figure 6.9: Velocity profiles along the wave for Case B

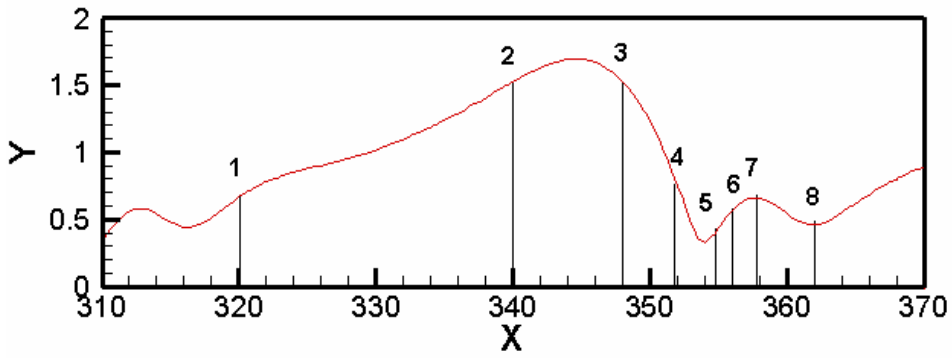

(a) Taken points along the wave

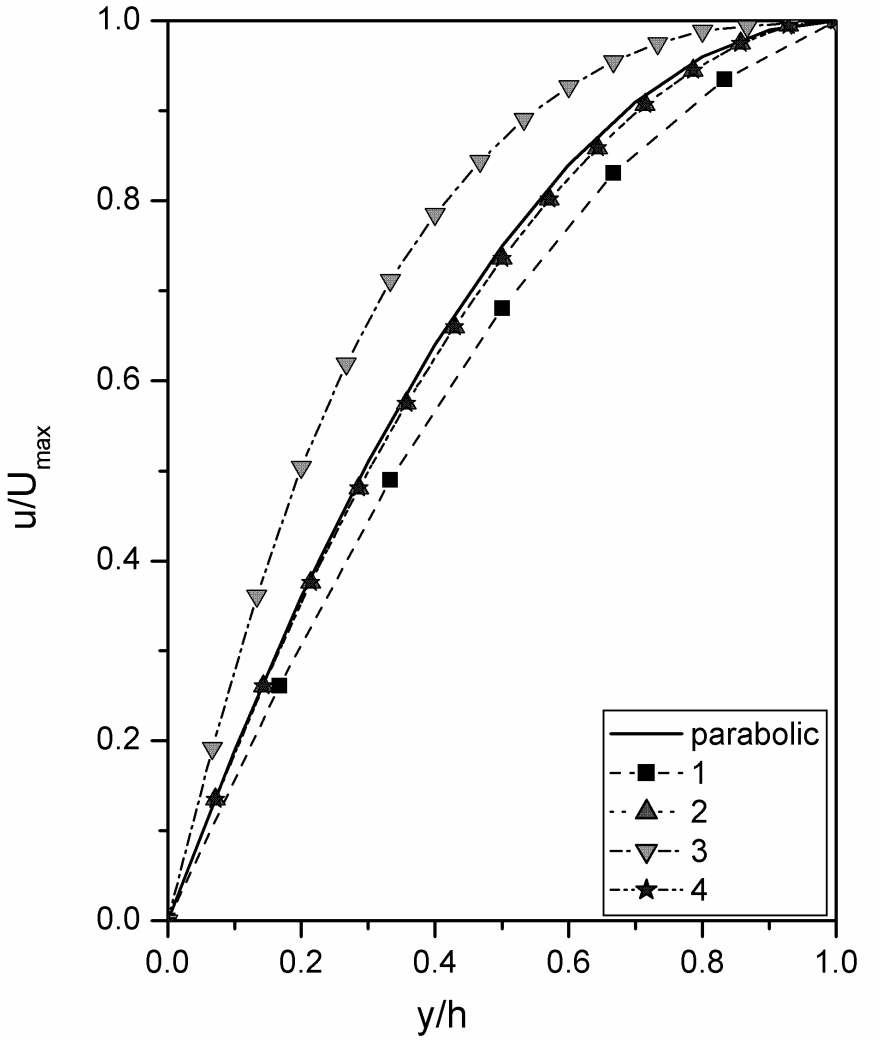

(b) Streamwise velocity profiles in the normal direction for Case C

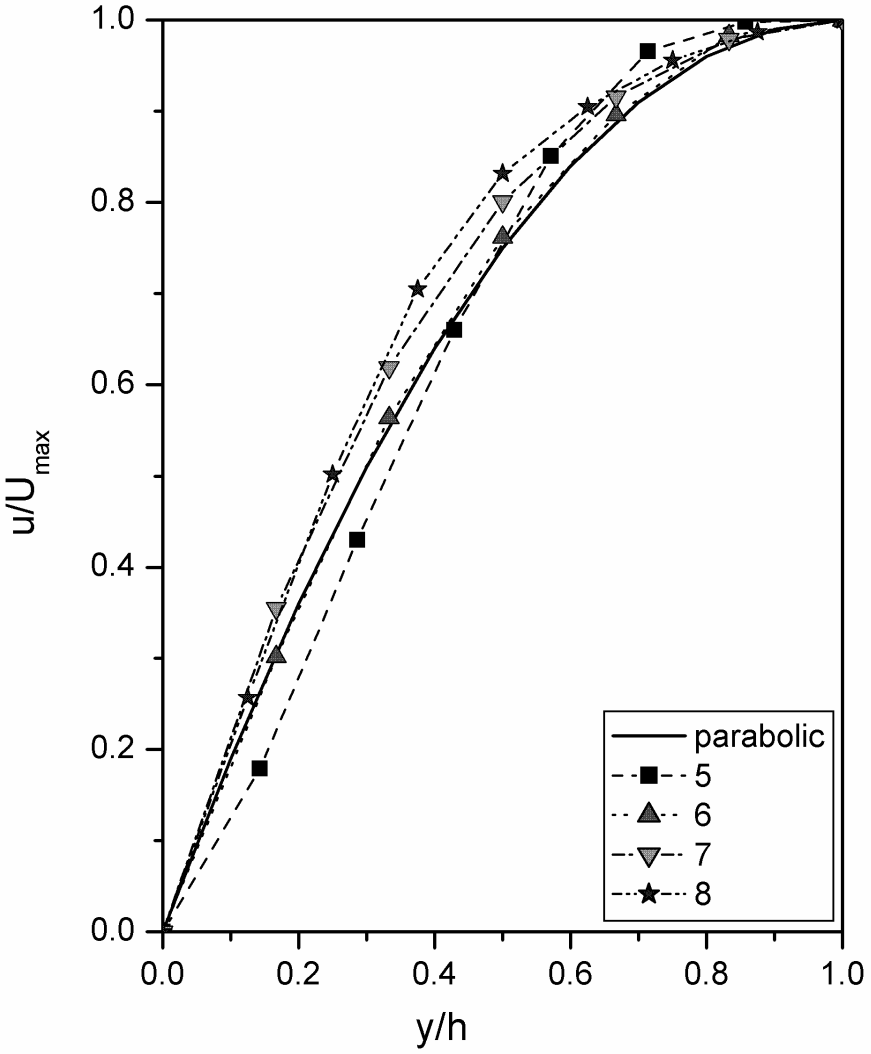

(c) Streamwise velocity profiles in the normal direction for Case C

Figure 6.10: Velocity profiles along the wave for Case C

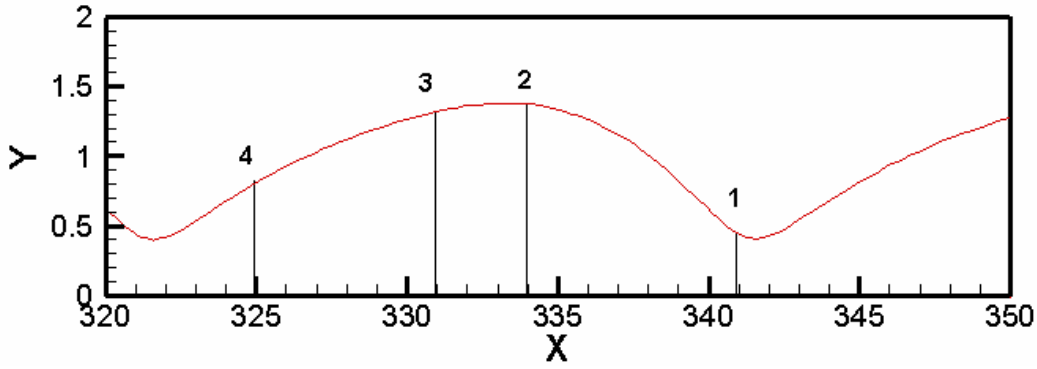

(a) Taken points along the wave

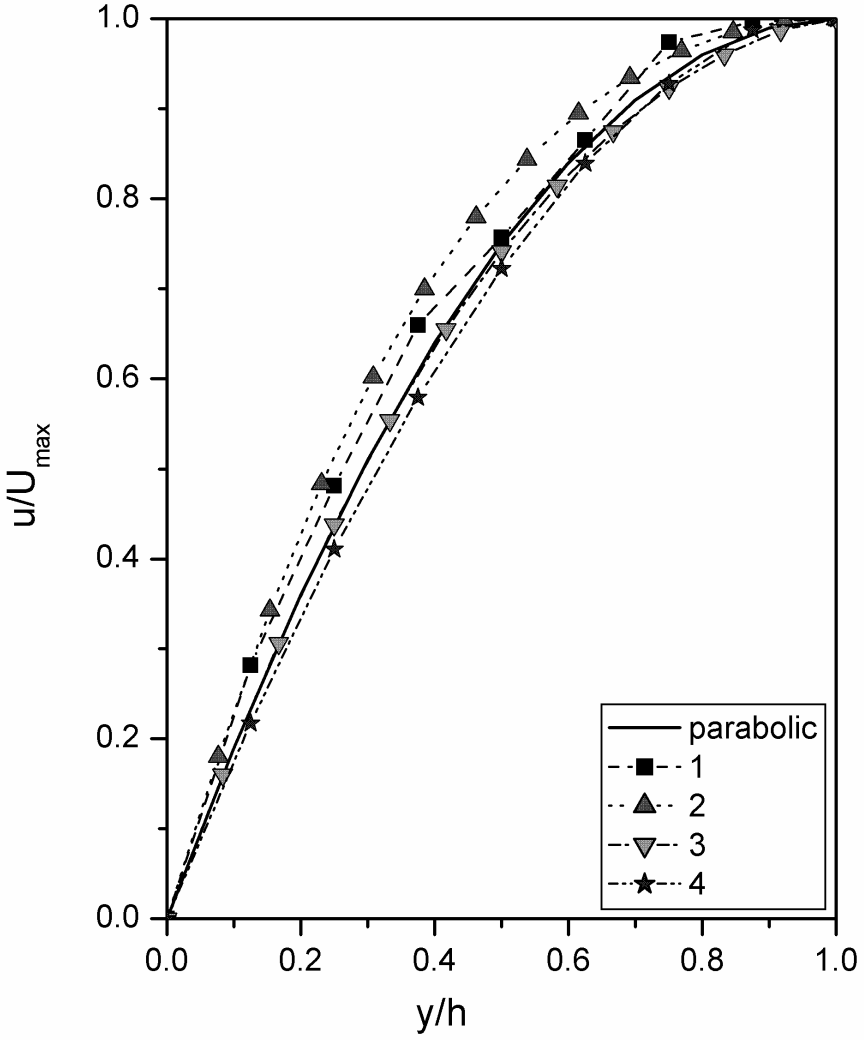

(b) Streamwise velocity profiles in the normal direction for Case D

Figure 6.11: Velocity profiles along the wave for Case D

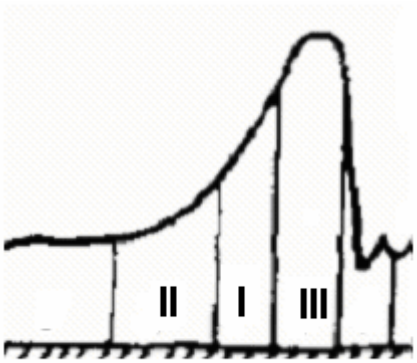

(a) Plot regions in Alekseenko et al. (1985)

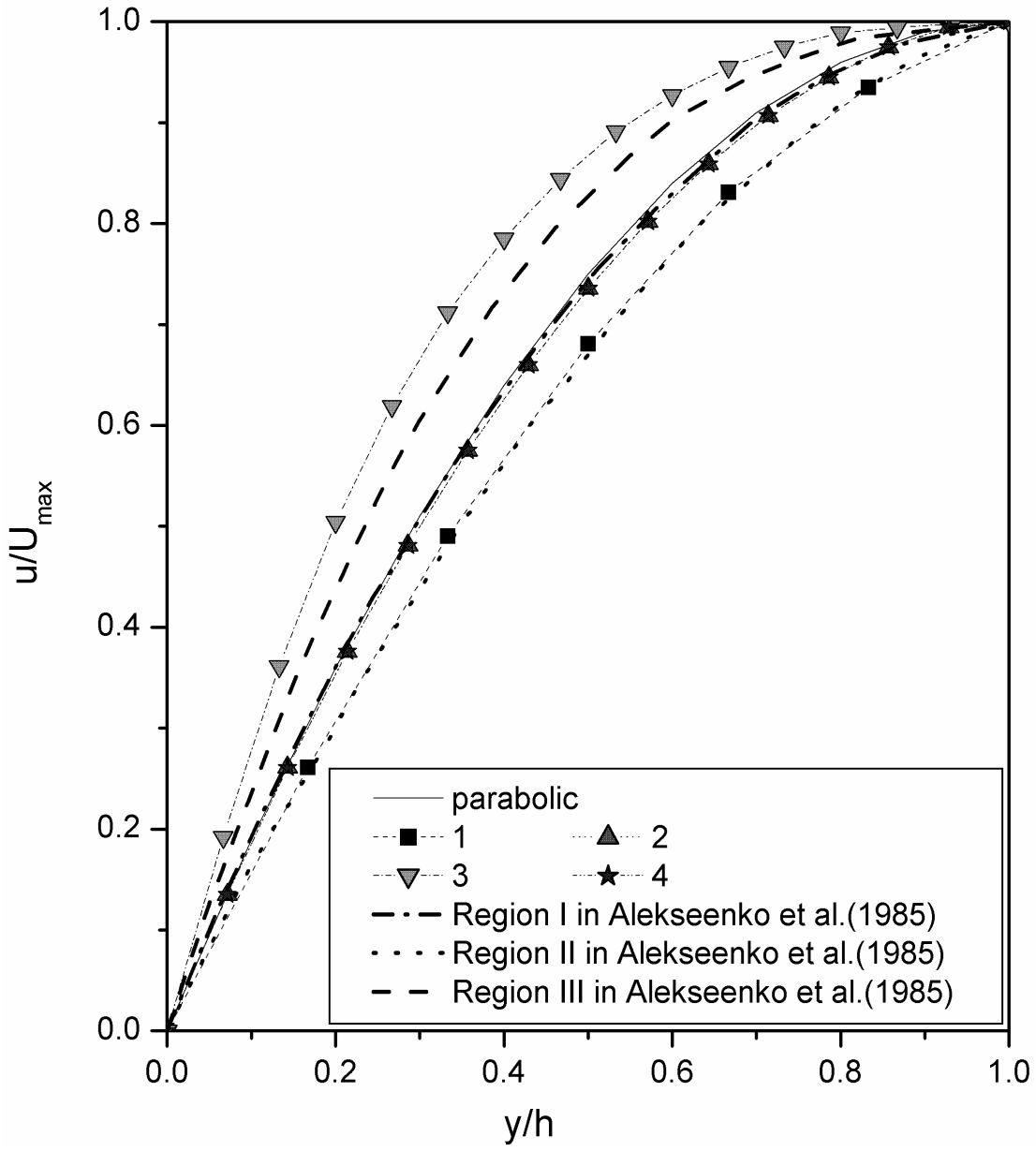

(b) Streamwise velocity profiles in the normal direction for Case C

Figure 6.12: Velocity profile comparison

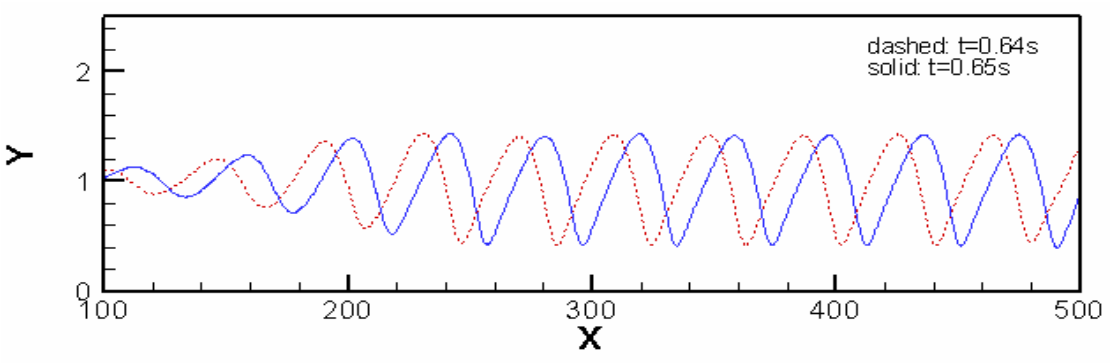

(a) Two trains of wave for Case A

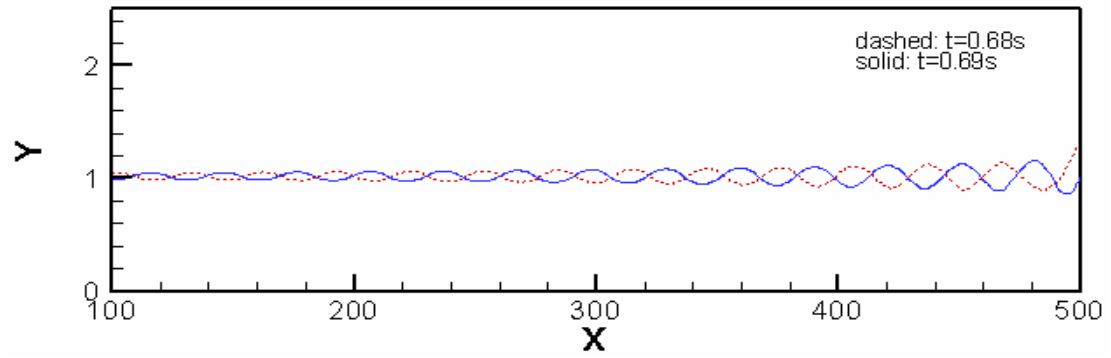

(b) Two trains of wave for Case B

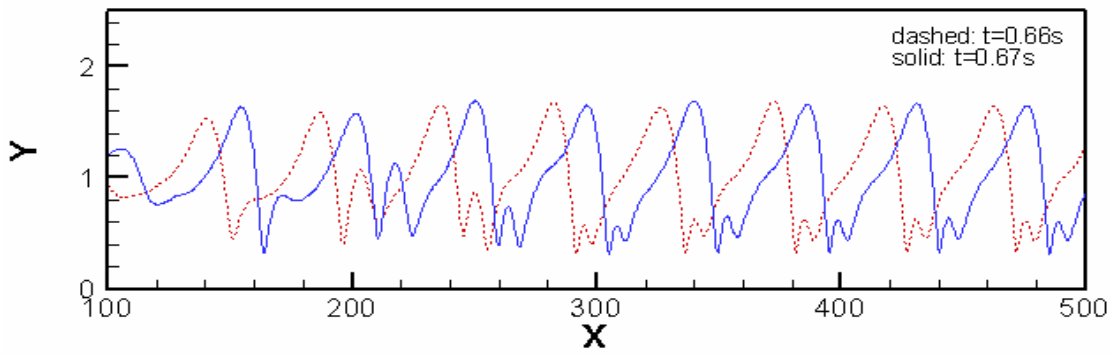

(c) Two trains of wave for Case C

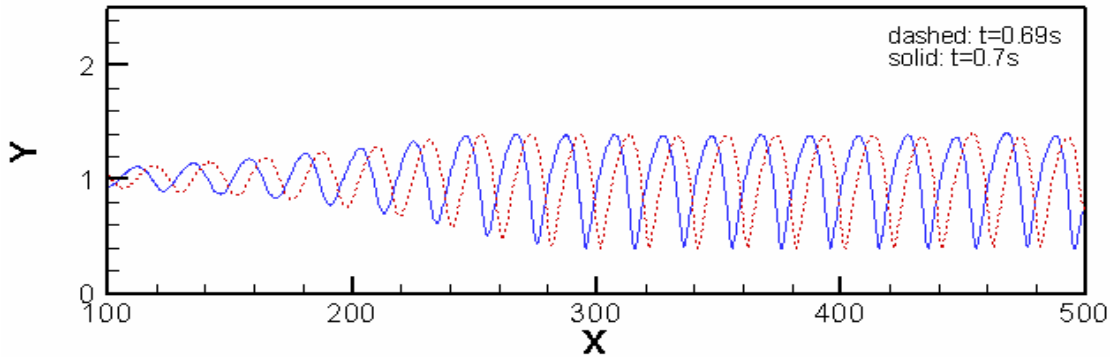

(d) Two trains of wave for Case D

Figure 6.13: Two successive trains of wave

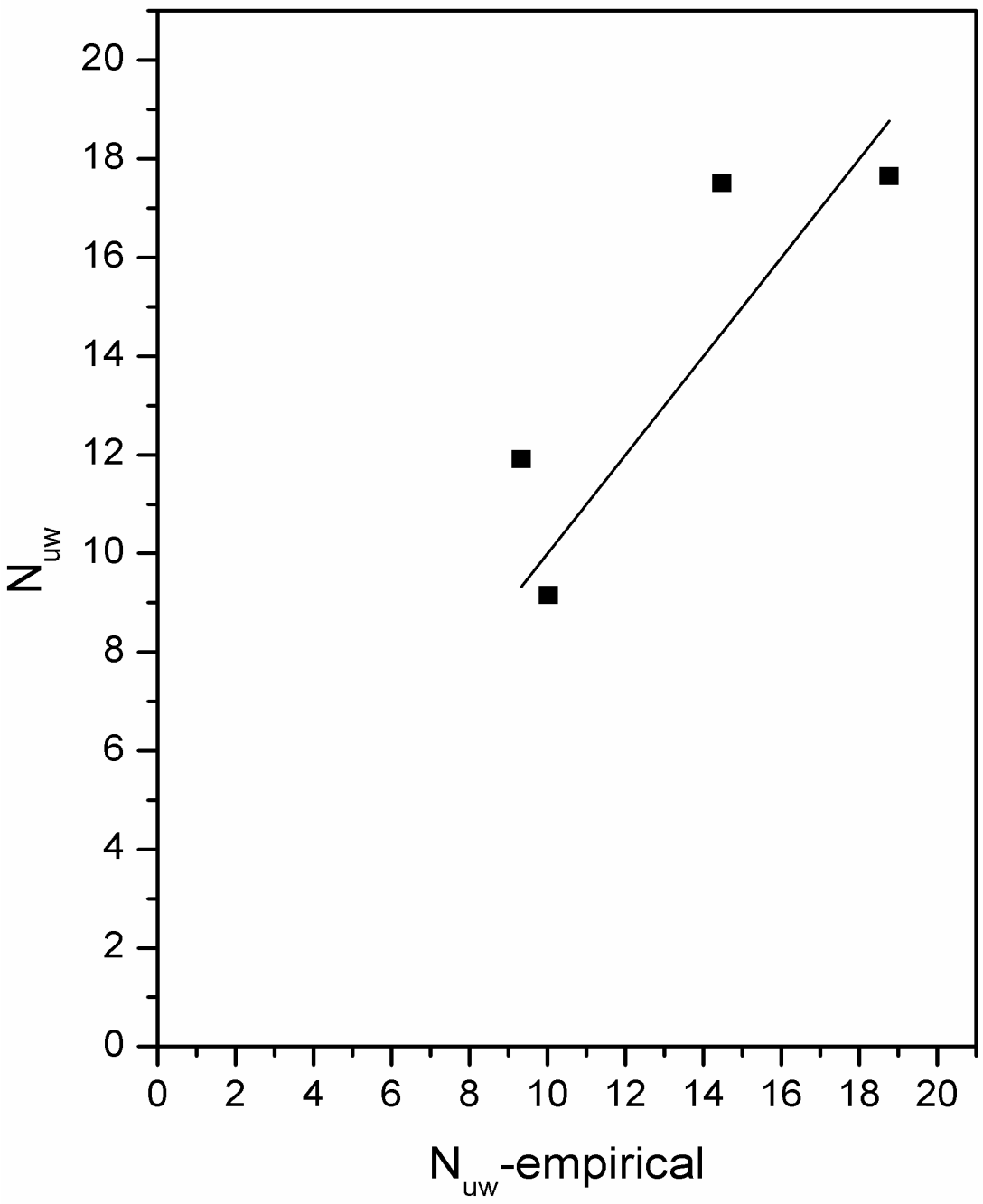

Figure 6.14: Comparison of N_{uw} with Nosoko et al.'s empirical relationship

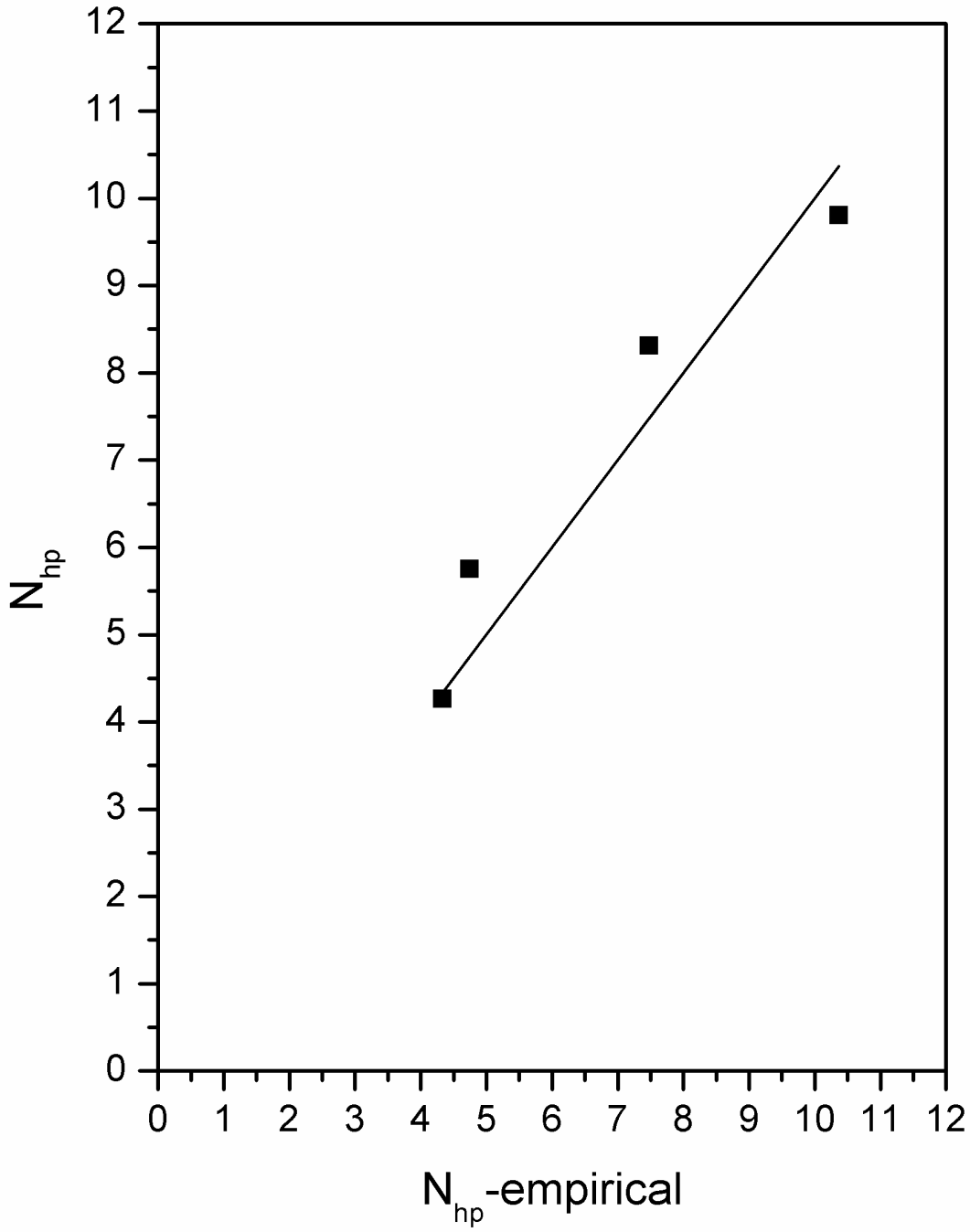

Figure 6.15: Comparison of N_{hp} with Nosoko et al.'s empirical relationship

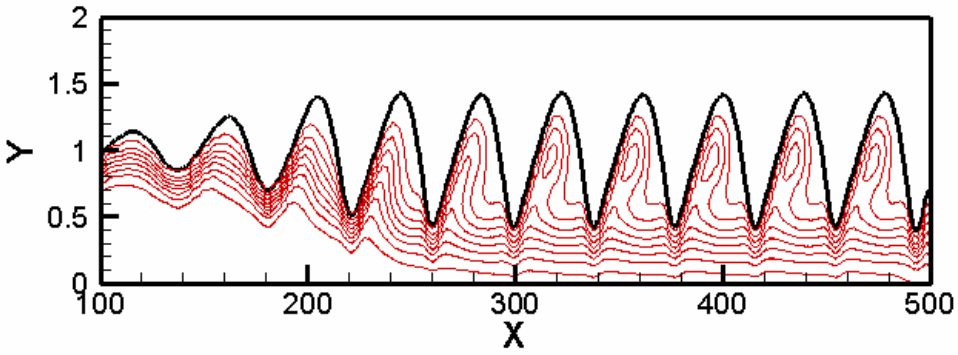

(a) Instantaneous concentration profile for Case A

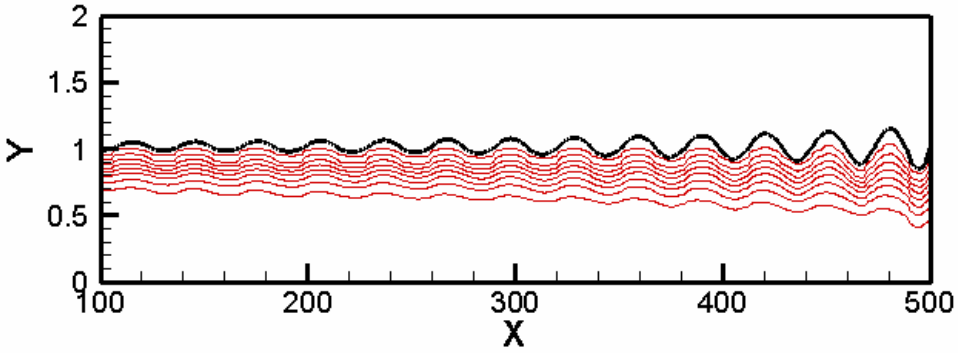

(b) Instantaneous concentration profile for Case B

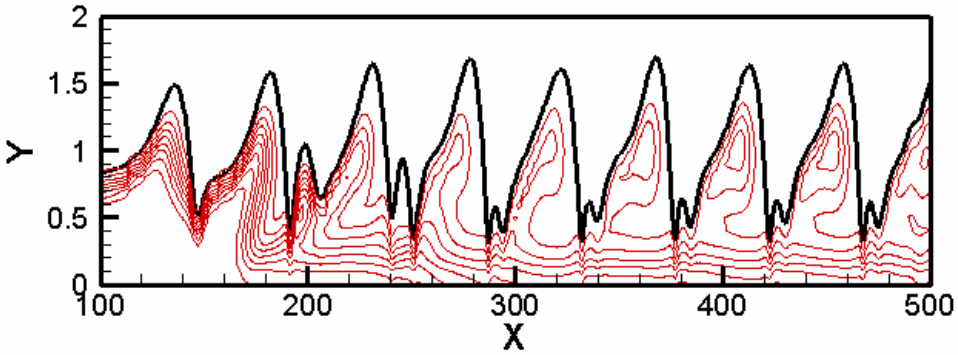

(c) Instantaneous concentration profile for Case C

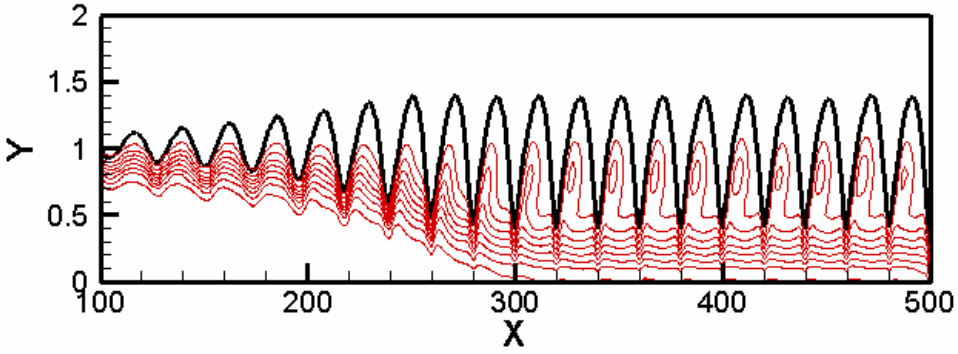

(d) Instantaneous concentration profile for Case D

Figure 6.16: Instantaneous concentration profiles along the wave

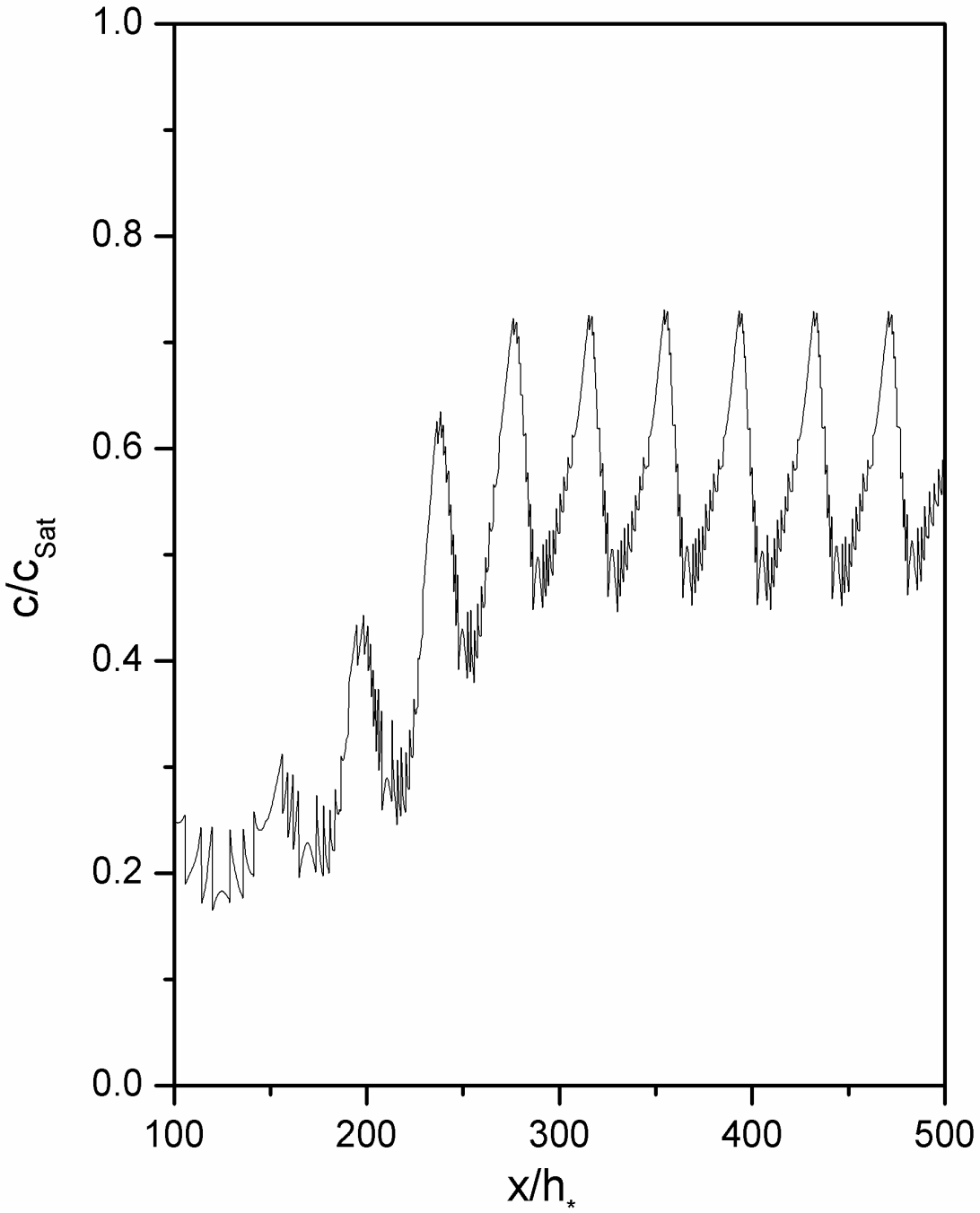

Figure 6.17: Instantaneous bulk concentration variation with non-dimensional distance for Case A

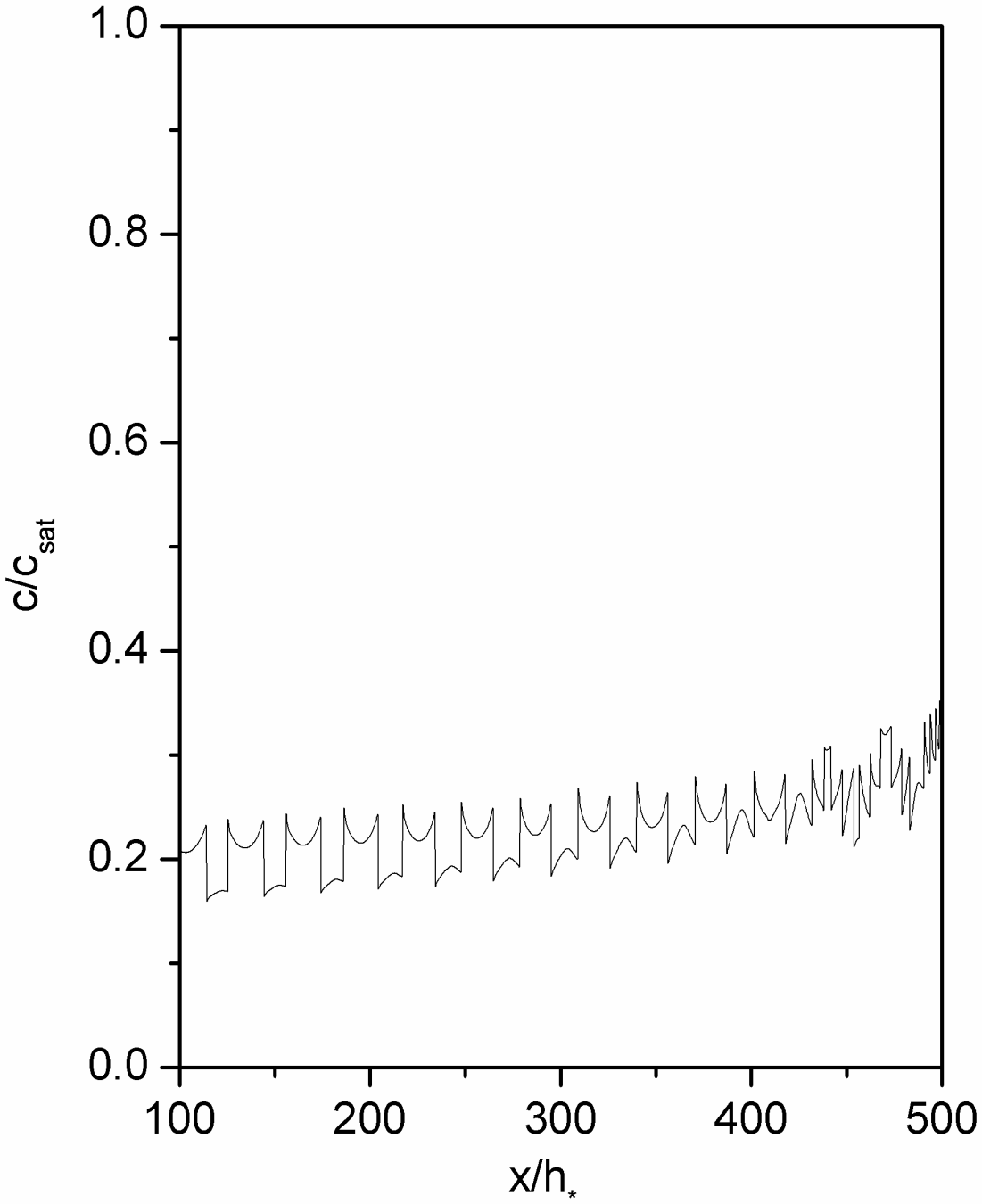

Figure 6.18: Instantaneous bulk concentration variation with non-dimensional distance for Case B

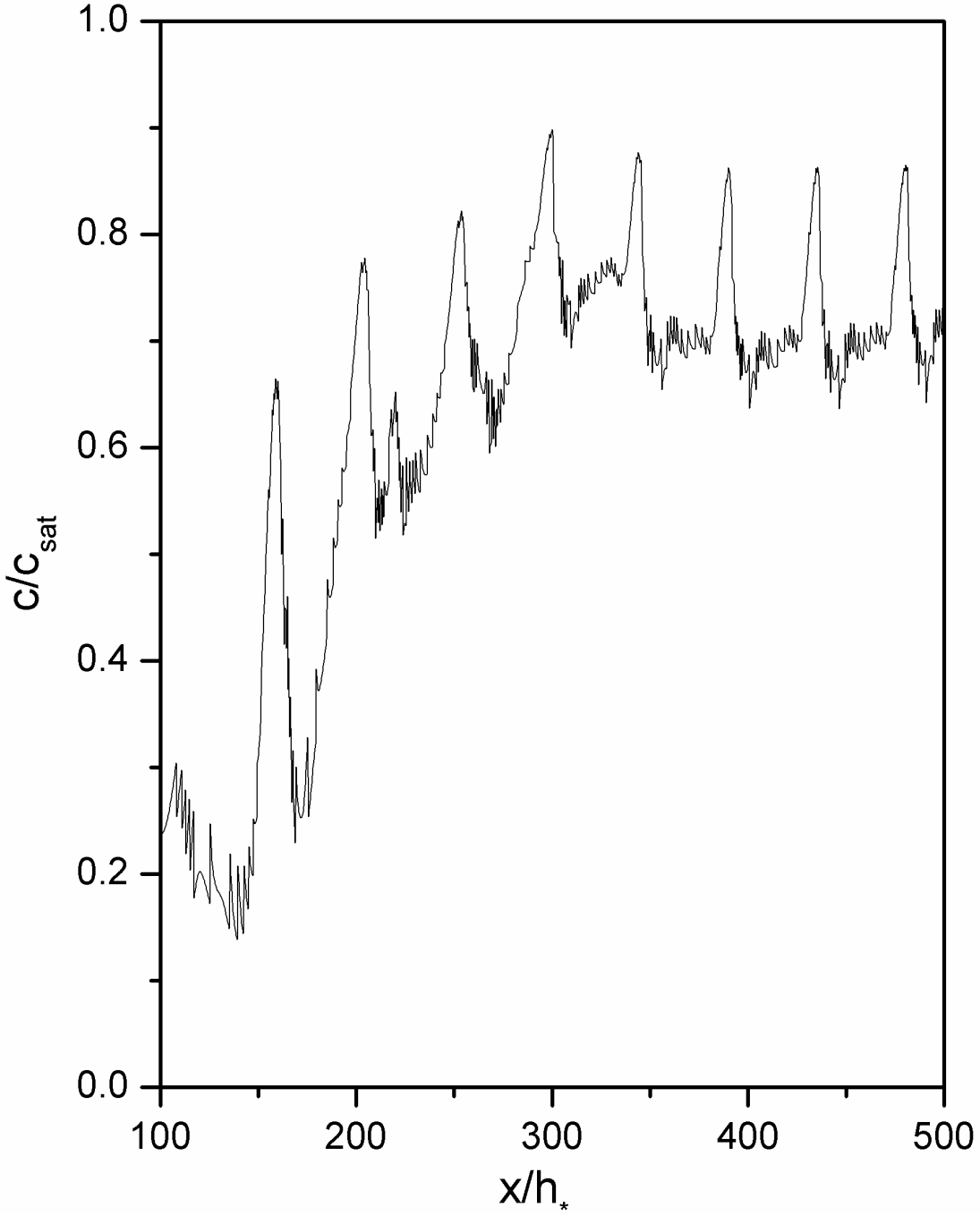

Figure 6.19: Instantaneous bulk concentration variation with non-dimensional distance for Case C

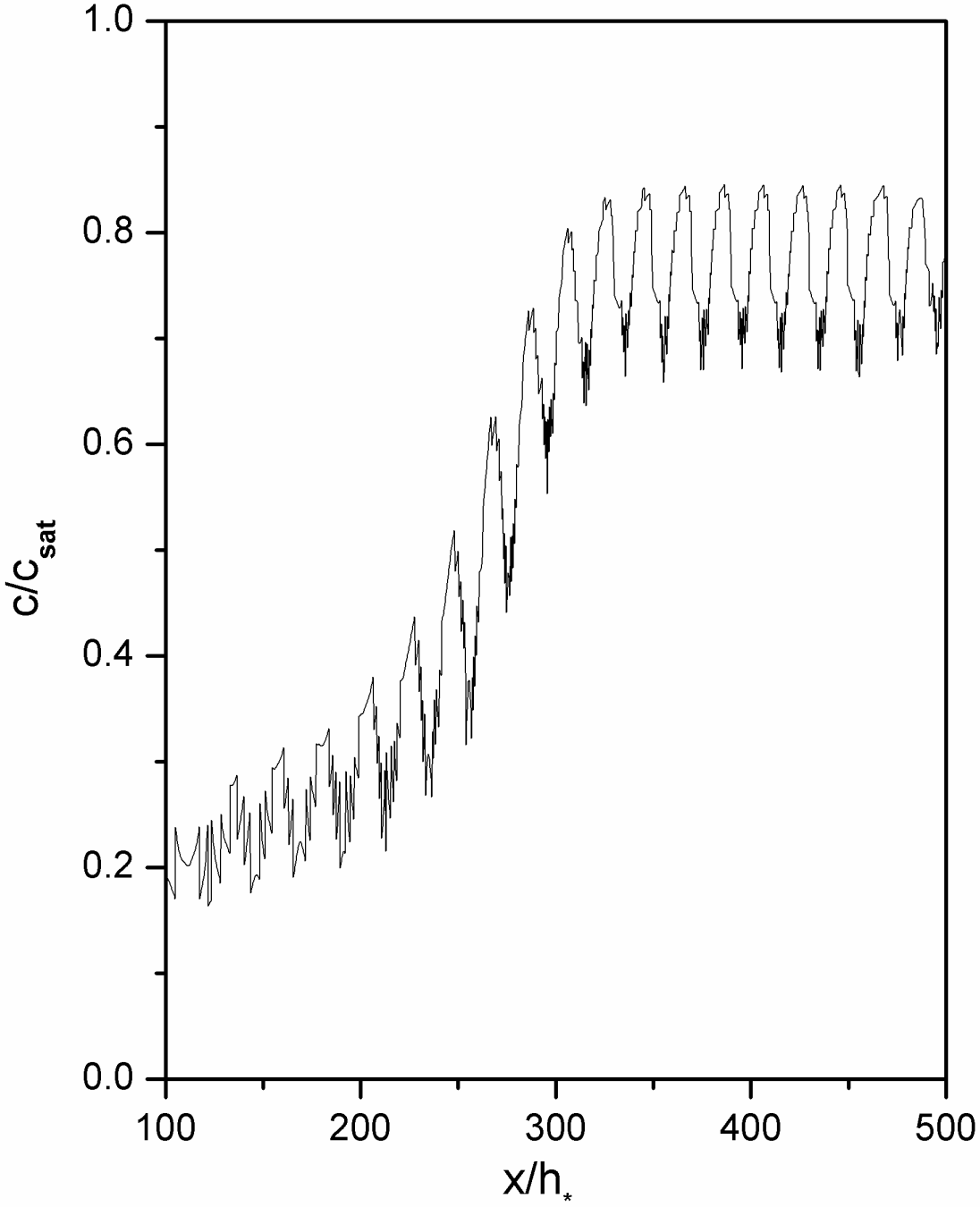

Figure 6.20: Instantaneous bulk concentration variation with non-dimensional distance for Case D

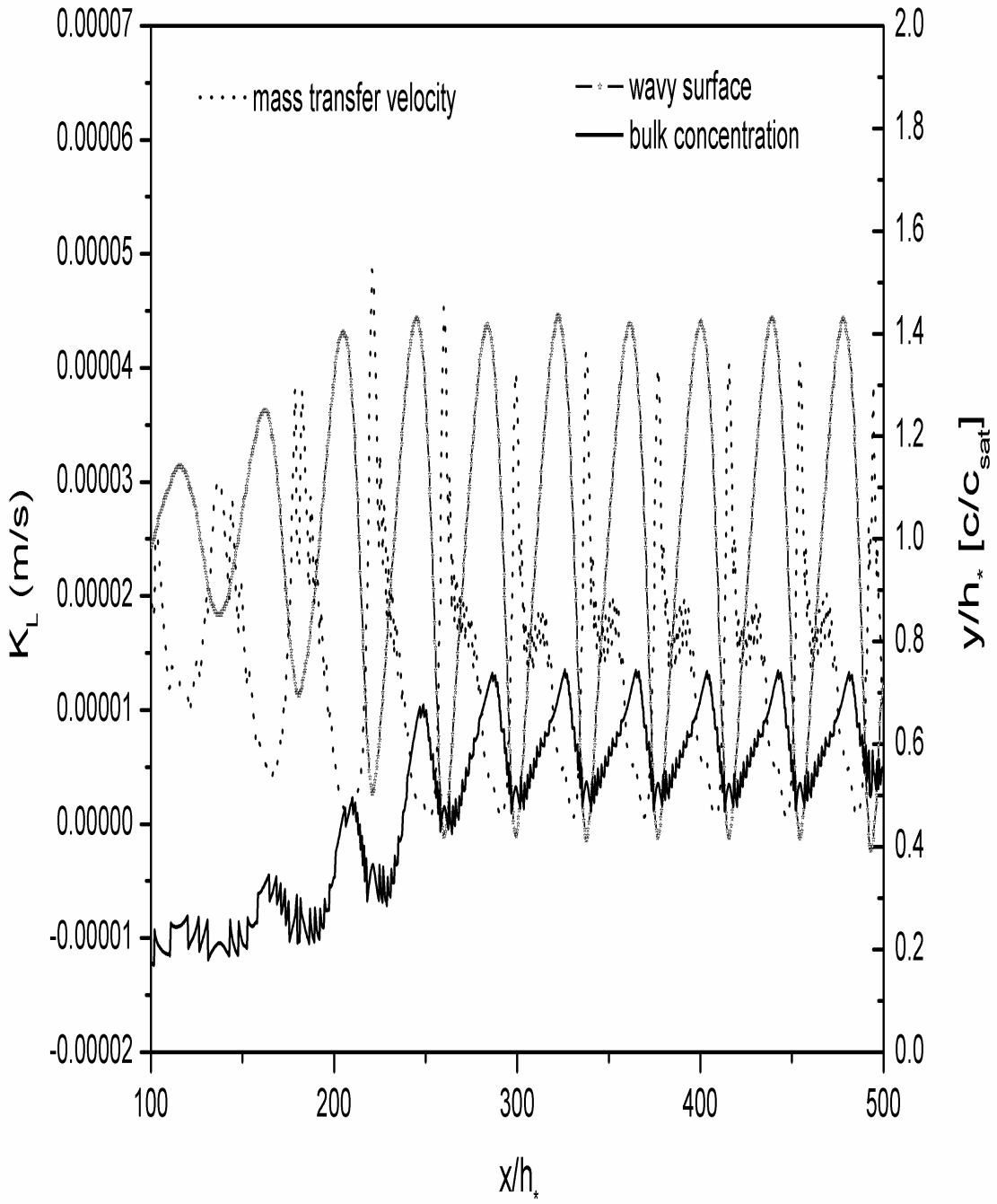

Figure 6.21: Instantaneous mass transfer velocity variation with distance for Case A

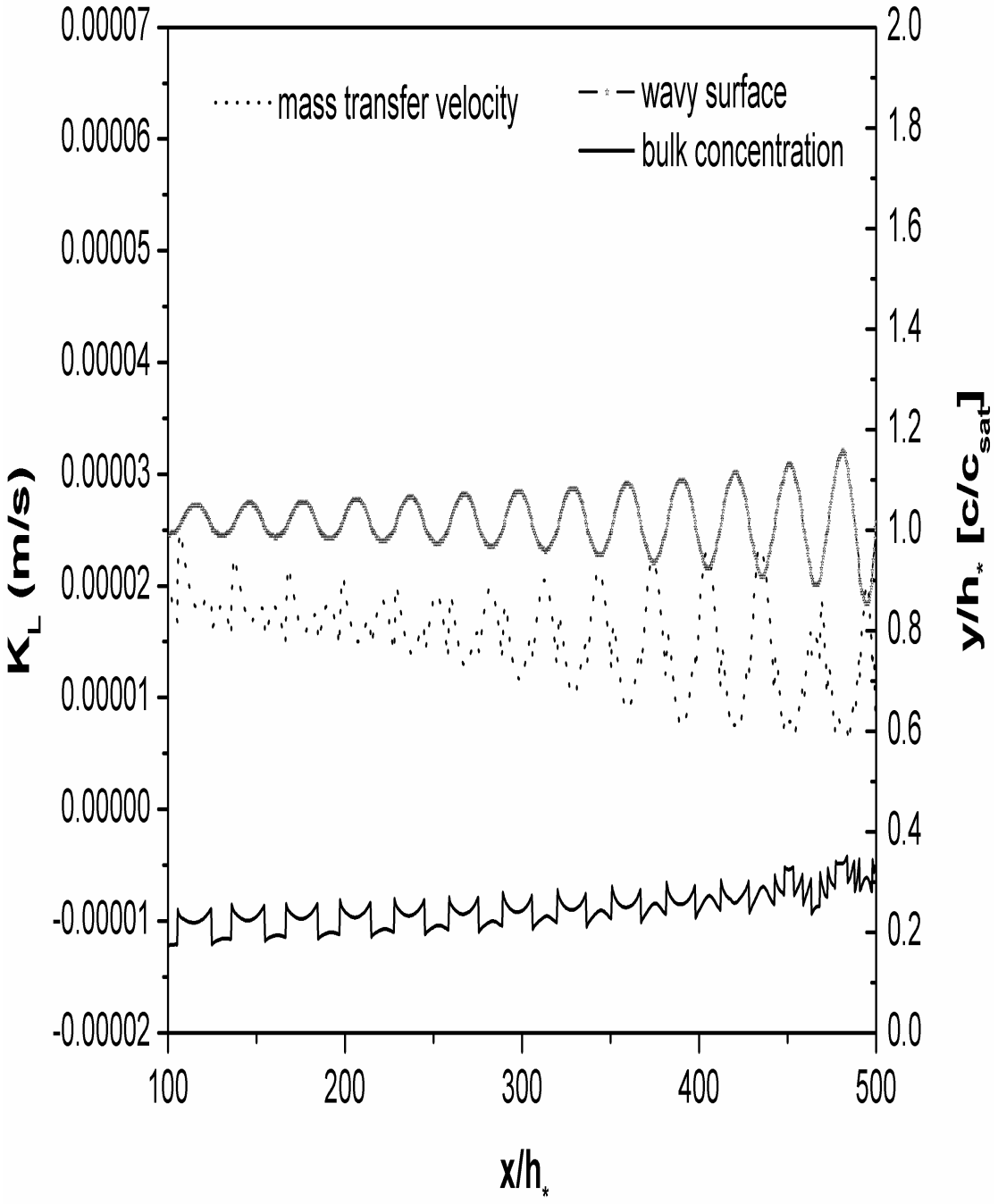

Figure 6.22: Instantaneous mass transfer velocity variation with distance for Case B

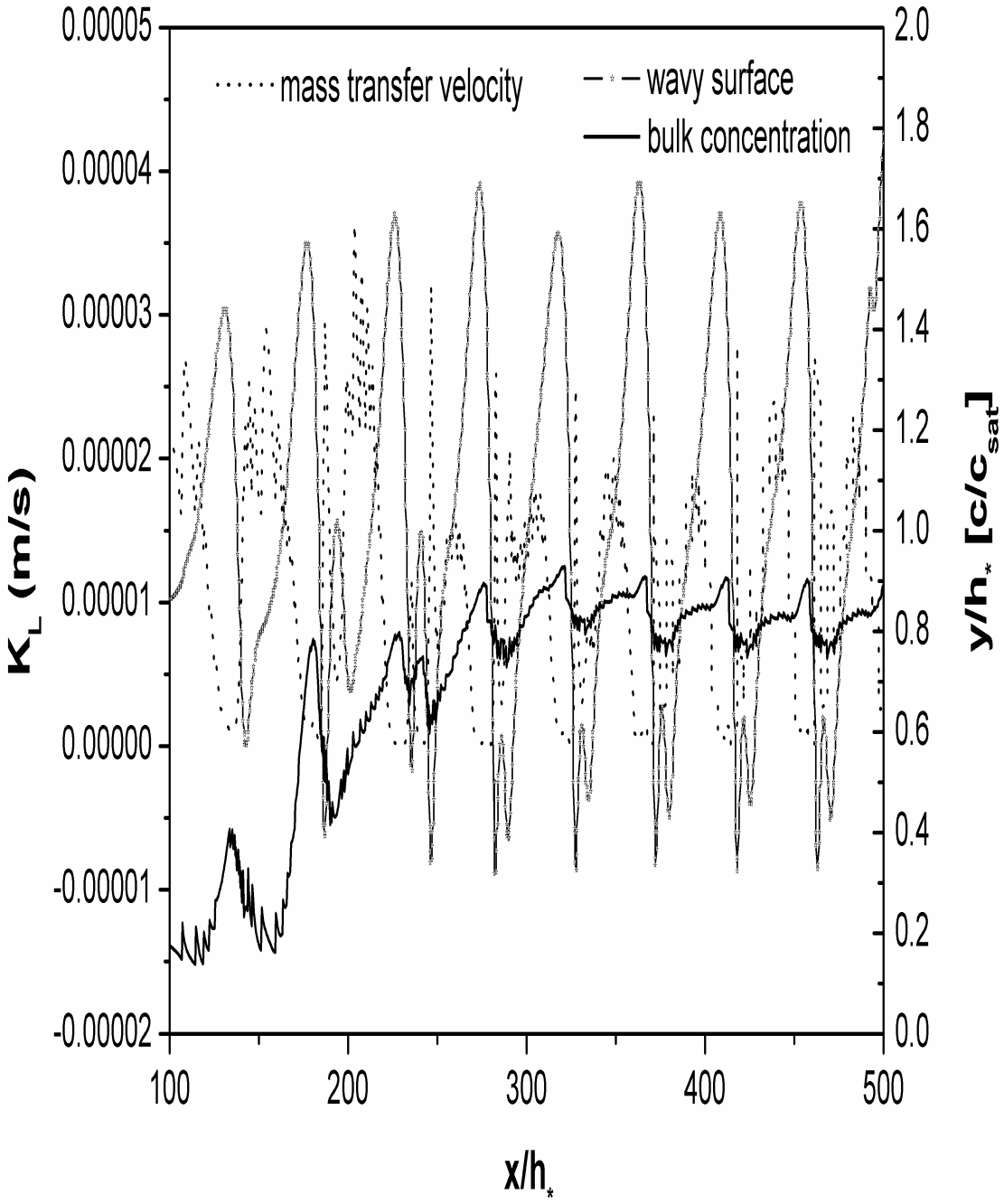

Figure 6.23: Instantaneous mass transfer velocity variation with distance for Case C

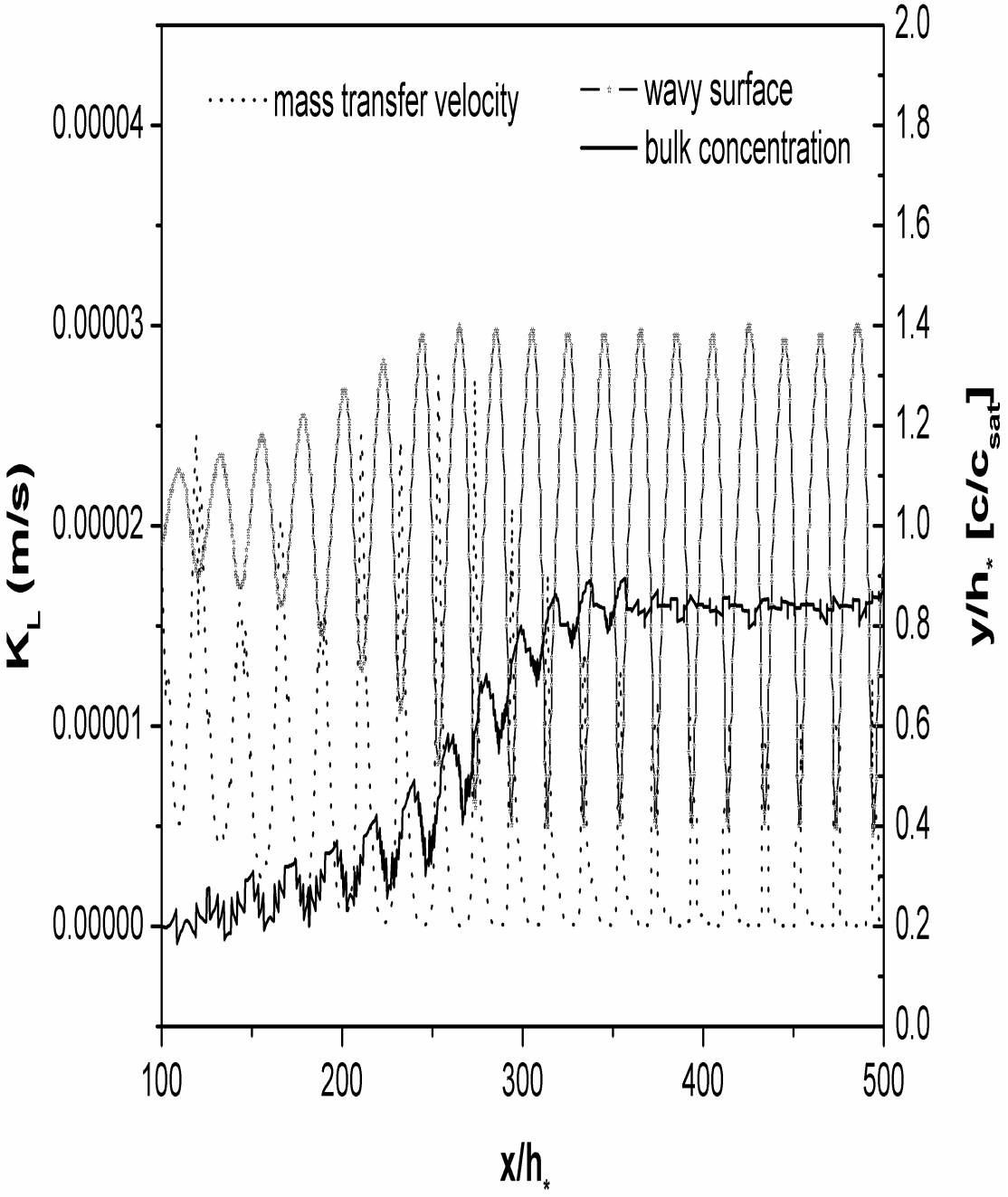

Figure 6.24: Instantaneous mass transfer velocity variation with distance for Case D

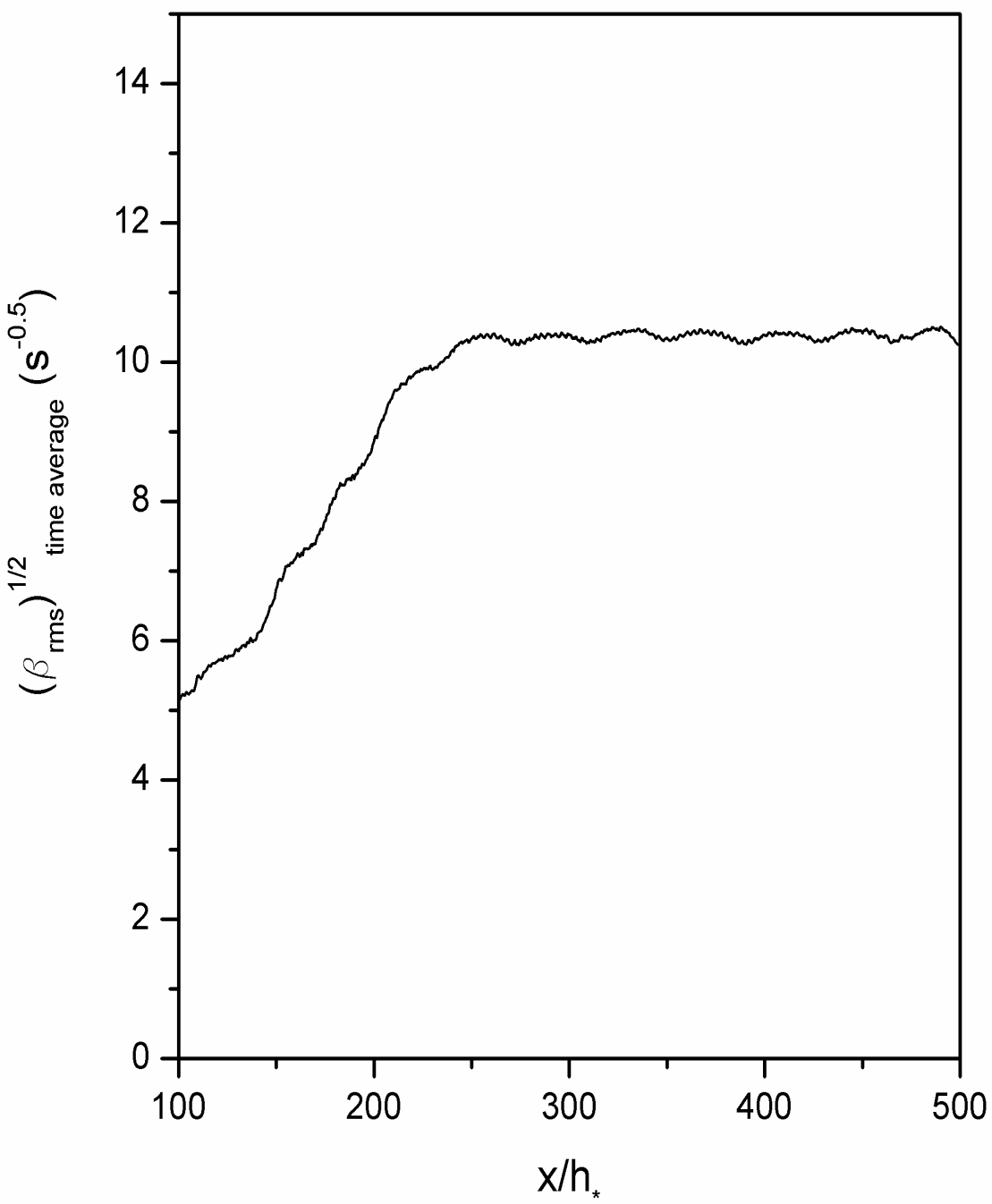

Figure 6.25: Variation of $(\beta_{rms})^{1/2}_{time\ average}$ with distance for Case A

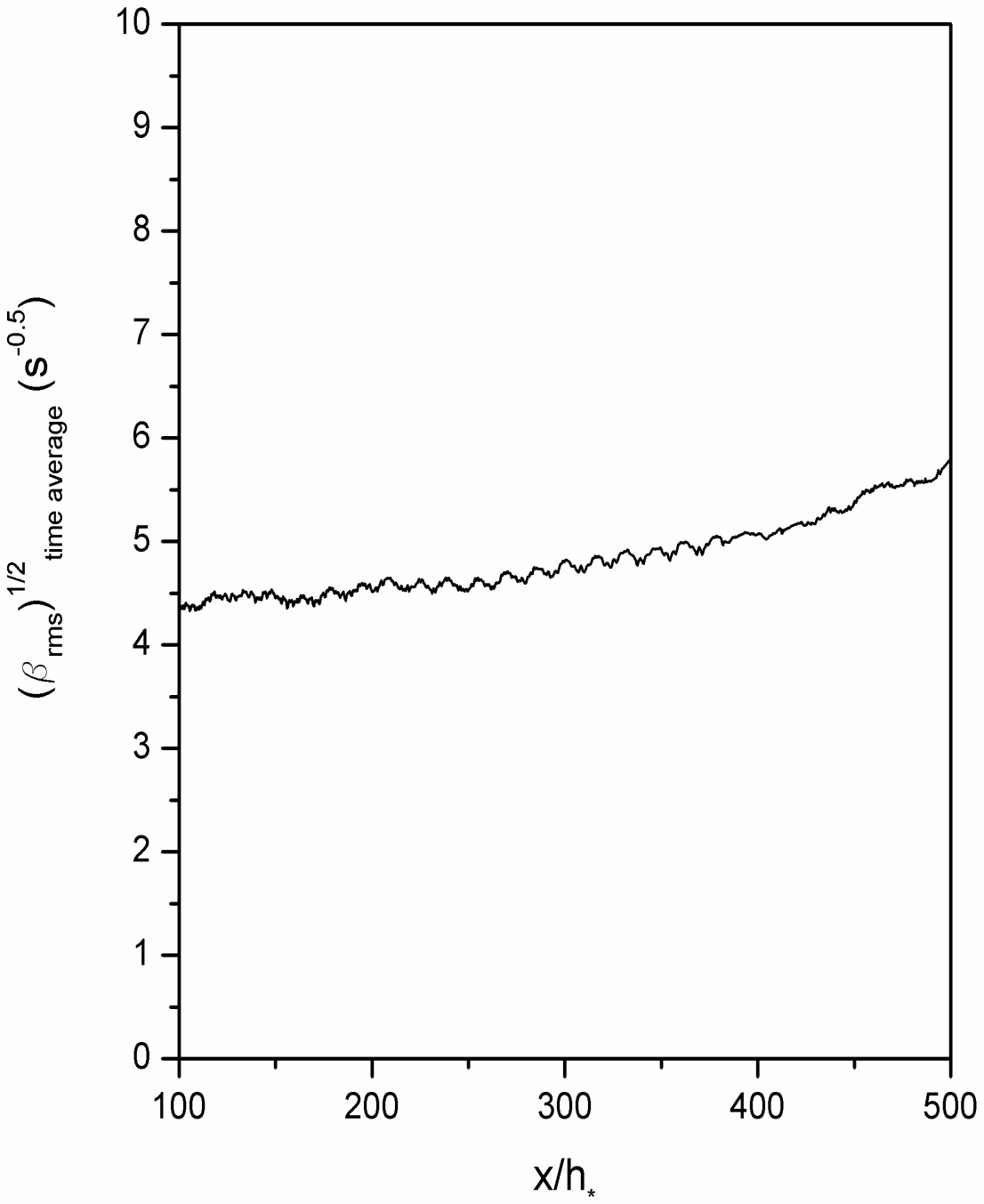

Figure 6.26: Variation of $(\beta_{rms})^{1/2}_{time\ average}$ with distance for Case B

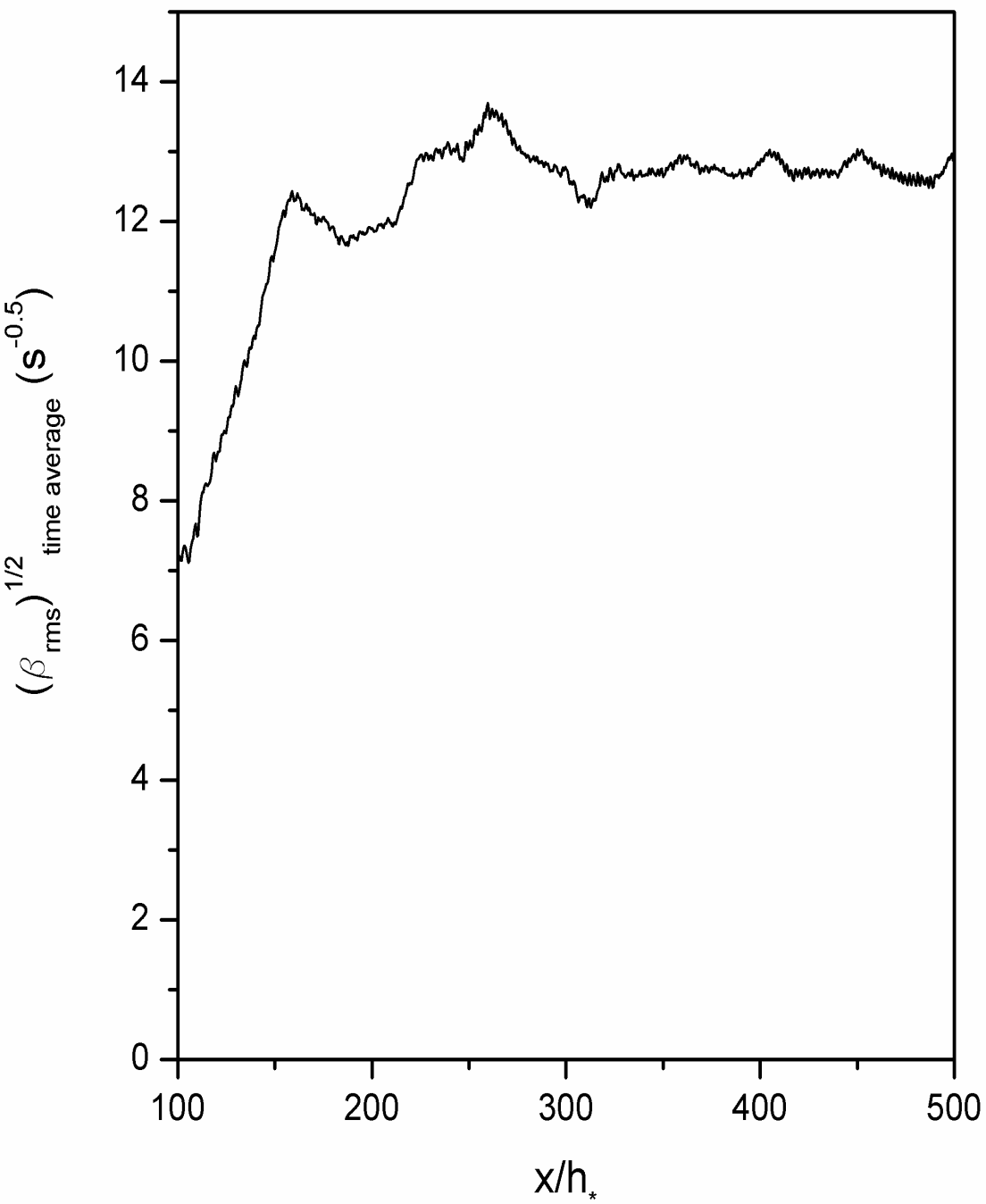

Figure 6.27: Variation of $(\beta_{rms})^{1/2}_{time\ average}$ with distance for Case C

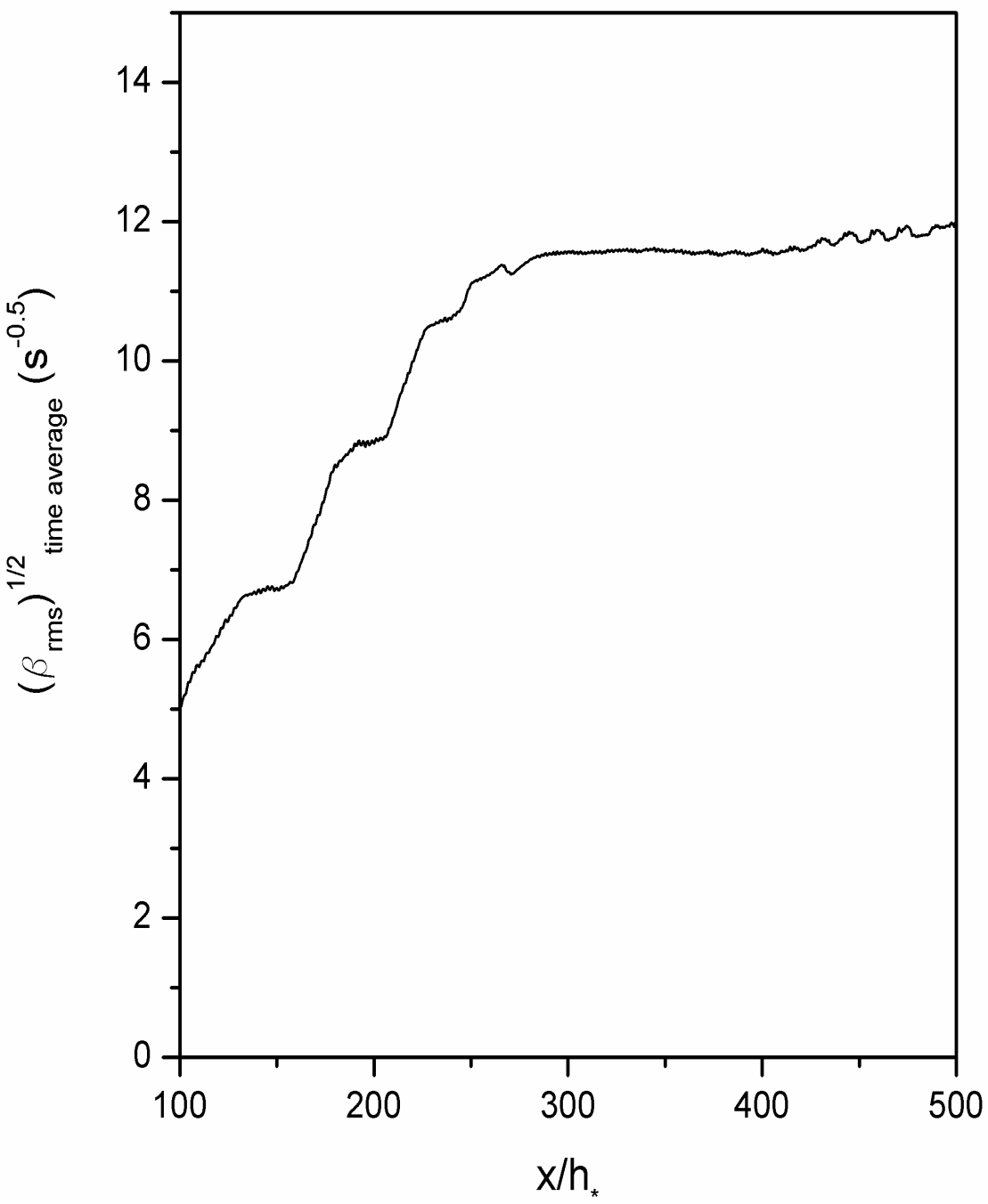

Figure 6.28: Variation of $(\beta_{rms})^{1/2}_{time\ average}$ with distance for Case D

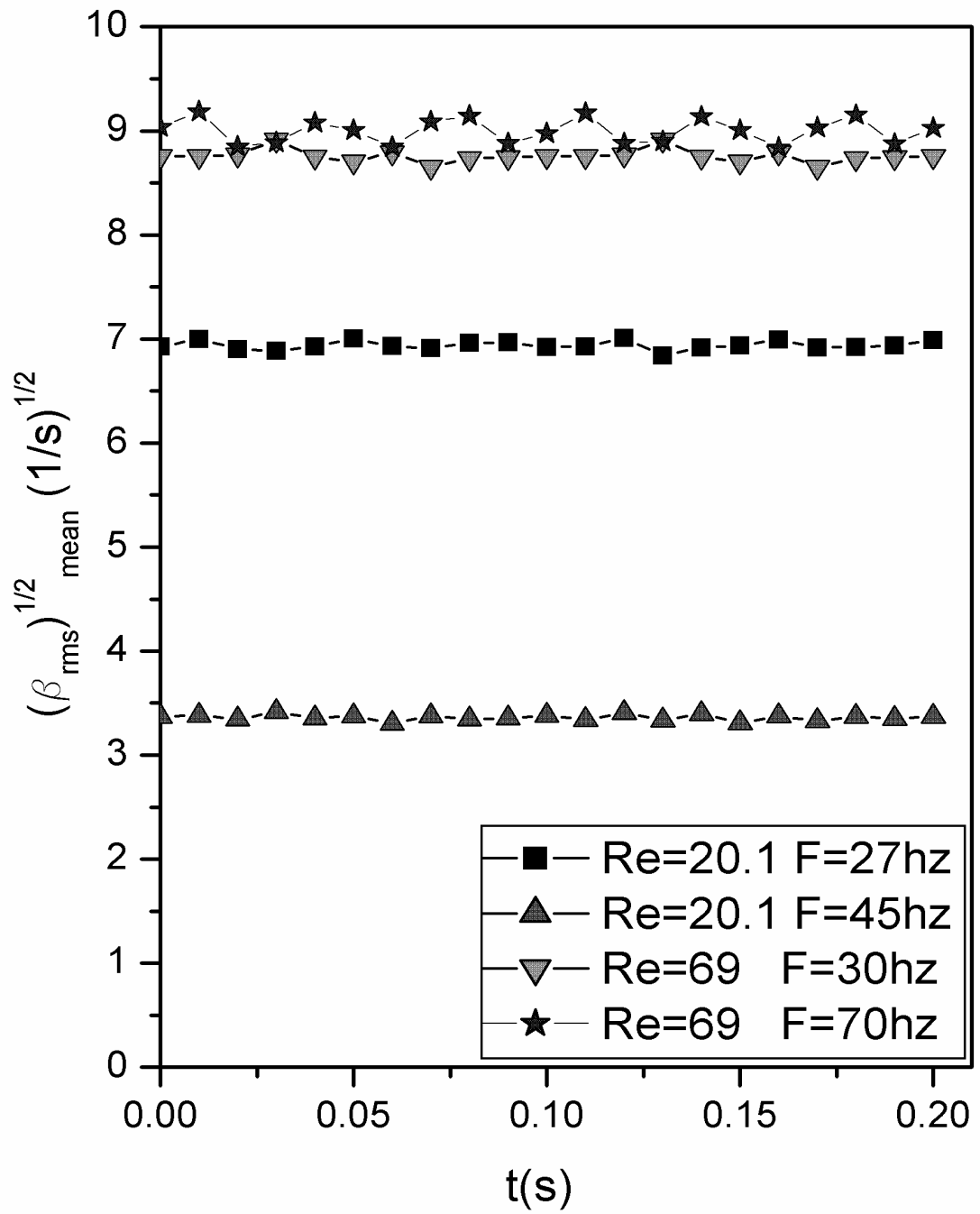

Figure 6.29: Variation of $(\beta_{rms})^{1/2}_{mean}$ with time

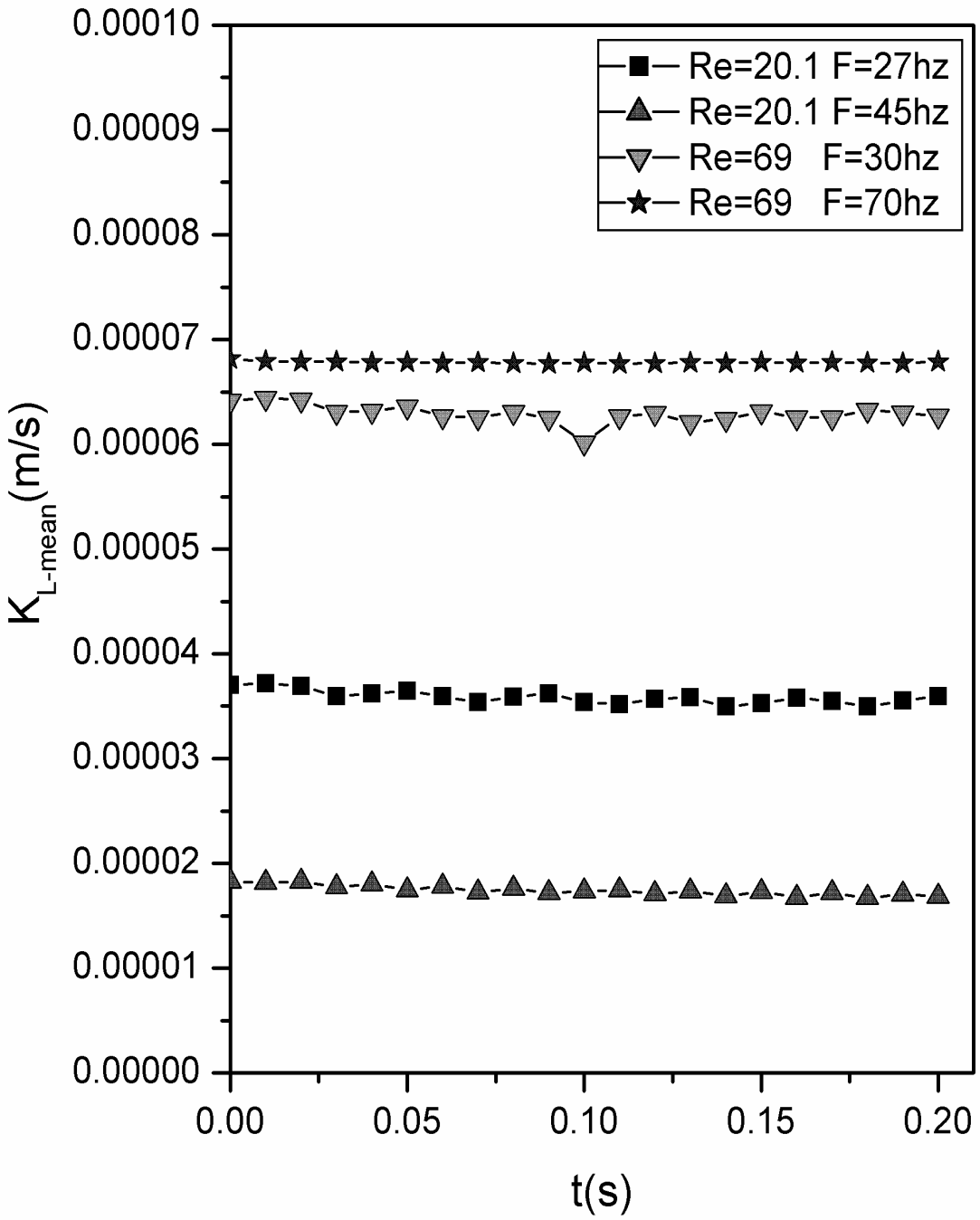

Figure 6.30: Variation of K_{L-mean} with time

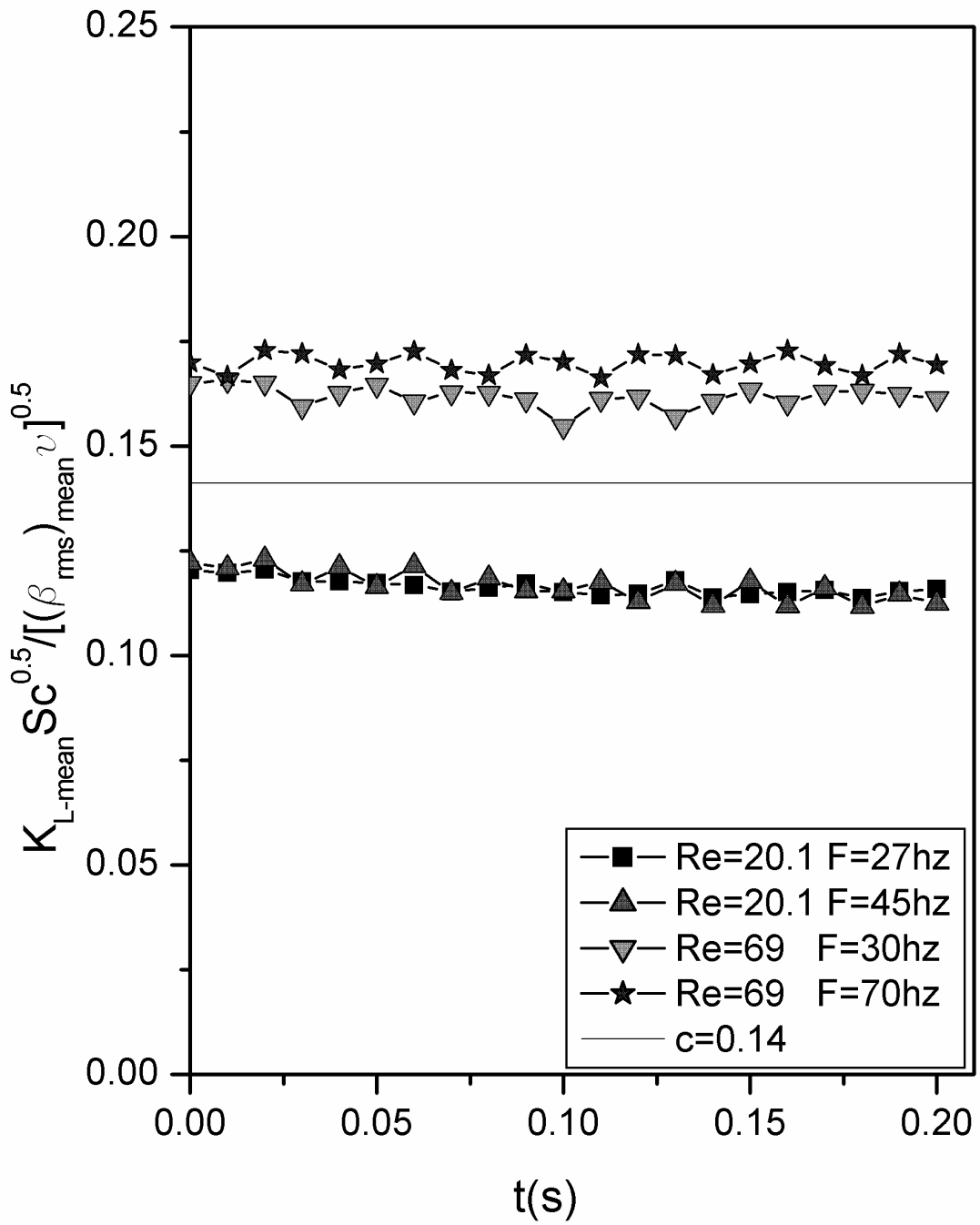

Figure 6.31: Variation of $K_{L-mean}Sc^{0.5}/\left[(\beta_{rms})_{mean}\nu\right]^{0.5}$ with time

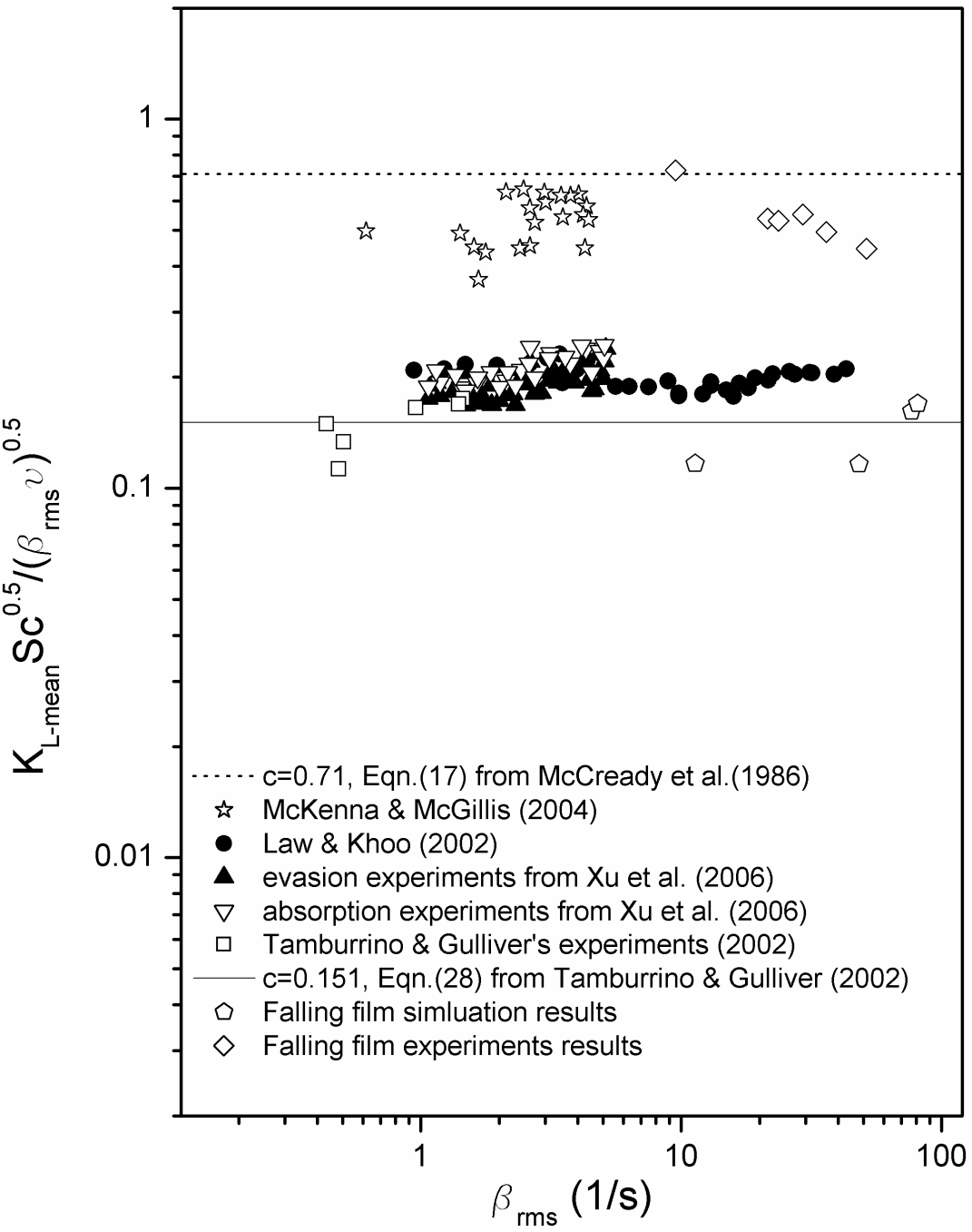

Figure 7.1: Comparison of various works